Stereology And Automated Measurement Of The Human Brain

YIN Kai-Ming

DOCTOR OF PHILOSOPHY

THE UNIVERSITY OF EDINBURGH

2018

DECLARATION

I declare that this thesis was composed by myself, that the work contained herein is my own except where explicitly stated otherwise in the text, and that this work has not been submitted for any other degree or processional qualification except as specified.

YIN Kai-Ming

SIGNATURE: _____

ABSTRACT

Stereology supplies image sampling rules to estimate geometric quantities such as volume, surface area, feature length and number. The method is well suited to non-invasive image acquisition methods such as Magnetic Resonance Imaging (MRI). Meanwhile, in Magnetic Resonance (MR) images analysis area, automated software packages have been continuously developed and become well-established tools especially in human brain MR images processing. The aims of the thesis are (1) to combine proper rules to sample MR images with automated or semi-automated data acquisition methods, in order to implement four different design unbiased stereological volume estimators in the study of the human brain, and (2) to compare volume estimates with those obtained from automated software packages.

In volume estimation of three-dimensional (3D) objects, besides one traditional stereological method (i.e. the CAVALIERI method), in recent years a number of newly design-based unbiased methods have been published, which include three used in this thesis (i.e. the ISOTROPIC CAVALIERI (ICAV), INVARIATOR (INV) and DISCRETIZED NUCLEATOR (DN) methods). The ICAV and INV methods both allow the estimation of surface area too. The ICAV method enables volume estimation to be unbiased and precise in individual objects while the INV and DN methods make it efficient to estimate the mean volume of a big cohort. To make it be practical in estimating the volume of human brain solely from MR images, in the thesis the ICAV, INV and DN methods were given two operating protocols for rotation and measurement on a commercial software (i.e. ANALYZE) and were performed in a fetal brain study. The ICAV, INV and DN methods were also programmed in three scripts for rotation, gridding and measurement purposes respectively using three freely available software packages (i.e. FSL, R and IMAGEJ), which were applied in three adult brain studies.

A fetal brain study was carried out to test the application of the ICAV, INV and DN methods. Ten fetuses from three maternal backgrounds (i.e. five healthy, three maternal psychological stress and two maternal substance misuse) were scanned in MRI at both the second and third trimesters of pregnancy. Then fetal brain images were motion corrected using SLIMMER software. Volumes of brain parenchyma (the functional tissue of the brain which is made of two types of brain cells, namely neurons and glia) including ventricles were estimated by the ICAV method in isotropic (i.e. having no preferred orientation) and uniformly random (i.e. uniformly distance (interval) apart) (IUR) triplet of orthogonal section planes (i.e. the ICAV ortrip method) and by the INV and DN methods in isotropically random (IR) triplet of orthogonal section planes through a fixed pivotal point (i.e. the INV ortrip and DN ortrip methods). Due to

observation of artefacts in MR images and manual input in the methods, inter- and intra-rater reliability studies were performed to investigate both point counting for the ICAV method and segment length measurement for the INV and DN methods among three raters on five fetal brains from the second and five from the third trimesters. Surface area was also estimated using the ICAV method for error prediction. High reliability (Pearson's $r > 0.997$) was shown in inter- and intra-rater studies. In both the second and third trimesters, there were no significant difference in mean volumes of all ten brains estimated by the three methods ($p > 0.1$). For individual estimates, The predicted coefficients of error (CEs) for the ICAV method were $1.5\% \pm 0.1\%$ in the second trimester and $2.1\% \pm 0.1\%$ in the third trimester. Basing on one IR section plane for each data, empirical CEs for the INV method in both trimesters were $19.4\% \pm 2.9\%$ and $18.5\% \pm 11.6\%$, and were $21.4\% \pm 4.5\%$ and $24.1\% \pm 11.7\%$ for the DN method. CEs could be decreased to 8.1%, 5.5% for the INV ortrip method and 10.3%, 9.7% for the DN ortrip method in both trimesters. This study showed the ICAV method performed precisely in individual volume measurements while the INV and DN methods worked efficiently in population mean volume estimation. Clinically, no significant differences ($p > 0.05$) of fetal brain volumes among three maternal groups were detected due to small sample size although potentially in comparison with normal fetal brain, volume might be bigger in the maternal stress group and might be smaller in the substance abused group.

As the CAVALIERI method is a design-unbiased method, the main source of potential bias (i.e. if a biased method is applied the mean of the estimated values deviates significantly from the true value) will come from observers in operation who would be the author in this PhD study. To examine whether there is bias caused by the author's manual point counting procedure in the CAVALIERI method, a slice-by-slice comparison on one adult brain volume estimation on MR images between the CAVALIERI method and an automatically reconstructing software (i.e. FREESURFER) was performed. One healthy elderly (male, age 71) brain MRI scan with good image quality was selected from a dataset of 40 patients affected by the ALZHEIMER's disease (AD) and 22 healthy elderly volunteers. FREESURFER was used to perform individual volumetric analysis on the adult brain automatically, which outlined grey matter and white matter in the cerebrum on each MR image slice. The CAVALIERI method was applied to a series of coronal images obtained with random starting position and at 1 cm intervals from the TALAIRACH transformed and intensity normalized 3D MR image (i.e. nu.mgz) displayed with the compartment boundaries identified by the FREESURFER pipeline suppressed. The uniformly random (UR) test system for point counting was superimposed on each image. The CAVALIERI method in combination with point counting strategy was used to estimate the volume of cerebrum excluding ventricles (the sum of the two cerebral hemispheres including blood vessels and meninges) using EASYMEASURE software on the grey scale MR images. Additionally, the author overlay the brain boundary segmented by FREESURFER on these selected test points and reassessed the images to compute two scores, namely (i) the total number of test points which had been counted but which were seen to lie outside the FREESURFER segmentation and (ii) total number of the new test points that now needed to be additionally included as lying within the FREESURFER segmentation.. The cerebral volume was 972 cm^3 estimated

by FREESURFER and 960 cm^3 by the author using the CAVALIERI method with CE of 0.34%. FREESURFER had 1.3% bigger measure than that estimated by the author. FREESURFER aided point counting estimate was between 948 cm^3 and 982 cm^3 with mean volume of 965 cm^3. The ratio of points counted by the author but were outside the pial boundary segmented by FREESURFER to total points number counted was between 2.6% to 4.0%, and the ratio of test points not counted by the author but were inside the pial boundary segmented by FREESURFER to total points number counted was between 2.7% to 4.9%. Therefore the author's estimate was in the range of FREESURFER aided estimation by the CAVALIERI method and both volume ratios were close to each other. No bias could be found between the author using the CAVALIERI method and FREESURFER, which gives the author confidence in performing following studies.

Furthermore, volume difference of cerebrum excluding ventricles between AD patients and healthy people were investigated using four stereological methods (i.e. the CAVALIERI, ICAV, INV and DN methods) and the FREESURFER software. From the same dataset of 40 AD patients and 22 healthy elderly volunteers, brain MR images of 13 patients and 13 volunteers were selected with good image quality. Inter-reliability and intra-repeatability studies were performed by two observers on three AD and three normal ageing brains. Both the inter-reliability and intra-repeatability studies showed good consistency. There was no significant difference of individual measures among the CAVALIERI and ICAV methods and FREESURFER. The average time taken for each cerebral volume estimation was less than 15 mins by each of the CAVALIERI, ICAV, INV and DN methods. Clinically, the cerebral volume was significantly smaller in the AD patients, which were found using both the CAVALIERI ($p = 0.01$) and ICAV ($p < 0.01$) methods and FREESURFER ($p = 0.01$) although the INV and DN methods were not able to detect this difference. In this adult brain group study, the volume estimates from the CAVALIERI and ICAV methods were competitive with those obtained from FREESURFER, while the INV and DN methods might be more useful if being applied with a larger sample size or the INV ortrip and DN ortrip methods were applied.

Lastly, a systematic investigation on potential imaging biomarkers for AD was performed by the FREESURFER software, one of the imaging biomarkers (i.e. volume ratio of cerebrum excluding ventricles to intra-cranium (the contents of the skull above the level of the foramen magnum)) was re-examined by the INV method manually. From the same dataset of 40 AD patients and 22 healthy elderly volunteers, the brain MR images of 27 AD patients and 16 healthy elderly controls between the maximal common age scope of 47 to 71 were selected, which were analysed by FREESURFER for each brain region. Furthermore, to see the effect of AD on normal ageing atrophy, the difference of volume ratios of each brain region to whole brain between AD patients and healthy controls was investigated. Volume ratios of many brain parenchymal regions (e.g. hippocampus (left $p = 0.002$, right $p < 0.001$), amygdala (left $p < 0.001$, right $p < 0.001$), accumbens area (left $p = 0.002$, right $p = 0.001$), left putamen ($p = 0.037$) and corpus callosum (mid anterior $p = 0.03$, mid posterior $p = 0.032$)) to whole brain were found smaller in AD patients while volume ratios of ventricles (both sides of lateral, inferior lateral and 3rd ventricles, $p < 0.001$) to whole brain were bigger in AD patients. Besides, the INV method was able to detect significant difference of volume ratio

of cerebral parenchyma to intra-cranium between AD patients and healthy elderly subjects too ($p < 0.01$). In comparison with normal ageing-related atrophy in healthy subjects, brain atrophy with ageing in AD patients presented in a different pattern in volume ratios (e.g. right ($p = 0.029$) and total cortex ($p = 0.013$) to brain, total grey matter to brain ($p = 0.01$), cerebral white matter to brain ($p = 0.003$), cerebellar cortex to brain (left $p = 0.019$, right $p = 0.032$), 5^{th} ventricle to brain ($p = 0.048$), left fimbria to left hippocampus ($p = 0.015$), left hippocampal-amygdaloid transition area (HATA) to left hippocampus and right presubiculum to right hippocampus ($p = 0.016$)). In this AD study, many volume ratios of brain regions to whole brain or other brain regions were found different in AD patients and especially volume ratio of cerebral parenchyma to intra-cranium showed potentiality as an imaging biomarker for AD. Ageing atrophy pattern was found different in AD patients too.

In conclusion, by programming in freely available R, FSL and IMAGEJ software packages, the CAVALIERI, ICAV, INV and DN methods were able to be performed conveniently and efficiently on human brain volume estimation using MRI. We made the first applications on the volume estimation of fetal brains, healthy brains and brains affected by AD using the ICAV, INV and DN methods. The volume estimates were competitive with those obtained from automated programme (i.e. FREESURFER).

Keywords: stereology , ISOTROPIC CAVALIERI , INVARIATOR , DISCRETIZED NUCLEATOR , CAVALIERI , Magnetic Resonance Imaging , fetal brain , ALZHEIMER's disease, FREESURFER , ANALYZE , R , FSL , IMAGEJ , EASYMEASURE

LAY SUMMARY

The volume of the human brain has been widely studied. Changes of brain volume can help from evaluating the development of a fetus, to diagnosing deteriorating stages of cognitive diseases suffered by a senior citizen.

There are many approaches to estimate the brain volume in living people, one recommanded way is to use Magnetic Resonance Imaging (MRI) technique. With brain images being captured from a MRI scanner, analyses can be performed subsequently using either automated or manual means.

Automated analyses are often more preferred because they are highly efficient in solving problems. However, the benefits come at a price. Most of the current automated methods can do their best only with healthy adult brains. As a result, estimating the brain volume of subjects such as fetuses or disease affected brains may be out of reach of these automated software packages. Besides, due to limits of Magnetic Resonance (MR) image quality, software algorithms and individual difference of brains, verification is still needed to compare how close the auto-obtained results are to true volumes. For both reasons, manual methods are demanded.

In this thesis, we focused on the application of three novel manual techniques in estimating the human brain volume, which were applied on the studies of both fetuses and patients with dementia.

A traditional manual method called planimetry can be time consuming and heavy in workload. Therefore we suggested a discipline named stereology which improved efficiency in a statistical way while still keeping estimated parameters unbiased. The bias of an estimator is the difference between the mean of all its possible estimates and the true value of the target parameter. An estimator with zero bias is called unbiased. Although the main focus of the study has been on volume, and to some extent, surface area, stereological methods are also available for unbiased estimation of length and number of three-dimensional (3D) objects in arbitrary shape using practical sampling strategies.

Specifically, we applied one traditional stereological method, known as the CAVALIERI method, and three new methods which were ISOTROPIC CAVALIERI (ICAV), INVARIATOR (INV) and DISCRETIZED NUCLEATOR (DN) methods to estimate volume of brain on MR images. We wrote a standard operating procedure (SOP) on one commercial software known as ANALYZE software for three new methods, and we also programmed our own scripts to run the methods more efficiently in combination with three free software packages (i.e. R, FSL and IMAGEJ languages).

The CAVALIERI, ICAV, INV and DN methods are design unbiased, and the CAVALIERI and ICAV methods are both precise in estimating individual volumes. Applying INV and DN methods are supposed to be more time-saving with expected big variance in individual volume estimates though. However, average volumes obtained by each of the four methods are close to each other, which implies prospect of using INV and DN methods in estimating mean volume from a large population. In the thesis, different operators repeated applying the new manual methods and we compared the estimates with results from an automated software package (i.e. FREESURFER) in adult brain studies too, which all showed high reliability.

Nevertheless, in practice, strict unbiasedness is hard to achieve, as it requires the measurements to be also free from observation artefacts. In other words, both the knowledge of brain anatomy and the experience of reading MR images among operators can have effects on the estimates from true values. To minimize variation due to boundary definition all the operators were from medical or biomedical background in our studies. Inter- and intra-rater reliability studies were performed, which supply some degree of confidence in terms of agreement between observers and consistency of measurements made by a single observer, but of course will not remove biases arising from unavoidable observation artefacts. Furthermore, in some cases (e.g. fetal brain study) item definition on MR images might be problematic. The quality of fetal brain MR images could be influenced due to active fetal movement in uterus. We solved this by using a software package called SLIMMER to correct MR images after scanning.

Clinically, although the difference was not significant probably due to the small sample size, we found that there might be a negative influence on the fetal brain development if the pregnant women were exposed to drugs, while there could be uncertain influence if some kinds of stress were existing during pregnancy. On the other hand, smaller brain tissue volume was found among the elderly patients with dementia than normal old people, and volume changes in some parts of their brains did not appear similar to normal ageing atrophy.

Measurement of the surface area of the brain is potentially of interest on account of the columnar arrangements of the neurons as a basic replication unit to contribute to brain development and be affected by brain atrophy. We also incorporated estimation of surface area in our studies. In future work this may provide additional and complementary information in clinical studies.

In conclusion, our work took the advantage of stereological methods to make manual estimation of human brain volume from MR images more reliable and practical. We hope our work can make brain volume estimation using the new stereological methods of ICAV, INV and DN be a more attractive option in clinical research and practice.

To my parents

To my maternal grandfather

To my great country

The People's Republic of China

谨以此论文献给我的父亲母亲，外公和我伟大的祖国 – 中国。

ACKNOWLEDGEMENTS

I would like to thank the China Scholarships Council/University of Edinburgh Scholarships[1] for the financial support awarding me the three-year PhD scholarship. I would also like to thank the University of Edinburgh Wellcome Trust Institutional Strategic Support Fund (WT-ISSF) (2013)[2] to support the fetal brain study.

I would like to express my deepest appreciation to my supervisor Prof. Neil ROBERTS for all his support, guidance, patience and wise thoughts throughout my PhD studies. I would also like to express my sincere gratitude to my supervisor Prof. Edwin VAN BEEK for his help.

I would like to thank Dr. Devasuda ANBLAGAN, Prof. Jane E. NORMAN, Prof. James BOARDMAN and Dr. Naomi D. DEAKIN for their help on the fetal brain studies. I am also grateful to Dr. Mirjam SCHUBERT for her support and patience on the Alzheimer's disease brain studies.

I am also grateful to Dr. LI (Lily) Xiang, Dr. Paul KENNEDY, Dr. Eric BARNHILL, Lucy V. HISCOX and Jonathan P. MURNANE, who provided valuable feedback and helpful advice in my PhD studies.

I would like to offer special thanks to Martin CONNELL, who, although no longer with us, continues to inspire by his brilliant mind and dedication to the colleagues and students he worked with over the course of his career.

My sincere thanks also go to Ashan JAYASUNDERA, Dr. HONG Sujin, Nadia SALLOUM, ZHOU David, HOU Lewis, Kirsteen MCJANNETT, who have participated in my projects.

I would also like to take this opportunity to extend a special thank to Dr. Calum GRAY and Dr. Tom MACGILLIVRAY for their support on the image analysis and the usage of the ANALYZE software. I would also like to appreciate Julian SPARROW for his help with the laptop and other devices. I also thank the Clinical Research Imaging Centre (CRIC) in Edinburgh for providing me the excellent infrastructure.

I am grateful to Prof. Hilary CRITCHLEY, Dr. Lucy WHITAKER, Dr. Moira NICOL, Dr. Alison MURRAY and Dr. Graham MCKILLOP for their understanding of the extension of my PhD work.

I greatly appreciate the assistance of Prof. Luis Manuel CRUZ-ORIVE, Prof. José Joaquín GUAL ARNAU, Dr. Maria del Carmen VALDÉS-HERNÁNDEZ and Dr. Mark E. BASTIN in

[1] http://www.ed.ac.uk/student-funding/postgraduate/international/region/asia/china-council

[2] http://www.edinburgh.ac.uk/medicine-vet-medicine/research-support-development-commercialisation/issf

thesis viva exam and suggestions in thesis corrections post viva.

Very special thank goes to my parents for giving me the opportunity to challenge myself in the life abroad, and I would like to appreciate them for their understanding, emotional support and love during my PhD studies. Finally, thank you to all my families and friends for listening, offering me advice and supporting me through this entire process.

TABLE OF CONTENTS

LIST OF PUBLICATIONS

Conference Abstracts

[1] Devasuda Anblagan, Kaiming Yin, Rebecca Reynolds, Fiona Denison, Mark Bastin, Colin Studholme, James Boardman, Scott Semple, Neil Roberts and Jane Norman. *PFM.34 Fetal brain development in offspring exposed to in-utero substance misuse: A Magnetic Resonance Imaging study*. OHBM. June, 2014. Hamburg, Germany. http://fn.bmj.com/content/99/Suppl_1/A93.1.

[2] Kaiming Yin, Devasuda Anblagan, Rebecca Reynolds, Jane Norman and Neil Roberts. *Estimation of foetal brain volume using MRI and three stereological methods*. The 14th International Congress for Stereology and Image Analysis. July, 2015. Liège, Belgium. http://popups.ulg.ac.be/0351-580X/index.php?id=3614.

[3] Kaiming Yin, Devasuda Anblagan, Rebecca Reynolds, Jane Norman and Neil Roberts. *Estimation of foetal brain volume using MRI and three stereological methods*. ESMRMB, 32nd Annual Scientific Meeting. October, 2015. Edinburgh, UK. https://www.ncbi.nlm.nih.gov/pubmed/26407574.

LIST OF TABLES

LIST OF FIGURES

LIST OF ABBREVIATIONS AND SYMBOLS

0D	zero-dimensional xxv, 2
1D	one-dimensional xxv, 2
2D	two-dimensional 1
3D	three-dimensional v, 1
AD	ALZHEIMER's disease vi, 4
ADNI	ALZHEIMER's Disease Neuroimaging Initiative 93
ANALYZE7.5	a file format for medical volume data, derived from the MAYO Clinic ANALYZE^{TM} software 15
ANCOVA	analysis of covariance 111
ApoE	apolipoprotein E 109
APPLE MAC OS X	Macintosh, a series of UNIX-based computer operating systems, developed and marketed by APPLE Inc. 15
CE	coefficient of error vi, 3
CRIC	Clinical Research Imaging Centre xiii, 45
CSF	cerebrospinal fluid 96
DICOM	Digital Imaging and Communications in Medicine, a file format for the raw medical volume data, covering comprehensive information and being implemented in almost every radiology, cardiology imaging, and radiotherapy device (X-ray, CT, MRI, ultrasound, etc.) 14
DN	the DISCRETIZED NUCLEATOR method v, 4
DTI	Diffusion Tensor Imaging 6
EEG	electroencephalogram 6
FLIRT	FMRIB's Linear Image Registration Tool, linear inter- and intra- modal registration 13
fMRI	functional Magnetic Resonance Imaging 6

FMRIB Oxford Centre for Functional Magnetic Resonance Imaging of the Brain 3

FREESURFER FREESURFER software suite, an open source software suite for processing and analysing (human) brain MRI images. vi, 3

FSFAST FREESURFER Functional Analysis Stream 7

FSL FMRIB Software Library v5.0, a collection of functional and structural brain image analysis tools v, 3

FSLUTILS A set of FMRIB's command-line utilities which allow the conversion, processing etc. of ANALYZE7.5 and NIFTI format MRI datasets 13

GA gestational age 44

GUI graphical user interface 14

HASTE half Fourier single shot turbo spin echo 45

HATA hippocampal-amygdaloid transition area viii, 121

ICAV the ISOTROPIC CAVALIERI method v, 4

IMAGEJ or known as one of its distribution called FIJI (`https://fiji.sc/`), is an image processing package v, 8

INV the INVARIATOR method v, 4

IR isotropically random v, 1

IUR isotropic and uniformly random v, 4

IVC inferior vena cava 45

LINUX a free UNIX-like computer operating system, which is packaged known as a LINUX distribution (e.g. DEBIAN, UBUNTU, LINUX MINT, FEDORA, etc.) for both desktop and server use 4

LM light microscope 1

MCI mild cognitive impairment 128

MEG magnetoencephalography 6

MICROSOFT WINDOWS several families of its own computer operating systems (e.g. MS-DOS), developed and marketed by MICROSOFT 31

MNI152 the MNI152 template is a standard-space average of 152 adult human brains; MNI: Montreal Neurological Institute 14

MR Magnetic Resonance v, 1

MRE Magnetic Resonance Elastography 110

MRI Magnetic Resonance Imaging v, 3

NIFTI Neuroimaging Informatics Technology Initiative, a file format for medical volume data, containing more information about orientation in space than the traditional ANALYZE7.5 format 13

nu.mgz Using Non-parametric Non-uniform intensity Normalization (N3), intensity non-uniformity in MR data is corrected while also an affine

	transform using a script called TALAIRACH is applied in the orig.mgz. MGZ format is compressed MGH format and the MGH format is a single-file format in which both pixel and meta data are stored. vi, 67
ortrip	orthogonal triplet v, 11
OS	operating system 14
PET	positron emission tomography 6
R	a free software environment for statistical computing and graphics, which can be extended via packages through the CRAN mirrors on its website (`https://www.r-project.org/`) v, 8
RLDP	right lateral decubitus position 45
SAR	specific absorption rate 45
SCP	superior cerebellar peduncle 123
SD	standard deviation 45
SLIMMER	Slice MRI Motion Estimation and Reconstruction v, 45
SPM	Statistical Parametric Mapping 4
T1W	T1-weighted 66
T2W	T2-weighted 45
TALAIRACH	an affine transform from the 'orig' volume to the MNI305 atlas applied in the FREESURFER software vi, 90
TE	echo time 45
TIFF	Tagged Image File Format 47
TR	repetition time 45
UR	uniformly random vi, 4
VBM	voxel-based morphometry 61
WT-ISSF	Wellcome Trust Institutional Strategic Support Fund xiii, 63
θ	the second angle for the vertical rotation in isotropically random rotation 15
τ	the third angle for the self spin in isotropically random rotation 15
ϕ	the first angle for the horizontal rotation in isotropically random rotation 15
ψ	the fourth angle rotated for orthogonal sections after isotropically random rotation 15

Chapter 1

Introduction

1.1 Introduction to Stereology

Stereology (http://www.stereology.info/) is a developing science providing practical techniques mostly applied in the light microscope (LM) section analysis for the quantitative description of morphological features. Methodologically, stereology has a close relationship with stochastic geometry and integral geometry [109]. The term 'stereology' stems from its greek roots *stereo* and *logos*, meaning 'science of studying solids' [6], and it is described as 'the method of quantifying two-dimensional (2D) and three-dimensional (3D) structures using estimation methods' [115]. Moreover, stereology is often defined as the science of estimating higher dimensional information from probes which have lower spatial dimension.

Stereological methods have traditionally been employed for the investigation of geometric quantities (e.g. volume, surface area, length and number) [103]. Stereology uses sampling strategies, and aims at minimising the workload, while still obtaining reliable, unbiased estimates of these quantities [92, 103]. Compared with making really time-consuming 3D reconstructions, stereology can be still reliable when automatic image analysis methods do not perform well.

The samplings of stereology use geometric probes (e.g. points, lines, lattices, arrays and planes), which are applied to needle biopsy, microscope images and Magnetic Resonance (MR) images, etc. Four basic types of probes [117] have been classified according to their dimensional characters (Table 1.1, Figure 1.1). The probes can be used in combination (e.g. points counting on section planes of an 3D object) [117]. Isotropically random (IR) orientation of test line or plane is required to estimate surface area but not volume except disector.

Two branches of sampling principles have been applied to 3D structures. Classical manual techniques base estimations on shape assumptions (e.g. sphere, ellipsoid), or on a random set model for the structure, which is referred to as model-based inference. Modern stereology selects plane sections at random, according to a specified random sampling protocol, which is referred as design-based sampling inference. Design-based stereology proves to be widely applicable and has gained increasing popularity in biomedical sciences (e.g. lung-, kidney-, bone-, cancer- and neuro- science). Importantly, to ensure the estimates are free from system-

Table 1.1: Four basic types of geometrical probes used in stereology; Yes: containing the property of, IR: isotropically random, S: surface area, V: volume, L: length.

Probes	Dimension	Position	Orientation
Point	0	Yes	No requirement
Line	1	Yes	IR for S, no requirement for V
Plane	2	Yes	IR for S and L, no requirement for V
Disector	3	Yes	IR through a fixed point for V [54]

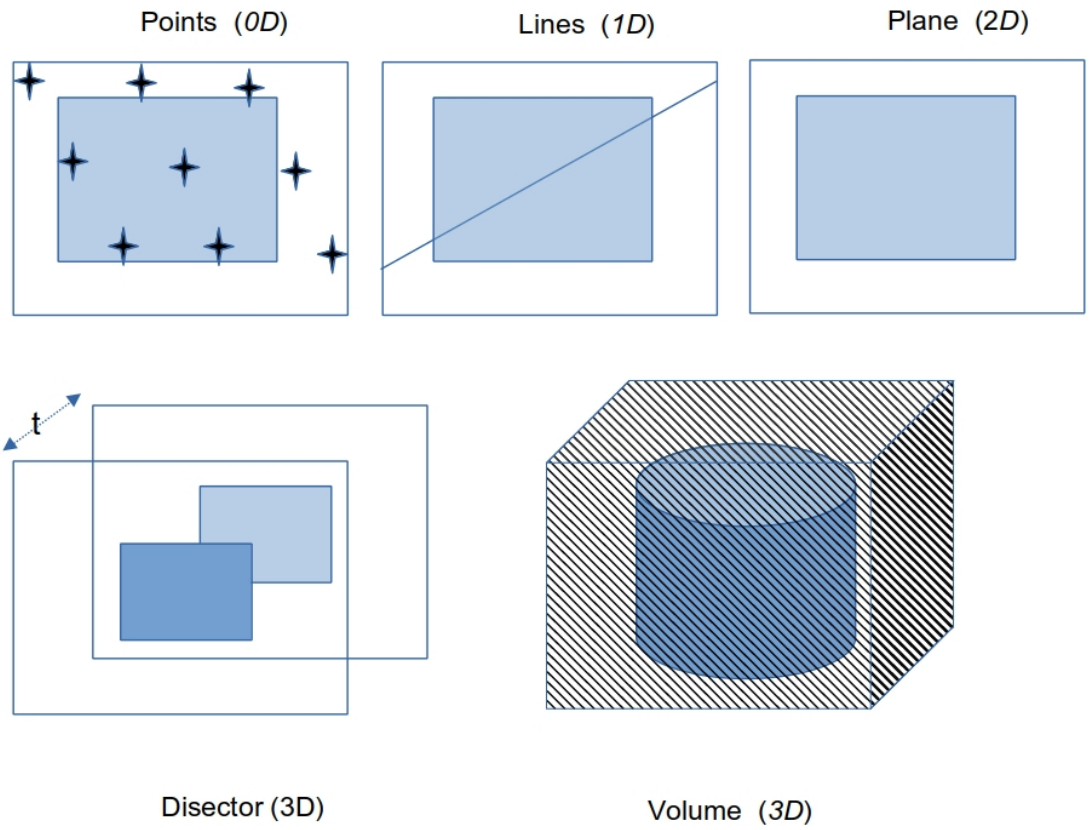

Figure 1.1: Geometrical probes used in stereology. When dimensions of a probe and a target parameter sum to three, the intersections can be counted rather than being measured in the estimation. For example, using points (zero-dimensional, 0D) to estimate volumes (3D), lines (one-dimensional, 1D) to estimate surface areas (2D), planes to estimate length (1D) and disectors (3D) to estimate numbers (0D). Otherwise, when the sum of dimensions is not three, measurement can be needed. For example, using lines (1D) to estimate volumes (3D).

atic error or bias, the probes must be applied at random positions and sometimes also isotropic orientations. Intersections between geometric probes and structural features are counted, and the counts can be easily put into formulae for obtaining unbiased estimates of the geometric quantities [83].

Design-based stereological methods require less prerequisite information on the structures being measured, and the inherent property of mathematical unbiasedness allows estimation of geometric quantities to be free from systematic error or bias [103]. A prerequisite for unbiasedness is that sampling can be representative of the whole structure. Rigorously, the sectioning of the structure of interest has to be able to present the structure with equal probabilities, and the orientation of sections needs to be isotropic when estimating features such as length and surface area [117].

On the biological sections (e.g. histology, bone and neuroanatomy) under LM, stereology has been systematically applied, which has accurately estimated the size of a particular organelle, the total length of a mass of capillaries, or the number of neurons or synapses in regions of the brain. Stereology has also shown its validity in comparative studies [117]. Meanwhile, on MR images, stereological techniques have been attempted as well, e.g. in brain studies. Sub-regions of the brain, e.g. hippocampus, have been focused on the measurement of volume and surface area of the structure, mainly using the CAVALIERI method [117].

What distinguishes the CAVALIERI's principle[1] from previous approaches to volume estimation (e.g. Archimedes[2]'s method to obtain the volume of a sphere from a cylinder) is that no assumption needs to be made regarding the shape of the structure to be measured. Moreover, the CAVALIERI's theorem[3] is equivalent to the Principle of LIÚ Huī and ZǓ Gèng (aka ZǓ-Gèng's axiom)[4] [60, 80]. The above two examples may indicate the generalization of this theory. These geometrical principles and usage of statistics allow stereology to quantitatively and concisely describe a complex object, which is not only essential in evaluating the morphology, but also helpful in further disclosing the dynamics of the structure, and the relationships between structure and function [117].

In the image analysis of human brain structure using Magnetic Resonance Imaging (MRI), volume can be estimated using the CAVALIERI method in combination with point grids, and surface area can be estimated using other stereological methods (e.g. vertical sections with cycloid probes [7, 26]). A low coefficient of error (CE, or 'relative standard error' [103]) is desired in the practice of stereology. A CE $< 5\%$ of the estimates is generally considered to be practical to achieve [103] and five or six sections are suggested to start from by the CAVALIERI method [22].

Nowadays, reliable automated/semi-automated MRI human brain image registration/segmentation software packages (e.g. FREESURFER [38], the FMRIB Software Library (FSL) [112],

[1] Naming after Bonaventura Francesco CAVALIERI (1598-1647), an Italian mathematician.

[2] Archimedes of Syracuse, around 287 – 212 BC.

[3] CAVALIERI's Theorem (1635 AD): if two solids have the same height, and if their cross sections taken parallel to and at equal distances from their bases are always equal, then the solids have the same volume.

[4] ZǓ-Gèng's Axiom, 祖日恒原理, 等幂等积定理 (around 500 AD): If blocks are piled up to form volumes, and corresponding areas are equal, then the volumes cannot be unequal.

Statistical Parametric Mapping (SPM) [47], etc.) have become well established. They have shown advantages in providing direct and more detailed information, and also these software packages can run through a whole dataset in just a few hours or days in total by one batch processing on a LINUX cluster conveniently. However, the evaluation of accuracy, reproducibility and sensitivity of these results still needs more evidence in future studies [36, 75, 77, 94]. Meanwhile, there are always areas, either too difficult currently or newly discovered (e.g. fetal and neonatal brain studies, ex-vivo brain study, super high resolution image processing, etc.) which hitherto heavily depends on manual segmentations. Manual approaches such as computer-based planimetry and semi-automatic boundary tracing techniques become tedious and time-consuming especially in the process of highly convoluted brain images [103]. At the same time, stereology is a reliable and efficient option to balance a practical workload and reliability of accuracy for quantitative estimation.

In this PhD study, we implemented one traditional stereological method (i.e. the CAVALIERI method) and three novel design-based methods (i.e. the ISOTROPIC CAVALIERI (ICAV) [28, 25], INVARIATOR (INV) [21, 22, 24] and DISCRETIZED NUCLEATOR (DN) [24, 59] methods) for volume and surface area measurement on fetal brain (including both the second (weeks 24 to 26) and the third (weeks 35 to 38) trimesters) and the elderly brain (e.g. Alzheimer's disease (AD)), to have a demonstration of the application of different stereological methods on MR images of human brain covering different age ranges which are potentially difficult to segment automatically.

Furthermore, comparisons of the stereological results with those obtained from one automated algorithm (i.e. FREESURFER) were performed on 26 adult brains. Both a detailed and a group comparisons were investigated, to more clearly examine the reliability of stereological estimation.

1.1.1 Introduction to Stereological Methods of ICAV, INV and DN

ISOTROPIC CAVALIERI

The ICAV method takes a series of parallel section planes from a whole 3D structure of interest. A requirement of the ICAV method is that the parallel sections must be isotropical and uniformly random (IUR) [28]. Around five to ten sections are usually enough to obtain precise estimates of the structure, irrespective of its 3D shape or size [103]. A test system for points counting (e.g. crosses in a uniformly random (UR) square grid) is superimposed on each slice, and all the grids are independent to each other. The areas of all sections throughout the structure are estimated by points counting (i.e. calculating the number of test points hitting the structure on each section), whereupon volume is obtained by multiplying the sum of areas of all sections by the sectioning interval [103].

In assessing surface area, the ICAV method also adopts the same preliminary IUR design as in volume measurement. The procedure of surface area estimation uses a UR test grid on each slice, where the number of intersections between test lines and boundaries of the structure of interest is counted [103]. Crucially again, to avoid bias, the placement and orientation of

section planes and test grids probes must be random and isotropic [83].

The precision of both the volume and surface area estimation using the ICAV estimator is usually assessed by CE [103]. Practically a high precision of CE $\leq 5\%$ is pursued.

INVARIATOR

The INV method can be applied to estimate volume and surface area of isolated objects or fixed individual particles [28], e.g. cells with a single nucleolus, rat brains and grains of cemented carbide [21, 23, 28]. The convenience and difference from the CAVALIERI method is that the INV method is based on a single IR section plane (namely pivotal section) through a fixed point (namely pivotal point) correspondingly. This slice is measured with a combination of test lines and lattices, which are effectively motion invariant in space [23, 28].

The INV method has advantage in estimating population means of groups of subjects [28]. The mean value of estimates is comparable with that estimated using the ICAV estimator. However, each individual volume or surface area estimate obtained by the INV estimator may be quite different from the true value. Empirically, the CE can reach 30% or even more.

DISCRETIZED NUCLEATOR

Both the traditional NUCLEATOR and new DN methods are only capable of estimating volume. Neither can estimate surface area. Similar to the INV method, the DN method also only uses one IR pivotal section plane of the object for the estimation, and the CE is as high as that in the INV method in individual estimation. Likewise, the DN method is good at estimating population means of groups.

Comparisons of the ICAV, INV and DN methods are shown as below (Table 1.2).

Table 1.2: Comparisons of the ICAV, INV and DN methods applied on MR images.

	ICAV	INV	DN
3D MR Images	Required	Required	Required
IR Rotation	Required	Required	Required
MR Slices For Measurement	Multiple	One	One
Volume Estimation	Yes	Yes	Yes
Surface Area Estimation	Yes	Yes	No
Measuring Method for Volume	Points Counting	Lengths Measure	Lengths Measure
Measuring Method for Surface Area	Intersects Counting	Intersects Counting	/
Coefficient of Error	Theoretical	Empirical	Empirical
Individual Estimate Variance	Small	Big	Big
Group Mean Estimate	Accurate	Accurate	Accurate

1.2 Introduction to FREESURFER

FREESURFER (Athinoula A. Martinos Center for Biomedical Imaging, Boston USA; https://surfer.nmr.mgh.harvard.edu/) provides a suite of tools for visualization and analysis of human brain MRI data, which is documented, open source and free for downloading (https://surfer.nmr.mgh.harvard.edu/fswiki/DownloadAndInstall) [38]. FREESURFER allows automated and detailed analyses on brain structural MR images for both individual data and group comparison which covers both cross-sectional and longitudinal studies utilising statistics (Figure 1.2).

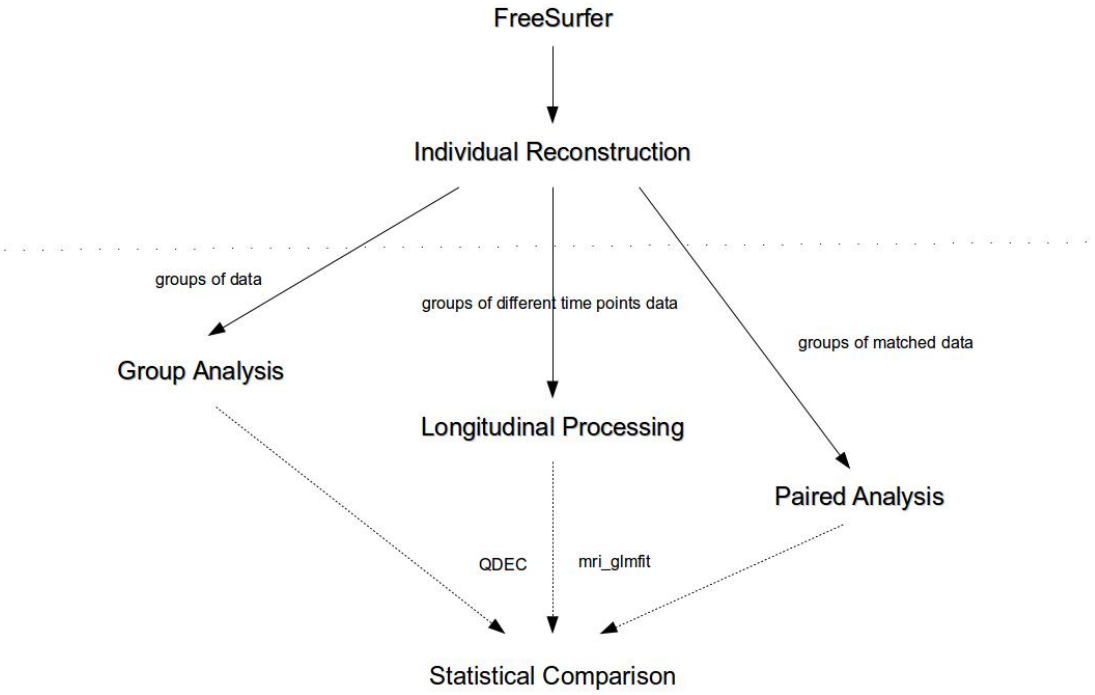

Figure 1.2: Brief work-flows in FREESURFER. The individual reconstruction step enables further group, longitudinal or paired analyses using statistics.

In structural analysis, simply put, FREESURFER performs both cortical reconstruction and volumetric segmentation. The procedures include skull stripping, image registration, subcortical segmentation, cortical surface reconstruction, cortical segmentation, cortical thickness estimation, etc. FREESURFER also integrates with multi-models, e.g. fMRI (task, rest and retinotopy), DTI tractography, PET, MEG and EEG. Moreover, FREESURFER is able to collaborate with other imaging analysis tools, e.g. FSL packages.

An overall review of FREESURFER has been described [38], and technical details of whole analysis stream are presented in a series of publications [29, 30, 39, 40, 41, 42, 43, 44, 45, 58, 69, 110]. FREESURFER deforms cortical surface, which comprises surface inflation [43] and registration to a spherical atlas which matches individual cortical folding patterns with

cortical geometry across subjects [44]. Parcellation of cerebral cortex and creation of maps of curvature and sulcal depth are based on the gyral and sulcal structures [34, 45]. The whole working stream utilises information of both image intensity and structure continuity from entire 3D MRI volume [39]. As a result, FREESURFER uses a tessellated surface which has a sub-voxel resolution and thus can detect sub-millimetre differences between groups [102]. The reliability of FREESURFER has also been validated against histological analyses and manual measurements.

FREESURFER packages have interactions with FSL tools which are skilled in fMRI analyses. The analysed functional activity data using either FREESURFER Functional Analysis Stream (FSFAST) or FSL, can be overlaid onto FREESURFER's cortical surfaces to have a structural analysis in combination. FREESURFER also utilises toolkits from software packages e.g. MNI MINC, VXL, Tcl/Tk/Tix/BLT, VTK., KWWIDGETS and Qt. Other programs for neuroimaging analysis e.g. CARET, AFNI/SUMA and 3D SLICER can import and visualize data processed by FREESURFER too.

In applications, FREESURFER packages work well on human brain from children of age four [51] to elderly subjects. Packages and tools are keeping on extending and making them more widely applicable in other study areas, e.g. infant and neonatal brain, ex-vivo brain, ultra high field (7 tesla) MRI, primates study and anatomy teaching etc. The version of FREESURFER used in this study is V6.0BETA (the latest version of stable V6.0 has been released in 2017), and the new features enable the analyses of hippocampal subfields [64] and brainstem substructures [65].

1.3 Introduction to The Thesis

This PhD thesis focusses on the application of stereological methods on volume estimation of human brain. In general, there were four studies concerning the improvement of operability and practicality of the novel stereological methods and three studies concerning volume estimation of fetal and adult brains in both the list below and Table 1.3.

Chapter 2 Three novel stereological methods (i.e. the ICAV, INV and DN methods) all carry out IR rotation of the object before further slicing and measurement. There are no MRI imaging processing software packages currently available for performing this specific purpose automatically. Furthermore, a free image processing tool which can be made readily available for other research groups to use is desired. We programmed a script based on R and FSL software packages and the aim of this chapter is to demonstrate the usage of the script to generate IR rotated MR images.

Chapter 3 For both the INV and DN methods, only one IR rotated MR image slice of the object is needed, upon which one UR test grid is overlaid for the measurement. However, generation of the test grid is inconvenient and time consuming, and again no software packages are available to implement it automatically. We programmed a IMAGEJ macro script called 'grid_inv_dn.txt' and the aim of this chapter is to demonstrate the usage of the script to generate and overlay a rotated UR grid onto a MR image slice.

Chapter 4 To make the measurement using the INV and DN methods as fast as possible, another IMAGEJ macro script called 'measure_inv_dn.txt' was programmed. The script helps the rater focus on performing segment lengths measurement while the script records the measurement automatically. The aim of this chapter is to demonstrate the usage of the script.

With the three scripts described in the above three chapters, together with another pre-existing free software (i.e. EASYMEASURE) for points counting purpose, it is convenient and quick to perform the CAVALIERI, ICAV, INV and DN methods on volume estimation of human brains on MR images.

Chapter 5 Previous applications of the ICAV and INV methods were on rat brains and the volume and surface area of whole brain (including the cerebellum) were estimated [28]. The human brain is much more complex in structure (i.e. the folding pattern of sulci and gyri) and therefore more difficult to estimate volume. The human fetal brain is a suitable option available for us to start our trials of the application of novel stereological methods. Besides, the development of fetal brain from the second to the third trimester provided gradually increasing complexity of human brain, which allowed us to test the parameters of applying the ICAV, INV and DN methods before applying to adult brain studies in the following chapters of the thesis.

There is neither an opportunity to obtain the true value of human brain volume in the case of an in-vivo study, nor a reliable automated software package to obtain fetal brain

volume at the moment of performing this fetal brain study. The aim of this chapter is to manually estimate in vivo human fetal brain volumes using MRI by applying the ICAV, INV and DN methods. All three methods are design-unbiased so that following repeat application there will be no significant difference between the mean estimate and the true target value. Besides, we also aim at surface area estimation using ICAV method for error prediction. Before three in-house scripts were available, this study was performed on one commercial software (i.e. ANALYZE) which not only had a built-in package for the CAVALIERI method but also allowed rotation operation and calliper measurement which could be used for the INV and DN methods on MR images. The way to examine our results was using inter-rater reproducibility and intra-rater repeatability assessment for both points counting and segment length measurements used in the methods. Furthermore, to assess the advantage of INV and DN methods on population mean volume estimation, we made a comparison of the mean values of all the brain volume estimated by the ICAV, INV and DN methods.

Chapter 6 In the case of adult brain studies, our first step was a detailed comparison of a traditional stereological method with a well established automated software on one healthy adult. Thus, the aim of this chapter is to make a slice-by-slice comparison of the point counting process in the CAVALIERI method with the profiles of segmentation in FREESURFER on volume estimation. The data were shared by Dr Mirjam SCHUBERT from Institute of Neuroradiology at the Klinikum Ingolstadt, Germany.

Chapter 7 To see whether the CAVALIERI, ICAV, INV and DN methods can be applied on adult brain, and whether the results can be comparable to those obtained from the FREESURFER package, this chapter applied the four stereological methods and the automated technique on volume estimation of cerebrum excluding ventricles using three scripts described in Chapter 2, Chapter 3 and Chapter 4 on 13 healthy elderly subjects and 13 AD patients. To assess the effect of potential uncertainty in boundary definition, we also performed the inter-reliability and intra-repeatability assessment on adult brains, and the average time cost in each brain measurement for the four manual methods were recorded. Another goal of this chapter is to examine the cerebral atrophy in AD using both the manual methods and the automated software. The data were shared by Dr Mirjam SCHUBERT from Institute of Neuroradiology at the Klinikum Ingolstadt, Germany.

Chapter 8 Volume changes of different brain regions can be reliable imaging biomarkers in evaluating brain diseases, especially e.g. AD. The aim of our final study is to perform a systematic volumetric analysis of the brains between AD patients and healthy volunteers using FREESURFER software, and also investigating the difference of ageing-related atrophy of brain volume ratios of each brain region to whole brain between AD patients and healthy participants. Furthermore, a general imaging biomarker should be able to work well with manual methods too. Thus one potential imaging biomarker (the ratio of cerebral parenchymal volume to intra-cranial volume) was chosen, and our last goal is

to examine it again by the INV method between the AD patients and the healthy participants. The data were shared by Dr Mirjam SCHUBERT from Institute of Neuroradiology at the Klinikum Ingolstadt, Germany.

Table 1.3: A brief summary of subjects' information, methods and software packages used in each chapter in this thesis.

Chapters	Subject Group	No.	Stereological Methods				Manual Software in Stereology					Automated Software
Chapter 2			CAV	ICAV	INV	DN			IMAGEJ	R	FSL	
Chapter 3					INV	DN			IMAGEJ			
Chapter 4					INV	DN			IMAGEJ			
Chapter 5	2nd Trimester 3rd Trimester	10 10	CAV	ICAV	INV	DN	ANALYZE					(not applicable)
Chapter 6	Health	1	CAV					EASYMEASURE	IMAGEJ			FREESURFER
Chapter 7	Health AD	13 13	CAV	ICAV	INV	DN		EASYMEASURE	IMAGEJ	R	FSL	FREESURFER
Chapter 8	Health AD	16 27			INV				IMAGEJ	R	FSL	FREESURFER

In summary, the objectives of the studies in this thesis were as following:

OB1 **Method development** (Chapter 2, Chapter 3, Chapter 4): programming scripts for running the novel stereological methods more practically and faster, which can also be freely available to the public and applicable on common personal computers;

- **OB1.1** Generating four random numbers for rotation angles in R;
- **OB1.2** Enabling R to process MR images (e.g. input and output of MR images) by combining multiple R packages;
- **OB1.3** Using the FSL software to perform rotations on MR images;
- **OB1.4** Combining the functions in FSL with R using the FSLR package in R;
- **OB1.5** Using R to manipulate MR images (e.g. initialising the MR images to a same transverse view, converting the images to the radiological convention, resampling the images into isotropic voxel size and padding the images to cubic image files);
- **OB1.6** Performing three orthogonal IR rotations on MR images automatically, and saving the results in both 3D MR images and one central slice of the images;
- **OB1.7** Illustrating the brain position in 3D space after being rotated by any of the four angles;
- **OB1.8** Illustrating the brain position in 3D space after being IR rotated by a combination of the four angles;
- **OB1.9** Illustrating the radiological and the neurological conventions (i.e. the position of left and right hemispheres of the brain) in 3D space;
- **OB1.10** Generating a UR test grid for the INV and DN methods in IMAGEJ;
- **OB1.11** Programming an IMAGEJ macro script to generate the test grid automatically;

OB1.12 Illustrating how to generate the test grid for the INV and DN methods using the script;

OB1.13 Programming an IMAGEJ macro script to record the measurement using the INV and DN methods in IMAGEJ automatically.

OB1.14 Illustrating how to measure the lengths of segments for the estimation of volume using the INV and DN methods using the script.

OB2 Fetal brain study (Chapter 5): testing the applicability of the ICAV, INV and DN methods on human brain, starting from fetal brains at both the second and third trimesters;

OB2.1 Performing motion correction on ten fetal brain MR images from the second and ten from the third trimesters using the SLIMMER tool;

OB2.2 Proposing operation procedures for applying the ICAV, INV and DN methods on the commercial software ANALYZE;

OB2.3 Applying the ICAV ortrip, INV ortrip and DN ortrip methods (i.e. basing on a isotropic triplet of orthogonal section planes of each data) to estimate whole brain volumes of fetuses at both the second and third trimesters;

OB2.4 Assessing the inter- and intra-reliability studies for points counting and length measurements on five brains from the second trimester and five from the third trimester by three raters;

OB2.5 Estimating both volume and surface area of fetal brains by the ICAV method to predicting theoretical CEs for the ICAV method;

OB2.6 Examining the sensitivity of the ICAV, INV and DN methods to detect difference between two trimesters;

OB2.7 Comparing the CEs for the ICAV, INV and DN methods;

OB2.8 Comparing the difference of CEs between the INV and INV ortrip methods, and between the DN and DN ortrip methods;

OB2.9 Comparing fetal brain volumes among maternal substance misuse, psychological stress and health groups.

OB3 Adult brain initial study (Chapter 6): comparing one stereological method with one automated software in details on one adult brain volume estimation;

OB3.1 Picking up one best image quality MRI data from 22 healthy elderly volunteers;

OB3.2 Applying the CAVALIERI method on one adult cerebral parenchymal volume estimation and run FREESURFER software on the same adult brain;

OB3.3 Aligning the points in slices from the CAVALIERI method to the segmentation profiles from FREESURFER software by matching the same brain image background;

OB3.4 Comparing the difference of volume obtained by the CAVALIERI method and FREESURFER;

OB3.5 Comparing the difference between the points counting in stereology and the segmentation profiles in FREESURFER (i.e. counting the points included in the CAVALIERI method but are outside the pial boundary segmented by FREESURFER, counting the points not included in the CAVALIERI method but are inside the pial boundary segmented by FREESURFER, and showing the difference of corrected volume between the two methods).

OB4 Adult brain group study (Chapter 7): applying the CAVALIERI, ICAV, INV and DN methods on two groups of adult brains (i.e. AD patients and healthy adults), examining the sensitivity of the methods to detect difference between two groups, and comparing the volume estimates with those from one automated software;

OB4.1 Picking up good image quality MRI data from 40 AD patients and 22 healthy elderly volunteers;

OB4.2 Using three in-house scripts to apply the CAVALIERI, ICAV, INV and DN methods on both the AD patients and healthy elderly subjects to estimate cerebral volumes;

OB4.3 Assessing the inter- and intra-reliability studies;

OB4.4 Applying FREESURFER software to analyse the same two cohorts of brains from the AD patients and the healthy elderly subjects;

OB4.5 Comparing volume estimates obtained by the CAVALIERI, ICAV, INV and DN methods and FREESURFER software;

OB4.6 Detecting the difference of cerebral volume between AD patients and healthy controls by the CAVALIERI, ICAV, INV and DN methods and FREESURFER software;

OB4.7 Recording the average time cost in each adult brain measurement using the CAVALIERI, ICAV, INV and DN methods.

OB5 AD imaging biomarker study (Chapter 8): analysing the potential changes of different brain region volumes as clinical imaging biomarkers for AD using one automated software, and analysing if any one of the four stereological methods can detect difference of AD patients from healthy adults using one of the potential imaging biomarkers.

OB5.1 Picking up MRI data in the maximum same age range from 40 AD patients and 22 healthy elderly volunteers;

OB5.2 Running FREESURFER software on both the AD patients and healthy adults;

OB5.3 Analysing the difference of volumes or volume ratios in each brain region from the FREESURFER outputs, and selecting one volume or volume ratio as the imaging biomarker to be examined by the manual method;

OB5.4 Applying the INV method to estimate the selected imaging biomarker on the same dataset, and analysing the difference of the estimates between the two groups;

OB5.5 Exploring the difference of volume ratio changes with ageing between the AD patients and the healthy elderly subjects.

Chapter 2

FSL and R Script for Three Orthogonal Isotropic Random Rotations and Pivotal Sectioning on MR Images

2.1 Introduction

Manipulation of MR images traditionally starts from a direct inspection of the images in three orthogonal orientations (i.e. coronal, sagittal and transversal views). The majority of MRI atlases of human anatomy are based on these three sectioning orientations. However, the brain or other organs in fixed position or orientation is not optimal for the application of modern stereological methods, which are mostly design-based and require 3D objects to be processed unbiasedly. An IR rotation [17] of MR images meets the criterion for unbiasedness and also simplifies the probes to be used in the stereological measurement (e.g. straight lines instead of cycloidal curves) [63].

Rotations on MR images can be performed by several software packages directly (e.g. FSL [112], FREESURFER [29], IMAGEJ [108], 3D SLICER [37], ANALYZE [101], ADOBE PHOTOSHOP, etc.) or after image format conversion (e.g. BLENDER, 3DS MAX, MESHLAB, etc.). FSL package, which reads MR images in the Neuroimaging Informatics Technology Initiative (NIFTI, https://nifti.nimh.nih.gov/) format, outperforms most of the other counterparts available free or commercially, has specific tools (e.g. FSLUTILS, FLIRT [66, 67], etc.) to manage orientation information and professionally aligns the brain MR images to standard spaces of brain templates.

Meanwhile, several packages in R [98] software have been developed for stereology by mathematicians. To be capable of handling MR images in R, relevant packages have been collected in a webpage titled as *CRAN Task View: Medical Image Analysis* (https://cran.r-project.org/web/views/MedicalImaging.html) where packages are filed by

specific purposes, e.g., ORO.DICOM [118], ORO.NIFTI [118] for 'Data Input/Output', and RNIFTYREG [15], FSLR [91] for 'General Image Processing'. Especially, FSLR package adapts a big portion of the FSL commands in R directly, as well as interfacing with the FSL tools after the installation of FSL software independently in the computer. Moreover, R also comprises packages for the purpose of rotation, e.g. ROTATIONS [113] and RGL [1], both of which give a precise control of angles operated in 3D rotation. Lastly, an R package SVDIALOGS [52] helps to create user friendly graphical user interfaces (GUIs) for the input of the data. With the above packages altogether, rotating MR images isotropically using an R script is convenient now.

After IR rotation of MR images being completed semi-automatically by the R script, three novel stereologcial methods can be performed directly using two other software packages, i.e. ICAV method [25, 28] in EASYMEASURE [96] software, INV [21, 22, 23, 24, 27, 28, 53] and DN [24, 55, 59] methods in IMAGEJ software, which enables geometrical properties (e.g. volume, surface area, etc.) of 3D objects to be estimated.

The aim of this chapter is to provide a general description on how to perform IR rotation on MR images using R and FSL software packages together. Hence stereology can be conducted for the estimation of volume and surface area of 3D objects.

2.2 Materials and Methods

Firstly, FSL and R software packages are required to be installed in the operating system (OS) independently. Currently the versions of FSL and R are 5.0.8 and 3.3.2 respectively. Then, in an R console, the R packages required are available by using the 'install.packages()' commands (LINUX users need to open R by 'sudo R' in the terminal to authorise the installations). After these, the R script in Appendix B can generate IR rotated MR images automatically.

The R script can be divided into eleven steps in sequence, which includes:

(1) load MRI data in the NIFTI format;

(2) or load MRI data in Digital Imaging and Communications in Medicine (DICOM, `http://dicom.nema.org/`) folder and transfer the files to NIFTI format;

(3) input rotation angles manually or auto-generate rotation angles randomly;

(4) convert to radiological convention;

(5) resample to isotropic voxel size of $1 \times 1 \times 1$;

(6) align brain images to the MNI152 template position;

(7) pad to cubic space;

(8) orient the starting position to a transverse view with nose downwards (2D central section plane), or alternatively to a sagittal view with nose leftwards;

(9) generate three orthogonal rotation matrices;

(10) rotate the MR images using the angles input or generated in step (3);

(11) output the 3D MR images in ANALYZE7.5 format (for EASYMEASURE), pivotal section planes, and the lists of rotation matrices, rotation angles in degrees and radians.

Setting up of the R script is a bit different depending on OS (i.e. LINUX and APPLE MAC OS X) (Figure 2.1a). Output directory can be chosen freely and input data can be either a single NIFTI file (.nii or .nii.gz) or a DICOM folder (Figure 2.1b). If the object is an adult brain MR image, there is an option to choose whether the brain image will be aligned to the MNI152 template (Figure 2.1c). The alignment will remove neck tissue if existing in the MR image, and also place the brains to a same position and orientation with more subtle and consistent adjustment (Figure 2.2). Therefore, the centre point of the aligned image is closer to a same brain centre, which can be used as a pivotal point and thus can improve the performance of INV and DN methods. The alignment is currently not applicable to other anatomical structures because we have not found respective templates. The rotation is optional and if needed all the four operational angles can be either generated automatically or input manually (Figure 2.1d). The script can be also used to generate a triplet of traditional orthogonal section planes without rotations (i.e. in sagittal, coronal and transverse views, Figure 2.4). Currently the script forces all the MR images to be in radiological convention (i.e. the graphical left is the anatomical right, see the 'Discussion' Section 2.4.1 in this chapter below). Then, the script transfers the image to isotropic voxel size of $1 \times 1 \times 1$, and pads the image to a cube, thus the rotations always swirl around the cubic centre. The script positions the MR images in the same orientation before any rotations so that all the subsequent rotations start from a 3D head placed vertically with the comb upwards and the nose facing inside while 2D section planes are in the transverse view (Figure 2.4). When performing the rotation, three angles (i.e. ϕ, θ and τ) are required in order to specify an IR rotation of the image (Figure 2.3) and a fourth angle (i.e. ψ) is additionally required to generate the ortrip. After the 3D brain is IR rotated an orthogonal triplet of MR images is sampled at the pivotal point. The output image is currently set to be in the ANALYZE7.5 format because it is the only format applicable in EASYMEASURE software (the other format which can be read by EASYMEASURE is DICOM). Besides, three rotation matrices and four angles in both degrees and radians are listed in the output folder too. The radians can be input manually in the script again to repeat the same rotations on either the same or any other different MR images. The rotated positions of 3D brain images can be checked using the IMAGEJ (or FIJI) 'volume viewer' plug-in.

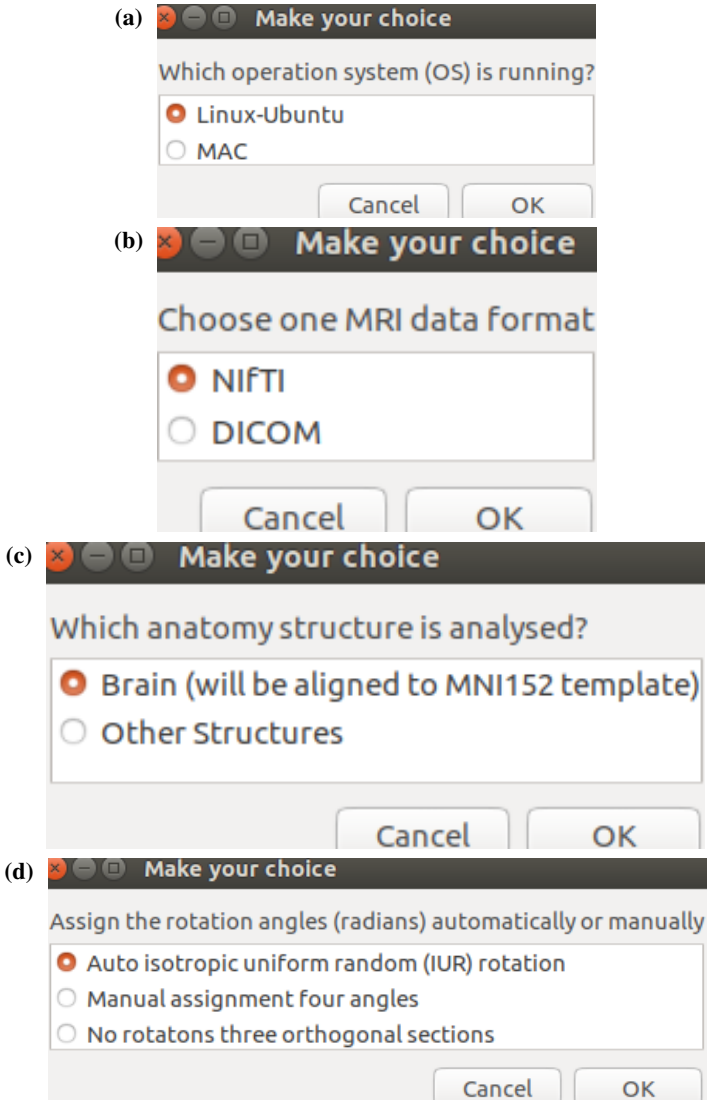

Figure 2.1: Initial options menus shown in the R script for rotation of MR images: (a) inputs of OS information, (b) choices of data formats, (c) targets of adult brain images or other structures and (d) ways of performing rotation angles.

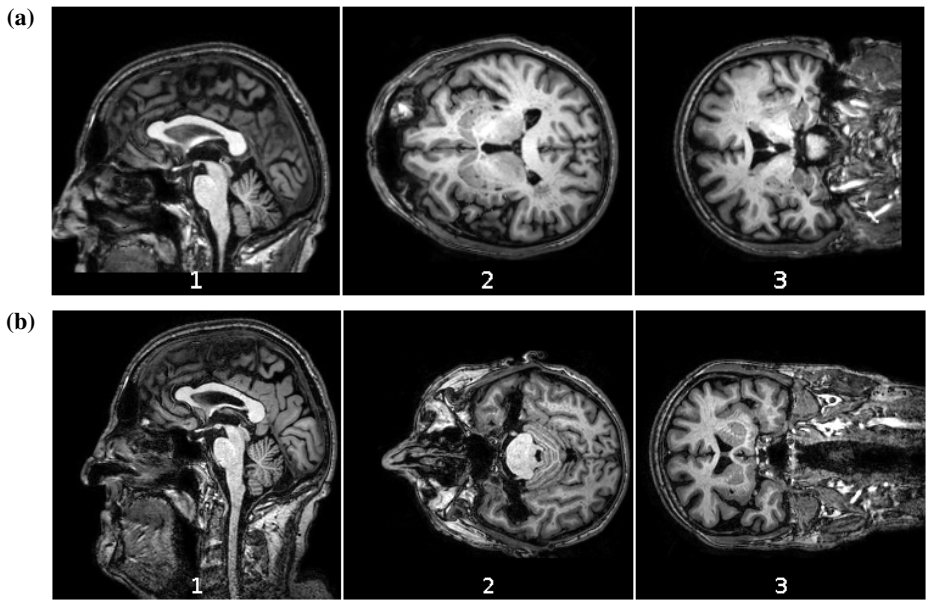

Figure 2.2: Two triplets of orthogonal central sectioning planes of one adult brain MR image without rotations (i.e. from 1 to 3: sagittal, trasverse and coronal planes). (a) The brain image is aligned to the MNI152 template; (b) the brain image is not aligned to the MNI152 template and as a result original neck tissue is still kept.

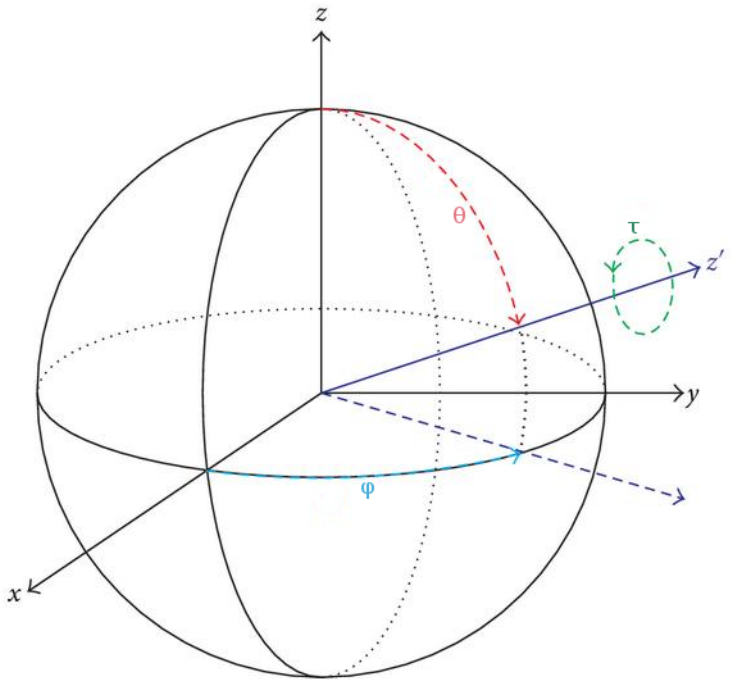

Figure 2.3: An IR rotation of X0Z-plane using three random angles. The object (Z-axis) is rotated by a horizontal angle ϕ and a vertical angle θ, then span by an angle τ about the Z'-axis defined by (ϕ, θ).

2.3 Results

2.3.1 Time costing

The time the R script cost to run from a DICOM folder or a NIFTI file on a DELL LATITUDE E6430 laptop (UBUNTU 15.10 OS) was $3'35"$ or $3'58"$, respectively.

2.3.2 Examples

Examples of rotations of one adult brain are shown below to illustrate how the four angles (i.e. ϕ, θ, τ and ψ) played roles both independently and in combination in the rotations, and at last two examples of three orthogonal IR rotations are displayed. In each example, firstly four applied angles are listed in both degrees and radians, and then a triplet of orthogonal central section planes and the respective 3D head positions are presented. All the examples of rotations can be repeated using the script and choosing the option of 'Manual assignment four angles' in the dialogue menu of 'Assign the rotation angles (radians) automatically or manually'.

The starting position

Initially the 3D head is formatted into a vertical up position with the section plane transverse. To output this position directly, choosing the option of 'No rotations three orthogonal sections' in the dialogue menu of 'Assign the rotation angles (radians) automatically or manually' in the script.

Table 2.1: Angles used in the example below of starting positions of one adult brain. Before rotation, all the four rotation angles are set to zeros.

Angles	Degrees	Radians
ϕ	0	0
θ	0	0
τ	0	0
ψ	0	0

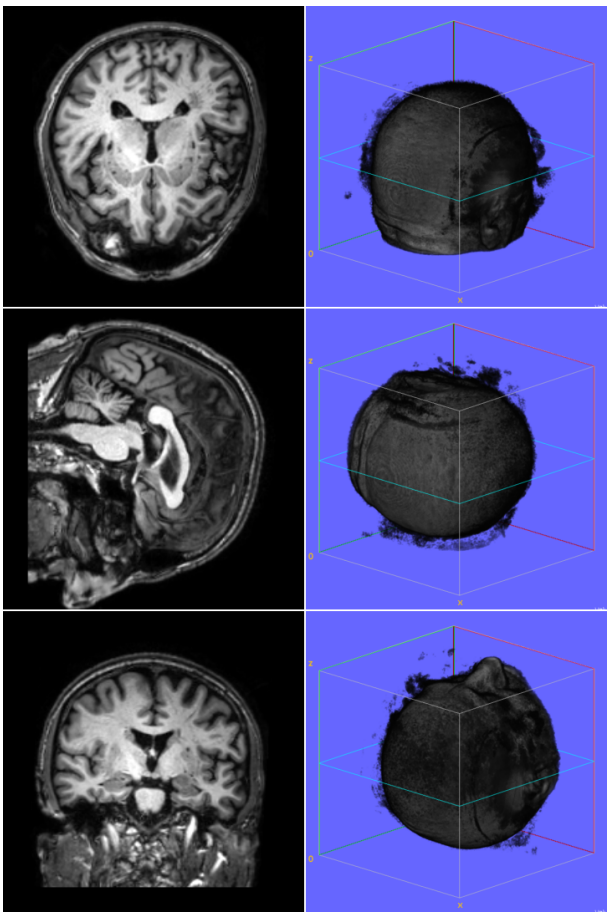

Figure 2.4: The starting three orthogonal positions of one adult brain before rotation are shown in 2D and 3D images. 2D section planes (left) are taken horizontally across the middle line of 3D coordinates cube (right).

Inputting ϕ in a right angle

When $\phi = 90°$, the vertical 3D head rotates leftwards and anticlockwise.

Table 2.2: An angle $\phi = 90°$ is used for yawing in the example below and all the other three rotation angles are kept as zeros.

Angles	Degrees	Radians
ϕ	90	1.57079632679
θ	0	0
τ	0	0
ψ	0	0

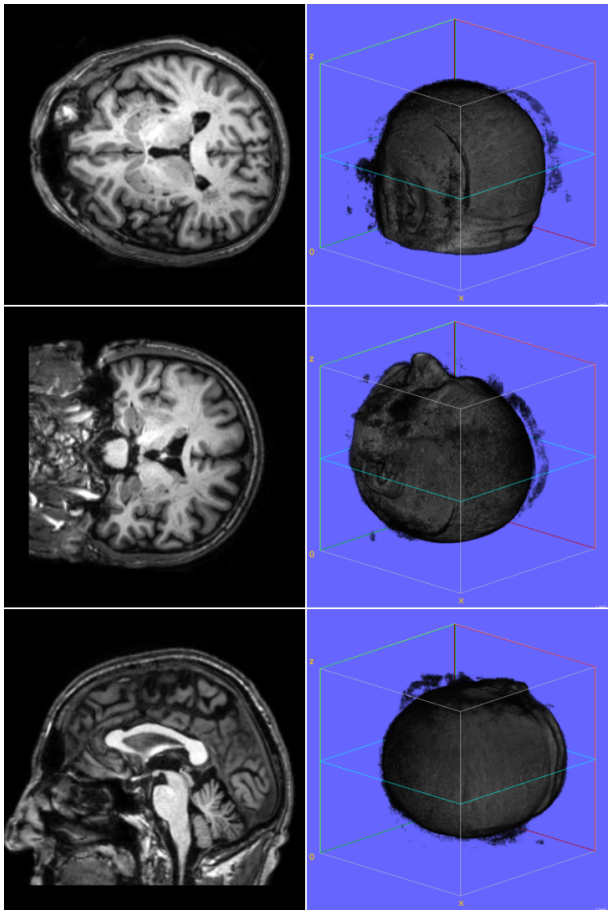

Figure 2.5: One adult brain is rotated by an angle $\phi = 90°$, and a triplet of orthogonal positions are obtained from the rotated brain, which are shown in both 2D and 3D images. The 3D head is rotated leftwards and anticlockwise from the staring positions above.

Inputting θ in a right angle

When $\theta = 90°$, the 3D head nods downwards.

Table 2.3: An angle $\theta = 90°$ is used for pitching in the example below and all the other three rotation angles are kept as zeros.

Angles	Degrees	Radians
ϕ	0	0
θ	90	1.57079632679
τ	0	0
ψ	0	0

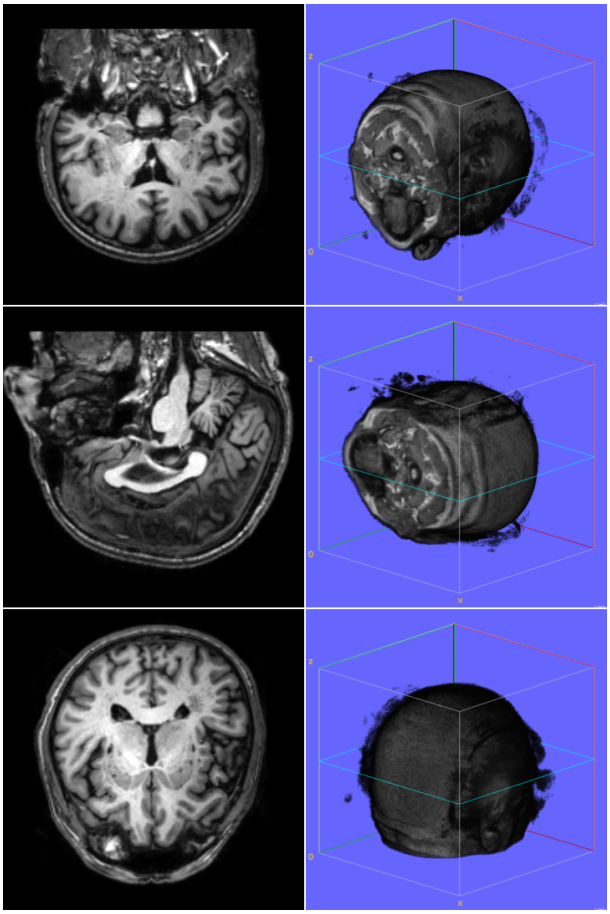

Figure 2.6: One adult brain is rotated by an angle $\theta = 90°$, and a triplet of orthogonal positions are obtained from the rotated brain, which are shown in both 2D and 3D images. The 3D head nods downwards from the staring positions.

Inputting τ in 45 degree angle

When $\tau = 45°$, viewing from the top of the head, the vertical 3D head spins leftwards and anticlockwise.

Table 2.4: An angle $\tau = 45°$ is used for spinning in the example below and all the other three rotation angles are kept as zeros.

Angles	Degrees	Radians
ϕ	0	0
θ	0	0
τ	45	0.78539816339
ψ	0	0

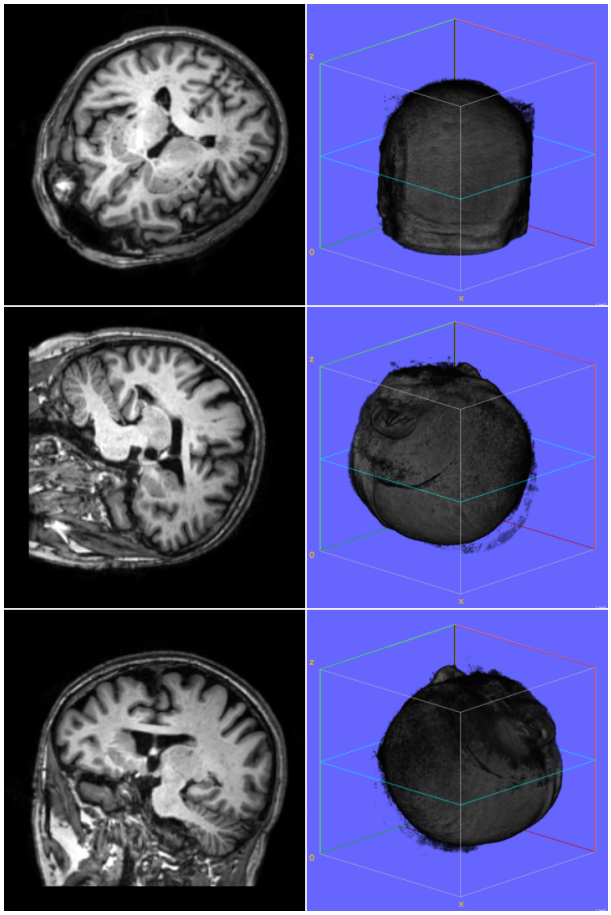

Figure 2.7: One adult brain is spun by an angle $\tau = 45°$, and a triplet of orthogonal positions are obtained from the spun brain, which are shown in both 2D and 3D images. The 3D head spins leftwards and anticlockwise from the staring positions.

Inputting ψ in 45 degree angle

When $\psi = 45°$, viewing from the top of the head, the 3D head in the two orthogonal views rotates rightwards and clockwise.

Table 2.5: An angle $\psi = 45°$ is used for spinning for orthogonal planes in the example below and all the other three rotation angles are kept as zeros.

Angles	Degrees	Radians
ϕ	0	0
θ	0	0
τ	0	0
ψ	45	0.78539816339

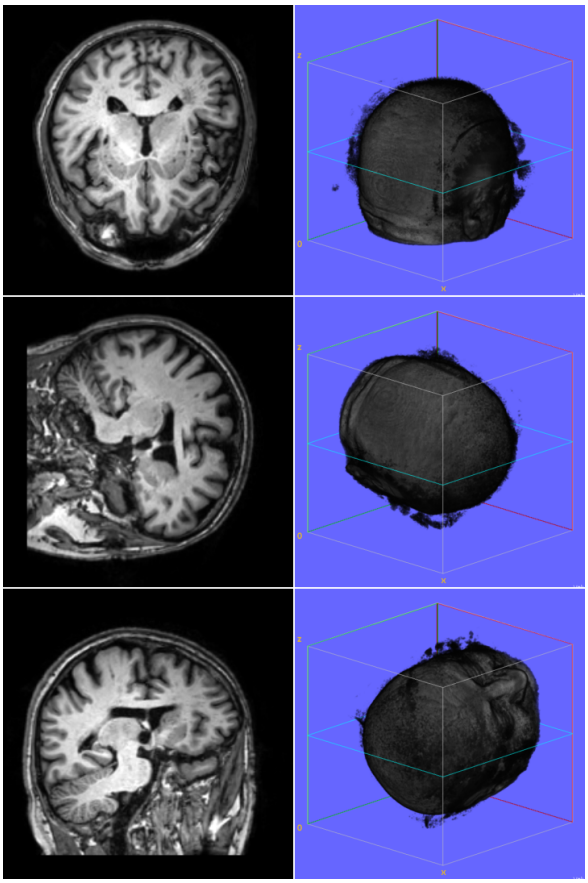

Figure 2.8: A triplet of orthogonal positions are obtained from one adult brain, and the latter two orthogonal positions are further spun by an angle $\psi = 45°$ to get two new orthogonal positions, which are shown in both 2D and 3D images. The 3D head in the two orthogonal views rotates rightwards and clockwise after spinning.

Inputting ϕ and θ in right angles

When $\phi = 90°$ and $\theta = 90°$, performing the θ rotation first and then the ϕ rotation. The 3D head lays in the prone position with the head's top towards the left hand side of the cube/screen.

Table 2.6: Two angles $\phi = 90°$ and $\theta = 90°$ are used for yawing and pitching in the example below and the other two rotation angles are kept as zeros.

Angles	Degrees	Radians
ϕ	90	1.57079632679
θ	90	1.57079632679
τ	0	0
ψ	0	0

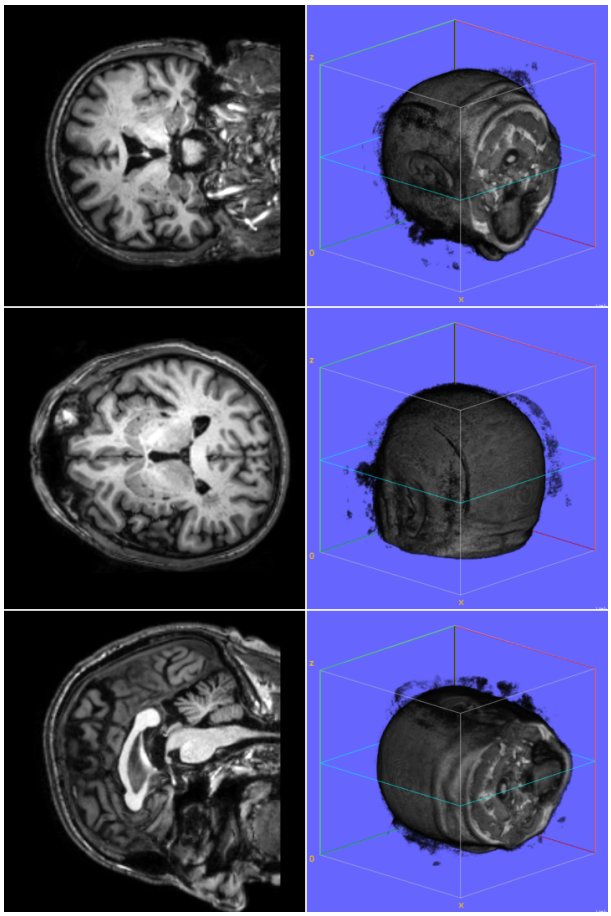

Figure 2.9: One adult brain is rotated by two angles $\phi = 90°$ and $\theta = 90°$, and a triplet of orthogonal positions are obtained from the rotated brain, which are shown in both 2D and 3D images. After rotation, the 3D head lies in the prone position with the head top towards left.

Inputting ϕ, θ in right angles and τ in 45 degree angle

When $\phi = 90°$, $\theta = 90°$ and $\tau = 45°$, performing the τ rotation first, then the θ rotation and lastly the ϕ rotation. The 3D head lays in the prone position with the head's top towards the left side of the cube and the nose facing between left front and bottom of the cube.

Table 2.7: Three angles $\phi = 90°$, $\theta = 90°$ and $\tau = 45°$ are used for yawing, pitching and spinning in the example below and the fourth angle ψ is kept as zero.

Angles	Degrees	Radians
ϕ	90	1.57079632679
θ	90	1.57079632679
τ	45	0.78539816339
ψ	0	0

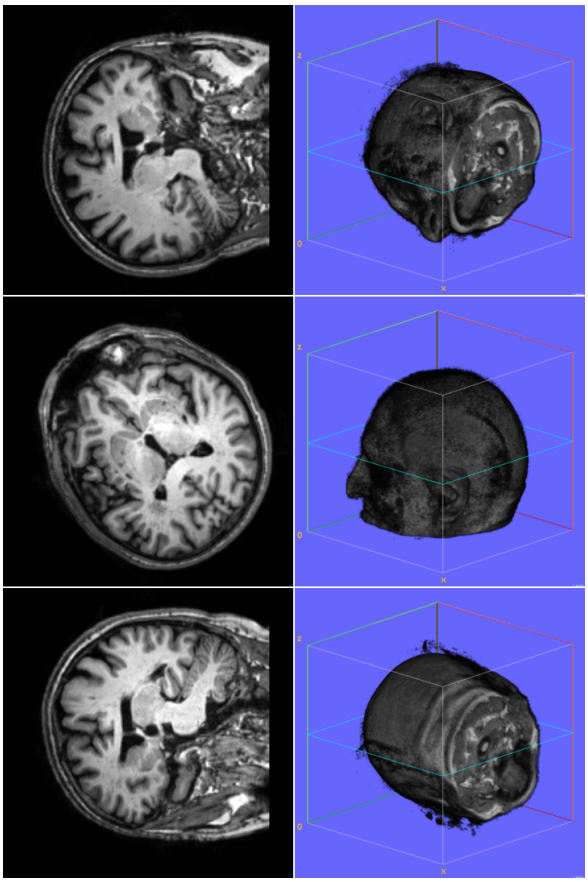

Figure 2.10: One adult brain is rotated by three angles $\phi = 90°$, $\theta = 90°$ and $\tau = 45°$, and a triplet of orthogonal positions are obtained from the rotated brain, which are shown in both 2D and 3D images. After rotation, the 3D head lies in the prone position with the head top leftwards and the nose facing between left front and bottom faces of 3D coordinates cube.

Inputting both ϕ and θ in right angles and both τ and ψ in 45 degree angles

When $\phi = 90°$, $\theta = 90°$, $\tau = 45°$ and $\psi = 45°$, performing the τ rotation first, then the θ rotation and lastly the ϕ rotation for the IR rotation, and performing the additional ψ rotation before all the three other angles for the orthogonal views. The 3D head lays in the position the same as above, but the other two orthogonal section planes are additionally rotated.

Table 2.8: Four angles $\phi = 90°$, $\theta = 90°$, $\tau = 45°$ and $\psi = 45°$ are all used for yawing, pitching and spinning in the example below, within which the fourth angle ψ is used for spinning orthogonal positions.

Angles	Degrees	Radians
ϕ	90	1.57079632679
θ	90	1.57079632679
τ	45	0.78539816339
ψ	45	0.78539816339

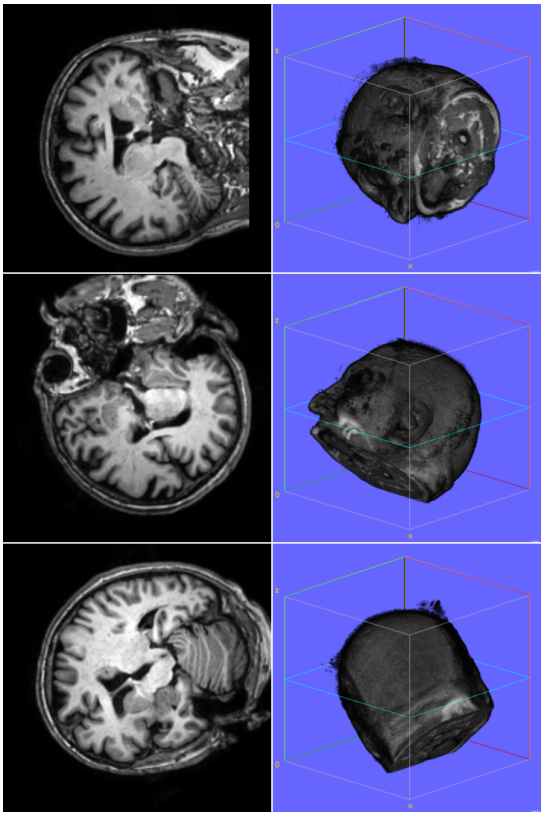

Figure 2.11: One adult brain is rotated by three angles $\phi = 90°$, $\theta = 90°$ and $\tau = 45°$. A triplet of orthogonal positions are obtained from the rotated brain with a further spin by a fourth angle $\psi = 45°$, which are shown in both 2D and 3D images. After rotation, the 3D head lies in the same position as above, but the other two orthogonal 3D head positions are spun additionally.

IR rotation: inputting ϕ in 17, θ in 102, τ in 153 and ψ in 237 degree angles

The first example of a three orthogonal IR rotation of a brain is displayed below with four random rotation angles of values: $\phi = 17°$, $\theta = 102°$, $\tau = 153°$ and $\psi = 237°$.

Table 2.9: Four angles $\phi = 17°$, $\theta = 102°$, $\tau = 153°$ and $\psi = 237°$ are used for yawing, pitching and spinning in the example below, within which the fourth angle ψ is used for spinning orthogonal positions.

Angles	Degrees	Radians
ϕ	17	0.304384145061411
θ	102	1.78135270834232
τ	153	2.66507070661799
ψ	237	4.12962650511987

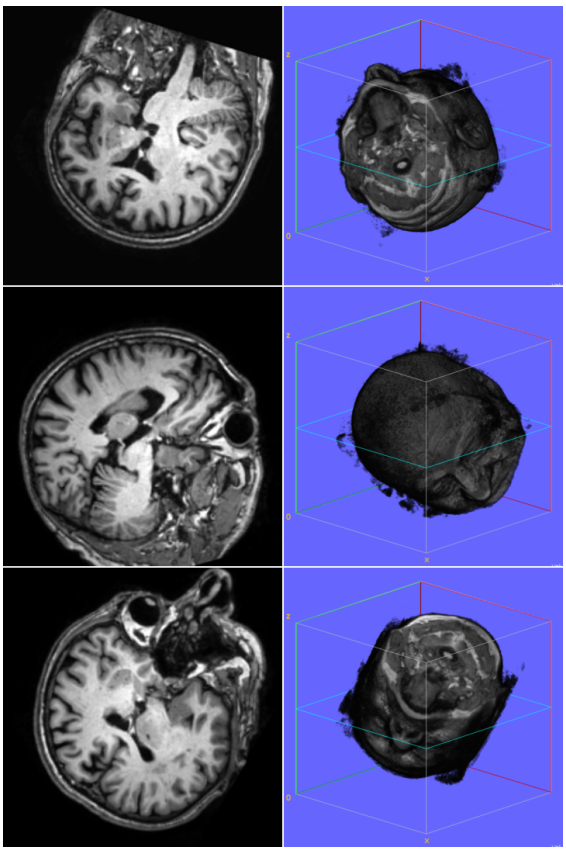

Figure 2.12: One adult brain is rotated by three angles $\phi = 17°$, $\theta = 102°$ and $\tau = 153°$. A triplet of orthogonal positions are obtained from the rotated brain with a further spin by a fourth angle $\psi = 237°$, which are shown in both 2D and 3D images. After rotation, the 3D head lies in an IR rotated position.

IR rotation: inputting ϕ in 70, θ in 119, τ in 100 and ψ in 211 degree angles

The second example of a three orthogonal IR rotation of a brain is displayed below with four random rotation angles of values: $\phi = 70°$, $\theta = 119°$, $\tau = 100°$ and $\psi = 211°$.

Table 2.10: Four angles $\phi = 70°$, $\theta = 119°$, $\tau = 100°$ and $\psi = 211°$ are used for yawing, pitching and spinning in the example below, within which the fourth angle ψ is used for spinning orthogonal positions.

Angles	Degrees	Radians
ϕ	70	1.22501201263312
θ	119	2.07780096464723
τ	100	1.74488495775944
ψ	211	3.68810304015818

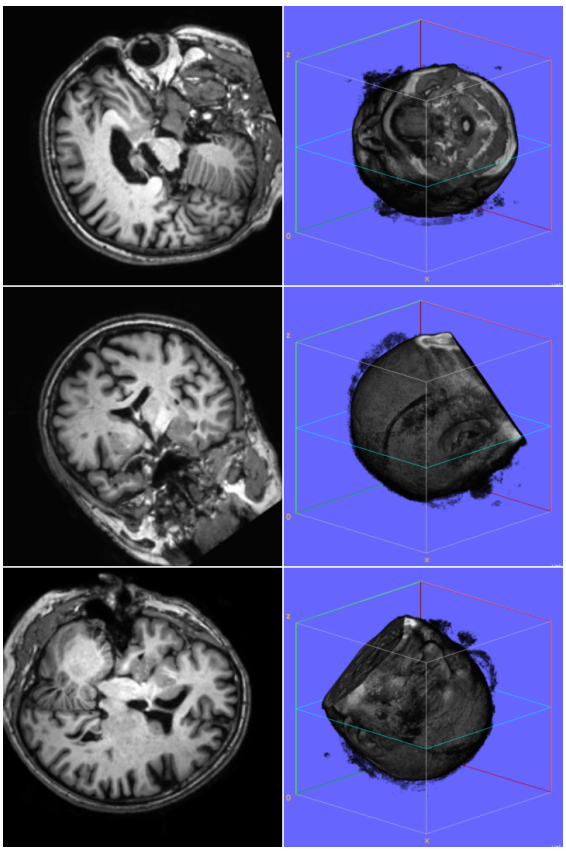

Figure 2.13: One adult brain is rotated by three angles $\phi = 70°$, $\theta = 119°$ and $\tau = 100°$. A triplet of orthogonal positions are obtained from the rotated brain with a further spin by a fourth angle $\psi = 211°$, which are shown in both 2D and 3D images. After rotation, the 3D head lies in an IR rotated position.

2.4 Discussion

2.4.1 Left And Right, Radiological And Neurological

The MR images, especially the brain images, can be oriented following a radiological convention or a neurological convention. For example, two brain MR images, one in the radiological convention (named as 'avg152T1_LR_nifti.nii.gz', Figure 2.14a) and the other in the neurological convention (named as 'avg152T1_RL_nifti.nii.gz', Figure 2.14b), were displayed below. Both of the brain images were marked with 'L' and 'R' in the two hemispheres respectively. The radiological brain has 'R' in the left hemisphere and 'L' in the right hemisphere while the neurological brain has 'L' in the left hemisphere and 'R' in the right hemisphere. The two images were in the NIFTI format and were downloaded from the NIFTI website (http://nifti.nimh.nih.gov/nifti-1/data).

Currently for the convenience of brain MR images manipulation, the script orients all the MR images (i.e. not just brain images) into the radiological convention (Figure 2.14c). As a result, the original neurologically oriented MR images will have their hemispheres shifted after being manipulated by the script. Certainly, the script can be modified to convert all MR images to the neurological convention as well, or even to give options to choose the orientation according to the need (e.g. the brain MR images could be forced to radiological convention while the other structural MR images remain unchanged).

2.4.2 Advantage of the script

This R script is written by the author solely and is open source, moreover, all the programs used within the script are freely available, therefore the script is easy to share. The script is flexible to modify and users are free to change the codes depending on their own demands. Besides, the script can be further developed along with the update of the R packages and FSL software. In comparison with the other manual methods for IR rotations on MR images (e.g. using the commercial ANALYZE software), advantages of the script include: firstly the input of the script can be the original DICOM files and thus is more convenient; secondly all the subsequent operations are performed automatically and thus much faster; thirdly for a group of brain images, the alignment to the MNI152 template makes the pivotal points more consistent and thus the results more trustworthy; and lastly it is easier to repeat the rotations using the angles information recorded by the script after each performance.

2.5 Acknowledgement

Thanks to John MUSCHELLI for the FSLR package in R, Bryan STANFILL for the ROTATIONS package in R, and FSL experts for all the trivial questions discussed in the FSL mailing list.

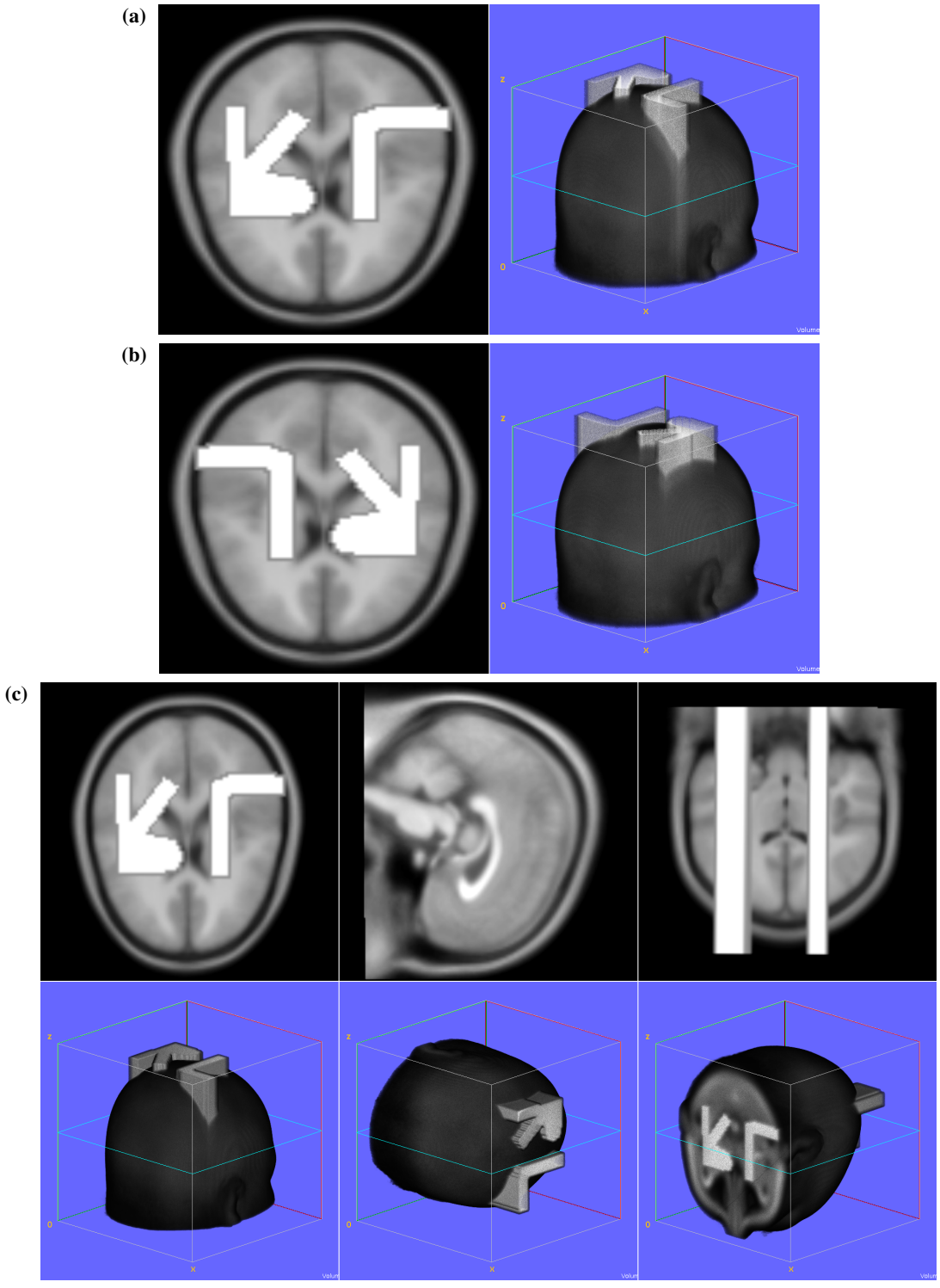

Figure 2.14: The relative position of left (labelled as an upside down 'L') and right (labelled as an upside down 'R') brain hemispheres in MR images is kept correct after rotation by the script. (a) A radiological view of brain 'avg152T1_LR_nifti.nii.gz' shown in both 2D and 3D images before being processed by the script. (b) A neurological view of brain 'avg152T1_RL_nifti.nii.gz' before being processed by the script. (c) The brain in radiological convention after being processed by the R script in three orthogonal positions.

Chapter 3

ImageJ Grid INV DN Macro

3.1 Introduction

Two new stereological methods (i.e. the INV [21, 22, 23, 24, 27, 28, 53] and DN [24, 55, 59] methods) were proposed more than a decade ago. The two methods are quite similar in operation. On MR images, with a pivotal sectioning plane of an IR rotated 3D object being obtained, which can be quickly done using an in-house R/FSL script (Chapter 2), and then with a UR test grid being overlaid on the pivotal plane, measurement using both the INV and DN methods can be easily performed.

However, there is no specific software available to perform estimation using either of the methods on MR images. The ANALYZE [101] software, which is commercial and costly, has a toolkit for the CAVALIERI method which is a traditional stereological method. The toolkit can be manually adapted for the two new methods but still it turns out to be inconvenient and it takes time to generate the test grid and lines, which is inconsistent with the aim of both methods to be highly efficient.

IMAGEJ [108] software, or FIJI [106] software which is developed from IMAGEJ and is complemented with more practical plug-ins, is free and runs on all major operating systems (OSes) (i.e. MICROSOFT WINDOWS, APPLE MAC OS X and LINUX). IMAGEJ or FIJI allows users to record and edit any purpose-specific macro scripts, which therefore could be a convenient and efficient way to perform the INV and DN methods.

The purpose of this chapter is to introduce an in-house IMAGEJ macro script (i.e. 'grid_inv_dn.txt' in Appendix C) to semi-automatically generate test grids and lines for applying both the INV and DN methods.

3.2 Materials and Methods

3.2.1 Installation

To install the IMAGEJ macro script 'grid_inv_dn.txt', save the text script file into `ImageJ/macros/toolsets/` folder, and then activate it in '≫' drop down menu at the right end of the IMAGEJ window, after which a new tool icon will turn up (Figure 3.1).

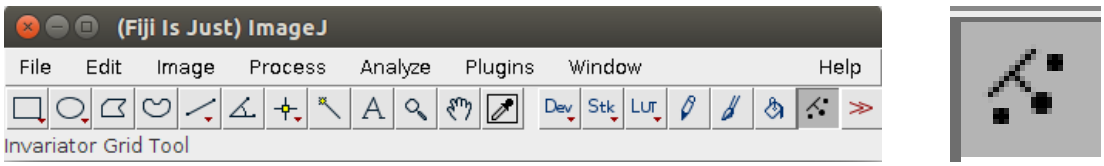

Figure 3.1: GUI for IMAGEJ software and icon for the 'grid_inv_dn.txt' script in IMAGEJ.

3.2.2 Running

To use this script, a MR image with an isotropic voxel size of $1 \times 1 \times 1$ is preferred because IMAGEJ seems to have difficulty in recognizing other voxel sizes. In IMAGEJ, click on the script icon to activate it, then load one pivotal slice of the rotated MR image into IMAGEJ, a dialogue menu pops up after clicking on the image (Figure 3.2). Three options are available to decide the ways to choose grid lattice size: (1) by grid lattice side length; (2) by grid lattice area; (3) by points number.

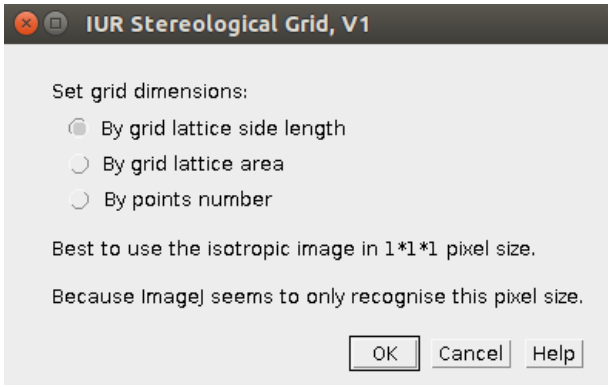

Figure 3.2: The first options menu for the 'grid_inv_dn.txt' script, which suggests how user prefers to set up grids for stereology.

Afterwards, a second menu pops up to decide the parameters for the grid (Figure 3.3). The test grid can be either rotated or without rotation for other purposes. Three options are available in the dialogue menu to set up the grid: (1) 'Isotropic & Random Offsets' gives a rotated UR grid automatically; (2) 'Assigned Orientation & Offsets' allows users to fill in the specific rotation angles and starting offsets, which is useful in reliability study; (3) 'No Rotation & Half Offsets' gives regular horizontally and vertically aligned lattices, and the starting position is half lattice side length away from the top left corner.

In the same dialogue menu, the grid lattice side length can be randomized by percentage, e.g. a lattice side length is set to 35, and a following randomizer is set to 0.15 ($\pm 15\%$), thus the final lattice side length can be one random value between 30 to 40 (Figure 3.3). In the panel, there are also options to choose whether the test points representing lattices or the circled cross (aka sun cross, solar cross or wheel cross) representing the pivotal point needs to be visible or not.

Each run of the script will generate two plotted images which include: (1) one grid with the test lines for the INV method and the other grid for the DN method (in the 'TEST LINES'

part in the dialogue menu (Figure 3.3), choose the option of 'Invariator & Dis Nucleator'); (2) two identical copies of grids for the INV method (choose the option of 'Invariator'); (3) two identical copies of grids for the DN method (choose the option of 'Discretized Nucleator'); (4) two identical copies of grids without any test lines, which only have the lattice crosses plotted (choose the option of 'No Lines'); The purpose of two copies of the same grid in each run is that one copy can work as a reference or a backup in the following process of measurement.

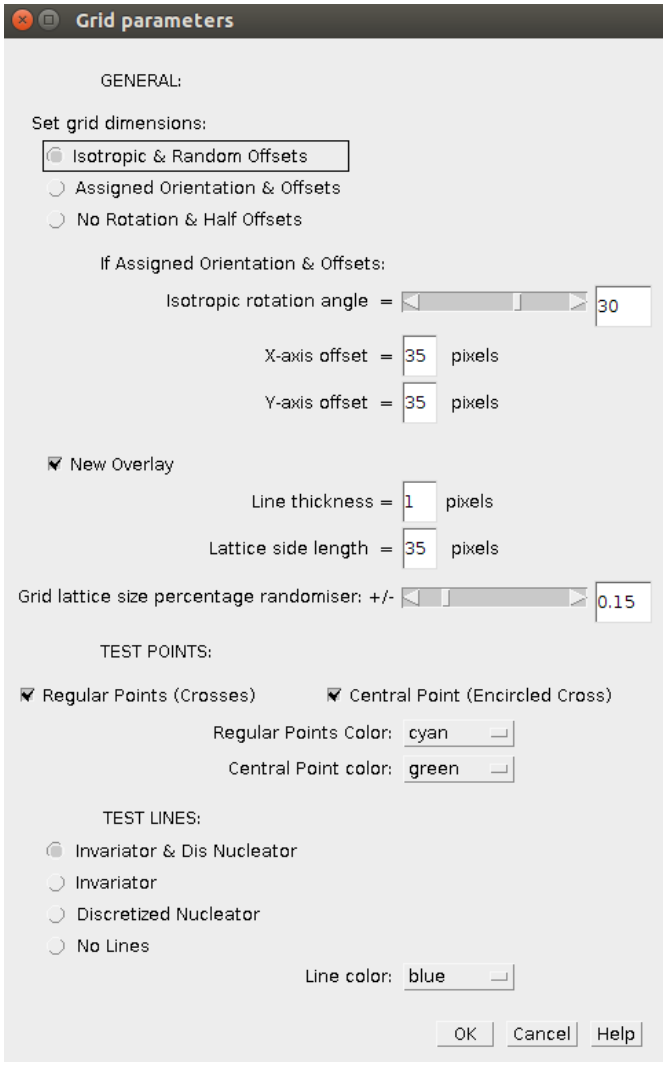

Figure 3.3: Second options menu for the 'grid_inv_dn.txt' script, within which parameters of grids, points and lines for different methods can be decided.

A 'help' page is available as well which covers: (1) a concise description about the options in the menu, (2) formulae for volume and surface area by the INV method and (3) formula for volume by the DN method (Figure 3.4).

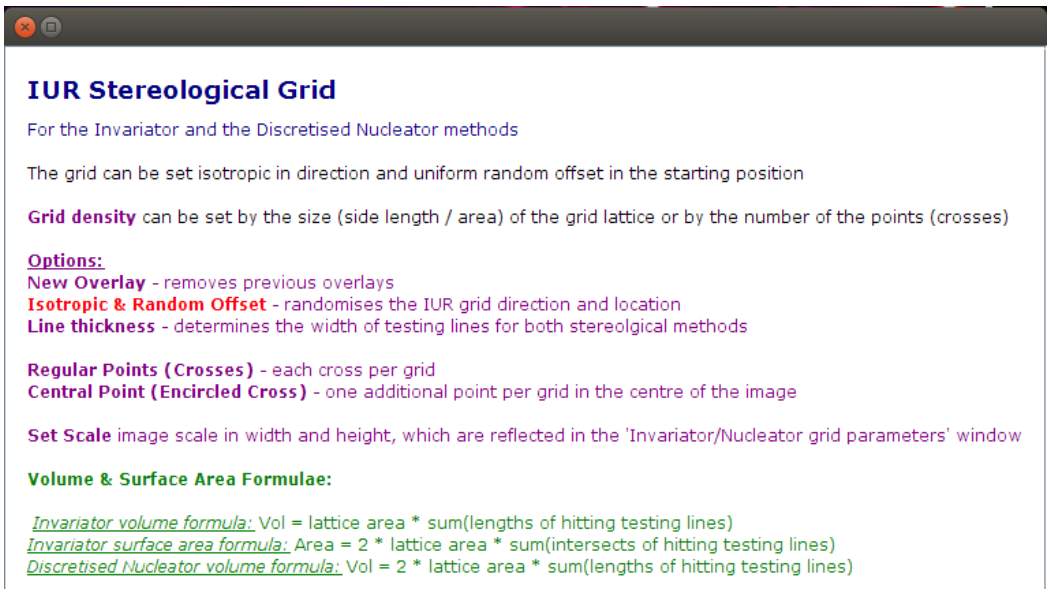

Figure 3.4: A help page is available from the right bottom corner of the above options menu panel for the 'grid_inv_dn.txt' script. The help page introduces basic concepts of parameters used in the script and lists volume and surface area formulae for the INV and DN methods.

3.3 Results

After each run of the script, information of parameters of images and grids, and test time were all listed in a text window as shown below.

> (The text file contains both the parameters and test starting time. The parameters can be different for the subsequent images.)
> *Invariator/Nucleator grid for image: [data_orth1_inv.img]*
> *Start time: 14:47:10, 25 April 2016*
>
> *Image size = 240 × 240 voxels*
> *Voxel size = 1 × 1 × 1 voxels*
> *Scale in width = 1, Scale in height = 1*
>
> *Grid lattice side length = 40 voxels*
> *Grid lattice area = 16 cm^2*
> *Grid points number approx = 30*
> *X-axis offset = 24 voxels, Y-axis offset = 3 voxels*
> *Isotropic rotation angle = 45.2276 degree, [-90, 90]*
>
> - - - - - - - - - - - - - - -

3.3.1 Examples

Three groups of examples of the grids generated by the script are shown below. The first group shows two UR test grids with only points, with one grid rotated and the other not rotated. The second group shows two UR test grids with both points and lines for the INV and DN methods respectively. The last group shows two UR test grids overlaid on a brain pivotal sectioning plane, for the two stereological methods referred previously.

Example One: Test Points

Test grid optionally can be a rotated UR or a not rotated UR grid (Figure 3.5).

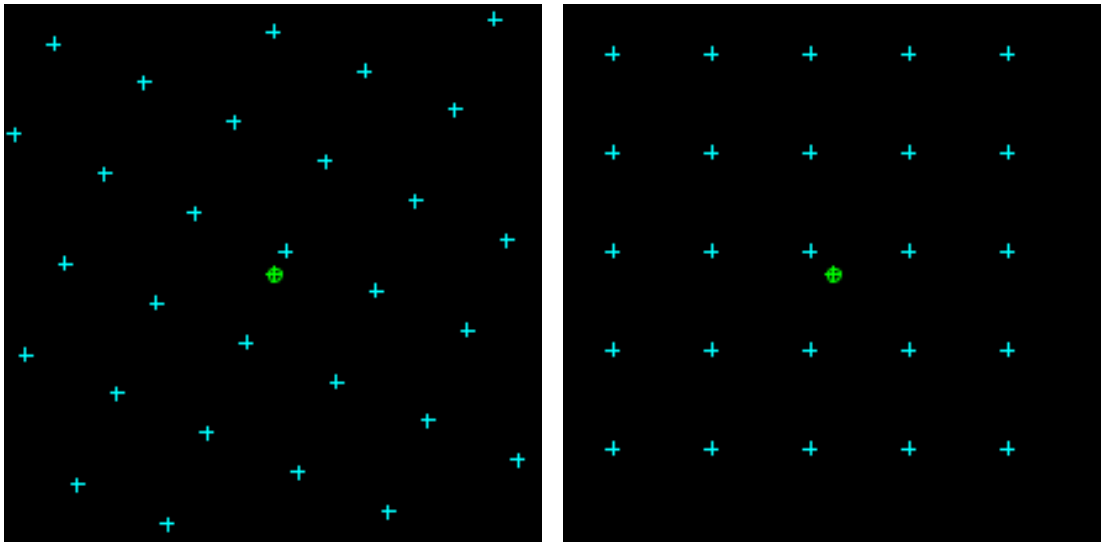

Figure 3.5: Two examples of test grids (left: a rotated UR grid, right: a not rotated UR grid) for the 'grid_inv_dn.txt' script. Cyan points are grid lattices, and green encircled cross is the centre point of the image, which represents pivotal point.

Example Two: Test Lines And Ray Lengths

The INV method requires the proper use of a system of test lines whereas the DN method only requires the measurement of ray lengths (Figure 3.6).

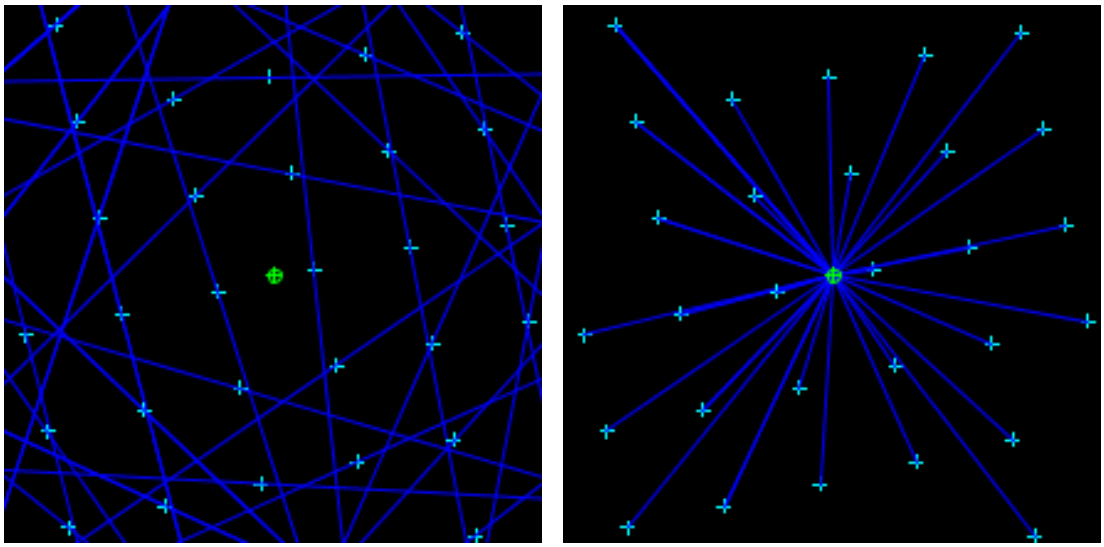

Figure 3.6: Two examples (left: test lines for the INV method, right: test ray lengths for the DN method) for the 'grid_inv_dn.txt' script.

Example Three: Test Lines And Ray Lengths On Brain

Test lines for the INV method and ray lengths for the DN methods superimposed over an IR rotated brain MR image slice (Figure 3.7).

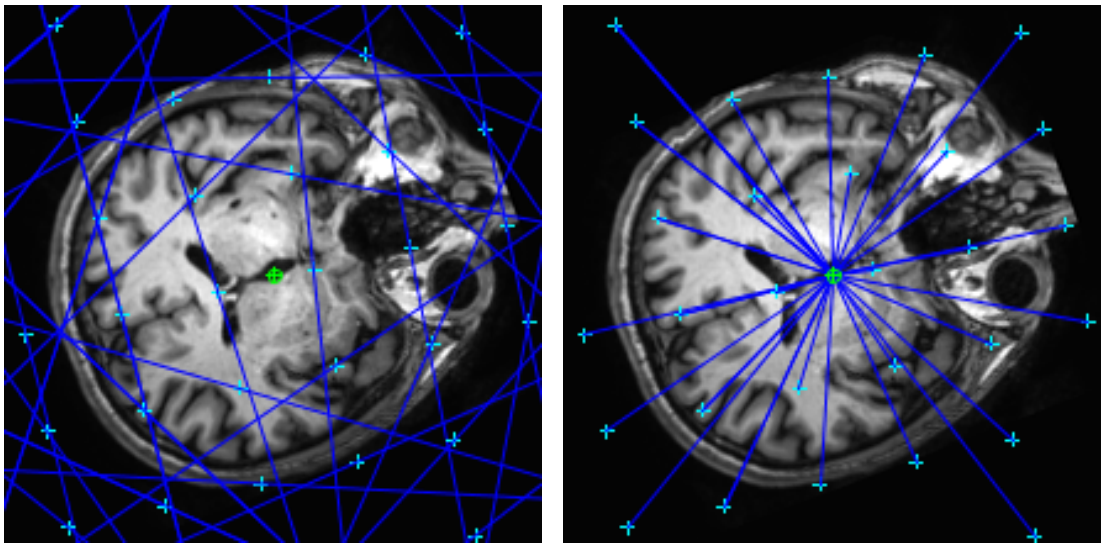

Figure 3.7: Two examples (left: test lines for the INV method, right: test ray lengths for the DN method) for the 'grid_inv_dn.txt' script, which are both overlaid on a slice of IR rotated brain MR image.

3.4 Acknowledgement

Thanks to the ImageJ macro script 'grid_multipurpose.txt' by Aleksandr MIRONOV (http://rsb.info.nih.gov/ij/macros/Multipurpose_grid.txt), which helped in creating the dialogue menus in this script.

Chapter 4

ImageJ Measure INV DN Macro

4.1 Introduction

Using two novel stereological methods, i.e. the INV [21, 22, 23, 24, 27, 28, 53] and DN [24, 55, 59] methods, the heaviest labour work in the estimation of volume and surface area of a 3D object, e.g. a brain MR image, is probably the manual measurement on the lengths of the segments from test grid and lines overlaid upon the pivotal slice of the object. This manual procedure takes not only the majority of the time cost for the whole estimation but also a lot of energy and efforts of operatives.

One step in the manual measurement is to record results including lengths, positions and orientations of measured segments. Sum of lengths contributes to the volume estimation and coordinates of the segments contribute to both an inspection of the results and a repeat study. Besides, the time cost in the measurement is also needed to record to examine efficiency of the stereological methods.

An in-house IMAGEJ macro script (i.e. 'grid_inv_dn.txt') was introduced in Chapter 3 to generate test grid and lines for both the INV and DN methods. Therewith, to make the manual measurement procedure consistent with the grid-generating script in operation and be efficient and easy to use too, especially for the recording step, another in-house IMAGEJ [108] macro script (i.e. 'measure_inv_dn.txt' in Appendix D) was programmed. The aim of this chapter is to introduce the usage of the new script.

4.2 Materials and Methods

Installation of this IMAGEJ macro script is the same as other IMAGEJ scripts, i.e. copy the text script file 'measure_inv_dn.txt' into `ImageJ/macros/toolsets/` folder, and then tick the newly added script option in '≫' drop down menu at the right end of a newly opened IMAGEJ window, thus a new tool icon will turn up in the window (Figure 4.1).

After loading one rotated MR image slice and generating a test grid with lines from another IMAGEJ script 'grid_inv_dn.txt' (Figure 4.4a, 4.6a), left click on the new icon in IMAGEJ window to activate measuring function. Then, to do volume measurement of a human brain (e.g.

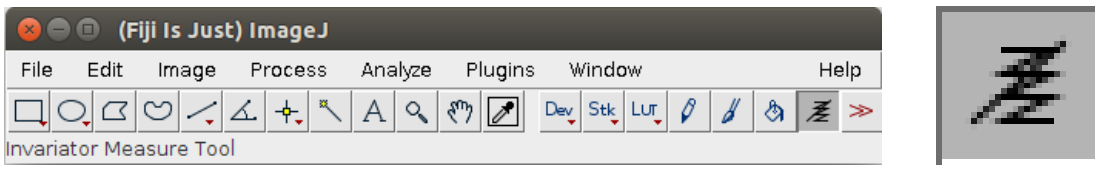

Figure 4.1: GUI for IMAGEJ software and icon for the 'measure_inv_dn.txt' script in IMAGEJ.

volume of cerebrum including ventricles in the example below) in the MR image, left click and drag the mouse to draw a segment along test lines covering target tissue. When modification on the length of the segment is needed, still left click on either end of the segment and move the segment freely. To finish the drawing of one segment, right click anywhere on the image and the new segment will be added to the 'ROI Manager' automatically (Figure 4.2a).

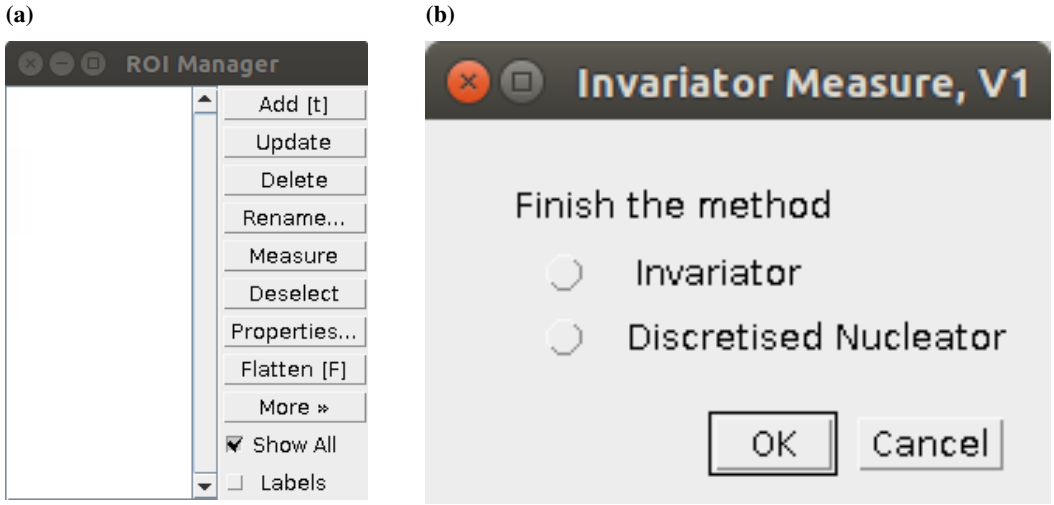

Figure 4.2: (a) The 'ROI Manager' menu and (b) the finishing menu activated in the 'measure_inv_dn.txt' script.

When all segments covering target tissue have been drawn, double click on the icon in IMAGEJ window to pop-up finishing menu (Figure 4.2b). Choose the method applied in the menu and click 'OK'. The results will be saved in the same directory where the MR image slice is. Four new files for the measurement (Figure 4.3) will be created, including: (1) a zip file for the records of segments in 'ROI Manager', (2) a xls file for the list of length measures, (3) a snapshot in PNG format of the segments drawn in the MR image (Figure 4.4b, 4.6b), and (4) a text file recording the finishing time of the measurement. The starting time has already been recorded in the same text file from the IMAGEJ script 'grid_inv_dn.txt' (as shown in the text file excerpt below), therefore the total time for each measurement can be calculated.

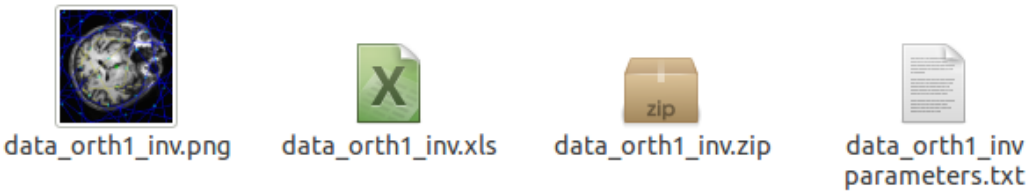

Figure 4.3: Four new files are generated after finishing measurement on the image by the 'measure_inv_dn.txt' script. The PNG image gives a screenshot of all the measurement; the XLS table records all the measures; the ZIP file backs up all the operations in IMAGEJ and the TXT document records the information of parameters and time which is shown in the text file excerpt below.

(A text file generated by the script, e.g. 'data_orth1_inv parameters.txt' in Figure 4.3, records the starting time and the finishing time. Therefore time for processing can be obtained.)

Invariator/Nucleator grid for image: [data_orth1_inv.img]
Start time: 14:31:23, 3 May 2016
...
- - - - - - - - - - - - - - -
~/data_orth1_inv_inv
finish time: 14:40:16

~/data_orth1_inv_dn
finish time: 14:44:8

Additionally, because all measures on the current image will be cleared automatically after the files of results are saved, it is suggested not to close the images or text windows by yourself before the measurement is completed, otherwise the script may not be able to find the MR image directory and the results will be saved to the IMAGEJ software directory by default.

4.3 Results

Examples of (1) volume estimation using the INV method, (2) surface area estimation using the INV method and (3) volume estimation using the DN method on one adult brain MR sectioning plane are displayed below. The results are estimated based on the measures by one observer.

4.3.1 Volume Estimation By The INV Method

In this brain volume estimation example, the sum of lengths measured by the INV method was 677.62 mm (Figure 4.4b). Thus, with the lengths and grid parameters available, whole brain volume was estimated as 1084.2 cm^3 (Equation (4.1)). The time spent in the measurement was approximately 9 mins.

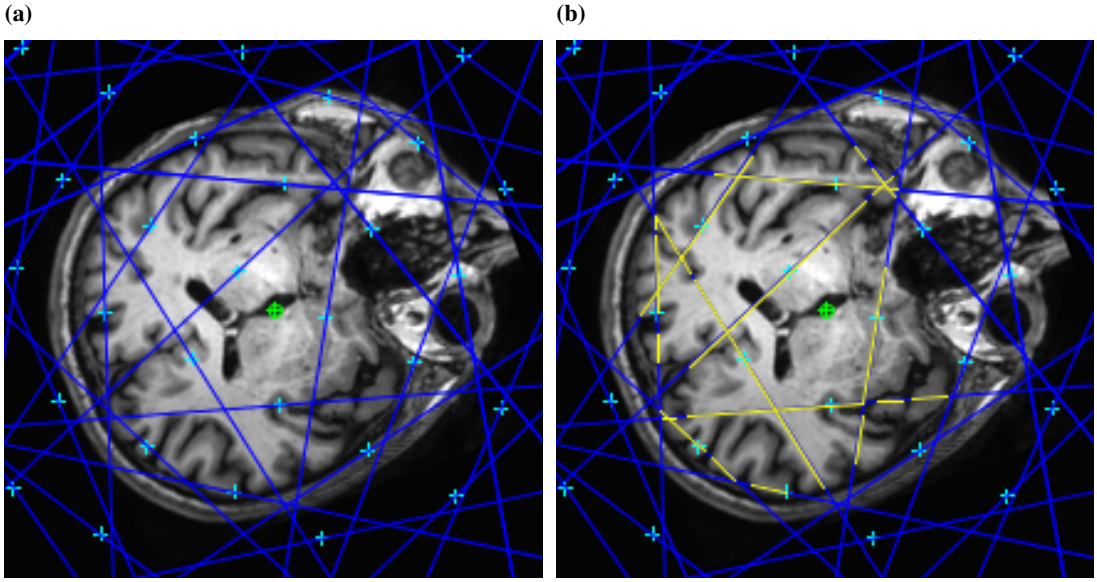

Figure 4.4: Length measurement of segments covering whole brain tissue on MR image for estimating whole brain volume by the INV method using the 'measure_inv_dn.txt' script. (a) Test grid and lines (blue) before the measurement; (b) test grid and lines (yellow) after the measurement.

$$\widetilde{V}_{INV} = d^2 \times \sum_{i=1}^{n} L_i = 40^2 \times 677.62 = 1084192\ mm^3 = 1084.2\ cm^3 \tag{4.1}$$

4.3.2 Surface Area Estimation By The INV Method

In this brain surface area estimation example, the number of intersects between the test lines in the INV method and the brain cortical gyri and sulci was around 59 (Figure 4.5). Thus, pial surface area was estimated as 1888.0 cm^2 (Equation (4.2)).

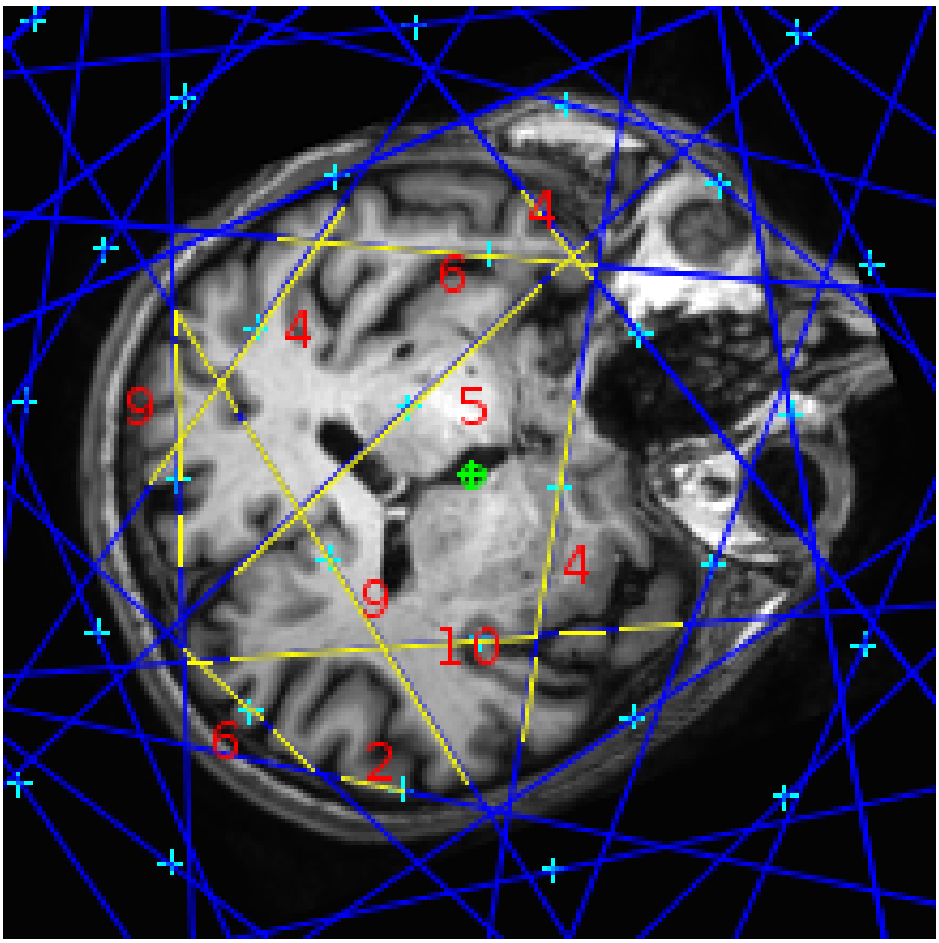

Figure 4.5: Intersects counts for the pial surface area by the INV method using the 'measure_inv_dn.txt' script. The numbers (red) indicate the intersects between each line and the pial surface.

$$\widetilde{S}_{INV} = 2 \times d^2 \times \sum_{i=1}^{n} I_i = 2 \times 40^2 \times 59 = 188800\ mm^2 = 1888.0\ cm^2 \qquad (4.2)$$

4.3.3 Volume Estimation By The DN Method

In this brain volume estimation example, the sum of the lengths measured by the DN method was 448.78 mm (Figure 4.6b). Thus, whole brain volume was estimated as 1436.1 cm^3 (Equation (4.3)). The time spent in the measurement was approximately 4 mins.

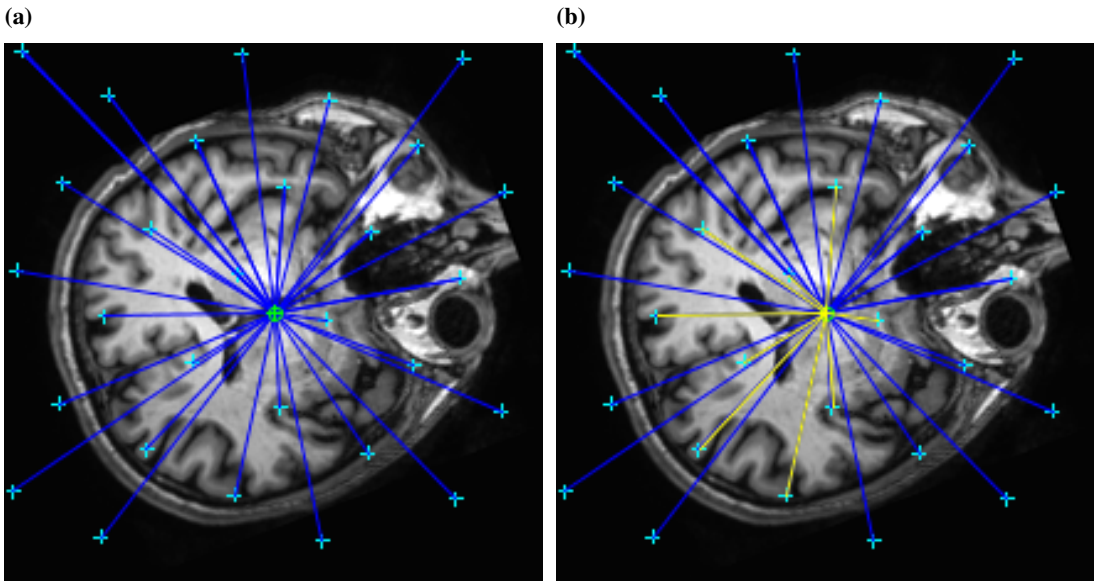

Figure 4.6: Length measurement of segments covering whole brain tissue on MR image for estimating whole brain volume by the DN method using the 'measure_inv_dn.txt' script. (a) Test grid and lines (blue) before the measurement; (b) test grid and lines (yellow) after the measurement.

$$\widetilde{V}_{DN} = 2 \times d^2 \times \sum_{i=1}^{n} L_i = 2 \times 40^2 \times 448.78 = 1436096\ mm^3 = 1436.1\ cm^3 \qquad (4.3)$$

Chapter 5

Estimation of Fetal Brain Volume on MRI Using Three Stereological Methods

5.1 Introduction

Stereology may be defined as statistical inference of geometric parameters (e.g. volume and surface) from sampled information (e.g. points, lines and sections). Designed-based stereological methods are mathematically unbiased. Systematic sampling makes stereology highly efficient. Error prediction makes stereology practical in operation.

A traditional stereological method is the CAVALIERI method [56], which starts at a UR position and cuts an object in a series of parallel sections with an equal sectioning interval. On each section plane, a test system containing a rotated UR square grid is overlaid. Volume is estimated from the total area covered by all points hitting the object multiplied by slice interval. The CAVALIERI method can not obtain an unbiased estimate of surface area of a 3D object, which requires a different initial sampling design (e.g. IR rotation, vertical sectioning and Fakir (bed of nails)).

Measurements on in vitro studies (e.g. microorganisms and cells) and parts of in vivo studies (e.g. plants) can be performed by stereology in a physical way where specimens not only can be physically cut but also generally do not require to be reassembled. However, these invasive operations are probably impossible in in-vivo studies (e.g. animals and humans). A solution for human studies is using MRI which obtains 3D images (i.e. array of voxels) and the information can be resampled in different orientations as required.

In human fetal brain development, significant abnormality can be detected directly using clinical imaging techniques such as ultrasound or MRI. Along with the rapid development of techniques such as fast fetal imaging and fetal motion correction [114], quantitative description of structural changes of fetal brain from the images has become achievable. Different factors, for example, maternal exposure to neurotoxins (e.g. alcohol, lead, and pesticides) during different stages of fetal development often results in various degrees of deficits in fetal brain

structure and function [12]. Maternal exposure to psychosocial stressors, which was usually thought of as risk factors, may also have uncertain effects on the development of fetal brain of both humans [35] and monkeys [84]. Effects of stressors are depending on the context, intensity, duration and timing of stressors and the social support systems to the mothers.

Stereology, specifically the CAVALIERI method, has been applied to estimate fetal brain volume previously in both in-vitro [11] and in-vivo [50] studies. The aim of this chapter is to investigate the application of three new stereological methods (i.e. the ICAV [28, 25], INV [21, 22, 24], and DN [24, 59] methods) for estimating volume and surface area of in-vivo human fetal brain in MR images using ANALYZE 11.0 [101] software (MAYO Foundation, Minnesota, USA, http://analyzedirect.com/).

The operation of the ICAV method is similar with that of the CAVALIERI method with an additional preparation of isotropic rotation of a 3D object. The precision of each individual estimate is predicted theoretically by CE, and a CE $< 5\%$ is desirable [103].

The operations of the INV and DN methods are both based on just one isotropically rotated section plane from the whole 3D image of the object. The more data there are in a cohort, the more highly precise and efficient population mean estimates will be. When real volume (or surface area) of each data (or biological variances of the dataset) is available, empirical CEs can be estimated to predict stereological error variances in both the INV and DN methods [28].

The ICAV and INV methods have only been applied to investigate volume and surface area of rat brain in vitro on MR images of a small cohort [28], The previous study had to physically rotate and spin gel balls which were embedded with specimens to obtain isotropic orientation before MRI scanning.

In this article, the ICAV, INV and DN methods are applied as practical means of estimating brain volume of human fetuses at both the second (14 to 27 weeks) and the third (28 to 40 weeks) trimesters of gestational age (GA) [4] in vivo on MR images. The estimates were made from isotropic triplets of orthogonal orientations for each method (i.e. the ICAV ortrip, INV ortrip and DN ortrip methods), and the results from each orientation for each method were compared with each other to test precision for the three methods. Assessments of inter-rater reproducibility (the CAVALIERI method was additionally performed) and intra-rater repeatability were also performed by three students all specializing in medicine or biomedicine to investigate practicability in application. Clinically, the fetal brains were divided into three groups according to different maternal conditions (i.e. healthy, maternal stressed and maternal substance abused), and influence of these conditions on the development of fetal brain volume estimated by the ICAV ortrip method was assessed.

5.2 Materials and Methods

5.2.1 Subjects

A cohort of ten pregnant women were recruited following ethics committee approval, among which five were healthy, three were diagnosed with maternal psychological stress and two

were with maternal exposure to substance (methodone, diazepam and trazadone). All the ten mothers were scanned twice between mean GA 24.9 ± 0.7 standard deviation (SD) weeks (range 24.1 to 26.6 weeks GA) and mean GA 36.4 ± 0.4 SD weeks (range 35.6 to 37.3 weeks GA) respectively (Table 5.1). No side effects was found on mothers after MRI scanning and the GA at the time of delivery was mean age 39.2 ± 1.5 SD weeks (range 36.9 to 41.6 weeks). Anonymization was performed before further investigation on all the fetal brain MR images.

Table 5.1: Time information of ten fetuses who took MR scans at both the second and third trimesters of GA. Besides, days of GA at birth of ten fetuses are listed too. In 'ID' column, the prefixes 'LC', 'LM' and 'LS' indicate the health, substance and stress groups, respectively.

ID	Gestational Age at Scans				Gestational Age at Birth	
	2nd Trimester		3rd Trimester			
	Weeks	Days	Weeks	Days	Weeks	Days
LC4235	24	169	36	254	38	266
LC4232	24	170	36	254	39	274
LC4234	24	174	36	253	39	273
LC4267	24	174	36	254	40	282
LC4229	25	177	37	261	40	284
LM4245	24	169	36	253	40	280
LM4203	25	177	36	256	41	291
LS4201	24	173	36	257	37	261
LS4287	25	175	36	255	39	278
LS4254	26	186	35	249	36	258

5.2.2 Data acquisition and Motion Correction

MRI studies were performed on a 3 tesla scanner (MAGNETOM Verio; Siemens AG, Germany), using body and spine matrix coil elements at the Clinical Research Imaging Centre (CRIC) in Edinburgh. Non-breath-hold, multi-slice, half FOURIER single shot turbo spin echo (HASTE) T2-weighted (T2W) sequences were acquired repeatedly three times in each axial, sagittal and coronal scanning directions (TE = 94 ms, TR = 4200 ms, $0.55 \times 0.55 \times 3$ mm^3 voxels, 25–50 slices). Specific absorption rate (SAR) was < 2.0 W/kg, and the right lateral decubitus position (RLDP) was taken to avoid inferior vena cava (IVC) compression.

The image series were then motion corrected and reconstructed using the Slice MRI Motion Estimation and Reconstruction (SLIMMER) [76] tool (University of Washington, USA, `http://depts.washington.edu/bicg/software/SLIMMER/slimmer.php.html`) to form a single 3D high resolution brain image ($1 \times 1 \times 1$ mm^3) (Figure 5.1).

5.2.3 Stereological Analysis

The ICAV, INV and DN methods were applied for the volume estimation of ten fetal brains including cerebrum, ventricles (the lateral, the third and the fourth), midbrain, pons and cerebellum. The brainstem beneath the cerebellum was excluded.

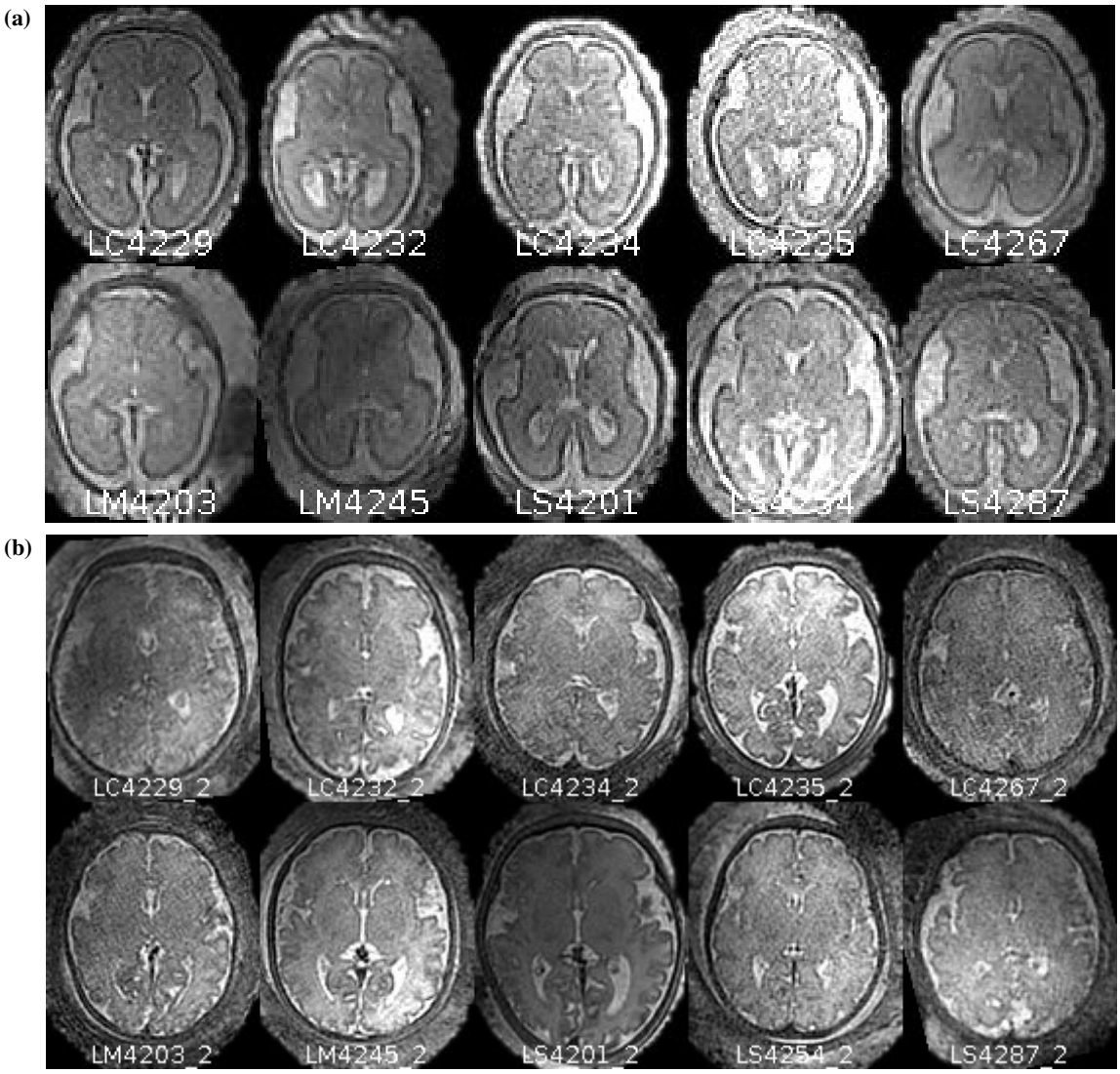

Figure 5.1: After being motion corrected using SLIMMER tool, quality of fetal brain MR images is improved. (a) Central slices in the transverse view of ten fetal brain images in the second trimester of GA; (b) paired ten fetal brain central slice images in the third trimester of GA.

For IR ortrip rotation and UR section of each data, four uniform random numbers U_1, U_2, U_3, U_4 in the interval of $[0, 1)$ were generated by a free software R (http://www.r-project.org/, using 'runif' command). Three of the numbers were transferred into IR ortrip rotation angles ϕ, θ, τ ($0 \leq \phi < 2\pi$, $0 \leq \theta \leq \pi$, $0 \leq \tau < 2\pi$) by Equation (5.1). The last random number was transferred for the offset t ($0 \leq t < T$, where T was the slice interval) of the starting position of the pivotal section plane in ICAV method by Equation (5.2) [28]:

$$\phi = 2\pi U_1 \ , \quad \theta = \cos^{-1}(1 - 2U_2) \ , \quad \tau = 2\pi U_3 \tag{5.1}$$

$$t = TU_4 \tag{5.2}$$

Rotations of images for the ICAV, INV and DN methods were performed on ANALYZE software using the angles of ϕ, θ and τ. Firstly, the images in the ANALYZE7.5 format (.hdr/.img) were padded into a cubic file with the head being adjusted towards the same orientation. Then, the rotation could be executed in two operating protocols: either using ANALYZE MATRIX tool (Appendix A.1) or using both MATRIX and FLY tools (Appendix A.2). In this study, an isotropic triplet of orthogonal rotations were performed on each data (Figure 5.2).

After rotations, for the ICAV method, a series of section planes were generated with a random start (using the offset t) and a constant inter-slice distance (using the interval T) by ANALYZE OUTPUT MANEUVER option, which was the same as the slicing process in the CAVALIERI method. Then, each of the triplet of orthogonal sections was superimposed with an independently rotated UR test grid in STEREOLOGY MEASURE dialogue window in ANALYZE. Lattices of the grids hitting the tissue were manually counted for volume estimation, and intersects between grids and boundaries of tissue were counted for surface area estimation (Figure 5.3a). For the INV and DN methods, one pivotal section going through a common pivotal point (e.g. a central point of an image cube in this study) across the dataset was saved for each data, which would be the only image information needed in further measurement. Overlaid with one sheet of randomly rotated grid and one fixed pivotal point cross, the whole image was screen captured in the original size in Tagged Image File Format (TIFF), and the latter was loaded into the LINE PROFILE MEASURE dialogue window in ANALYZE, where the CALIPER tool was then applied as a T-square ruler point by point throughout the grid. The test points to be counted should cover the whole image space for INV method, but should be just within the profile of brain tissue for DN method. Lastly, in the INV method, lengths of lines perpendicular to radiating lines in the T-square ruler, which covered the target brain tissue in each measure were summed for volume estimation, and intersects were summed for surface area estimation (Figure 5.3b). In the DN method, lengths of radiating lines in the T-square ruler, which were between the lattices which hit the target tissue and the pivot point were summed for volume estimation. There was no surface area estimation available in the DN method (Figure 5.3c).

The parameters of section and counting, such as slice interval (T) and side length (d) of lattice in the test grid, were adjusted according to the growth of fetal brain. The sum of points counted ($\sum_{i=1}^{n} P_i$) per subject is suggested to be less than 200 upon 10 to 15 slices, to achieve

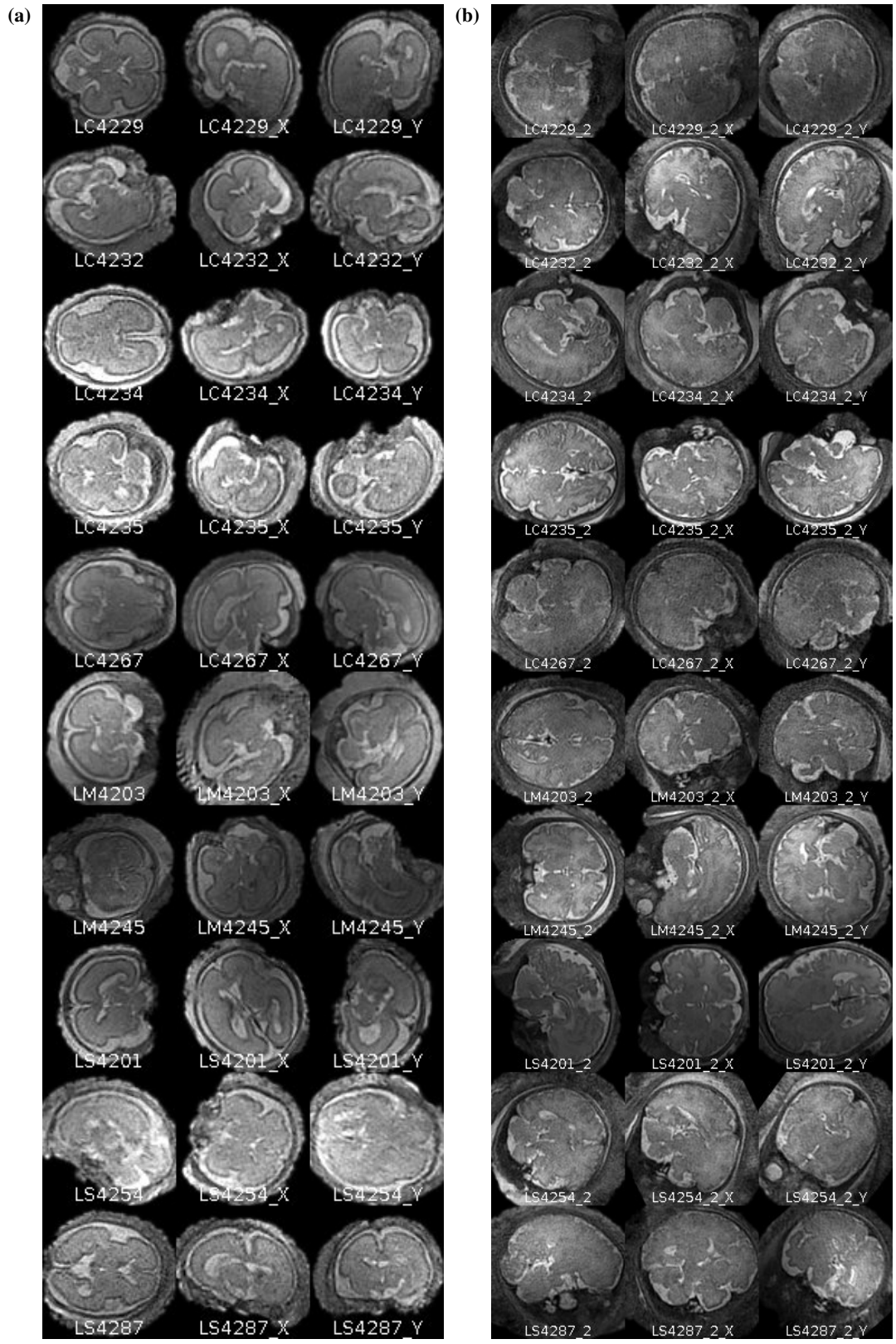

Figure 5.2: Ten fetal brains are displayed for triplets of orthogonal IR rotations in both the second and third trimesters of GA. Each row contains three central slices (i.e. pivotal planes) of orthogonal IR rotated MR images of one fetal brain in (a) the second or (b) the third trimester.

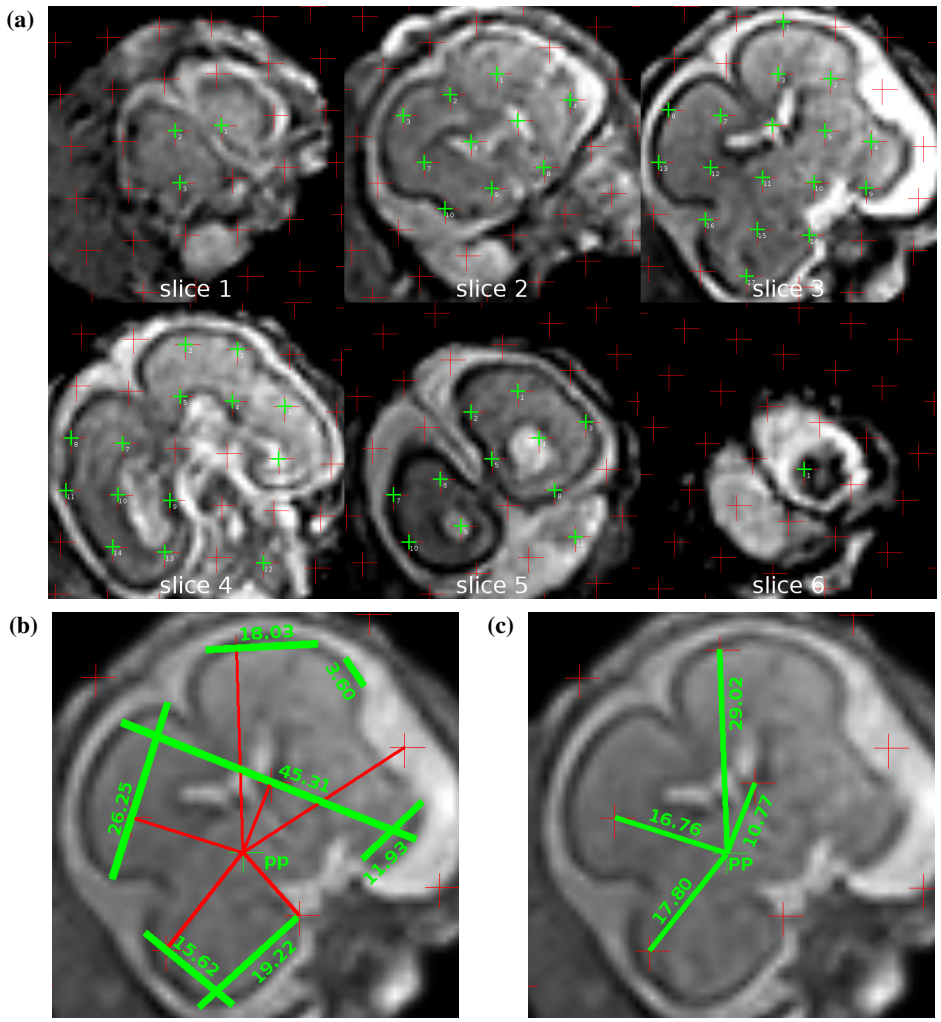

Figure 5.3: Examples of volume estimation by the ICAV, INV and DN on one fetal brain in the second trimester. (a) In the ICAV method, test points counting (green) is performed in six successive slices for estimating whole volume of cerebrum, ventricles and cerebellum. (b) In the INV method, length measurement of green segments covering the cerebrum and ventricles is performed for volume estimation. Green segments are perpendicular to red segments and the latter connect between each red cross over the whole image and pivotal point cross. (c) In the DN method, length measurement of green segments connecting each of the test points hitting the target tissue and pivotal point cross is performed for volume estimation of cerebrum and ventricles. In both (b) and (c), the pivotal point cross is a green cross in the centre of the image and is labelled as 'PP'.

both high precision and practical efficiency [63]. In this study, the parameters of T and d, and the time consumed in counting the points, intersects and measuring the lengths are summarized in Table 5.2.

Table 5.2: Parameters and time consumed for points, intersects counting and lengths measurement by the CAVALIERI, ICAV, INV and DN are listed for the application on fetal brains in both the second and third trimesters.

GA	Parameters (mm)			Time for Point, Length Counting ($mins$)				
	ICAV/CAVALIERI		INV/DN	ICAV	CAVALIERI	INV	DN	ICAV
	T	d	d		Volume			Surface Area
2nd Trimester	7	6	10	15	10	15	5	15
3rd Trimester	9	10	15					20

5.2.4 Reproducibility and Repeatability Assessment

Three raters (i.e. AJ, KY and SW) participated independently in the assessments. All raters were blinded to the data information during the measurement. For each of the ICAV, INV and DN methods, as well as the traditional CAVALIERI method which was used as a reference method additionally, two raters were randomly chosen for inter-rater reproducibility assessments and one rater repeated two estimations for intra-rater repeatability assessments (Table 5.3). In both the second and third trimesters, five best image quality data were selected out of ten and one random section plane was selected out of a triplet of orthogonal section planes in each data. The parameters in all inter- and intra-observer assessments were identical as those used in the whole ten data measurement, except for random position of test grids. Pearson's product moment correlation coefficient (Pearson's r, $-1 \leq r \leq 1$, where -1 means total negative correlation, 0 means no correlation, and 1 means total positive correlation) was computed using R software for each assessment.

Table 5.3: Three raters participated in the reliability assessment of four stereological methods. '+' means measuring volume for once, and '++' means measuring for twice.

Raters	ICAV	INV	DN	CAVALIERI
AJ		++	++	
KY	++	+	+	++
SW	+			+

5.2.5 Volume, Surface Area And CE Formulae

Volume ($\widetilde{V}$) is proportional to the total points counted ($\sum_{i=1}^{n} P_i$) or total length measured ($\sum_{i=1}^{n} L_i$) in the ICAV, INV and DN methods. Also, surface area ($\widetilde{S}$) for the ICAV and INV methods is proportional to the total intersects counted ($\sum_{i=1}^{n} I_i$). In cubic image with voxel size of $1 \times 1 \times 1\ mm^3$, volume and surface area estimator formulae can be simplified by Equation (5.3)(5.4)(5.5). CE estimator is predictable for ICAV method (Equation (5.6)(5.7)), but

is only empirical for INV and DN methods (Equation (5.8)(5.9)), where $var(\widetilde{V}|V)$ is stereological error variance, $var(\widetilde{V})$ is total variance, $var(V)$ is baseline (biological) variance, and $mean\{\widetilde{V}\}$ is the mean volume of the group dataset in the INV and DN methods [28].

ICAV *Volume & Surface Area Estimator*

$$\widetilde{V} = T \times d^2 \times \sum_{i=1}^{n} P_i \,, \quad \widetilde{S} = T \times d \times \sum_{i=1}^{n} I_i \tag{5.3}$$

INV Volume & Surface Area Estimator

$$\widetilde{V} = d^2 \times \sum_{i=1}^{n} L_i \,, \quad \widetilde{S} = 2 \times d^2 \times \sum_{i=1}^{n} I_i \tag{5.4}$$

DN Volume Estimator

$$\widetilde{V} = 2 \times d^2 \times \sum_{i=1}^{n} L_i \tag{5.5}$$

ICAV *CE*

$$var(\widetilde{V}|V) = (0.008727\, T^4 + 0.056891\, Td^3)\widetilde{S} \tag{5.6}$$

$$ce(\widetilde{V}|V)\% = 100\, \sqrt{var(\widetilde{V}|V)}/\widetilde{V} \tag{5.7}$$

INV/DN CE (Empirical)

$$mean\{var(\widetilde{V}|V)\} = var(\widetilde{V}) - var(V) \tag{5.8}$$

$$ce(\widetilde{V}|V)\% = 100\, \sqrt{mean\{var(\widetilde{V}|V)\}}/mean\{\widetilde{V}\} \tag{5.9}$$

As an example, for the subject 'LC4232' in the second trimester, shown in Figure 5.3, the volumes estimated by the ICAV, INV and DN methods were 67200 mm^3, 55984 mm^3 and 59480 mm^3, respectively (Equation (5.10)).

$$V_{ICav} = T \times d^2 \times \sum_{i=1}^{n} P_i = 12 \times 10^2 \times (3+10+17+14+11+1) = 67200\, mm^3 \tag{5.10}$$

$$V_{INV} = d^2 \times \sum_{i=1}^{n} L_i = 20^2 \times (45.31+18.03+3.60+26.25+15.62+19.22+11.93) = 55984\, mm^3$$

$$V_{DN} = 2 \times d^2 \times \sum_{i=1}^{n} L_i = 2 \times 20^2 \times (10.77+29.02+16.76+17.80+74.35) = 59480\, mm^3$$

5.3 Results

5.3.1 Reproducibility and Repeatability

Volume estimates of the reliability studies for the CAVALIERI and ICAV methods are shown in Table 5.4, and those for the INV and DN methods are shown in Table 5.5.

Table 5.4: Results of inter- and intra-rater studies of whole brain volume estimation using the CAVALIERI and ICAV methods by rater KY and SW are listed below. Five fetal brains in the second trimester and five in the third trimester were measured.

ID	Whole Brain Volume (cm^3)							
	ICAV				CAVALIERI			
	Rater KY			Rater SW	Rater KY			Rater SW
	Repeat 1	Repeat 2	Mean		Repeat 1	Repeat 2	Mean	
2nd Trimester								
LC4267	84.4	84.4	84.4	81.9	81.6	81.6	81.6	82.7
LC4229_X	100.0	97.5	98.8	96.0	98.0	94.5	96.3	91.2
LM4245_Y	70.3	72.1	71.2	64.5	69.6	69.0	69.3	67.8
LS4201	87.4	89.7	88.6	83.4	86.4	84.2	85.3	85.4
LS4287_X	97.3	97.3	97.3	90.7	96.8	94.0	95.4	93.7
3rd Trimester								
LC4234_2_X	272.7	279.0	275.9	278.1	267.4	256.9	262.2	277.2
LC4235_2_Y	255.6	252.9	254.3	259.2	254.1	249.9	252.0	256.9
LC4232_2	290.7	288.0	289.4	282.6	276.5	274.4	275.5	290.5
LM4245_2_Y	293.4	293.4	293.4	272.7	284.9	270.2	277.6	273.7
LS4201_2_X	333.9	335.7	334.8	334.8	324.8	315.0	319.9	315.7

Table 5.5: Results of inter- and intra-rater studies of whole brain volume estimation using the INV and DN methods by rater AJ and KY are listed below. Five fetal brains in the second trimester and five in the third trimester were measured.

ID	Whole Brain Volume (cm^3)							
	INV				DN			
	Rater AJ			Rater KY	Rater AJ			Rater KY
	Repeat 1	Repeat 2	Mean		Repeat 1	Repeat 2	Mean	
2nd Trimester								
LC4267	82.4	82.6	82.5	83.3	88.0	87.5	87.8	88.0
LC4229_X	98.0	98.1	98.1	96.9	101.1	100.8	101.0	100.0
LM4245_Y	70.4	70.1	70.3	70.2	72.1	72.2	72.2	71.6
LS4201	70.5	70.6	70.6	71.6	69.8	70.9	70.4	76.8
LS4287_X	93.7	93.8	93.8	97.1	98.1	97.9	98.0	99.2
3rd Trimester								
LC4234_2_X	299.6	298.6	299.1	312.3	365.3	364.9	365.1	347.0
LC4235_2_Y	246.5	248.0	247.3	245.3	216.0	215.9	216.0	200.7
LC4232_2	275.0	275.0	275.0	269.3	288.9	288.0	288.5	288.9
LM4245_2_Y	339.2	341.4	340.3	346.7	364.7	363.8	364.3	364.1
LS4201_2_X	271.8	272.3	272.1	271.1	243.7	243.1	243.4	243.5

The Bland-Altman plots of volume estimates in both trimesters obtained using the ICAV method and CAVALIERI method by the same rater (SW) showed no significant difference or bias (Figure 5.4a). Besides, the Pearson's r produced correlation coefficients ranged from 0.997882 to 0.999993 for all the inter- and intra-observer reliability assessments. The inter-rater assessments of the ICAV, INV, DN and CAVALIERI methods showed high reliability in both trimesters (Figure 5.4b).

5.3.2 Coefficients of Error

The theoretical CE for volume estimation in the ICAV method requires both volume and surface area estimates of the data. In this study, only nine data in the second trimester and five in the third trimester had surface area estimates due of limitation of image quality caused by fetal motion although SLIMMER software improved the quality already. The CE was $1.5\% \pm 0.1\%$ in the second trimester and $2.1\% \pm 0.1\%$ in the third trimester (Table 5.6).

Table 5.6: CE for each volume estimate by the ICAV method. In the table, volume (Vol, mm^3), surface area (Area, mm^2), stereological error variance ($var(\widetilde{V}|V)$) and CEs ($ce(\widetilde{V}|V)\%$) are shown for nine data in the second trimester and five paired data in the third trimester.

	LC4235	LC4232	LC4234	LC4267	LC4229	LM4245	LM4203	LS4201	LS4287
2nd Trimester									
Vol (mm^3)	63504	76860	74088	83664	98028	73332	87948	86184	94752
Area (mm^2)	11771	12660	13044	14660	15881	13025	15422	15399	16369
$var(\widetilde{V}\|V)$	1259176	1354275	1395352	1568220	1698834	1393320	1649733	1647273	1751036
$ce(\widetilde{V}\|V)\%$	1.8	1.5	1.6	1.5	1.3	1.6	1.5	1.5	1.4
3rd Trimester									
Vol (mm^3)	254700	284400	264600			285300		311400	
Area (mm^2)	59527	60800	50187			60952		67127	
$var(\widetilde{V}\|V)$	33887343	34612032	28570297			34698562		38213847	
$ce(\widetilde{V}\|V)\%$	2.3	2.1	2			2.1		2	

The empirical CE for volume estimation in the INV and DN methods requires biological variance (i.e. true volume variance) of fetal brain volume. In ICAV method, whole variance of volume estimation is composed of stereological error variance and biological variance (Table 5.7). The latter can be used as the baseline in assessing the empirical stereological error variance in the INV and DN methods. In this study, the empirical CE for each of three orthogonal section planes was $19.4\% \pm 2.9\%$, $18.5\% \pm 11.6\%$ in either trimester respectively by INV method, and $21.4\% \pm 4.5\%$, $24.1\% \pm 11.7\%$ respectively by DN method. Furthermore, the empirical CE for the mean of three orthogonal sections reduced to 8.1%, 5.5% in either trimester for the INV ortrip method, and 10.3%, 9.7% for the DN ortrip method (Table 5.8).

(a)

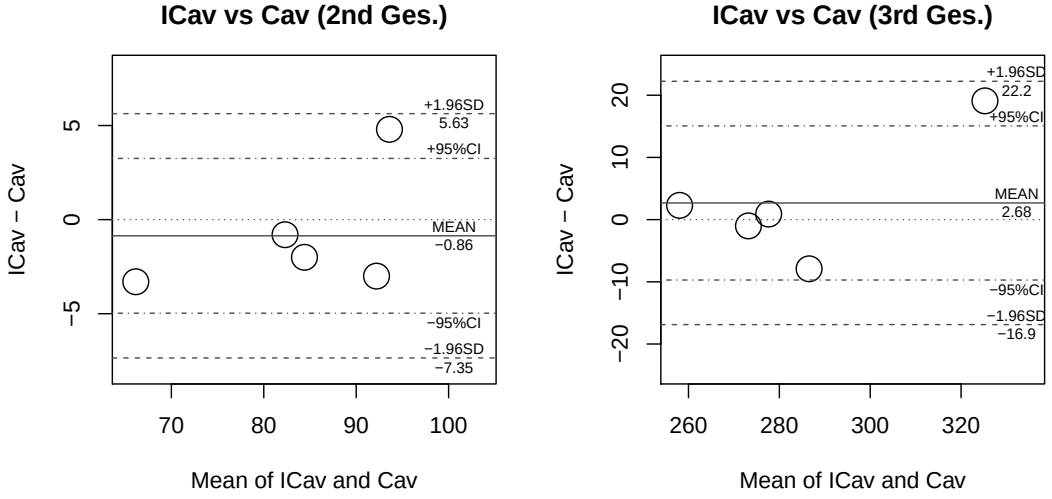

(b)

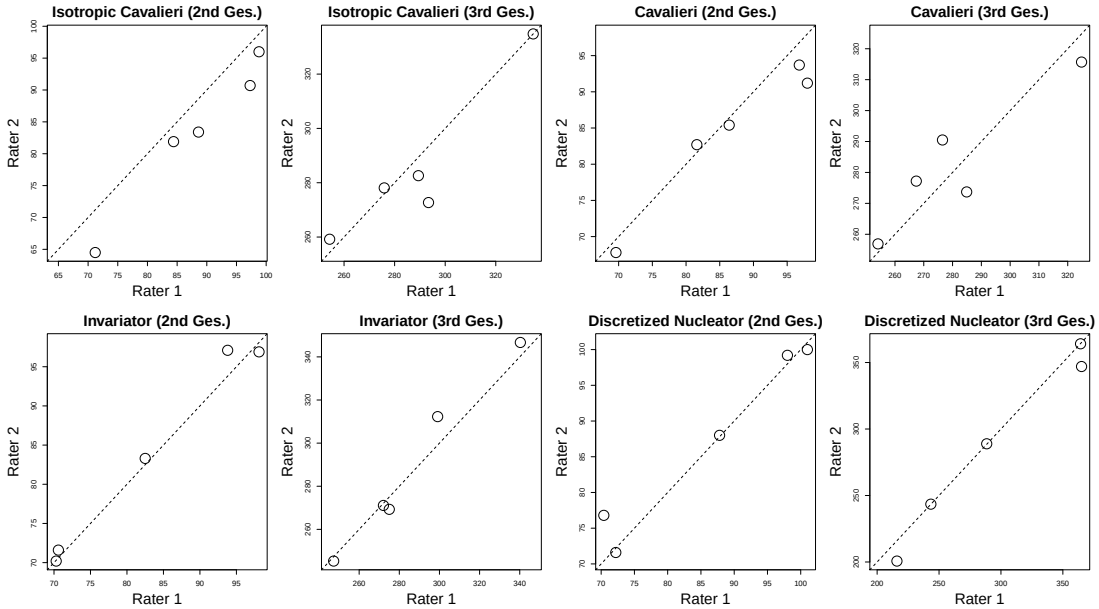

Figure 5.4: (a) The Bland-Altman plot: comparison of the ICAV and CAVALIERI methods by one same rater in both the second (left) and third (right) trimesters. (b) Scatter plots of inter-rater reliability assessments using the ICAV (top left two plots), CAVALIERI (top right two plots), INV (bottom left two plots) and DN (bottom right two plots). Each method is plotted in the second and third trimesters respectively.

Table 5.7: Biological variance of the whole fetal brain dataset ($var(biology)$) can be estimated by the variance of volume estimates in the sample group ($var(volumes)$) subtracting the stereological error variance obtained using the ICAV method ($mean\{var(\widetilde{V}|V)\}$, see Equation (5.6)).

	$var(volumes)$	$-$	$mean\{var(\widetilde{V}\|V)\}$	$=$	$var(biology)$
2nd Trimester	122675616		1524135		121151481
3rd Trimester	477657000		33996416		443660584

Table 5.8: Empirical CEs for volume estimation by the INV and DN methods. CEs $(ce(\widetilde{V}|V)\%)$ in each of three orthogonal sections and the mean of three orthogonal sections are shown in both second and third trimesters.

	INV	INV_X	INV_Y	INV_Mean	DN	DN_X	DN_Y	DN_Mean
$var(volume)$								
2nd Trimester	355561111	493616111	342473611	168615001	361287778	616680000	421090000	200168108
3rd Trimester	2146272188	1085415188	10999688625	702115313	2348736750	2928818250	14942130750	1216136250
$var(stereology)$								
2nd Trimester	234409630	372464630	221322130	47463520	240136297	495528519	299938519	79016627
3rd Trimester	1702611604	641754604	10556028041	258454729	1905076166	2485157666	14498470166	772475666
$meanvolume$								
2nd Trimester	84511	84789	85389	84896	87044	83933	87133	86037
3rd Trimester	284625	269685	325665	293325	274410	262170	321120	285900
$ce(\widetilde{V}\|V)\%$								
2nd Trimester	18.1	22.8	17.4	8.1	17.8	26.5	19.9	10.3
3rd Trimester	14.5	9.4	31.5	5.5	15.9	19.0	37.5	9.7

5.3.3 Fetal Brain Volume

Whole brain volume (including cerebrum, ventricles and cerebellum) of ten fetuses paired in both second and third trimesters, which was obtained using the ICAV ortrip, INV ortrip and DN ortrip methods, is shown in Table 5.9.

Table 5.9: Whole brain volumes of ten fetuses in both the second and third trimesters. Estimates by the ICAV, INV and DN in three orthogonal sections and their mean values are displayed. In 'ID Pair' column, the prefixes 'LC', 'LM' and 'LS' indicate the health group, the substance group and the stress group, respectively.

ID Pair	ICAV ortrip (cm^3)				INV ortrip (cm^3)				DN ortrip (cm^3)			
	Vol	Vol_X	Vol_Y	Vol_Mean	Vol	Vol_X	Vol_Y	Vol_Mean	Vol	Vol_X	Vol_Y	Vol_Mean
2nd Trimester												
LC4235	63.5	66.5	67.8	65.9	80.2	56.2	70.0	68.8	84.2	54.4	62.8	67.1
LC4232	76.9	69.0	68.8	71.6	80.1	51.4	94.7	75.4	85.2	41.6	93.2	73.3
LC4234	74.1	71.3	72.6	72.7	96.7	78.3	57.2	77.4	100.6	76.4	68.2	81.7
LC4267	83.7	84.4	81.6	83.2	83.3	86.4	91.7	87.1	88.0	84.8	104.8	92.5
LC4229	98.0	95.3	92.7	95.3	101.2	96.9	114.0	104.0	110.8	100.0	114.4	108.4
LM4245	73.3	72.8	69.6	71.9	55.2	79.1	70.2	68.2	53.2	80.0	71.6	68.3
LM4203	87.9	86.7	84.9	86.5	72.9	93.3	106.1	90.8	72.0	95.4	115.0	94.1
LS4201	86.2	87.4	85.9	86.5	71.6	124.4	88.8	94.9	76.8	123.6	84.4	94.9
LS4287	94.8	96.0	92.2	94.3	119.4	97.1	75.8	97.4	112.6	99.2	69.8	93.9
LS4254	109.9	107.9	108.1	108.6	119.5	93.7	156.6	123.3	111.6	90.4	138.8	113.6
3rd Trimester												
LC4234_2	264.6	268.2	275.4	269.4	311.0	312.3	225.5	282.9	306.5	347.0	216.5	290.0
LC4235_2	254.7	255.6	246.6	252.3	351.2	227.5	245.3	274.7	319.5	207.0	200.7	242.4
LC4232_2	284.4	289.8	287.1	287.1	269.3	288.0	320.9	292.7	288.9	279.9	323.1	297.3
LC4267_2	297.9	299.7	305.1	300.9	366.8	248.0	318.8	311.2	333.5	248.4	322.2	301.4
LC4229_2	357.3	350.1	340.2	349.2	290.3	384.8	393.1	356.1	324.0	372.2	398.3	364.8
LM4245_2	285.3	292.5	287.1	288.3	235.6	249.5	346.7	277.3	197.6	233.6	364.1	265.1
LM4203_2	262.8	265.5	266.4	264.9	348.3	207.9	250.4	268.9	378.5	202.5	241.2	274.1
LS4254_2	285.3	293.4	299.7	292.8	303.8	301.3	281.7	295.6	311.0	296.6	286.7	298.1
LS4287_2	304.2	315.9	317.7	312.6	351.0	385.9	279.2	338.7	355.1	383.4	294.8	344.4
LS4201_2	311.4	324.0	318.6	318.0	256.1	271.1	490.1	339.1	259.7	243.5	501.3	334.8

In each subject, comparing with the INV ortrip and DN ortrip methods, individual volume estimates in each of three orthogonal sections obtained by the ICAV ortrip method were closer to mean volumes of the three estimates (Figure 5.5). Group means of ten fetal brain

volumes estimated by the ICAV ortrip, INV ortrip and DN ortrip methods in the second and third trimesters of GA were compared (Figure 5.6, 5.7). Mean volumes of three sections obtained by all the three methods respectively were close to each other. Logarithm transformed Bland-Altman plots were applied on the whole data from one randomly selected section planes in both trimesters, where volume obtained by the ICAV ortrip method only (as a reference method) was referred as the horizontal axis [10, 78]. The plots showed no bias in the volume obtained among the three methods (Figure 5.8).

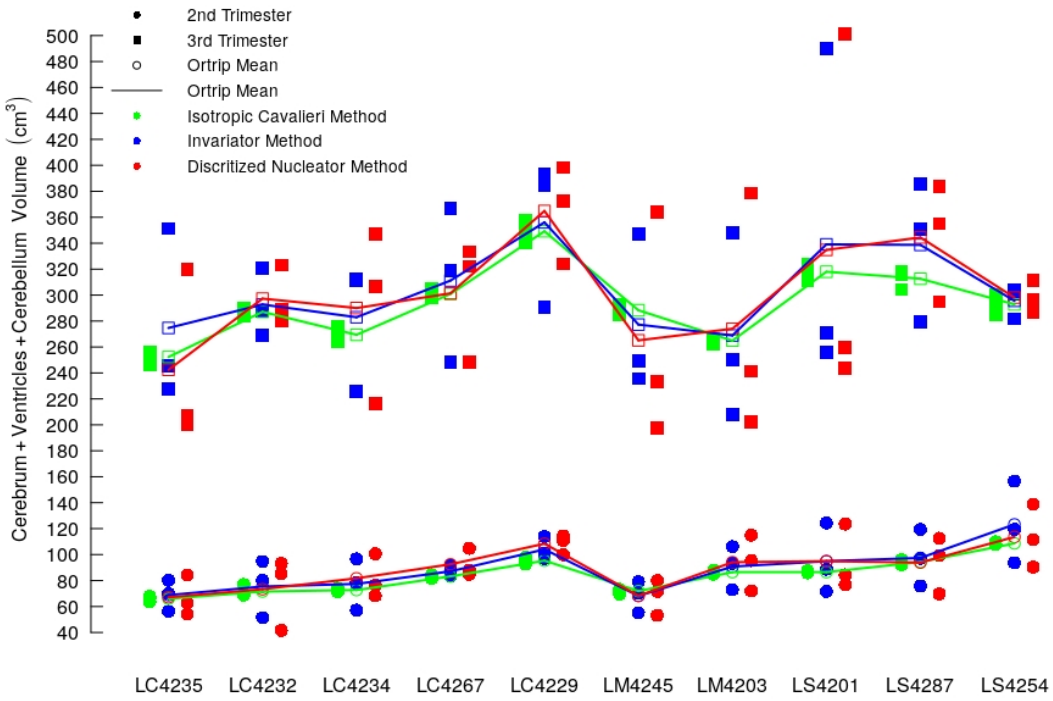

Figure 5.5: Comparison of mean values of three orthogonal estimates using the ICAV ortrip, INV ortrip and DN ortrip in each individual fetal brain. Ten fetal brain volumes (including cerebrum, ventricles and cerebellum) in both the second and third trimesters are displayed.

In each of three clinical groups, although the sample size was only five, three and two in either trimester respectively, linear regression was used to predict growth difference of brain volume in three groups on the same day which was the mean of GA of all the ten fetuses. The regression prediction was repeated from each of three orthogonal sections and the mean of three sections (Figure 5.9). As a result, the brain volume of the maternal stress influenced fetuses was relatively bigger while that of the maternal substance affected fetuses was potentially smaller. However, statistically no significant difference was found in both the trimesters.

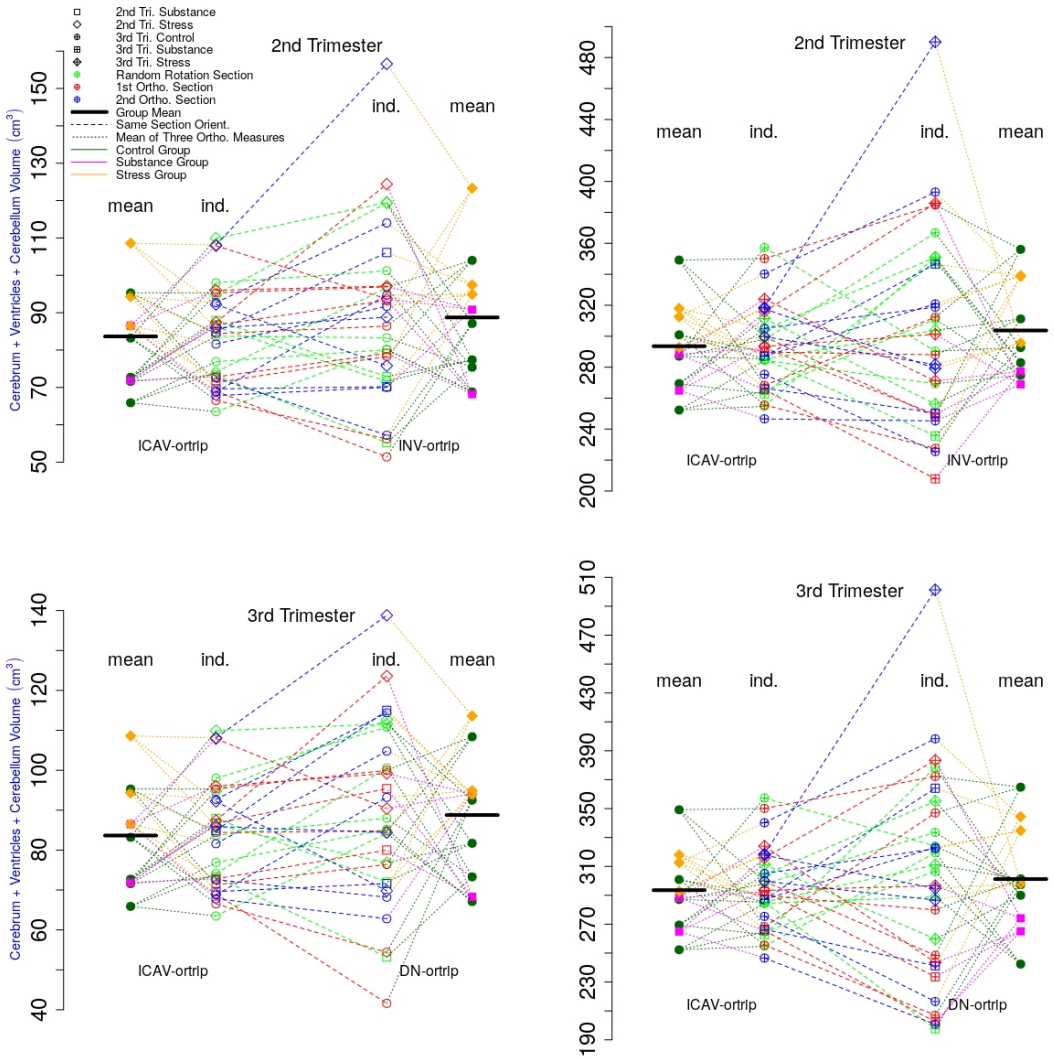

Figure 5.6: Comparison of group means of ten fetal brain volumes estimated by the ICAV ortrip, INV ortrip and DN ortrip methods in the second and third trimesters. Abbreviations: Tri. = Trimester, Ortho. = Orthogonal, ind. = individual (i.e. section slice(s) in one orientation). The 'mean' column is mean volume estimates obtained from ortrip section planes in each method.

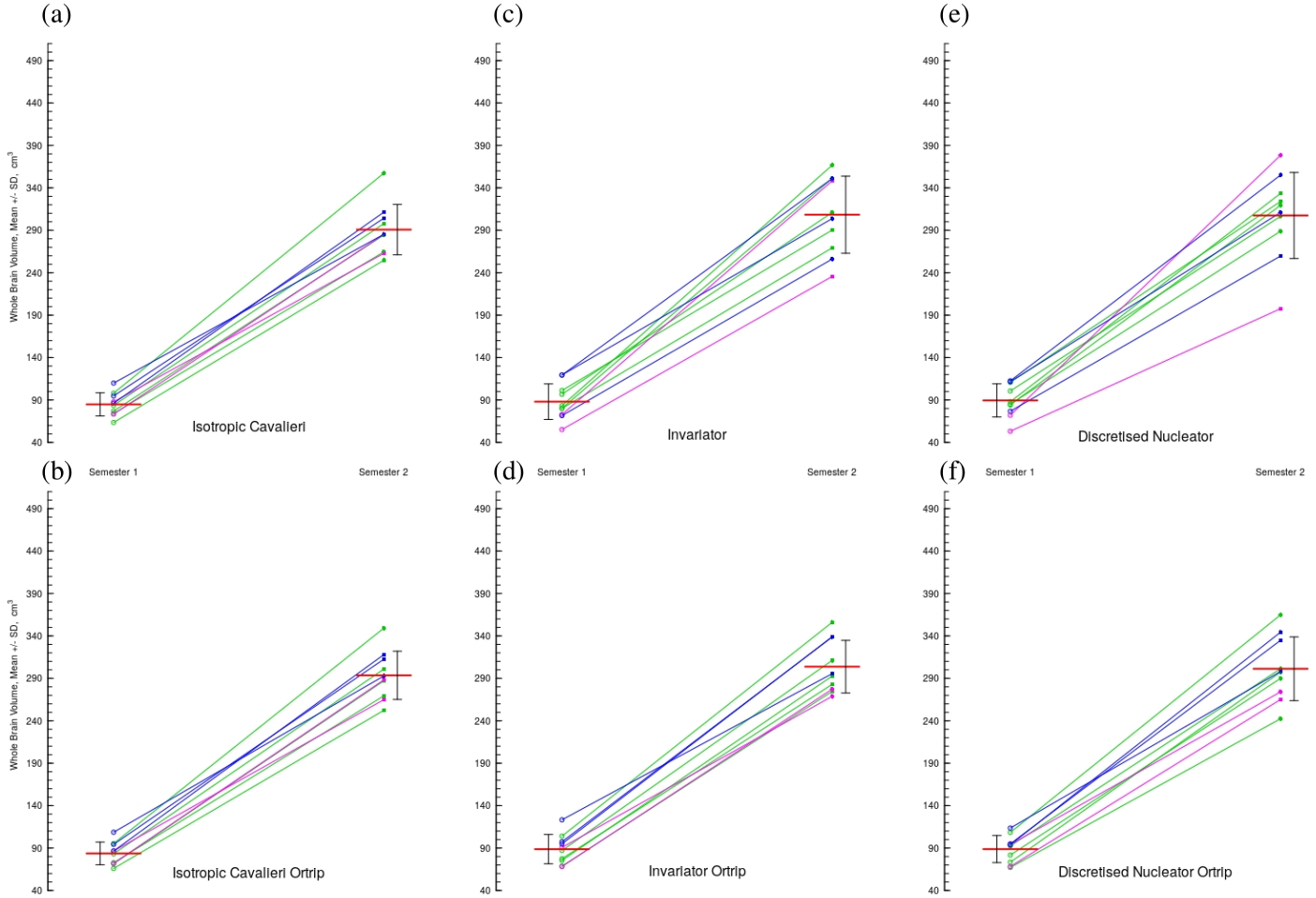

Figure 5.7: Paired comparison among whole brain (i.e. cerebrum, ventricles and cerebellum) volumes obtained from ten fetuses in both the second and third semesters GA by stereological methods. In each sub-image, the left dots represent ten fetal brain volumes in the second semester and the right filled dots represent volumes in the third trimester. Brain volumes of the same fetus in both the semesters are connected. Different colours represent different clinical group (i.e. green represents health group, pink represents maternal substance group and blue represents maternal stress group). (a) using the ICAV method; (b) the ICAV ortrip method; (c) the INV method; (d) the INV ortrip method; (e) the DN method; (f) the DN ortrip method. Mean (red horizontal bars) and SD values are displayed in each group.

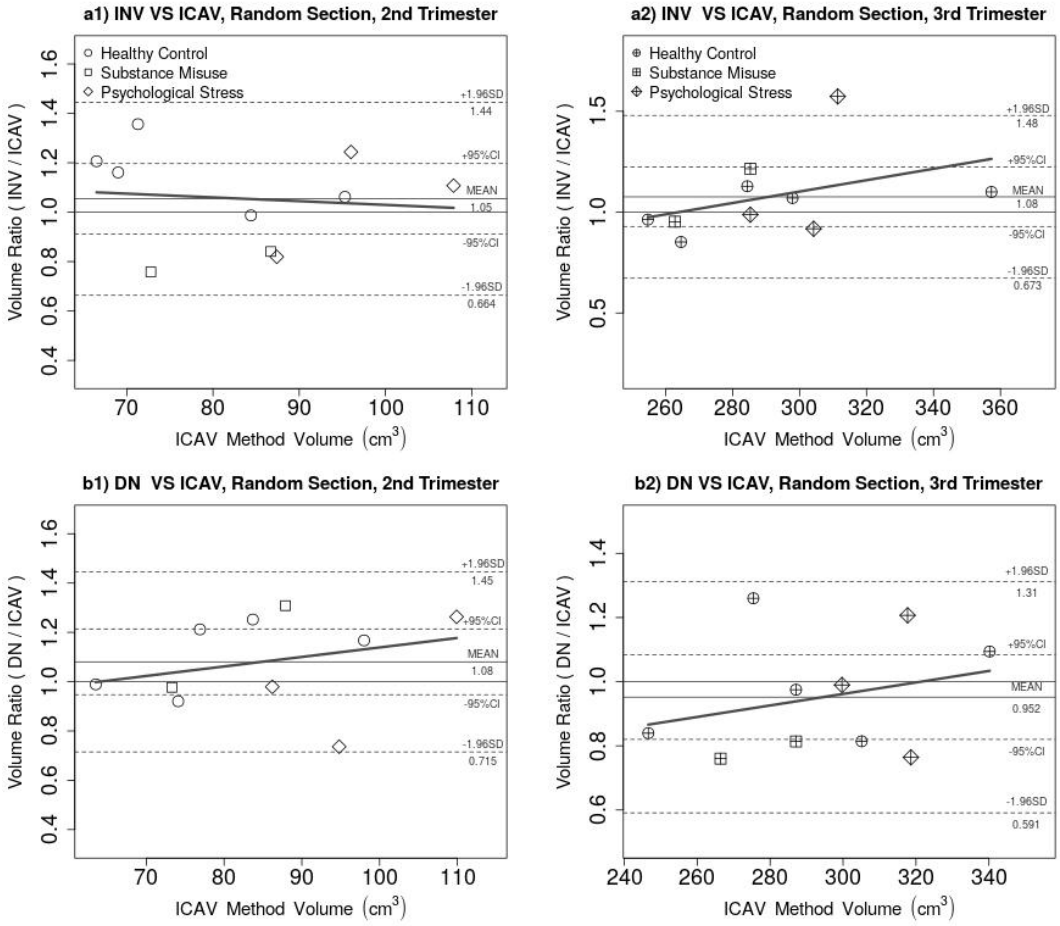

Figure 5.8: Pairwise comparison of the INV and DN methods with the ICAV method for ten fetal brain volume estimates in random one out of three orthogonal sections at both the second and third trimesters, using log transformed Bland-Altman plots. a1) INV (random section) vs ICAV (the first orthogonal section) in the second trimester; a2) INV (the second orthogonal section) vs ICAV (random section) in the third trimester; b1) DN (the second orthogonal section) vs ICAV (random section) in the second trimester; b2) DN (the first orthogonal section) vs ICAV (the second orthogonal section) in the third trimester.

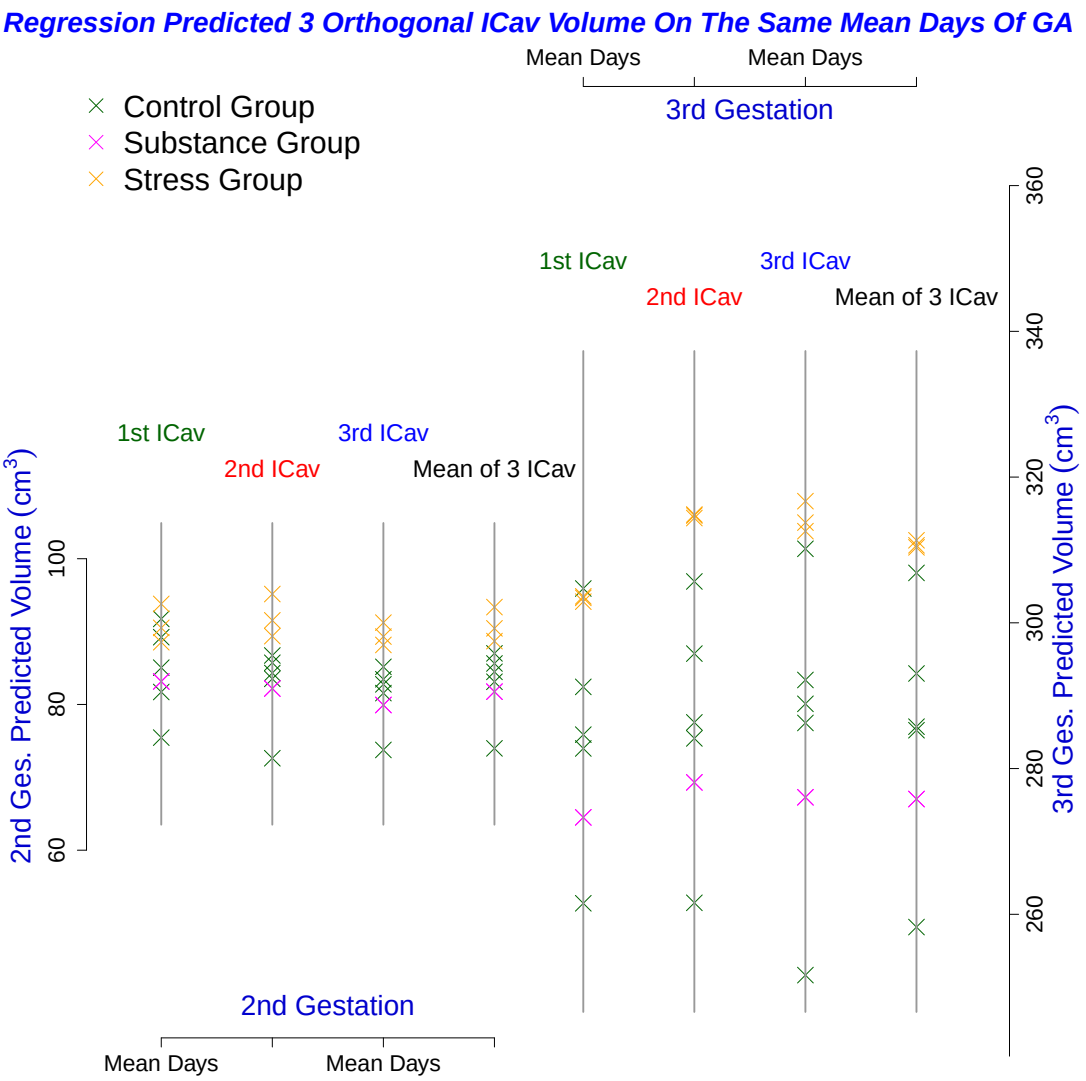

Figure 5.9: Linear regression predicted fetal brain volumes of normal control, substance abused and stress groups on a same day in either the second or third trimester based on estimates obtained by the ICAV ortrip method. The predicted volumes in the second trimester are presented on four short vertical bars on the left of the image while the predicted volumes in the third trimester are presented on four long bars on the right of the image. Each vertical bar represents one of three orthogonal sections and the fourth bar represents mean values from three orthogonal sections. Each predicted volume estimated from one of the three orthogonal sections is plotted onto the respective vertical bar. Using linear regression, volumes of ten fetal brains are predicted on a same day which is the mean of MR scanning days of all the ten fetuses in both the second and third trimesters.

5.4 Discussion

This protocol applied in practice three novel design-based stereological means of estimating volume of human fetal brain in vivo on MR images using ANALYZE software, which gave alternative choices to the traditional CAVALIERI method in volume estimation. The ICAV and INV methods were both capable of estimating surface area of fetal brain when gyrification was not fully developed [48, 102]. Precision of the ICAV ortrip method in each individual estimate were examined from three orthogonal isotropic orientations, and precision of population mean estimates using the INV ortrip and DN ortrip methods was approved as well. CE was available for the prediction of precision in ICAV estimation, but only empirical CE was available for the INV and DN methods. High reliability of the three stereological methods was supported, and procedures were efficiently performed by raters from medical or biomedical background.

Processing fetal brain images using voxel-based morphometry (VBM) methods is still difficult, which is caused by both the effect of myelination on MRI signal and active fetal movement in uterus. Application of the three new stereological methods requires availability of a 3D image dataset and also this is particularly challenging in the case of the fetus due to fetal motion. Fortunately, image processing techniques have recently been developed for analysing multiple sections obtained at different orientations through the fetus in a way which corrects fetal motion and produces a 3D image dataset.

Planimetry (i.e. region drawing technique) on MR images also shares common defects of the other manual methods. Furthermore, (1) heavy workload makes planimetry not practical [62] but stereology is very efficient. Planimetry is still more time consuming and painstaking than stereology even with the same number of section slices. (2) While planimetry can be used to measure transect exactly, even slice by slice, there is still uncertainty between the adjacent section planes, and this variance is unpredictable. (3) Also the hand can frequently waver as one draws a boundary, which contributes to the variance of within sections that is mathematically unpredictable. This uncertainty of wavering does not happen with point counting in stereology. (4) Planimetry heavily depends on the image quality for details in brain parcellation. If we can not see clearly what we wish to measure we should not be measuring in the first place. Performing planimetry does not get past this drawback due to image quality.

Although the design unbiased estimators which have been used are unbiased (i.e. the ICAV, INV and DN methods), MR images are not 'black and white' and feature boundaries are seldom perfectly delineated so that a second observer, or the same observer at a different time, may make a different decision in regarding whether, for example, a point lies in or outside a feature of interest. Inter- and intra-rater reliability studies have therefore been performed to measure this variability.

Within other stereological methods, the CAVALIERI method is efficient for volume estimation but not for surface area which requires isotropy design prior to unbiased estimation, while the ICAV, INV and DN methods are all applied in isotropic orientation. On the other hand, in this study, the CE for individual volume estimation in the ICAV method is less than 5%. Although, as expected, the empirical CE for each individual in both the INV and DN methods

is close to 30% [28], which can be reduced to around 10% when repeated in three orthogonal orientations. The theoretical stereological error variance of the INV and DN estimators is still under development [28].

IR rotation of images can make brain structure difficult to recognise, especially for local areas defined by 3D spatial location or anatomical landmarks. Traditional radiographic practice is based on anatomical planes in transverse, coronal and sagittal views. A preprocess using parcellation methodology may be a practical protocol for regional volume and surface area measurement [57, 62]. In surface area estimation, designs such as the vertical sections method [7, 88] and the isotropic fakir method [79] can also be alternative choices [28].

Whilst a variety of software packages exist for performing point and intersection counting on sampled sections, there is no specific software available for performing the relevant sampling designs for the ICAV, INV and DN methods. Fortunately, we extended ANALYZE software for this purpose. ANALYZE software provides built-in stereology measure function, which is however specifically designed for the CAVALIERI method. As a result, it is not perfectly compatible to perform the three novel methods using ANALYZE. For example, in the INV and DN methods, each single image has to be screenshot to allow the grid file generated in the STEREOLOGY MEASURE menu being loaded into the LINE PROFILE MEASURE menu. An update version of INV method [27] is potentially more readily applied in combination with MRI because the test system comprises horizontal (posteriori-weighted) as opposed to radial (priori-weighted) test lines which are more convenient to overlay on digital images software suite such as ANALYZE. In the ICAV method, during point or intersect counting procedure, the grid file needs to be regenerated in each slice in order to have a new random position of lattices. A combination usage of software such as FMRIB Software Library (FSL)[1] [112] for sectioning and EASYMEASURE [103] for point and intersect counting can be more practical during the measurement [102].

Additionally, in this study we disclosed that in both the second and third trimesters, maternal substance abuse might cause decrease (not significant though) in fetal brain volume comparing with normal pregnancy. In contrast, maternal psychological stress might cause increase (not significant either) in fetal brain volume. Our volume estimates of the substance group are consistent with the smaller infant head circumference for GA at birth and the asymmetrical intrauterine growth retardation which have been reported in previous studies [9, 82, 111, 119], and this may continue to extend to the brain growth retardation in children at school age [100]. Our volume estimates of the psychological stress group, however, suggest maybe some types of stress in pregnancy work differently on fetal brain growth. Studies show that maternal psychological stress can cause delayed fetal maturation that continues to the infant and children periods, which may disrupt the emotional, cognitive, learning and memory performance [105]. Furthermore, for the hippocampal development, even if no difference is found in volume at birth, prenatal maternal anxiety can still slow down the hippocampal growth over the first six months after birth [97]. However, the effects and degrees of prenatal maternal stress vary from both different timing of exposure during pregnancy and the sensitivity of fetal systems

[1] http://fsl.fmrib.ox.ac.uk/fsl/fslwiki/

developing at each stage of GA. Also, the types of maternal stress can influence differently in fetal brain development. Subjective stress (e.g. mental illness) in early GA can predict smaller head circumferences, whereas objective stress (e.g. famine, cold war) can predict slightly larger head circumferences [31]. Still, the effects conflict in different studies, but our study gives a mean of direct volume investigation on fetal brain development, which may be competent to assist in obtaining better understanding of mechanisms on fetal brain development in uterus.

5.5 Conclusions

This protocol provides a practical way of combining the usage of three stereological methods with ANALYZE software in volume measurement on human brain MR images. The sampling and counting protocols developed in ANALYZE software provide convenient means of applying the ICAV, INV and DN stereological methods for the study of appropriate 3D imaging datasets. Notably, ANALYZE provided the opportunity to pioneer the application of the attractive (such as direct prediction of CE, opportunity for additional unbiased estimation of surface area) ICAV method in MRI studies. The INV and DN methods may be useful for comparison of population mean volumes and again ANALYZE makes it highly practical to perform these investigations.

5.6 Acknowledgement

Funding: Jane NORMAN, Rebecca REYNOLDS, Scott SEMPLE, Mark BASTIN, Neil ROBERTS, Fiona DENISON, James BOARDMAN, Jane WALKER, David WILLSHAW, Colin STUDHOLME, Anne O'HARE, Sue Fletcher WATSON and Ian MURRAY; In utero MR biomarkers of abnormal brain development – a proof of concept study; The University of Edinburgh Wellcome Trust Institutional Strategic Support Fund (WT-ISSF) (2013). Kaiming YIN is supported by the China Scholarship Council/University of Edinburgh joint Scholarship. All the authors have no conflict of interests to declare. The authors would like to thank Professor Luis CRUZ-ORIVE for his suggestion on stereology. The authors thank Simiao WU and Ashan JAYASUNDERA for both the inter- and intra- reliability studies.

Chapter 6

Comparison of Point Counting in the CAVALIERI with FREESURFER Segmentation on One Adult Brain Volume Estmaition

6.1 Introduction

There have been a variety of automated/semi-automated software available to perform volumetric analysis on human brain MR images. Among these, FREESURFER [38] image analysis suite which uses both surface-based [29, 43] and volume-based [41, 45] algorithms[1] has acquired good evaluations on the analysis of in-vivo adult brain MR images [94], although other software packages are competitive for different purposes too [18, 33, 36, 61, 77].

On the other hand, traditional manual techniques have also developed besides planimetry or tracing methods which can be time consuming. Modern design-based stereological methods can perform unbiased estimation on volume with practical labour work. For example, the CAVALIERI method in conjunction with point counting [56, 86, 103], which is one of the most commonly used stereological methods, has been successfully applied on the volumetric measurement of adult brains [70, 73, 74].

The comparison between automated and stereological approaches in the volume estimation of human brain on MR images has been conducted in a few studies [19, 71, 85]. Specifically, FREESURFER and the CAVALIERI method were compared in the volume estimation of thalamus, which showed high consistency [71]. High agreement was also seen between FREESURFER and CAVALIERI in the measurement of total brain volume and intracranial volume in toddlers [85]. However, low correlation was reported too in the frontal lobe brain volume measurement between both the methods although the anatomy definition adopted by the two methods seemed not to be consistent [19].

[1] http://surfer.nmr.mgh.harvard.edu/fswiki/FreeSurferAnalysisPipelineOverview

All the above studies focused on group comparison, i.e. a number of brain MR images were measured using both FREESURFER and the CAVALIERI method, and the results obtained respectively were compared statistically. There is no direct investigation on individual brain MR image estimation between FREESURFER and the CAVALIERI method yet. The aim of this chapter is to make a slice-by-slice comparison for one adult brain of the volume obtained automatically by using FREESURFER and volume obtained by manual application of the CAVALIERI method in combination with point counting.

6.2 Materials and Methods

6.2.1 Participant and MRI

40 AD patients and 22 healthy elderly volunteers were recruited for brain MRI (T1-weighted) scans in Munich Germany, and one healthy elderly subject (male, age 71) with good image quality was used for this study. T1-weighted (T1W) MRI images were acquired using a 3 T Philips Achieva scanner with the following parameters: repetition time = 9.00, echo time = 4.00, flip angle = 8, imaging frequency = 127.79, slice thickness = 1, spacing between slice = 1, acquisition matrix = 240 $\times$ 240, scanning sequence = GR, acquisition type = 3D.

6.2.2 FREESURFER Volumetry and Segmentation

FREESURFER version v6.0Beta which was released in October 2015 was used in this study. The volumetric information of the brain measured from FREESURFER was collected in a statistical file called 'aseg.stats' in one subdirectory '(subject)/stats/'[2], which was generated by its own program 'mri_segstats'[3] among the final steps of the whole 'recon-all' workflow[4]. The volume of cerebrum excluding ventricles was acquired from the 'SupraTentorialNotVent'[5] output in 'aseg.stats'.

Meanwhile, the pial and the white matter surfaces of the cerebrum were denoted by red and yellow lines respectively. Image slices in the coronal view at the interval of ten were obtained by its inner screenshot function in a FREEVIEW graphical user interface (GUI) (Figure 6.1). To make the red lines of boundaries as thin as possible, the magnification factor of the screenshots was adjusted to six and therefore the image size was 5718×5718 in pixels. The screenshots were saved in the default PNG format.

[2] https://surfer.nmr.mgh.harvard.edu/fswiki/FsTutorial/AnatomicalROI
[3] https://surfer.nmr.mgh.harvard.edu/fswiki/mri_segstats
[4] https://surfer.nmr.mgh.harvard.edu/fswiki/ReconAllDevTable
[5] https://surfer.nmr.mgh.harvard.edu/fswiki/MorphometryStats

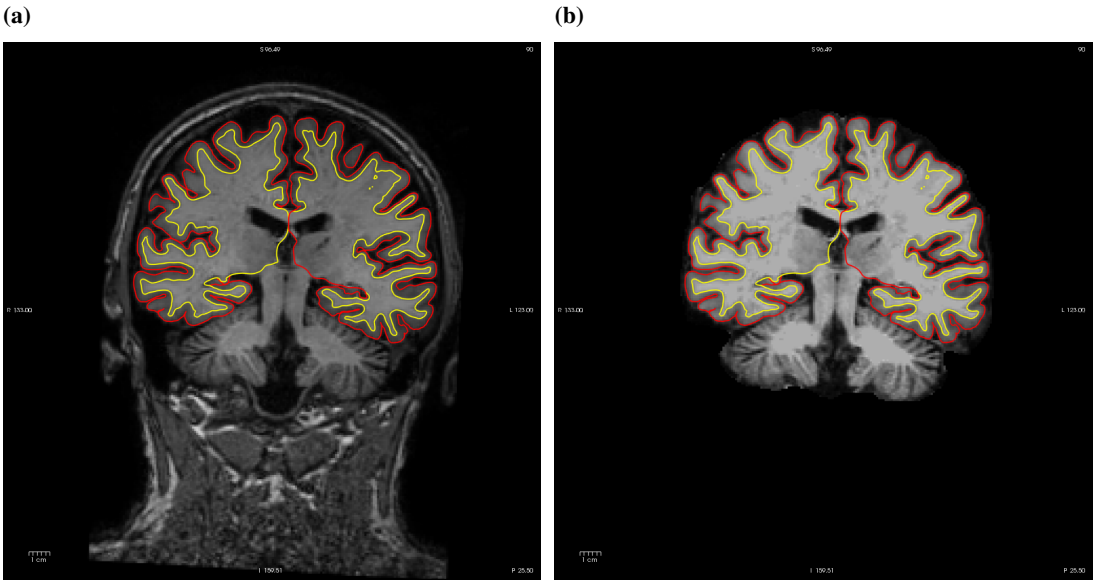

Figure 6.1: The 90th slice of a brain MR image in the coronal view processed by FREESURFER, which is displayed with (a) 'nu.mgz' and (b) 'brainmask.mgz' brain profiles.

6.2.3 CAVALIERI Point Counting

The CAVALIERI method was used by one rater to estimate the volume of cerebrum excluding ventricles. Instead of using the original MRI data of the subject, the 'nu.mgz' file generated by FREESURFER, which was converted to ANALYZE7.5 format, was used in the stereological estimation. EASYMEASURE software was used for point counting in the CAVALIERI method with the following parameters: view = coronal, grid size = 10 mm, section interval = 10 mm.

In EASYMEASURE, the section slices overlaid with the test points (both inside and outside the cerebral boundary), with and without brain profile background (Figure 6.2), were copied to the FIJI software for further alignment and comparison.

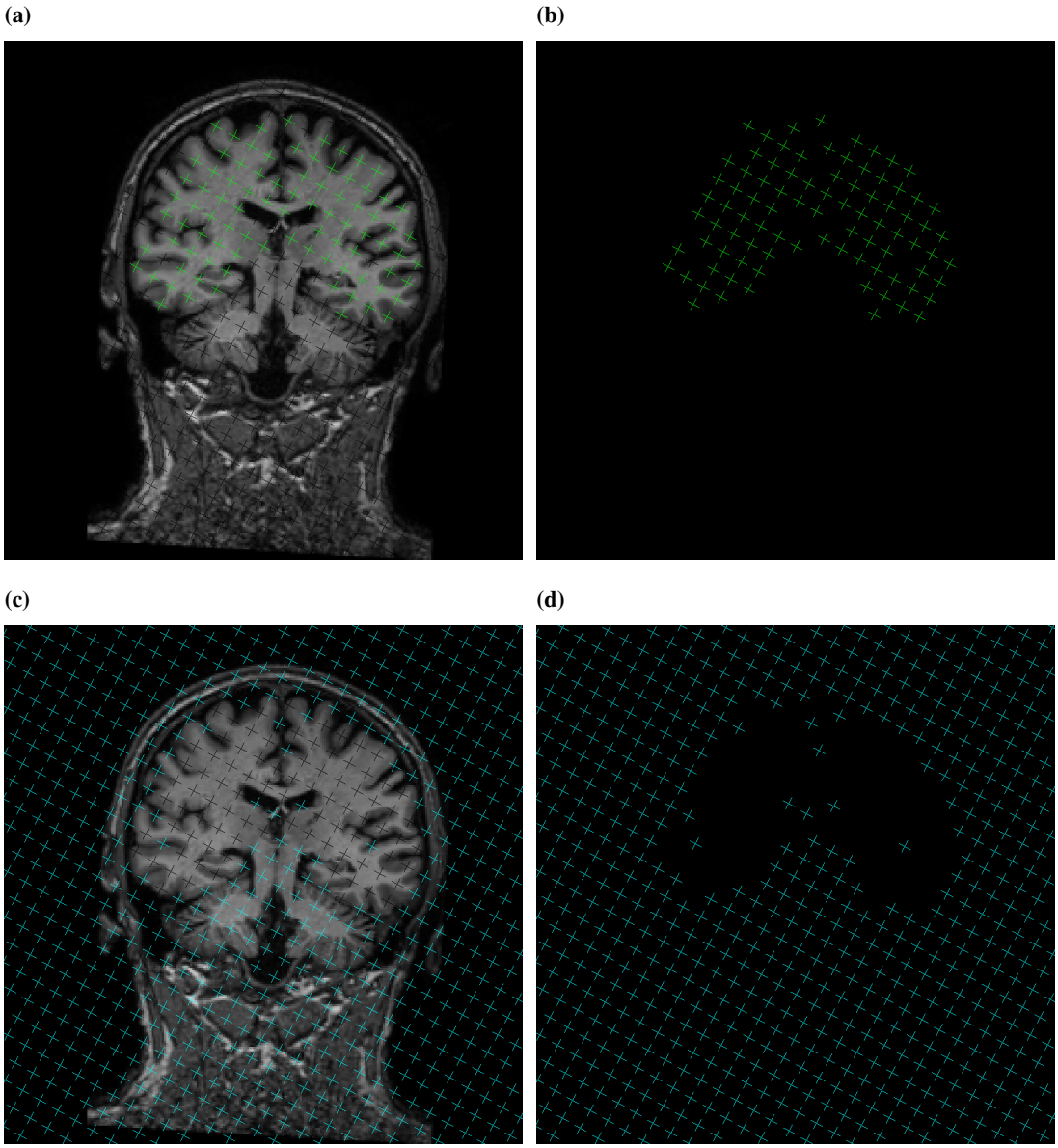

Figure 6.2: The 8th slice of a brain MR image in the coronal view processed by EASYMEASURE with (a) the counted test points (green) covering the cerebral parenchymal tissue are overlapped on a 'nu.mgz' brain profile; (b) the same counted grid (green) is extracted from (a) without brain profile background; (c) the uncounted grid (cyan) both outside the cerebral boundary and covering the ventricles is overlapped on a 'nu.mgz' brain profile; (d) the uncounted grid (cyan) is extracted from (c) without brain profile background.

6.2.4 Alignment Of FREESURFER and CAVALIERI

The image slices with the same brain profile background from FREESURFER and EASYMEASURE were picked up manually at the interval of 10 mm. All of the screenshots were loaded into FIJI software and then scaled to the same size. In FIJI, the images from FREESURFER (Figure 6.1a) were aligned to those from EASYMEASURE (Figure 6.2a, 6.2c) using the 'nu.mgz' brain profile with a small manual adjustment of the slice position. Then the images with test points only (without brain profile) from EASYMEASURE (Figure 6.2b, 6.2d) were superimposed onto those position adjusted and skull stripped brain profiles with boundary lines denoted by FREESURFER (Figure 6.1b). The merged section planes (Figure 6.3) were used for direct comparison between FREESURFER and the CAVALIERI method.

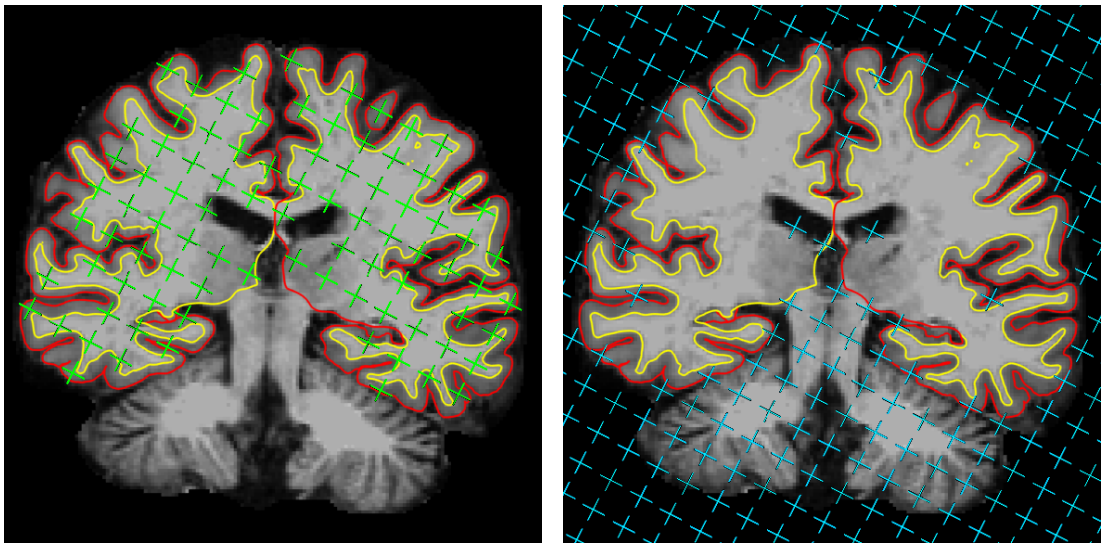

Figure 6.3: Both the counted test points (green on the left image) hitting the cerebrum and the uncounted probes (cyan on the right image) not hitting the cerebrum obtained from EASYMEASURE, and the profile boundary lines (red and yellow in both images) segmented by FREESURFER are superimposed on the same brain profile background.

6.2.5 Comparison Of Points Counting and Boundary Segmentation

Test points were categorised in two groups:

(A) Test points counted by the author (i.e. points the author believed hitting the target cerebral tissue) in the CAVALIERI method fell outside the grey matter boundary lines segmented by FREESURFER.

(B) Test points not counted by the author in the CAVALIERI method fell inside the grey matter boundary lines.

If a test point fell too close to (i.e. almost on) FREESURFER's grey matter boundary line to categorise, two strategies were adopted (also see the list below):

I Defining the boundary trace as belonging to the grey matter, whereby group (B) above would include test points not counted by the author fell both inside and almost on grey matter boundary. Group (A) above would be the same here.

II Defining the boundary trace as not belonging to the grey matter, in which case group (A) above would include test points counted by the author fell both outside and almost on grey matter boundary. Group (B) above would be the same here.

Strategy I		Strategy II	
if FREESURFER's boundary lines **belong to** the grey matter		if FREESURFER's boundary lines **not belong to** the grey matter	
(A)	• test points **counted** by the author / the CAVALIERI method • fell **outside** FREESURFER's boundary lines	(A+)	• test points **counted** by the author / the CAVALIERI method • fell **both outside and on** FREESURFER's boundary lines
(B+)	• test points **not counted** by the author / the CAVALIERI method • fell **both inside and on** FREESURFER's boundary lines	(B)	• test points **not counted** by the author / the CAVALIERI method • fell **inside** FREESURFER's boundary lines

6.3 Results

6.3.1 Volume

The cerebral volume (excluding ventricles) estimated by the author using the CAVALIERI method was 960 cm^3, with total points of 960 and the coefficient of error (CE) of 0.34%. Meanwhile, the volume estimated by FREESURFER was 972 cm^3, which was 1.3% bigger than that estimated by the CAVALIERI method.

6.3.2 Points Counting and Boundary Segmentation Comparison Slice by Slice

15 slices (two slices of empty background were excluded from 17 slices in total) of images with test points generated by the CAVALIERI method were aligned to the pial surface segmented by FREESURFER software (Table 6.1). To compare the difference between test points and pial segmentation, test points in Category (A), (A+) above were labelled slice by slice below (Figure 6.4, 6.5, 6.6, 6.7, 6.8, 6.9, 6.10, 6.11), and the test points in Category (B), (B+) above were labelled slice by slice below too (Figure 6.12, 6.13, 6.14, 6.15, 6.16, 6.17, 6.18, 6.19).

Table 6.1: Comparison between test points counting in the CAVALIERI and auto-pial segmentation in FREESURFER is shown among 15 slices. Test points number counted by the author is shown in each slice. I: defining the boundary trace as belonging to the grey matter, including: test points counted by the author but are outside FREESURFER segmented boundary lines; test points not counted by the author but are inside and on boundary lines. II: defining the boundary trace as not belonging to the grey matter, including: test points counted by the author but are outside and on boundary lines; test points not counted by the author but are inside boundary lines.

CAVALIERI	Group	FREESURFER	Slice Number															Total	Volume	Percent
By The Author		Pial Boundaries	2	3	4	5	6	7	8	9	10	11	12	13	14	15	16	Points	(cm^3)	(%)
Total Points Counted			22	54	77	84	88	83	87	94	83	83	71	61	41	25	7	960	960.0	100.0
Points Counted	I	Outside	0	2	1	3	0	2	3	4	4	3	2	0	0	0	1	25	25.0	2.6
		On	0	2	0	0	3	2	0	0	1	0	2	1	1	1	0	13	13.0	1.4
	II	Outside & On																38	38.0	4.0
Points Not Counted	II	Inside	2	6	3	1	3	0	2	2	0	3	0	1	1	2	0	26	26.0	2.7
		On	1	2	2	1	3	4	2	3	0	2	0	1	0	0	0	21	21.0	2.2
	I	Inside & On																47	47.0	4.9

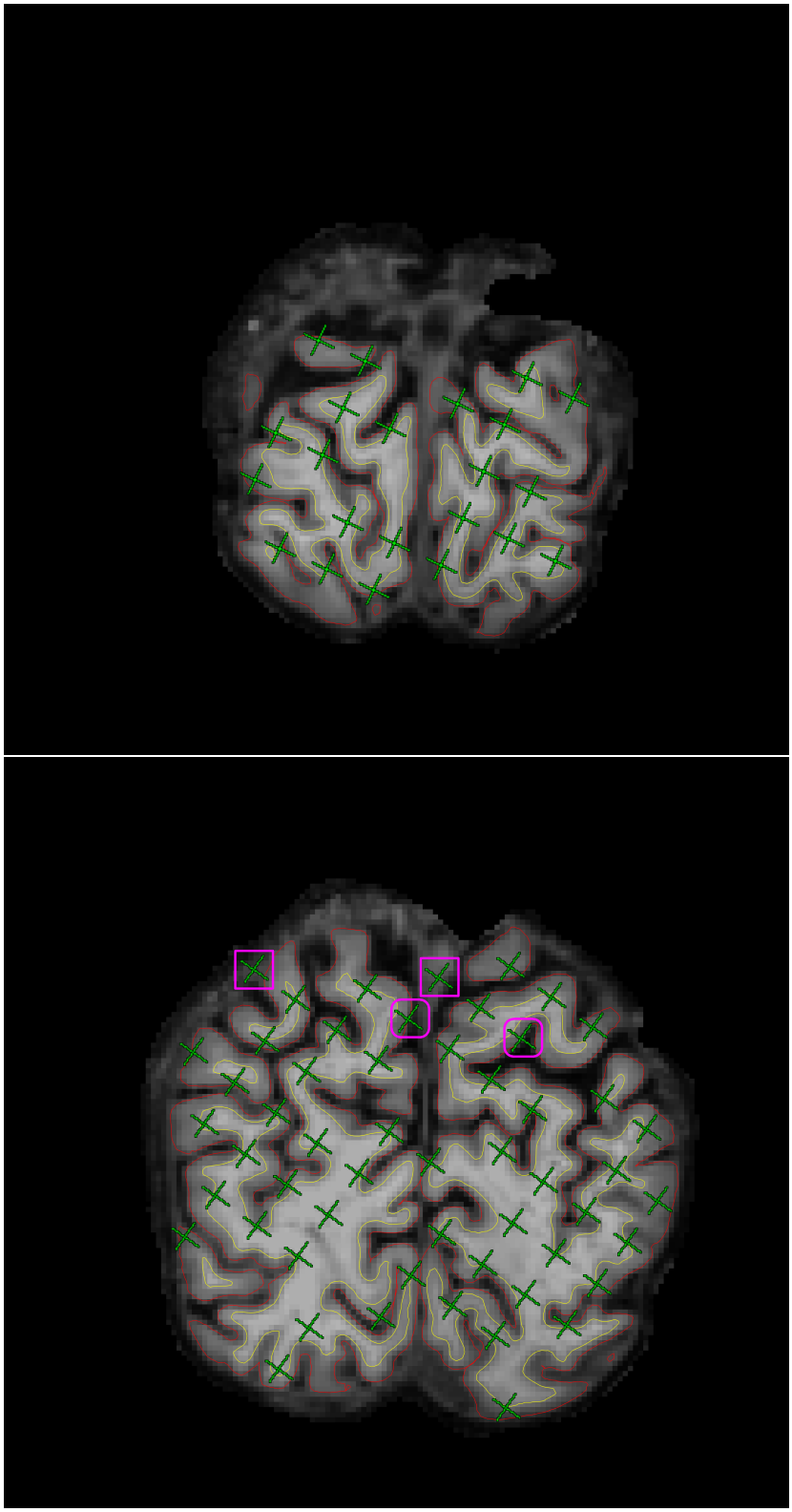

Figure 6.4: On the 2nd and 3rd slices of one brain MR image in the coronal view, counted test points (green) hitting the cerebrum (excluding ventricles) are overlaid onto pial profiles (red lines) segmented by FREESURFER. Rectangles (pink) mark the counted test points which fall outside the grey matter boundaries (red lines) and rounded rectangles (pink, racetrack-like) mark the test points hitting exactly on the grey matter boundaries.

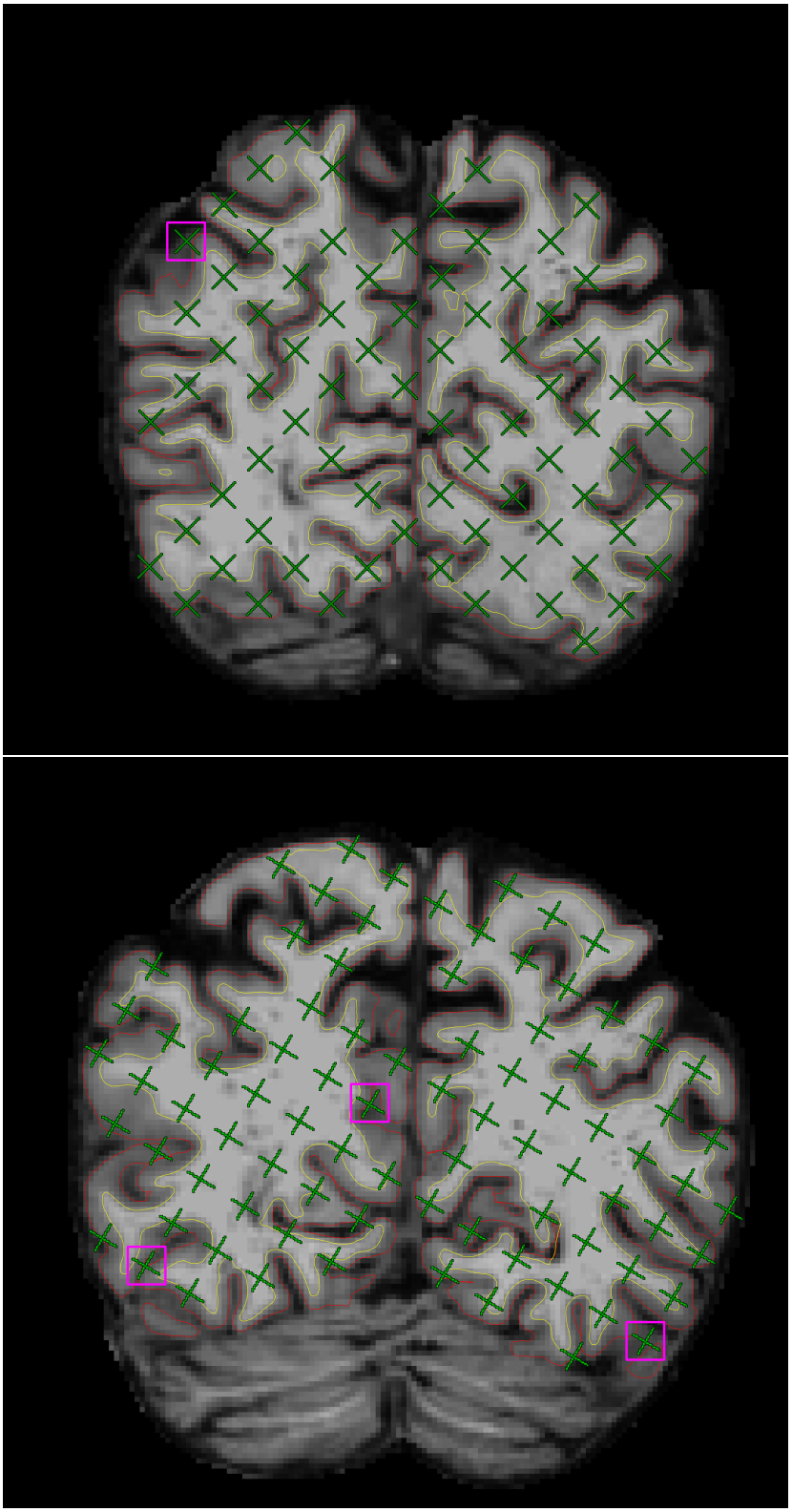

Figure 6.5: On the 4th and 5th slices of one brain MR image in the coronal view, counted test points (green) hitting the cerebrum (excluding ventricles) are overlaid onto pial profiles (red lines) segmented by FREESURFER. Rectangles (pink) mark the counted test points which fall outside the grey matter boundaries (red lines).

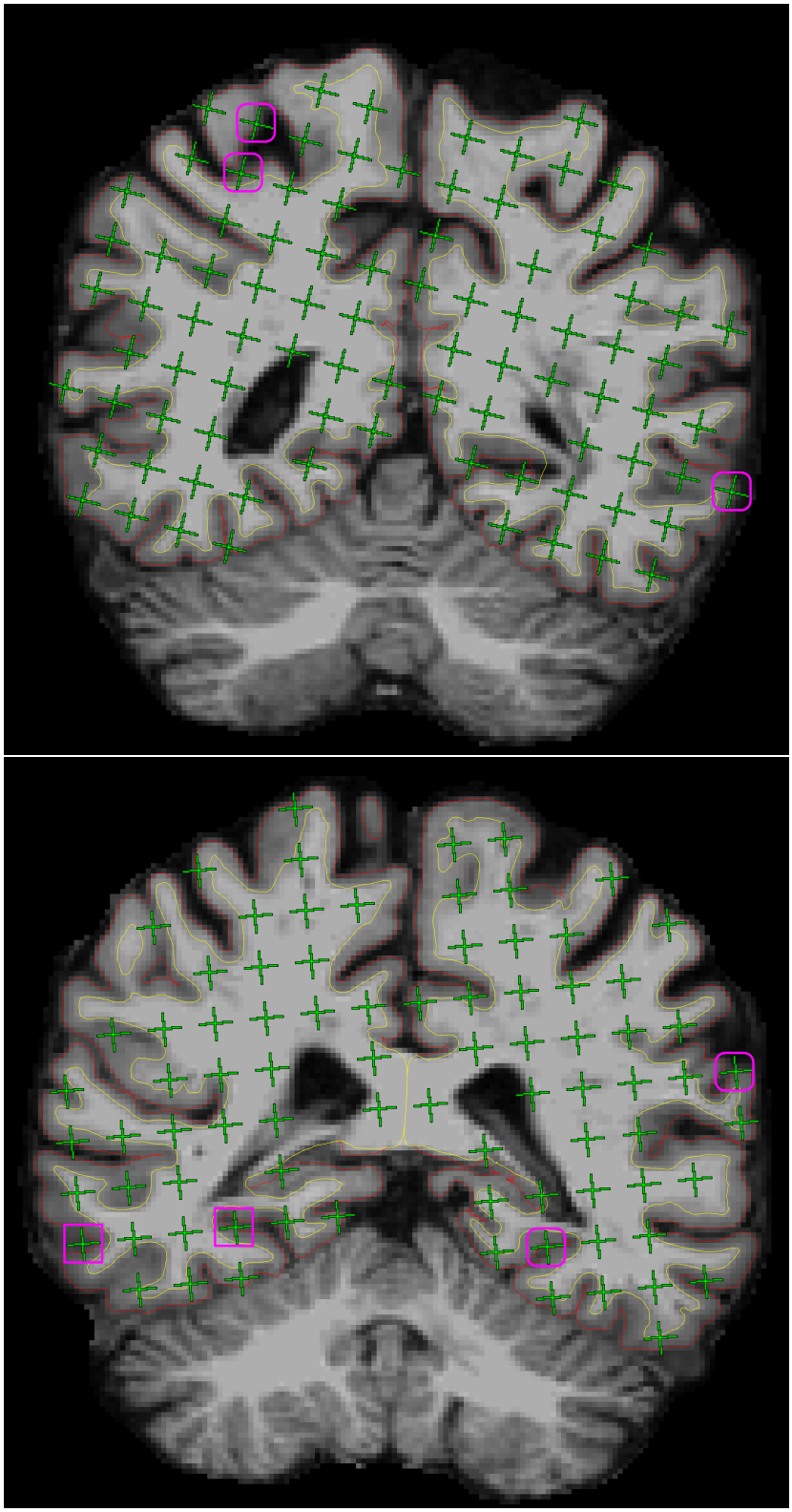

Figure 6.6: On the 6th and 7th slices of one brain MR image in the coronal view, counted test points (green) hitting the cerebrum (excluding ventricles) are overlaid onto pial profiles (red lines) segmented by FREESURFER. Rectangles (pink) mark the counted test points which fall outside the grey matter boundaries (red lines) and rounded rectangles (pink, racetrack-like) mark the test points hitting exactly on the grey matter boundaries.

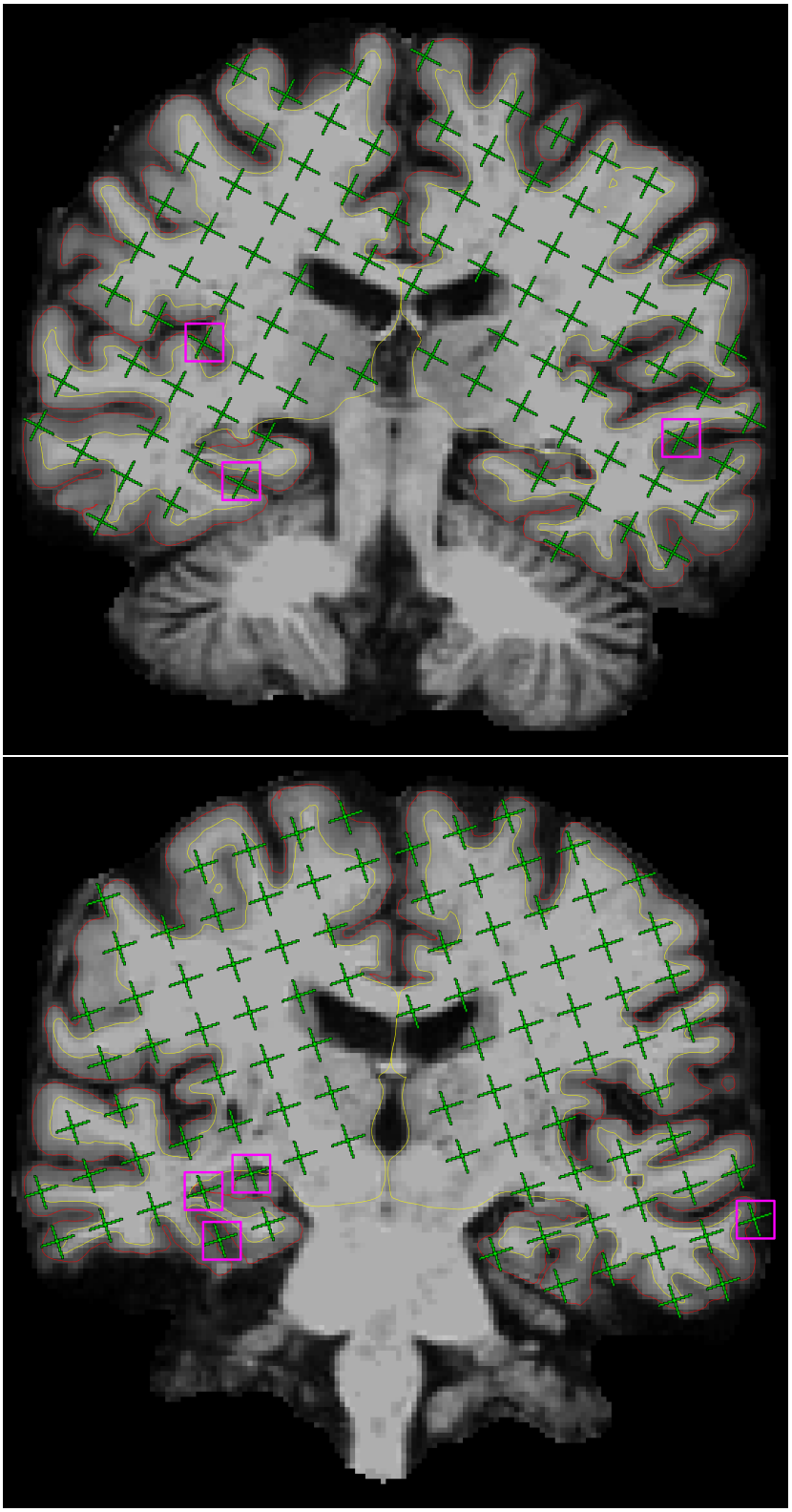

Figure 6.7: On the 8th and 9th slices of one brain MR image in the coronal view, counted test points (green) hitting the cerebrum (excluding ventricles) are overlaid onto pial profiles (red lines) segmented by FREESURFER. Rectangles (pink) mark the counted test points which fall outside the grey matter boundaries (red lines) and rounded rectangles (pink, racetrack-like) mark the test points hitting exactly on the grey matter boundaries.

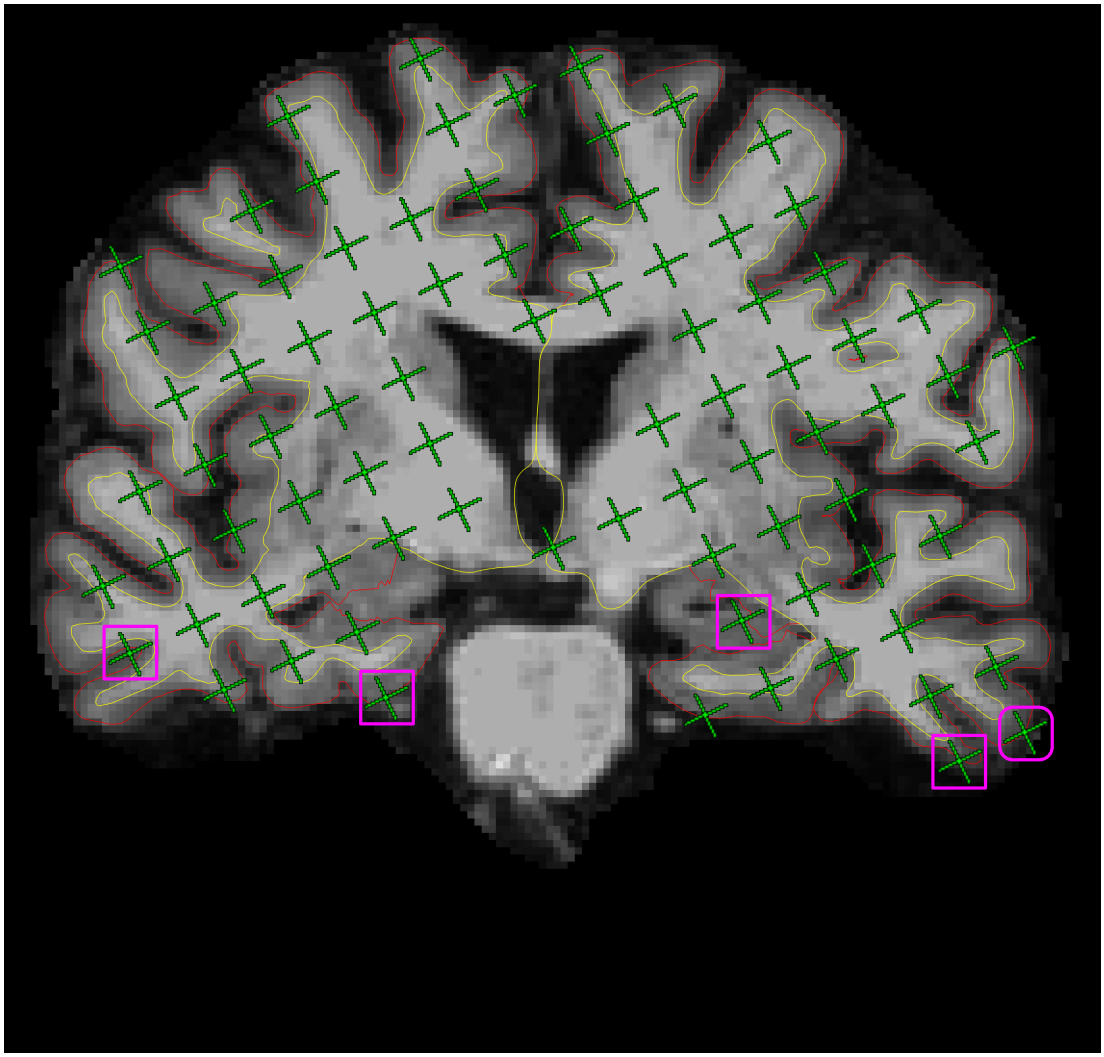

Figure 6.8: On the 10^{th} slice of one brain MR image in the coronal view, counted test points (green) hitting the cerebrum (excluding ventricles) are overlaid onto pial profiles (red lines) segmented by FREESURFER. Rectangles (pink) mark the counted test points which fall outside the grey matter boundaries (red lines) and rounded rectangles (pink, racetrack-like) mark the test points hitting exactly on the grey matter boundaries.

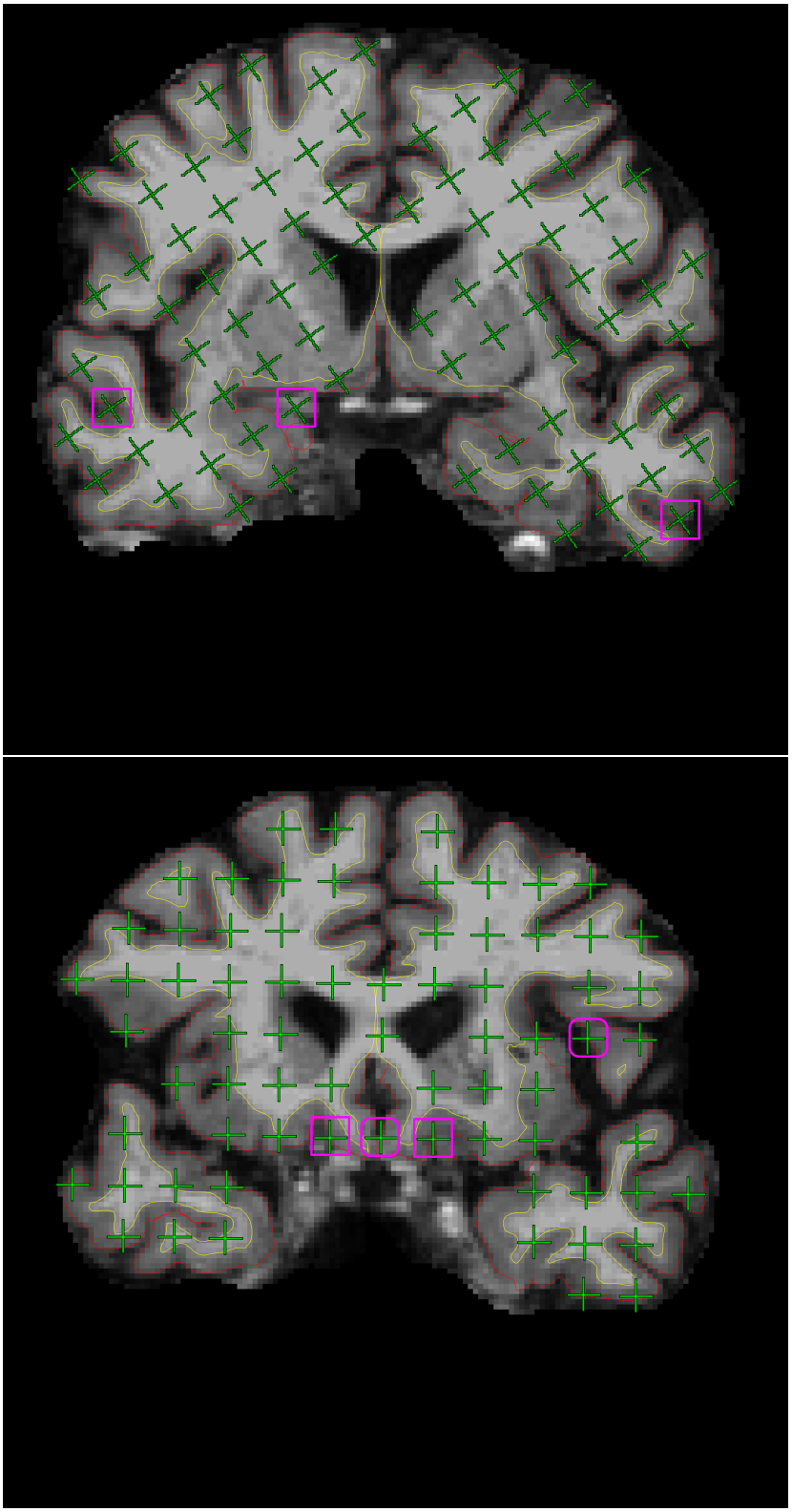

Figure 6.9: On the 11th and 12th slices of one brain MR image in the coronal view, counted test points (green) hitting the cerebrum (excluding ventricles) are overlaid onto pial profiles (red lines) segmented by FREESURFER. Rectangles (pink) mark the counted test points which fall outside the grey matter boundaries (red lines) and rounded rectangles (pink, racetrack-like) mark the test points hitting exactly on the grey matter boundaries.

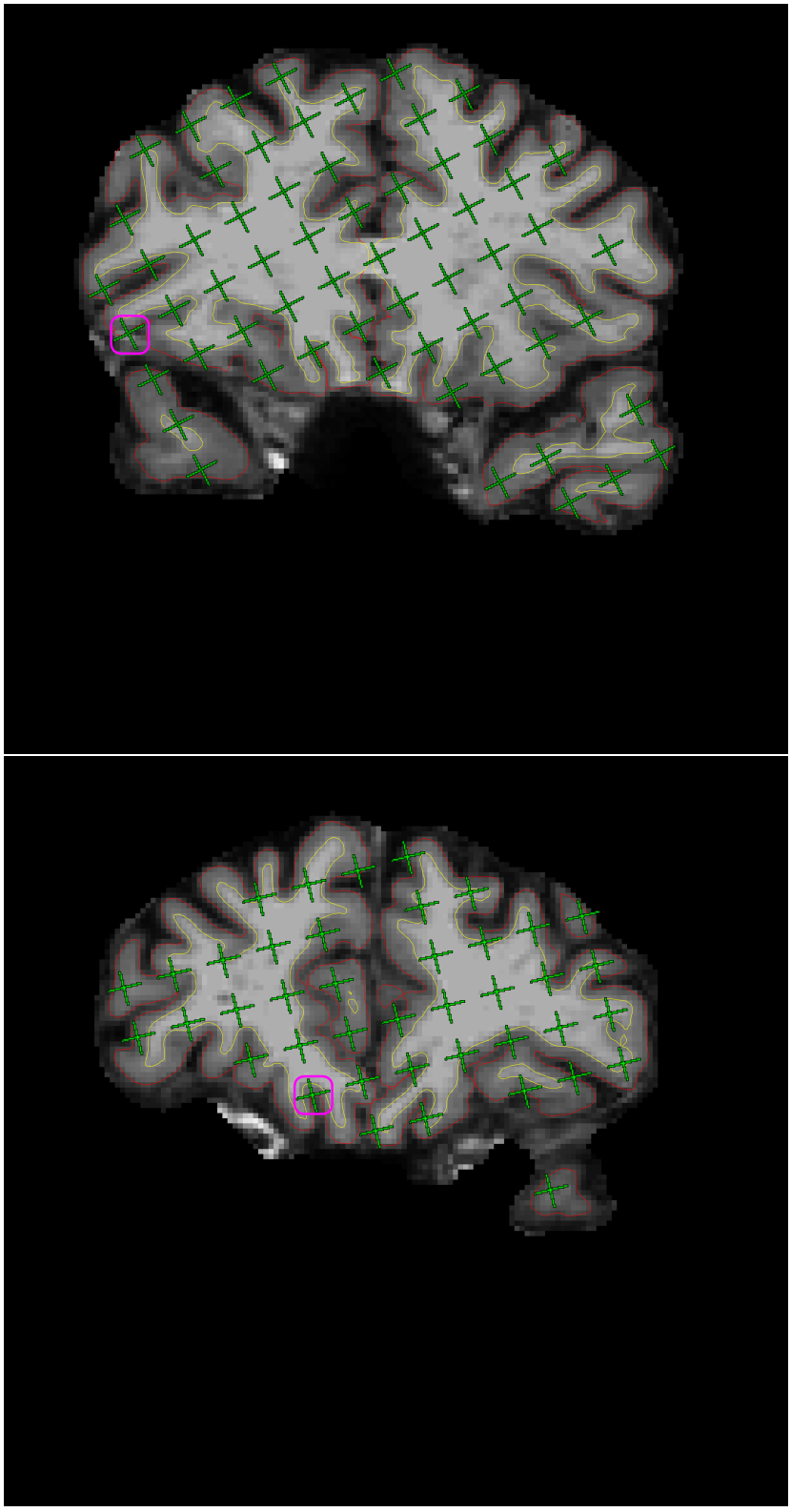

Figure 6.10: On the 13th and 14th slices of one brain MR image in the coronal view, counted test points (green) hitting the cerebrum (excluding ventricles) are overlaid onto pial profiles (red lines) segmented by FREESURFER. Rounded rectangles (pink, racetrack-like) mark the test points hitting exactly on the grey matter boundaries (red lines).

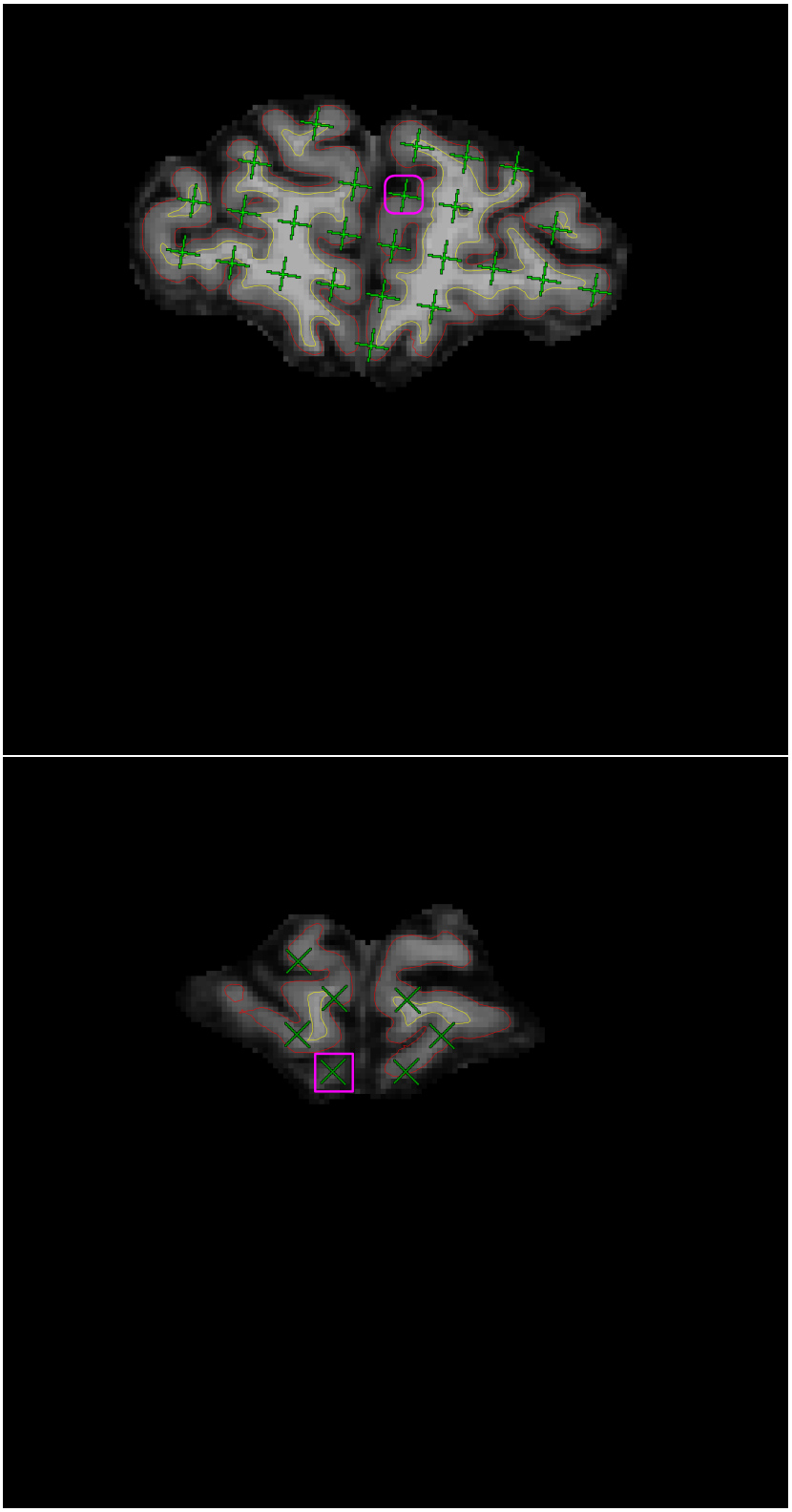

Figure 6.11: On the 15th and 16th slices of one brain MR image in the coronal view, counted test points (green) hitting the cerebrum (excluding ventricles) are overlaid onto pial profiles (red lines) segmented by FREESURFER. Rectangles (pink) mark the counted test points which fall outside the grey matter boundaries (red lines) and rounded rectangles (pink, racetrack-like) mark the test points hitting exactly on the grey matter boundaries.

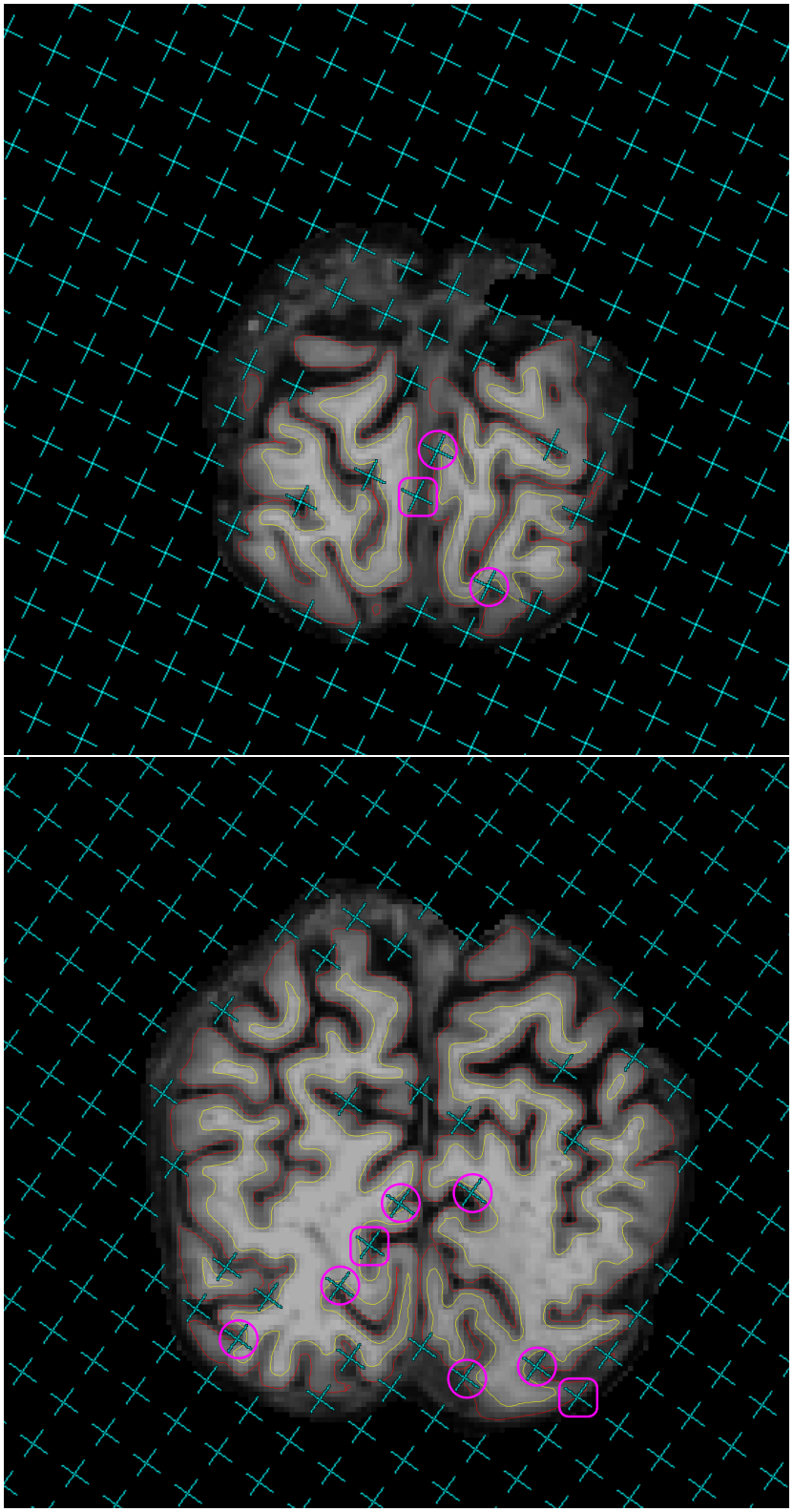

Figure 6.12: On the 2nd and 3rd slices of one brain MR image in the coronal view, uncounted test points (cyan) which miss the cerebral parenchyma or hit the ventricles are overlaid onto pial profiles (red lines) segmented by FREESURFER. Circles (pink) mark the uncounted test points which fall inside the grey matter boundaries (red lines) and rounded rectangles (pink, racetrack-like) mark the test points hitting exactly on the grey matter boundaries.

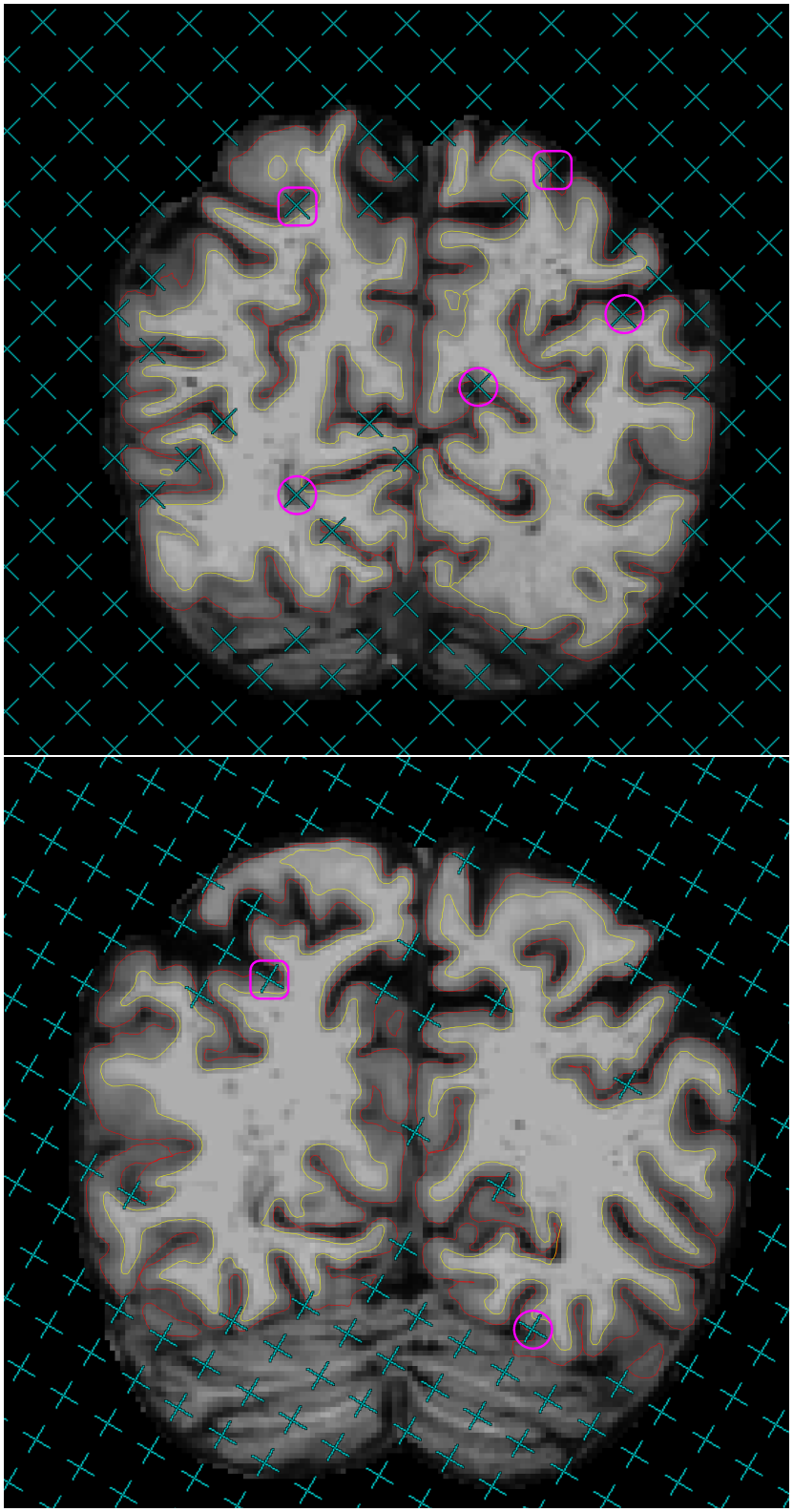

Figure 6.13: On the 4th and 5th slices of one brain MR image in the coronal view, uncounted test points (cyan) which miss the cerebral parenchyma or hit the ventricles are overlaid onto pial profiles (red lines) segmented by FREESURFER. Circles (pink) mark the uncounted test points which fall inside the grey matter boundaries (red lines) and rounded rectangles (pink, racetrack-like) mark the test points hitting exactly on the grey matter boundaries.

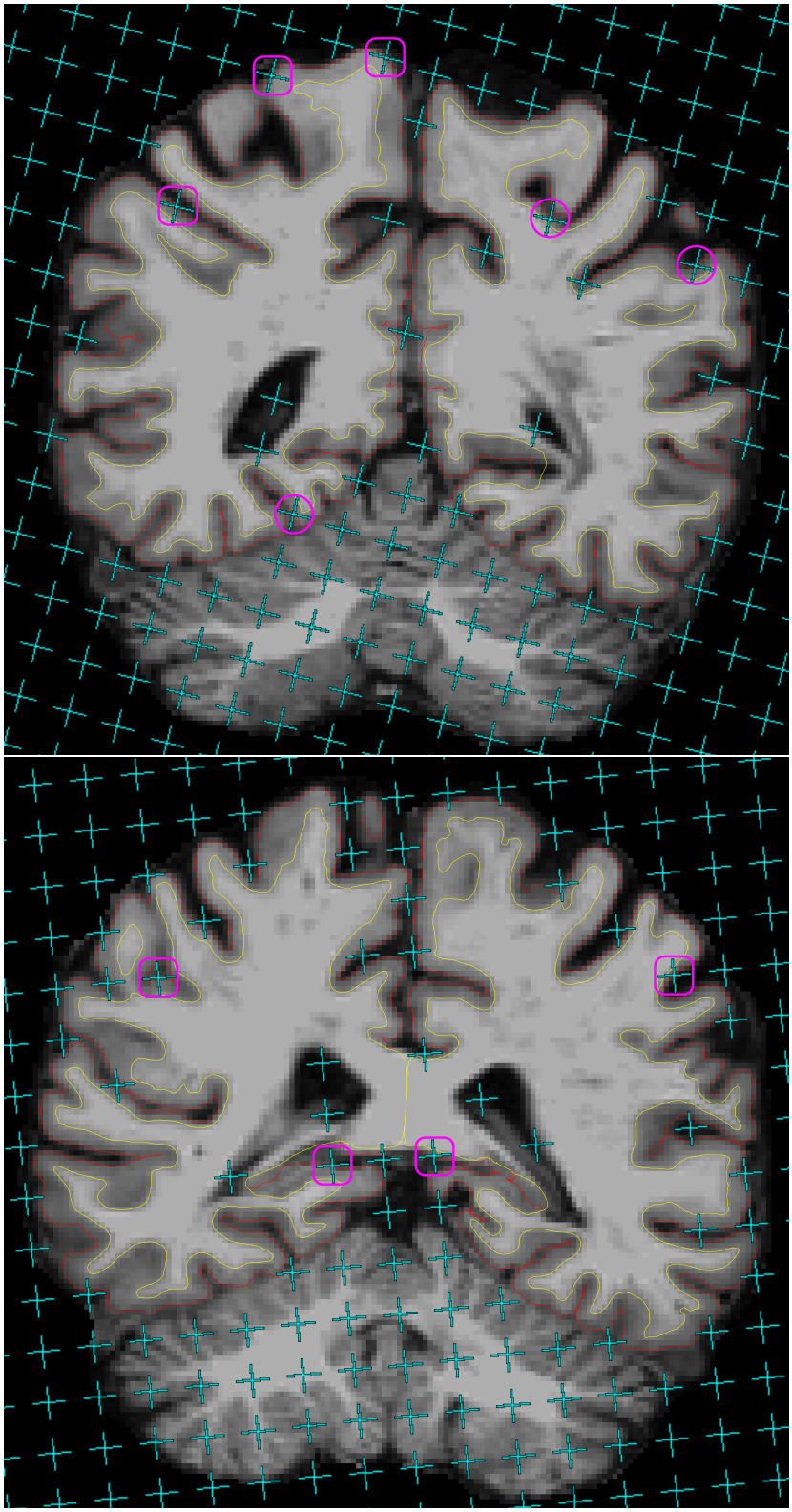

Figure 6.14: On the 6th and 7th slices of one brain MR image in the coronal view, uncounted test points (cyan) which miss the cerebral parenchyma or hit the ventricles are overlaid onto pial profiles (red lines) segmented by FREESURFER. Circles (pink) mark the uncounted test points which fall inside the grey matter boundaries (red lines) and rounded rectangles (pink, racetrack-like) mark the test points hitting exactly on the grey matter boundaries.

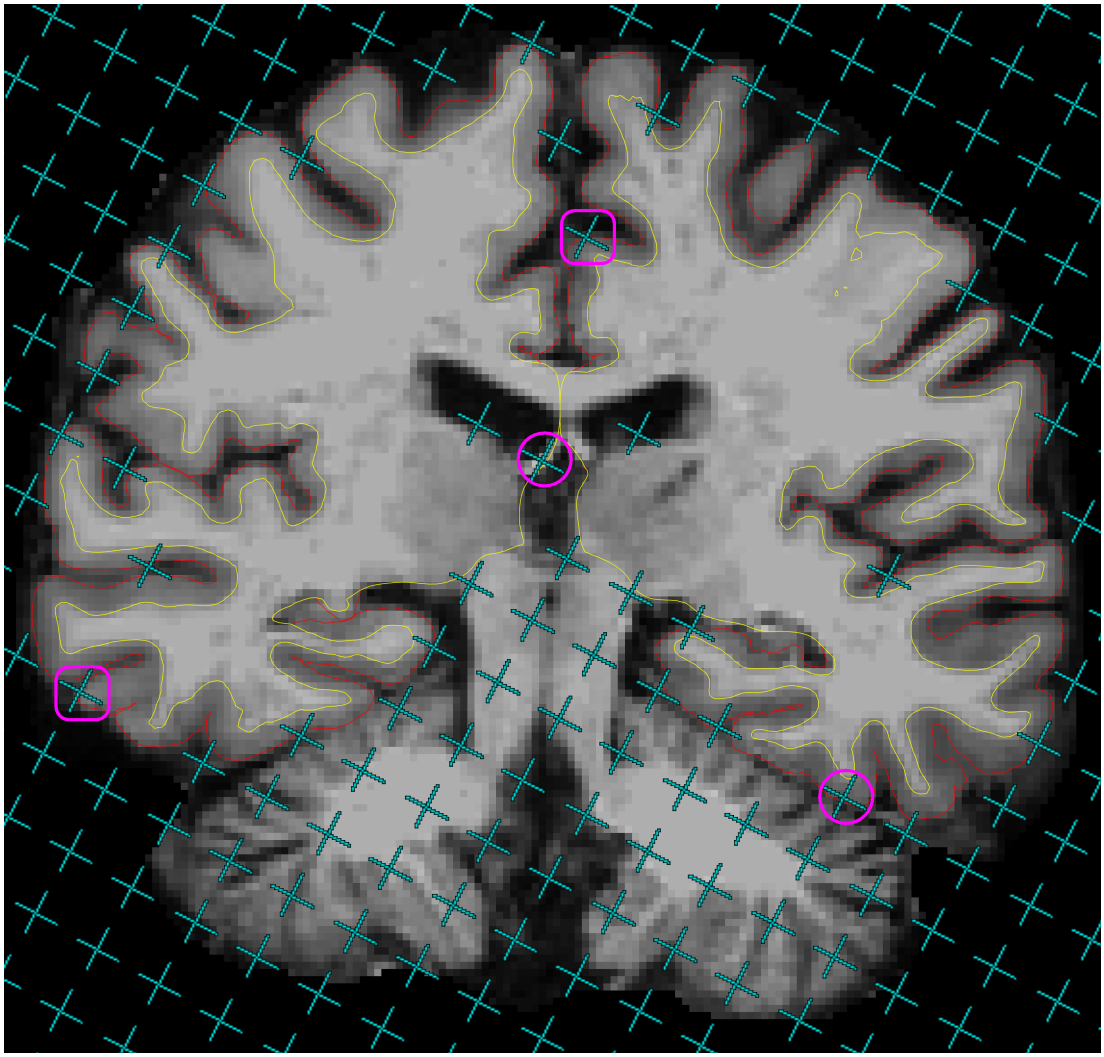

Figure 6.15: On the 8th slice of one brain MR image in the coronal view, uncounted test points (cyan) which miss the cerebral parenchyma or hit the ventricles are overlaid onto pial profiles (red lines) segmented by FREESURFER. Circles (pink) mark the uncounted test points which fall inside the grey matter boundaries (red lines) and rounded rectangles (pink, racetrack-like) mark the test points hitting exactly on the grey matter boundaries.

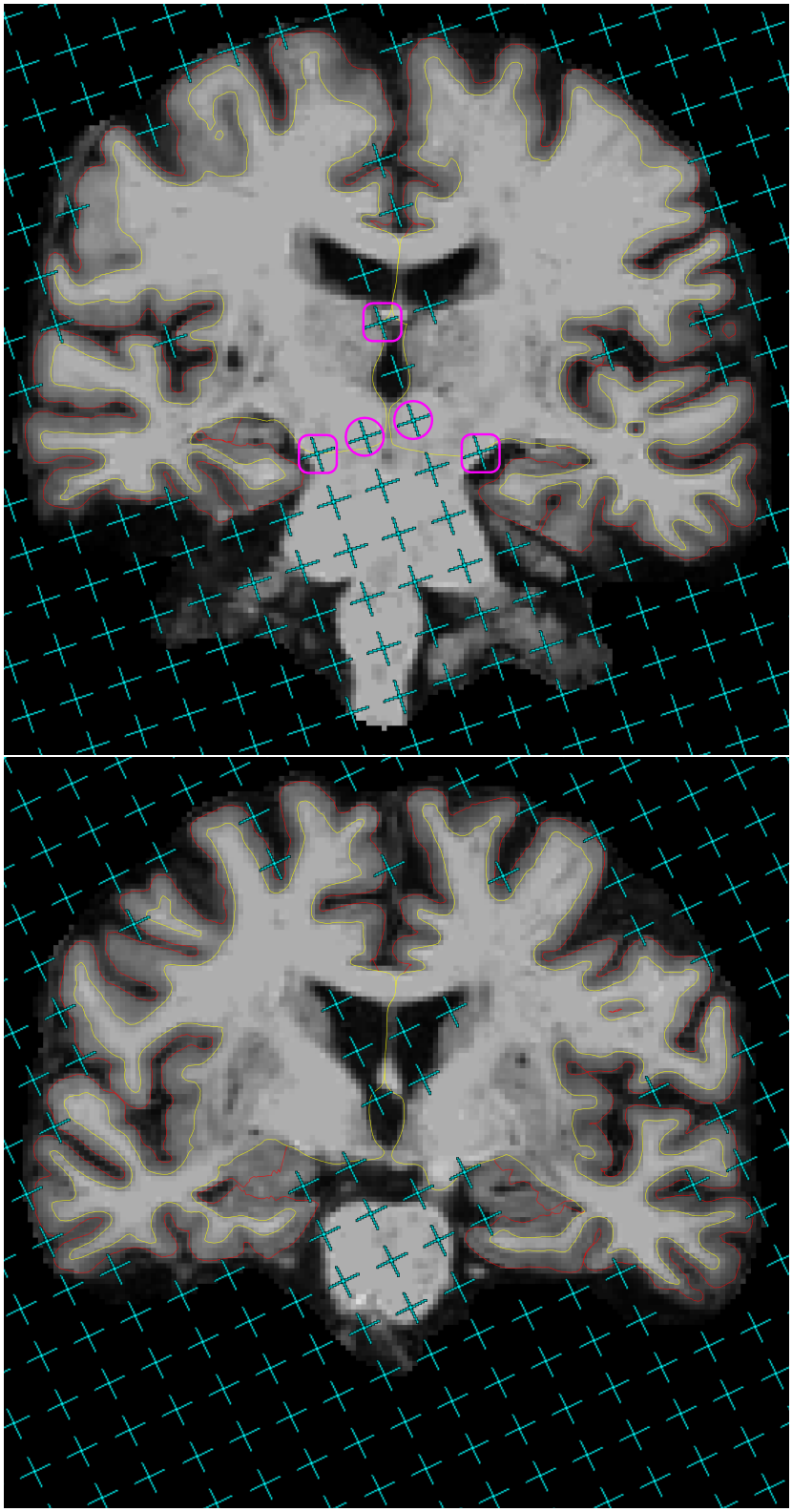

Figure 6.16: On the 9th and 10th slices of one brain MR image in the coronal view, uncounted test points (cyan) which miss the cerebral parenchyma or hit the ventricles are overlaid onto pial profiles (red lines) segmented by FREESURFER. Circles (pink) mark the uncounted test points which fall inside the grey matter boundaries (red lines) and rounded rectangles (pink, racetrack-like) mark the test points hitting exactly on the grey matter boundaries.

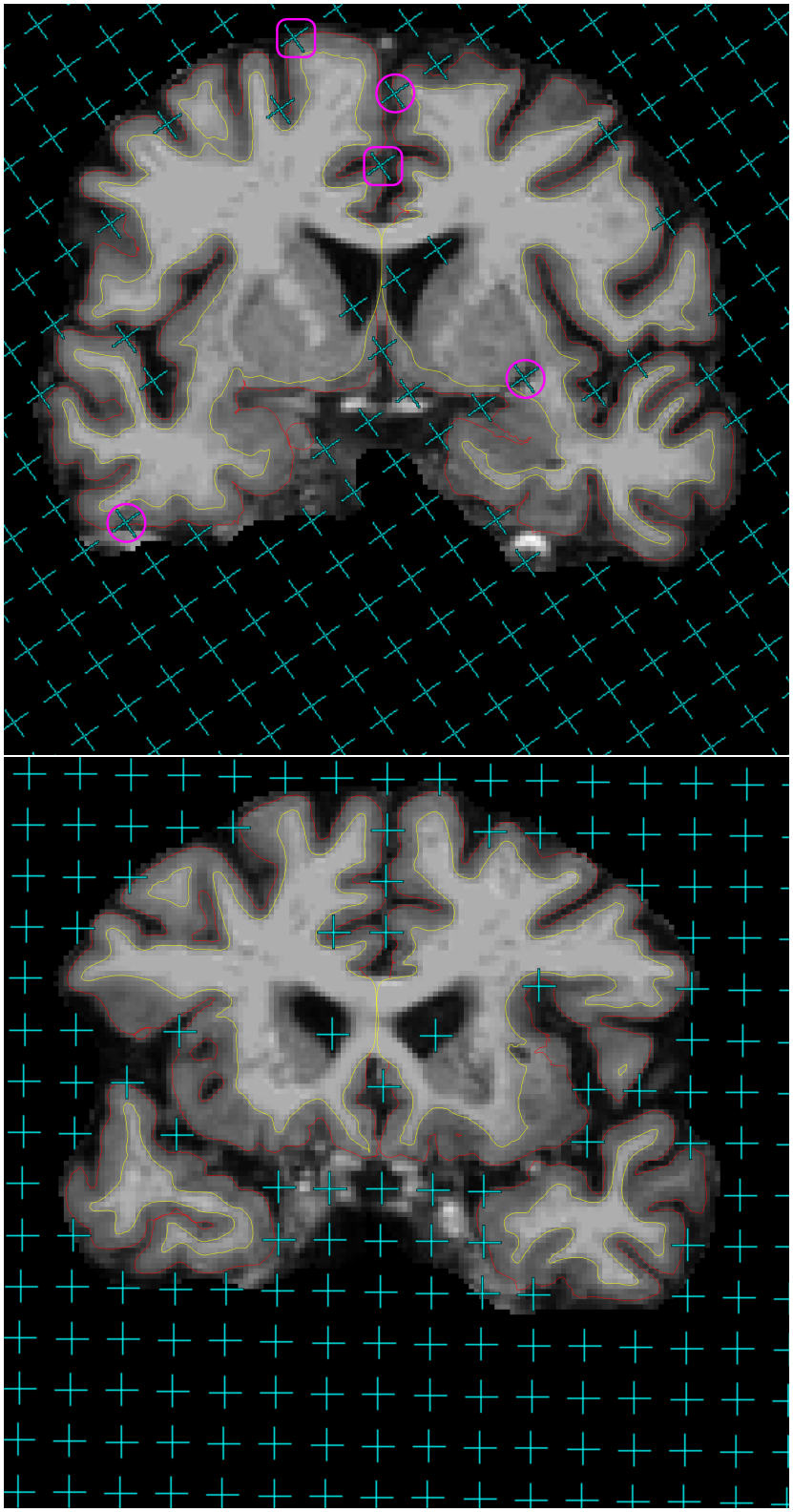

Figure 6.17: On the 11th and 12th slices of one brain MR image in the coronal view, uncounted test points (cyan) which miss the cerebral parenchyma or hit the ventricles are overlaid onto pial profiles (red lines) segmented by FREESURFER. Circles (pink) mark the uncounted test points which fall inside the grey matter boundaries (red lines) and rounded rectangles (pink, racetrack-like) mark the test points hitting exactly on the grey matter boundaries.

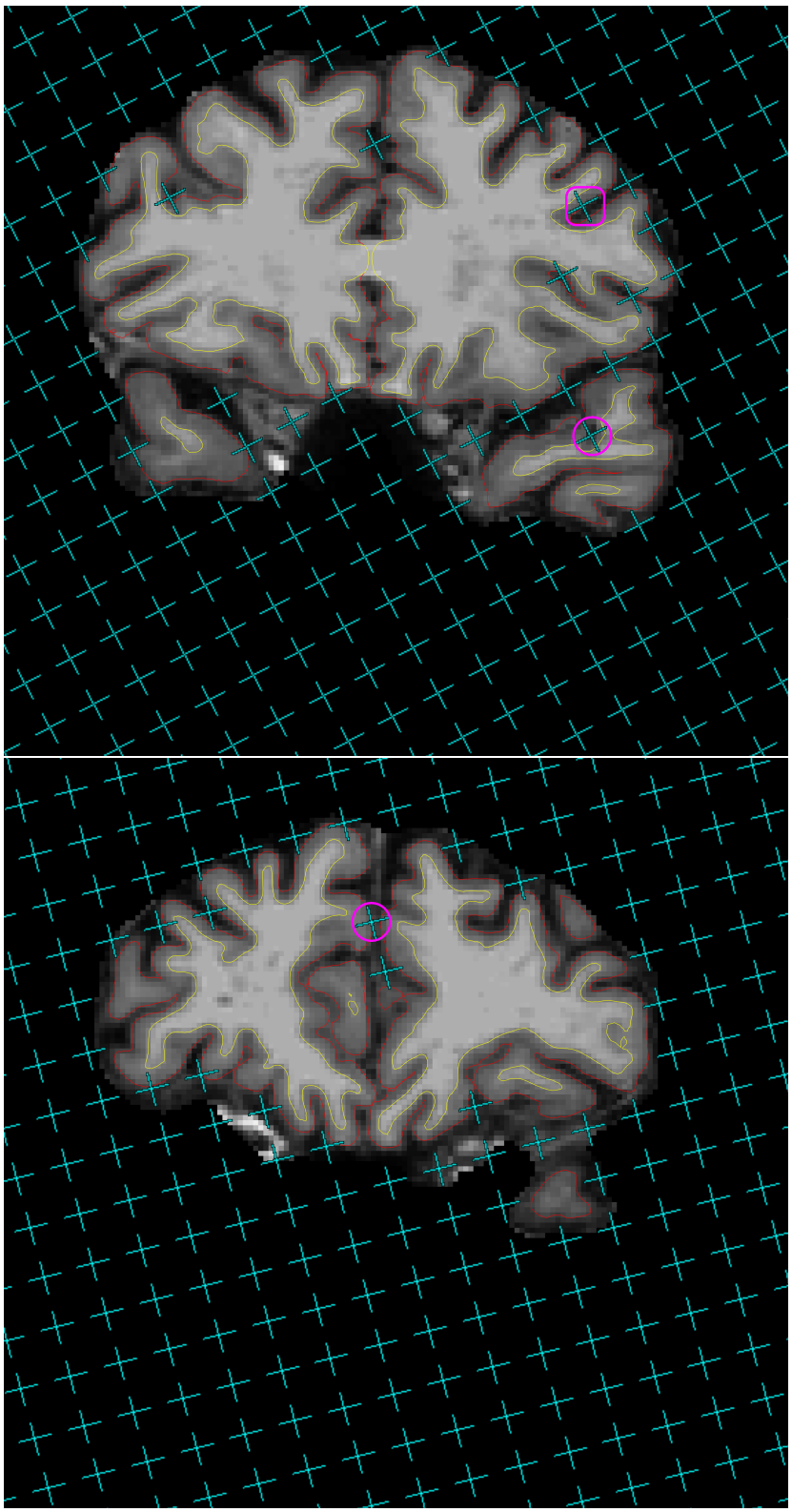

Figure 6.18: On the 13th and 14th slices of one brain MR image in the coronal view, uncounted test points (cyan) which miss the cerebral parenchyma or hit the ventricles are overlaid onto pial profiles (red lines) segmented by FREESURFER. Circles (pink) mark the uncounted test points which fall inside the grey matter boundaries (red lines) and rounded rectangles (pink, racetrack-like) mark the test points hitting exactly on the grey matter boundaries.

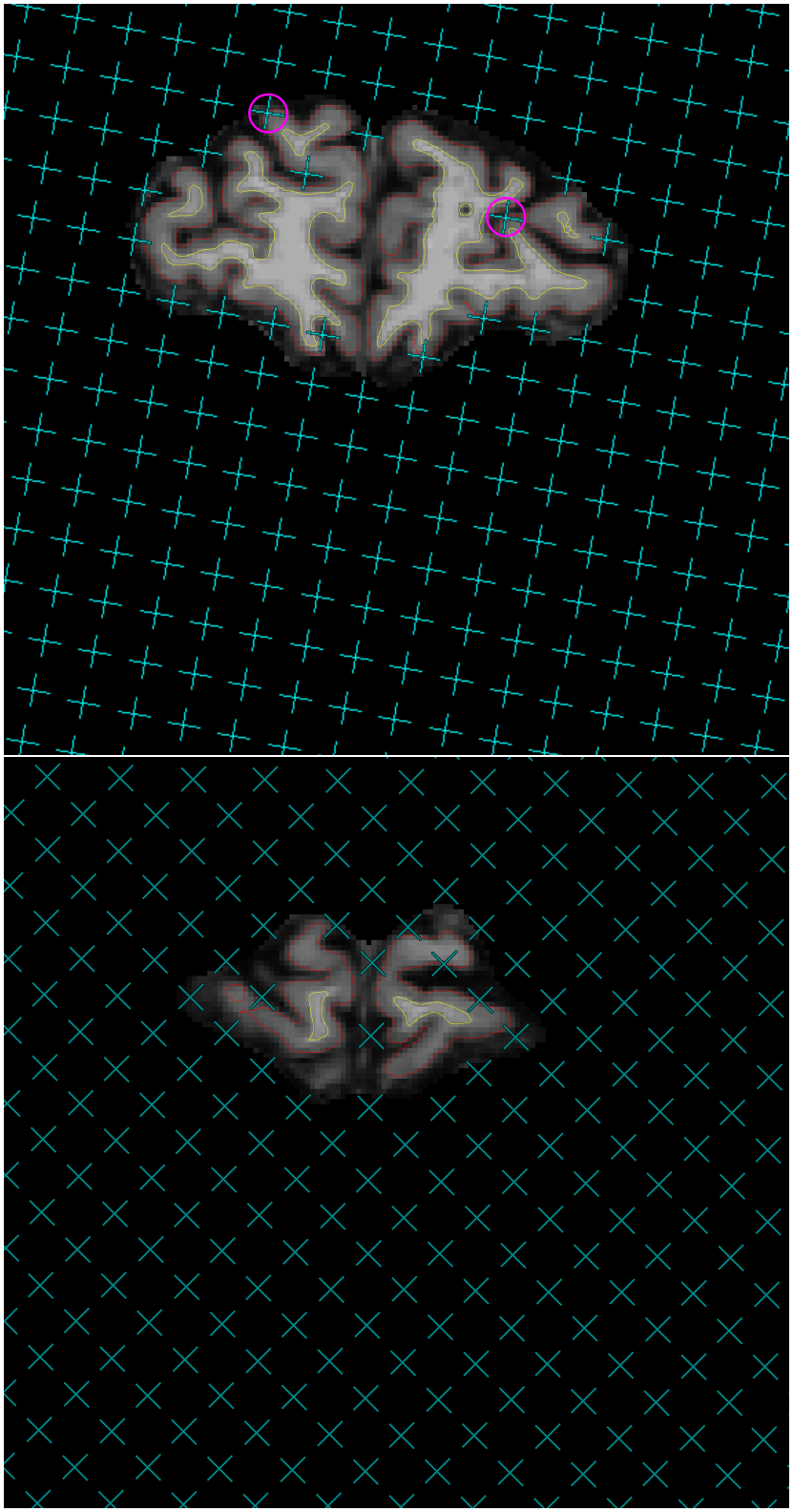

Figure 6.19: On the 15th and 16th slices of one brain MR image in the coronal view, uncounted test points (cyan) which miss the cerebral parenchyma or hit the ventricles are overlaid onto pial profiles (red lines) segmented by FREESURFER. Circles (pink) mark the uncounted test points which fall inside the grey matter boundaries (red lines).

6.4 Discussion

Stereology, as a manual method for volume estimation, the result of which is influenced by the factor of rater. Using the FREESURFER segmentation as a reliable reference for brain volume estimation, we can adjust the stereological results based on the pial surface denoted by FREESURFER, i.e. the test points counted by CAVALIERI which however were outside or on the pial boundaries segmented by FREESURFER could be subtracted, and the test points not counted by CAVALIERI which however were inside or on the pial boundaries segmented by FREESURFER could be added. The overestimate and underestimate ratios by the same observer were between 2.6% to 4.0% and -2.7% to -4.9%, respectively (Table 6.1). The adjusted cerebral volume could be between 948 and 982 cm^3 and the mean volume was 965 cm^3 (Table 6.2), which was quite close to the volume (972 cm^3) obtained by FREESURFER. This suggests that when all the test points used in CAVALIERI fit perfectly with the pial segmentation in FREESURFER, the volume estimates can be almost the same between the two methods. In other words, the point counting strategy in the stereological method does not generate bias in volume estimation.

Table 6.2: Original volume estimated by the CAVALIERI is adjusted based on FREESURFER pial segmentation. Strategy I: defining the boundary trace as belonging to the grey matter, test points counted by the author but are outside FREESURFER segmented pial boundaries are subtracted while test points uncounted but are both inside and on segmented pial boundaries are added. Strategy II: defining the boundary trace as not belonging to the grey matter, test points counted but are both outside and on segmented pial boundaries are subtracted while test points uncounted but are inside segmented pial boundaries are added. Avg. : average volume.

Volumes (cm^3)			Strategy I		Strategy II		Avg.
		Points	Outside	Inside & On	Inside	Outside & On	
		Pial Boundaries Segmented by FREESURFER					
By CAVALIERI Originally	960						
Points Counted By CAVALIERI		−	25		38		
Points Uncounted By CAVALIERI		+		47		26	
By CAVALIERI After Adjustment		=		982		948	965
By FREESURFER	972						

In the CAVALIERI method, the precision of the volume estimation can be influenced by (1) the rater's experience, (2) the quality of the MRI image and (3) the definition of the structure measured. The rater in this study has knowledge of both stereology and human brain anatomy. The observation artefact can be acceptable although unavoidable. Blurred or low resolution MR images can be difficult and time consuming to perform manual estimation, especially when test points hitting on the border of grey matter and dura matter (Figure 6.20). Lastly, ambiguity of the definition of brain structures can result in difference in volume estimates, e.g. when test points hitting on the border of white matter and brainstem (Figure 6.21).

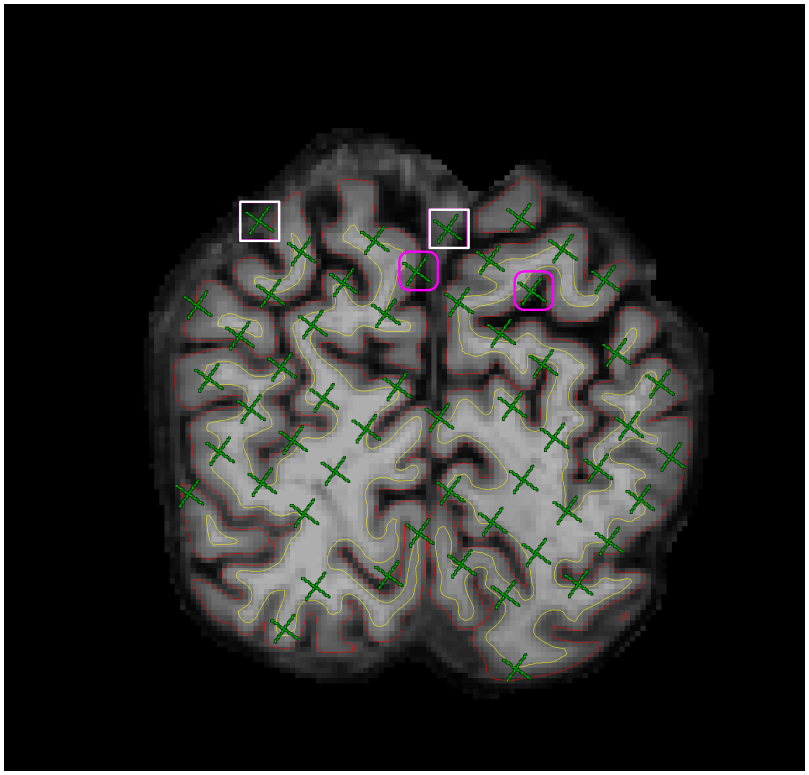

Figure 6.20: Test points (green) which were counted by the rater using the CAVALIERI method but did not hit the cerebral tissue are marked in rectangles (white).

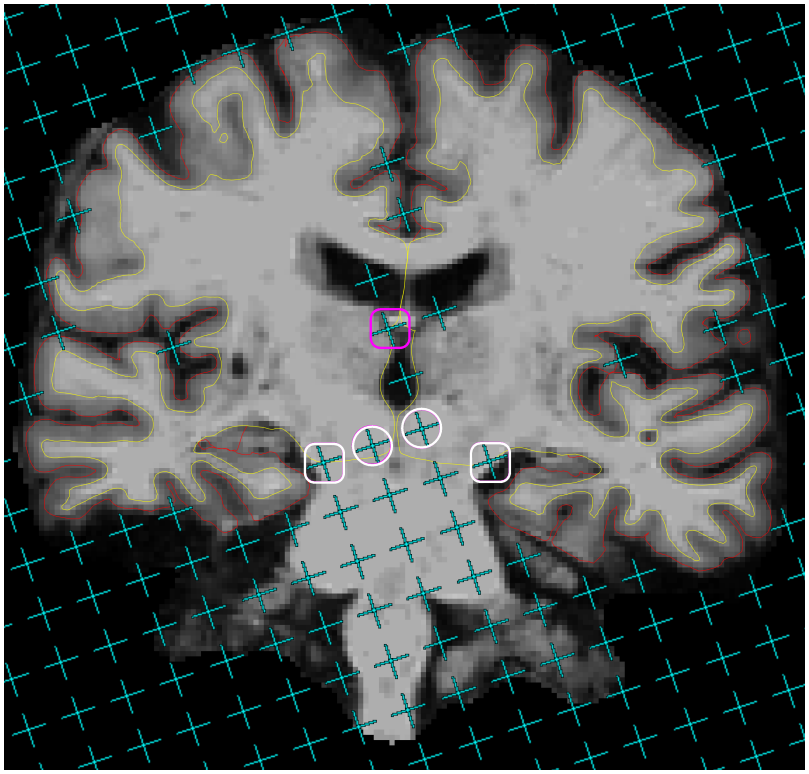

Figure 6.21: Test points (cyan) which were not counted by the rater using the CAVALIERI method but were included in the cerebral tissue by FREESURFER are marked in circles (white) and rounded rectangles (white).

There are two more points needing attention when doing this study.

(1) There seems to be a tiny deformation in the images which FREESURFER bases the segmentation on from the original MR images, e.g. the 'nu.mgz' file generated by FREESURFER is intensity normalized[6] and applied with TALAIRACH transform[7]. To make a better alignment and comparison between the two methods, the 'nu.mgz' image volume instead of the original MR images was used for the CAVALIERI method (Figure 6.22).

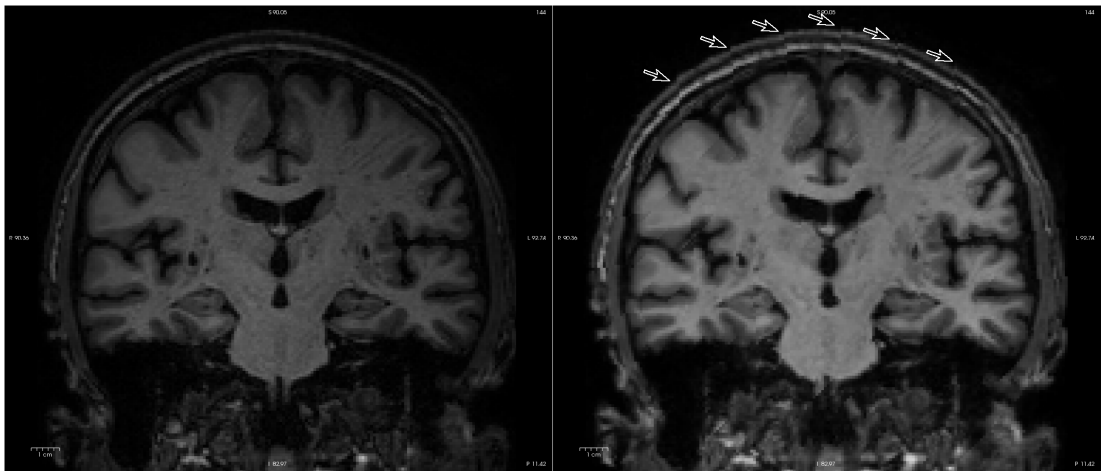

Figure 6.22: The original MR image '001.mgz' (left) and the processed MR image 'nu.mgz' (right) of one same brain. In 'nu.mgz', there are a few traces of vertical fractures (arrows), which suggests there is tiny deformation in the processed MR image.

(2) The probability that a test point hits a unidimensional boundary is zero. In practice, however, an artificial boundary drawn on an image will have a positive thickness. When the test points were overlaid onto the segmented brain profile, there were chances the test points could be hitting exactly on the boundary lines. In this study, the centre point of the cross was used to decide whether the test points should be included or excluded, although it could still be difficult to choose especially when the pial boundary line was too thick (Figure 6.23a). To make the line thinner, the images from FREESURFER were enlarged (six times in this study) before screenshots, which kept more voxel information, and thus the boundary lines became thinner and the comparison became easier (Figure 6.23b).

[6] https://surfer.nmr.mgh.harvard.edu/fswiki/ReconAllOutputFiles
[7] https://surfer.nmr.mgh.harvard.edu/fswiki/talairach

(a)

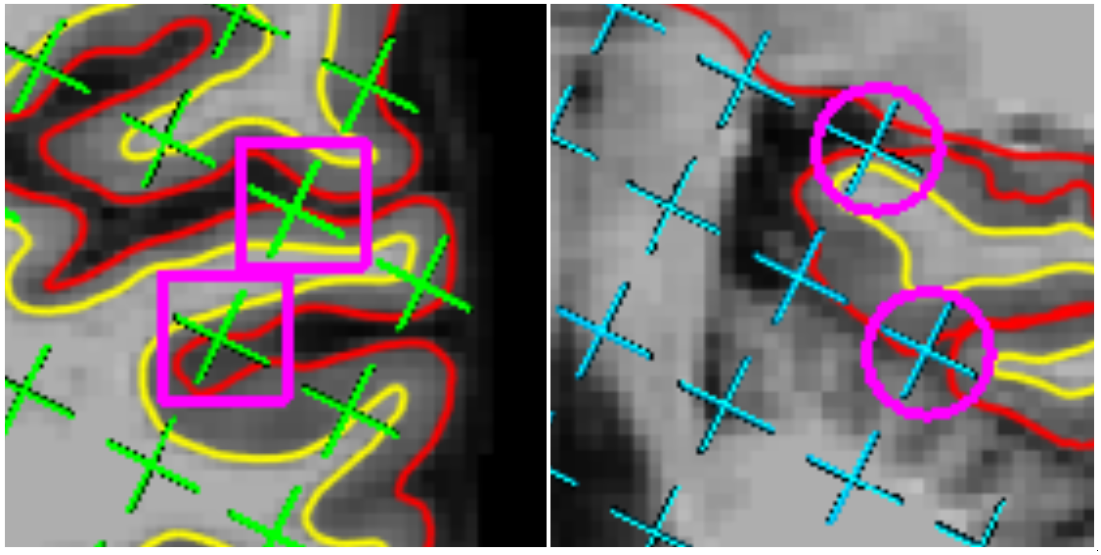

(b)

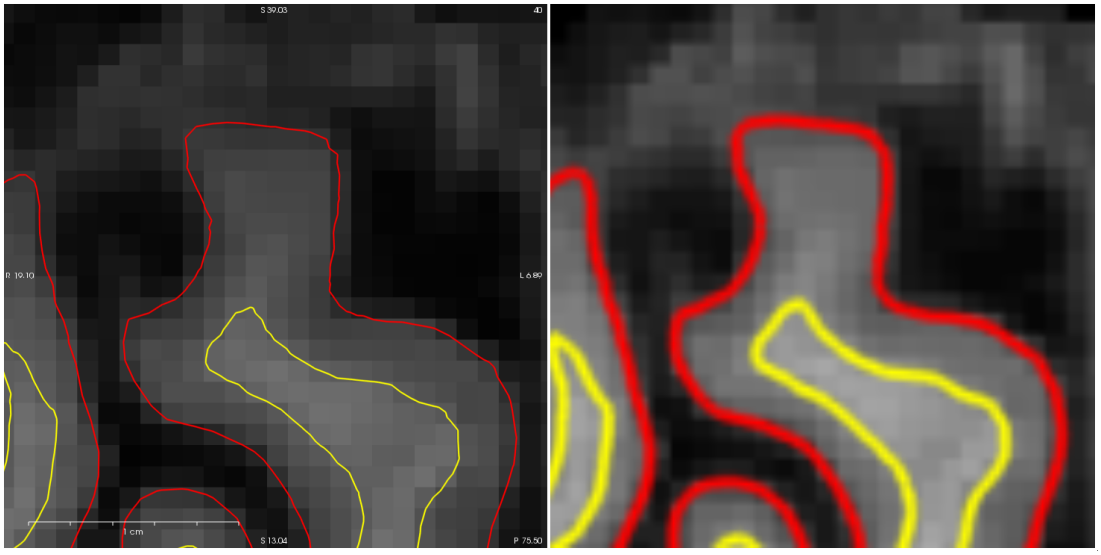

Figure 6.23: (a) Test points (inside pink rectangles on the left or circles on the right) hitting on thick pial surface boundaries (red) are difficult to tell whether the test points should be included or excluded. (b) The thickness of the pial surface boundary lines (red) becomes thinner when the MR image is enlarged (six times in this case) in FREESURFER before screenshot is taken (left) in comparison with red boundary lines in original scale (right).

There are limits in this study too. (1) Only one data was measured by one rater for one time using the CAVALIERI method. Repetition can improve the reliability of the results. (2) In the process of FREESURFER, manual correction was performed by the same rater. Corrections by experts (e.g. radiologists) may give more accurate estimates of volume. (3) The volume obtained by FREESURFER was regarded as the reference volume in this study. However, the ground truth of the cerebral volume of the subject was not available, which might bring bias in the comparison of the results.

In short, the findings reveal that adult brain volume estimation obtained by the author using the CAVALIERI method in combination with point counting strategy is consistent with that obtained automatically using the FREESURFER image segmentation pipeline.

6.5 Acknowledgements

Thanks to Dr. Mirjam SCHUBERT for kindly providing MRI data.

Chapter 7

Reproducibility of Stereology and FREESURFER in Cerebral Volume Estimation in Alzheimer's Disease

7.1 Introduction

AD has been widely studied using MRI. One example is the Alzheimer's Disease Neuroimaging Initiative (ADNI) study starting on 2004, which has combined different brain atrophy imaging biomarkers into the early diagnosis of AD [116].[1]

Based on the brain MRI, image analysis techniques are being developed to investigate details of structural and volumetric changes. Different voxel-based morphometry (VBM) algorithms have been applied to try to automatically screen AD patients, among which a surface-based and free software FREESURFER[2] [38] has been well-established [107]. More than one hundred of research papers have been published using FREESURFER in the recent ten years for the quantitative image analysis of the brains in AD patients.[3] For example, FREESURFER has been compared and supported in the measurement of hippocampal atrophy rates although not rated as the best automated algorithm [18]. However, inconsistency has been reported between FREESURFER and manual delineation method on the volume estimation of the hippocampus [33] which is a validated biomarker in diagnosing AD [2]. Furthermore, the absolute values of cortical thickness estimated across FREESURFER versions 4.1.0, 4.5.0 and 5.1.0 in the same individuals can result in significant differences [13], but the diagnostic classification is not affected when performing the estimation using the same software version through the whole data [13, 16].

In practice, the huge amount of time FREESURFER costs for each brain (i.e. roughly minimum eight hours per brain) and the high requirement of both computer hardware and programming knowledge limit its widespread application either in large population or on quick exami-

[1] http://adni.loni.usc.edu/
[2] http://surfer.nmr.mgh.harvard.edu/
[3] http://www.ncbi.nlm.nih.gov/pubmed/?term=FreeSurfer+Alzheimer

nation for diagnosis by clinicians. Hence a method with low requirements for the hardware and easy to operate (i.e. manual techniques) is still necessary as a complementary approach where stereology can be an option.

One traditional stereological method, i.e. the CAVALIERI method [20, 60, 80], has been applied on the estimation of volume among different parts of adult brain from either MR images or the postmortem, e.g. prefrontal cortex [62, 70, 95], frontal operculum (the Broca's area) [74], pars opercularis [73], pars triangularis [73], planum temporale [73], insula [73], hippocampus [49, 70], ventricles [3], cortical gray matter [89], white matter [68], cerebrum [8], cerebellum [5, 8] and total brain [3, 8]. Comparison between the manual method (e.g. CAVALIERI) and automatic or semi-automatic techniques (e.g. VBM) for different purposes and by operatives from various backgrounds have been briefly investigated [72]. Specifically, high consistency has been shown between CAVALIERI and FREESURFER in estimating volume of the thalamus [71].

Three novel design-based stereological methods, i.e. the ICAV [25, 28], INV [21, 22, 23, 24, 27, 28, 53] and DN [24, 55, 59] methods, have been developed for volume estimation. All the three methods are based on IR rotation of a 3D object or image. The ICAV and INV methods are also designed for surface area estimation. The INV method shows group mean estimates of volume and surface area of seven rat brains very close to those estimated by the ICAV method [28]. Both the INV and DN methods are highly efficient in estimating population means rather than individuals. Neither of the three methods have been applied for volume estimation in human adult brain yet.

The first purpose of this chapter is to examine the agreement of four manual stereological methods with the automated FREESURFER image analysis pipeline in estimating volume of adult brain on MR images. The second purpose is to examine the difference of the cerebral parenchymal volume between AD patients and healthy elderly subjects.

7.2 Materials and Methods

7.2.1 Participants

40 AD patients and 22 healthy elderly volunteers were recruited for brain MRI (T1-weighted) scans in Munich Germany, within whom subjects with good image quality were selected for this study, which comprised 13 AD patients (9 females, mean age 63.0 ± 10.0 SD, range $50-79$) and 13 healthy elderly controls (6 females, mean age 55.7 ± 11.9 SD, range $40-71$). There was no statistical difference in age between patients and controls ($t = 1.69, p = 0.10$). All study procedures received ethical approval from the participating institution, and all participants were given written informed consent prior to testing.

7.2.2 MRI Acquisition

Brain MRI data were acquired at the university hospital KLINIKUM RECHTS DER ISAR of the Munich Technical University, Germany. Eight AD patients and six elderly volunteers were

scanned in one SIEMENS BIOGRAPH MMR 3 tesla MR-PET scanner, and five AD patients and seven elderly volunteers were scanned in one PHILIPS ACHIEVA 3 tesla scanner. The scanning protocol comprised two 3D T1-weighted sequences (Table 7.1).

Table 7.1: DICOM information of two T1-weighted sequences.

ID	Name	Sequence 1	Sequence 2
0008,0070	Manufacturer	SIEMENS	Philips Medical Systems
0008,1090	Manufacturer's Model Name	Biograph_mMR	Achieva
0018,0020	Scanning Sequence	GR\IR	GR
0018,0021	Sequence Variant	SP\MP	MP
0018,0022	Scan Options	IR	OTHER
0018,0023	MR Acquisition Type	3D	3D
0018,0050	Slice Thickness	1	1
0018,0080	Repetition Time	2300	9
0018,0081	Echo Time	2.98	4.0009999275
0018,0082	Inversion Time	900	
0018,0083	Number of Averages	1	1
0018,0084	Imaging Frequency	123.191647	127.784241
0018,0085	Imaged Nucleus	1H	1H
0018,0086	Echo Numbers(s)	1	1
0018,0087	Magnetic Field Strength	3	3
0018,0088	Spacing Between Slices		1
0018,0089	Number of Phase Encoding Steps	239	240
0018,0091	Echo Train Length	1	164
0018,0093	Percent Sampling	100	100
0018,0094	Percent Phase Field of View	93.75	100
0018,0095	Pixel Bandwidth	238	169.3766937256
0018,1310	Acquisition Matrix	0 256 240 0	0 240 240 0
0018,1312	Phase Encoding Direction	ROW	ROW
0018,1314	Flip Angle	9	8
0018,5100	Patient Position	HFS	HFS
0028,0030	Pixel Spacing	1\1	1\1

7.2.3 Image Analysis

FREESURFER Volumetry

Volumetric analysis was performed by FREESURFER (6.0 Beta) software on a LINUX cluster. After a full run of the program on each data on the cluster, manual edits were performed on the auto-segmentation output of each individual on a LINUX laptop and then the results were re-analysed by FREESURFER. The modified results were checked by the rater again. The 'SupraTentorialNotVent'[4] values in the 'aseg.stats' files for the total 26 subjects were collected for comparison.[5]

Stereological Volumetry

Four stereological techniques, i.e. the CAVALIERI, ICAV, INV and DN methods, were applied to estimate the cerebral parenchymal volume, all of which were performed on freely available software packages (i.e. EASYMEASURE, IMAGEJ and R).

[4] http://surfer.nmr.mgh.harvard.edu/fswiki/MorphometryStats
[5] https://surfer.nmr.mgh.harvard.edu/fswiki/asegstats2table

Firstly, all the brain images were semi-automatically processed in an in-house R script (Appendix B). The images were aligned to the FSL's 'MNI152 standard-space T1-weighted average structural template image'.[6] As a result, the skull together with neck tissue was removed, the brains were placed around the centres of the images and the positions of the brains were almost in consistent. Then, the brain images were transferred to the radiological convention. Each MR image was padded into a cube in space. Transverse 2D section planes with the nose pointing downwards was initialized to all the images. Finally, triplets of orthogonal images in the sagittal, transverse and coronal views were output for the CAVALIERI method, the images undergone IR rotations in four angles were output in triplets of orthogonal views for the ICAV ortrip method, and the central slices of the rotated images were extracted in the above triplets of orthogonal views for the INV ortrip and DN ortrip methods (see Chapter 2).

The CAVALIERI and ICAV methods were applied in EASYMEASURE software (Figure 7.1). Each image was sliced evenly in the interval of 15 mm with a random start. Then the test grid with the lattice size of 15 $mm \times 15$ mm was randomly overlaid upon each of the slices. The time cost in manual points counting for each measurement was roughly 10 mins. In either the AD and health groups, there were four sagittal, four transverse and five coronal views of images randomly selected for the CAVALIERI estimation. IUR parallel sections of all the above 26 subjects were applied in estimation by ICAV.

The INV and DN methods were applied in two in-house IMAGEJ scripts (Appendix C, Appendix D, Figure 7.1). The test grids for these two methods were overlaid upon two identical planes semi-automatically. The lattice size of the grid was set to 35 mm and was randomized by 15% (i.e. 30 mm to 40 mm). The time cost in manual length measurement for each plane by the INV and DN methods was roughly 8 mins and 2 mins, respectively. The results were auto-saved in EXCEL tables and the sum of lengths could be obtained manually. All triplets of orthogonal planes of the 26 subjects were estimated by the INV ortrip and DN ortrip methods (see Chapter 3, Chapter 4).

Using the above stereological methods, the cerebral volumes excluding ventricles and cerebrospinal fluid (CSF) were estimated. Three orthogonal mean values of the volumes were also obtained using the INV ortrip and DN ortrip methods.

Repeatability studies were performed by two observers (KY and LH, both were neuroimaging PhD candidates) on three AD patients and three healthy elderly subjects from the dataset. One sagittal, one transverse and one coronal brain images were included in both AD and health groups for the CAVALIERI method; three IUR section planes of brain images were used for the ICAV method; three IR rotated brain images were used for both the INV and DN methods. On each subject, for the CAVALIERI and ICAV methods, the test grids applied in the inter- and intra- rater studies were in the same lattice size (i.e. 15 $mm \times 15$ mm) but in UR position and random orientation, and the sectioning interval was the same (i.e. 15 mm). For the INV and DN methods, on each subject, the exact same test grid (i.e. the same in size, position and orientation) were applied on the same sectioning plane between the two methods for each observer. The lattice sizes were the same as those used in the whole dataset estimation, which were set

[6] http://fsl.fmrib.ox.ac.uk/fsl/fslwiki/Atlases

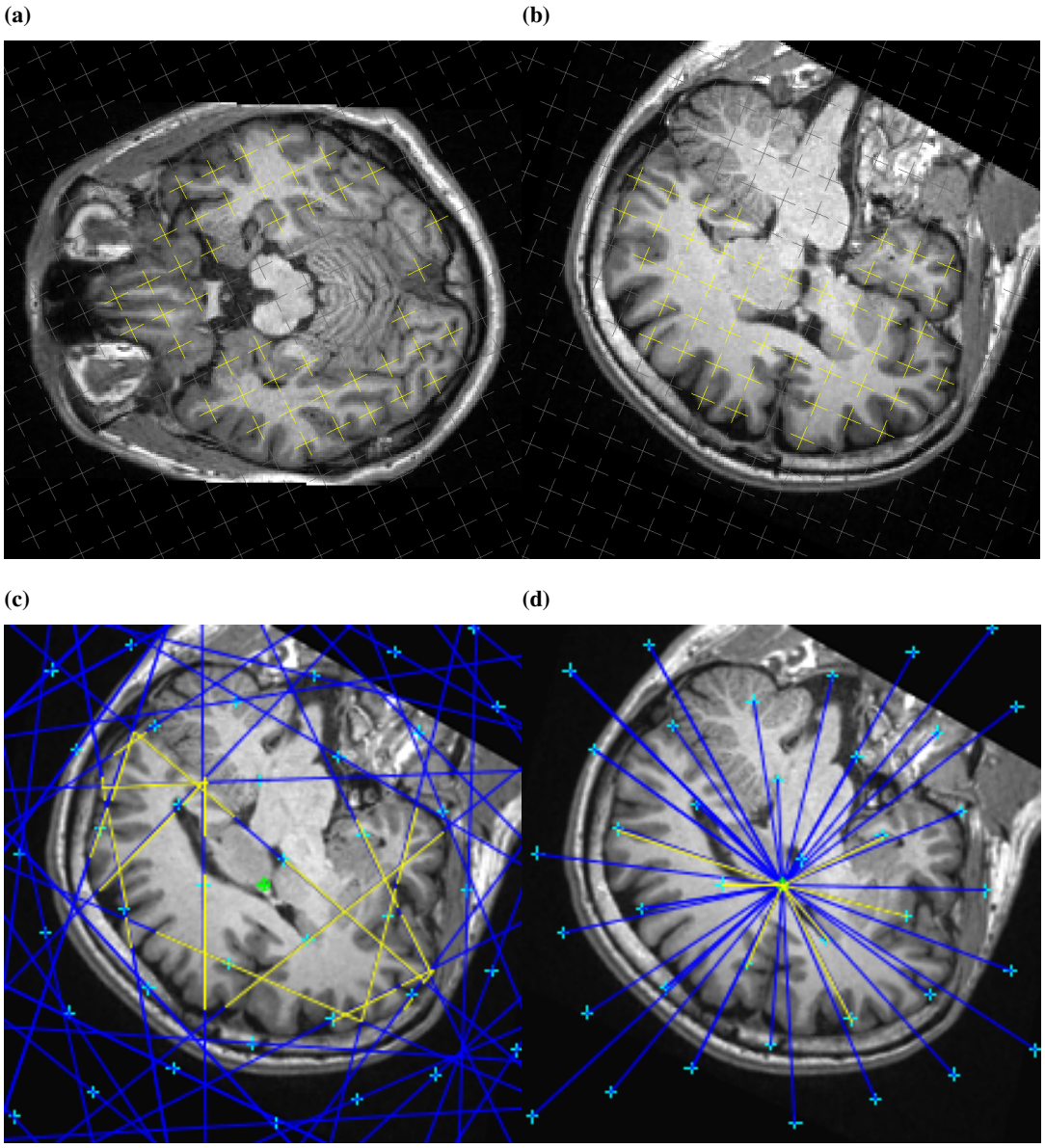

Figure 7.1: Examples of estimations of cerebral parenchymal volumes on a healthy brain MR image measured by four stereological methods: (a) the CAVALIERI method (yellow points counted on one slice in the transversal view), (b) the ICAV method (yellow points counted on one of IUR parallel slices), (c) the INV method (yellow segments on one IR rotated slice) and (d) the DN method (yellow segments on one IR rotated slice).

to 35 mm and were randomised by 15% (i.e. 30 mm to 40 mm). But the test grids were in UR position and random orientation and therefore were not exactly the same as those used in the whole dataset estimation.

7.2.4 Statistical Analysis

One-tailed two samples t-tests were performed and the null hypothesis was the cerebral volume of AD patients was no less than that of the healthy elderly subjects by each method. Correlational comparisons of each two methods were plotted. Statistics was performed in R software.

7.3 Results

The results of inter- and intra- rater studies were shown below (Table 7.2, Figure 7.2). No bias could be seen within or between the observers. In each subject, three volumes estimated using the CAVALIERI and ICAV methods by KY (twice) and LH were close to each other, which were also close to the volume obtained from FREESURFER. Three volumes estimated using the INV and DN methods by KY (twice) and LH in each subject had much higher variance. The estimates were closer to each other between the INV and DN methods comparing with those obtained by the CAVALIERI and ICAV methods.

Table 7.2: Inter- and intra-rater studies by KY (twice) and LH on three AD patients and three healthy elderly subjects. Cerebral parenchymal volumes measured by FREESURFER, the CAVALIERI, ICAV, INV and DN methods, together with slice and grid parameters for stereology are listed in the table (HE: healthy elderly subjects, FS: FREESURFER).

ID	Group	Rater	FS	CAVALIERI & ICAV		CAVALIERI	ICAV	INV & DN	INV	DN
			Vol cm^3	Slice cm	Grid cm	Vol cm^3	Vol cm^3	Grid cm	Vol cm^3	Vol cm^3
17	AD	KY1	907	15	15	834	901	37	876	1126
53	AD	KY1	904	15	15	915	911	39	813	700
112	AD	KY1	754	15	15	770	783	36	1241	1084
DK	HE	KY1	880	15	15	851	861	39	740	665
P02	HE	KY1	1041	15	15	1060	1073	36	831	1043
P12	HE	KY1	836	15	15	773	820	31	814	839
17	AD	KY2	907	15	15	844	908	37	825	821
53	AD	KY2	904	15	15	945	938	39	846	802
112	AD	KY2	754	15	15	699	709	36	1137	993
DK	HE	KY2	880	15	15	911	894	39	724	521
P02	HE	KY2	1041	15	15	1056	1063	36	844	882
P12	HE	KY2	836	15	15	797	881	31	794	847
17	AD	LH	907	15	15	1013	884	37	938	842
53	AD	LH	904	15	15	969	1036	39	928	933
112	AD	LH	754	15	15	817	759	36	1178	1266
DK	HE	LH	880	15	15	945	891	39	823	1170
P02	HE	LH	1041	15	15	1063	1060	36	758	908
P12	HE	LH	836	15	15	854	874	31	904	553

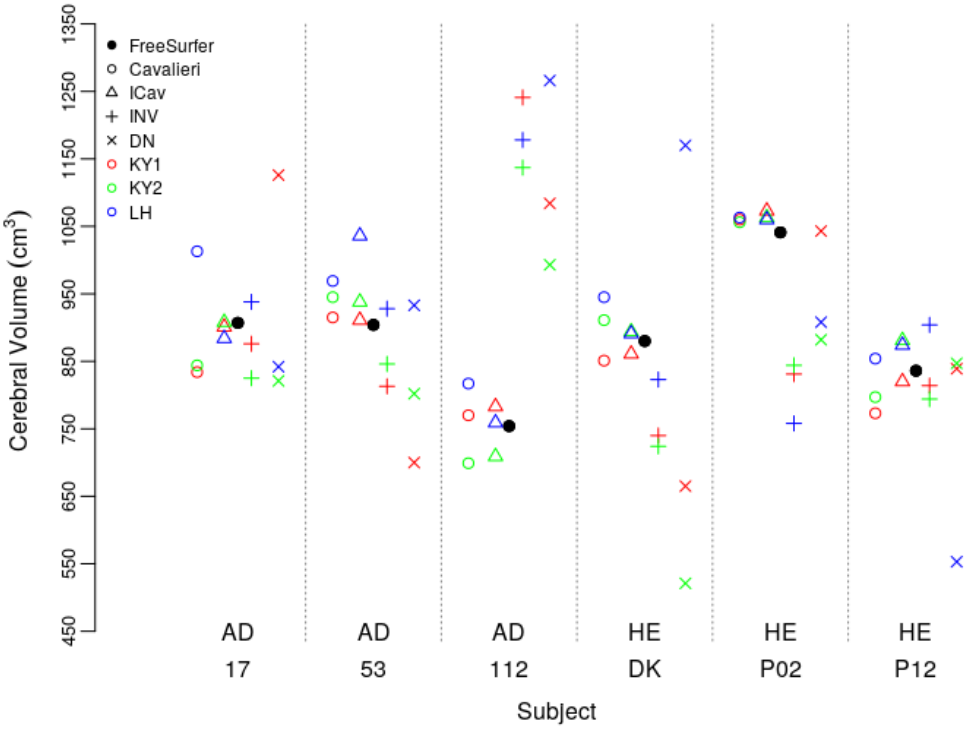

Figure 7.2: Inter- and intra-rater studies of cerebral volume estimation using the CAVALIERI, ICAV, INV and DN methods by KY and LH on three AD patients and three healthy elderly subjects are plotted in comparison with volumes obtained by FREESURFER.

There were significant difference of the cerebral parenchymal volumes between 13 AD patients and 13 healthy elderly subjects measured by FREESURFER, the CAVALIERI and ICAV methods (Table 7.3, Figure 7.3). The coefficients of error (CEs) for the CAVALIERI and ICAV methods were all below 5% (Table 7.3). However, the INV and DN methods were not able to detect the difference of volumes, neither could the INV ortrip or DN ortrip method by using the mean values of estimates obtained from triplets of orthogonal section planes (Table 7.3, Figure 7.4).

Table 7.3: Cerebral parenchymal volumes of 13 AD patients and 13 healthy elderly subjects measured by FREESURFER, the CAVALIERI, ICAV, INV ortrip and DN ortrip methods, together with CEs of the CAVALIERI and ICAV are listed in the table (Cav: the CAVALIERI, HE: healthy elderly people, FS: FREESURFER).

ID	Group	FS	Cav	Cav	ICAV	ICAV	INV 1	DN 1	INV 2	DN 2	INV 3	DN 3
		cm^3	Vol cm^3	CE %	Vol cm^3	CE %	Vol cm^3	Vol cm^3	Vol cm^3	Vol cm^3	Vol cm^3	Vol cm^3
003	AD	815	746	3.874	790	2.095	1328	1291	739	609	810	947
005	AD	702	638	1.895	689	2.576	695	759	740	756	756	808
007	AD	905	834	1.668	786	0.975	979	478	746	763	1183	1103
017	AD	907	834	3.378	901	1.311	876	1126	1308	1291	620	437
046	AD	837	793	1.223	827	1.338	1162	1159	728	1020	1096	1163
049	AD	779	783	1.591	803	2.015	781	551	696	510	1173	1066
052	AD	704	695	0.737	685	1.319	806	916	621	623	906	1205
053	AD	904	915	0.953	911	1.101	844	690	813	700	1147	1325
089	AD	756	736	2.947	702	1.299	708	1079	718	786	1062	1352
100	AD	876	884	0.787	844	0.887	845	371	814	664	873	773
105	AD	916	803	0.959	881	0.589	822	914	1490	1651	890	981
109	AD	812	773	1.560	729	1.396	1451	1774	717	590	730	683
112	AD	754	770	3.280	783	0.996	686	532	591	746	1241	1084
AB	HE	972	948	2.618	952	1.639	1355	1386	1096	943	813	877
AE	HE	854	837	1.064	871	0.903	666	756	798	857	938	1106
AK	HE	942	959	1.674	962	1.523	1000	998	932	655	957	964
DK	HE	880	851	2.545	861	0.839	740	665	1205	1233	781	982
HJ	HE	986	1013	0.812	1016	1.158	1466	1458	877	692	840	681
KCM	HE	904	888	0.727	898	0.824	1069	1252	879	876	827	816
PJ	HE	800	780	0.776	807	1.159	821	475	976	784	703	787
P02	HE	1041	1060	0.805	1073	0.635	1054	806	831	1043	1616	1635
P06	HE	1039	1060	1.493	1023	0.705	933	739	1037	843	1039	1275
P07	HE	1155	1144	0.885	1161	1.260	1092	1102	1456	1592	1199	1223
P08	HE	680	628	0.842	682	0.766	691	434	777	645	748	1010
P10	HE	877	824	1.109	861	0.853	785	625	785	798	1285	1153
P12	HE	836	773	1.355	820	1.186	1283	1324	744	673	814	839

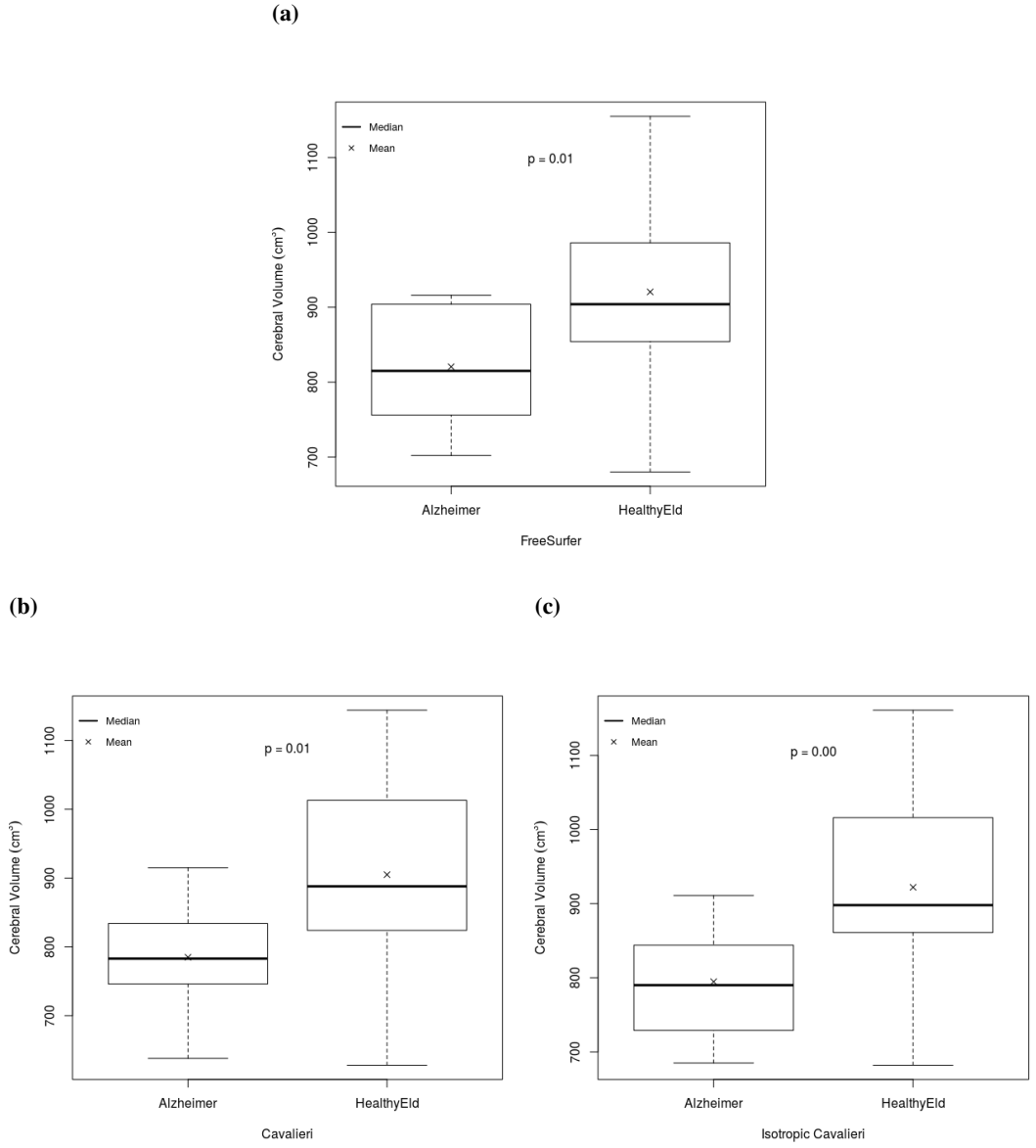

Figure 7.3: The comparison of cerebral parenchymal volumes between 13 AD patients and 13 healthy elderly subjects measured by: (a) FREESURFER, (b) the CAVALIERI and (c) ICAV methods.

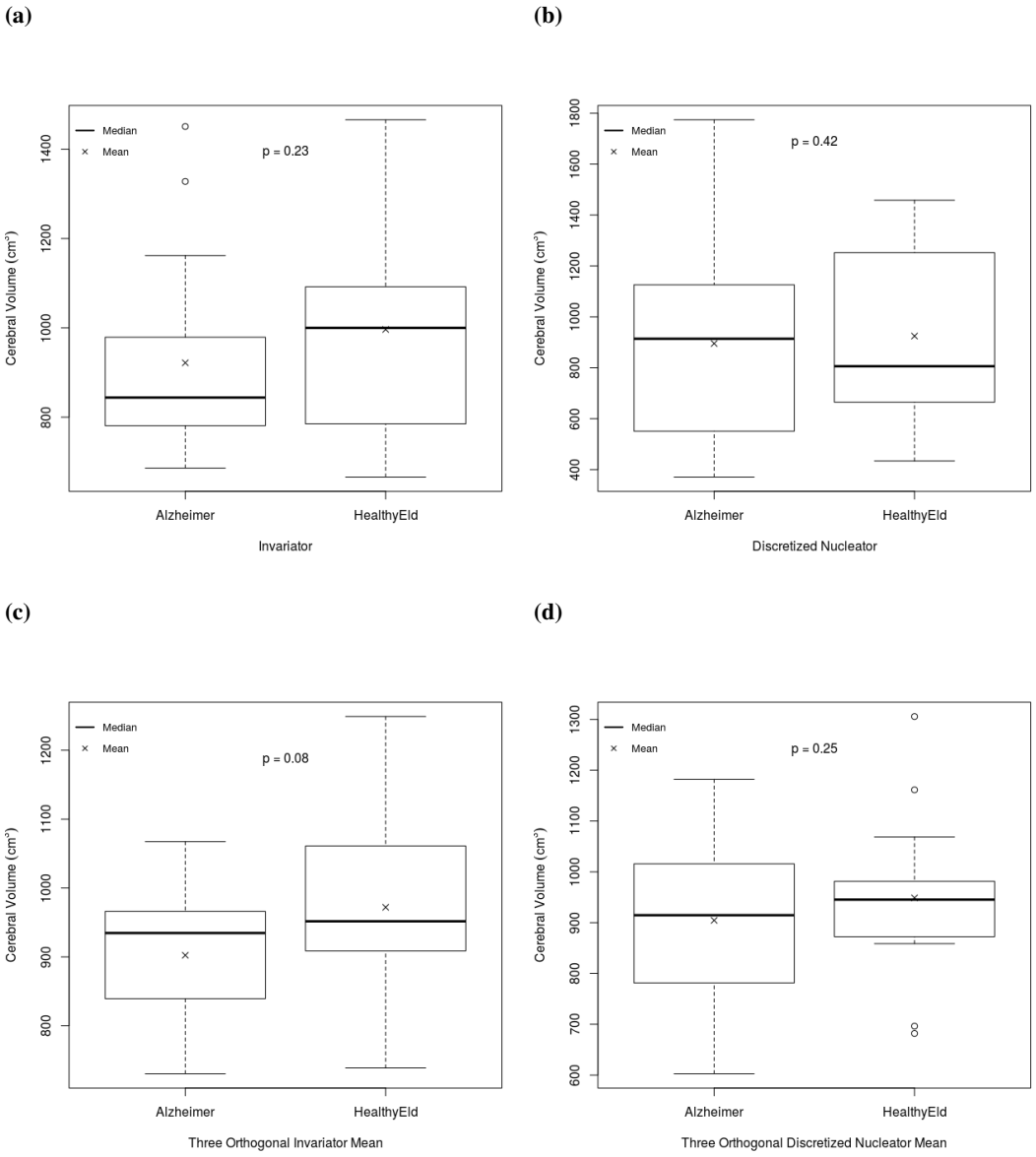

Figure 7.4: The comparison of cerebral parenchymal volumes between 13 AD patients and 13 healthy elderly subjects measured by: (a) the INV method in a single plane, (b) the DN method in a single plane, (c) the INV ortrip method (arithmetic means) and (d) the DN ortrip method (arithmetic means).

Strong positive linear relationships were shown between FREESURFER, the CAVALIERI and ICAV methods (Figure 7.5). Weak positive linear relationships were shown between FREESURFER, the INV and DN methods when the latter two methods were applied in a single IR plane. The linear relationships were improved to moderate positive when the INV ortrip and DN ortrip methods were applied (Figure 7.6).

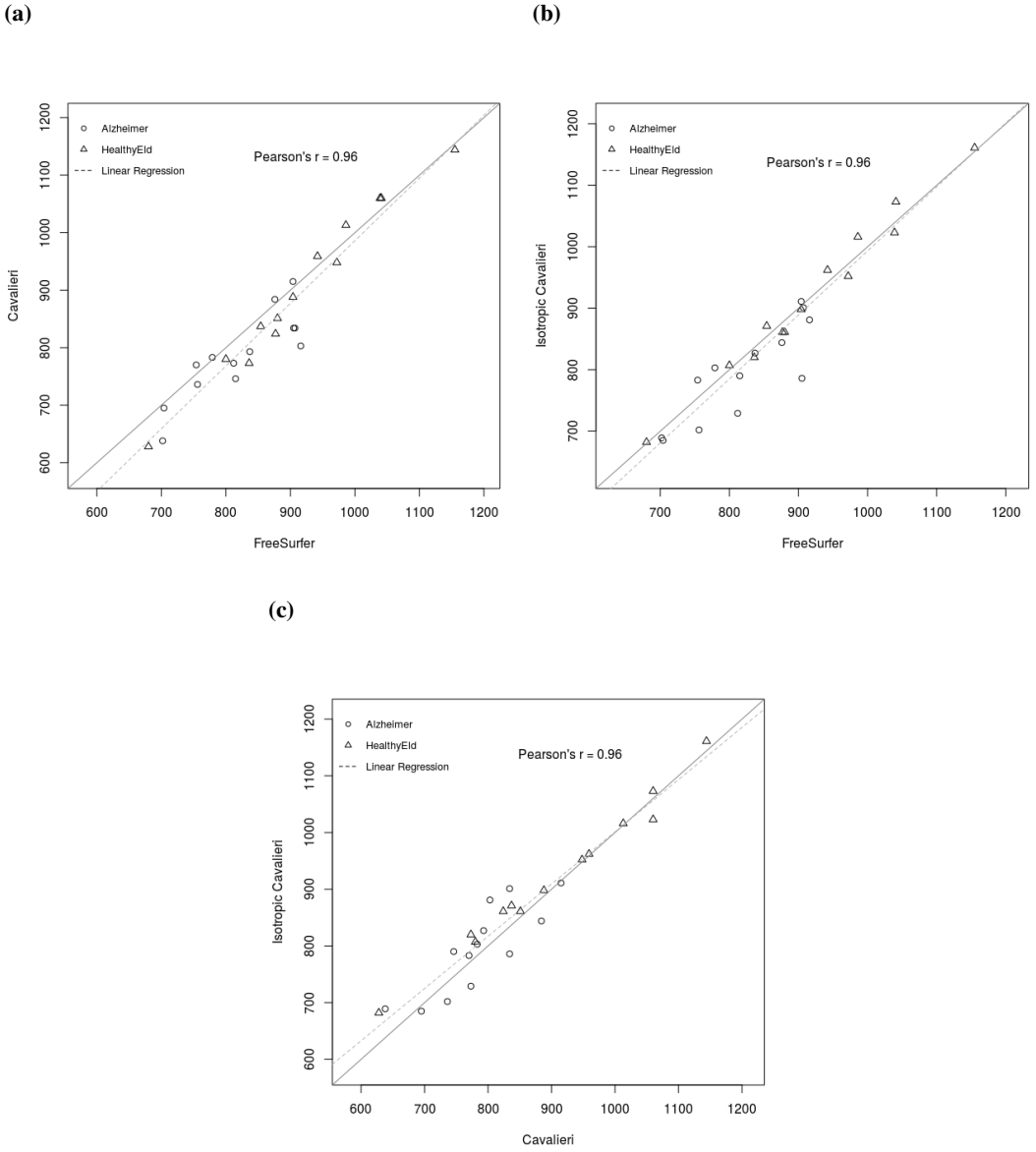

Figure 7.5: The linear relationships between the results from: (a) FREESURFER and the CAVALIERI method, (b) FREESURFER and the ICAV method, (c) the CAVALIERI and ICAV methods.

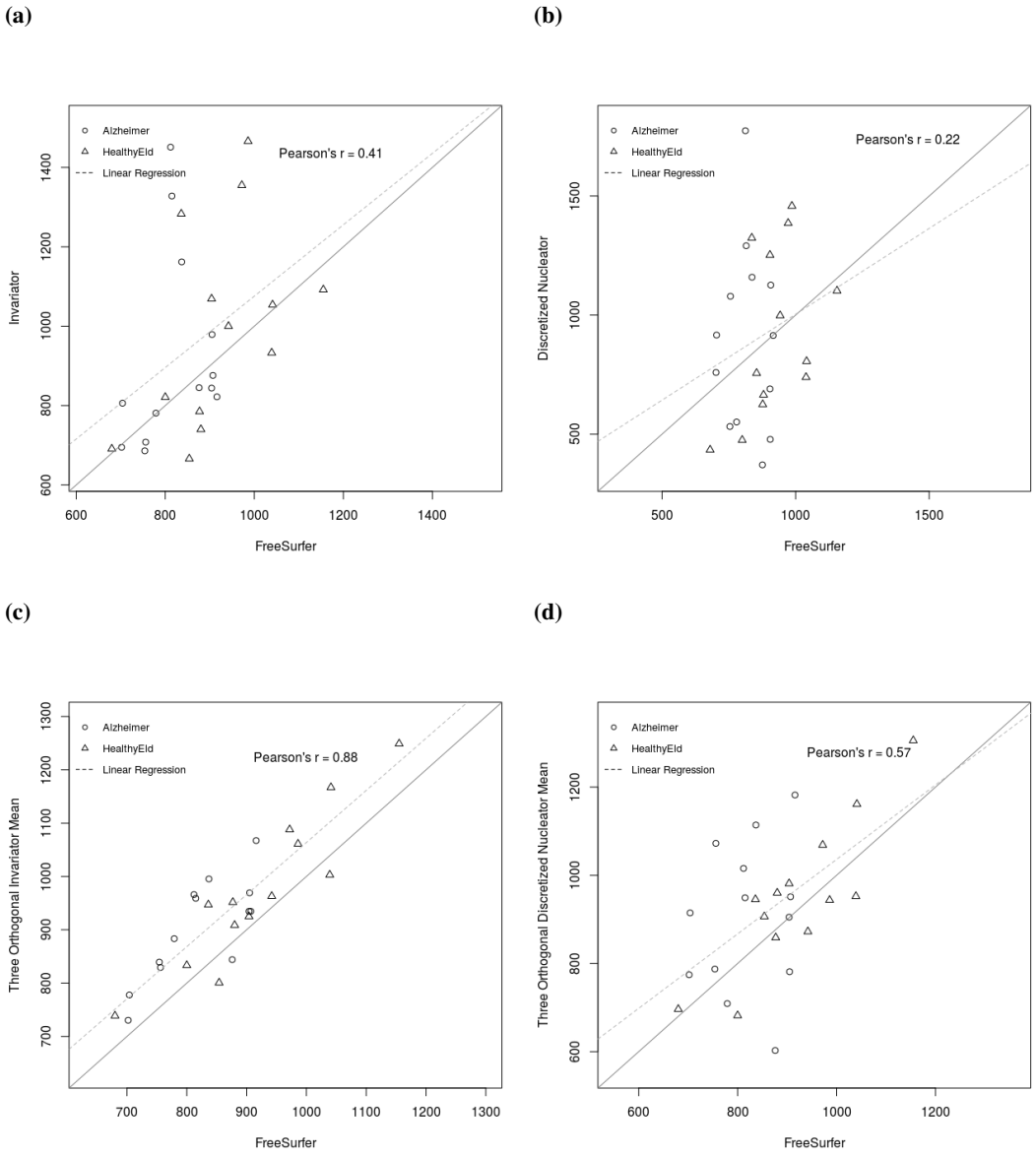

Figure 7.6: The linear relationships between the results from FREESURFER and: (a) the INV method in a single plane, (b) the DN method in a single plane, (c) mean of the INV ortrip method and (d) mean of the DN ortrip method.

Paired comparison between FREESURFER and stereological methods showed good consistency. The INV and DN methods obtained similar mean estimates with those obtained by FREESURFER. The INV ortrip and DN ortrip methods improved consistency in individual estimates (Figure 7.7, 7.8).

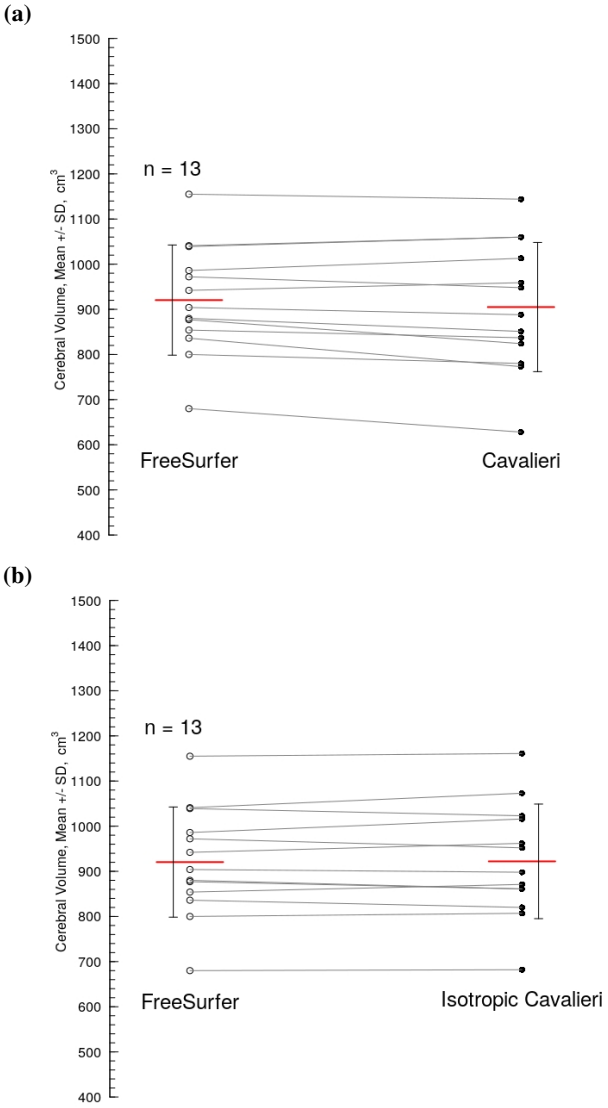

Figure 7.7: Paired comparison among cerebral volumes obtained from FREESURFER, the CAVALIERI and ICAV methods in the health group. (a) FREESURFER vs the CAVALIERI method; (b) FREESURFER vs the ICAV method. Red horizontal bars are mean values in each group.

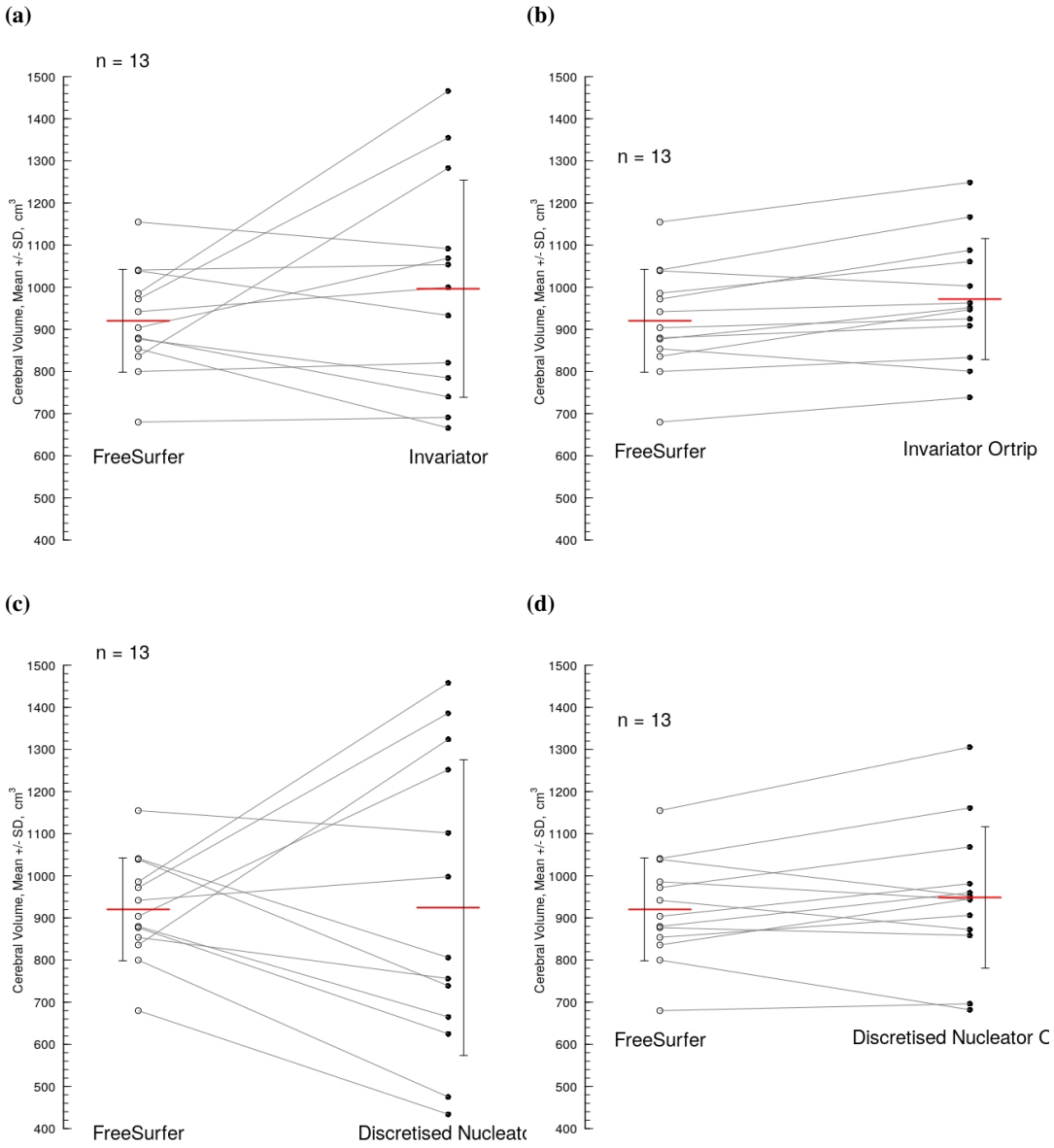

Figure 7.8: Paired comparison among cerebral volumes obtained from FREESURFER, the INV, INV ortrip, DN and DN ortrip methods in the health group. (a) FREESURFER vs the INV method; (b) FREESURFER vs the INV ortrip method; (c) FREESURFER vs the DN method; (d) FREESURFER vs the DN ortrip method. Red horizontal bars are mean values in each group.

7.4 Discussion

The traditional CAVALIERI method and the novel ICAV method are both reliable and efficient in comparing the cerebral parenchymal volume between two small groups of adult brains. Both the manual methods estimated the volumes close to those obtained by FREESURFER software. Although FREESURFER was used as a reliable automated reference method in this study, it is impossible to tell which method is the most accurate in measuring each individual adult brain volume.

Neither the INV nor DN method was reliable in this study, especially when the estimation was done just in a single section plane from each subject. The extension of the measurement to three orthogonal sections (i.e. the INV ortrip and DN ortrip methods) in each subject did improve the performance in the group comparison, but obviously this strategy was not enough to turn the methods sensitive in the adult brain volume estimation. Possibly the following suggestions can increase the precision for both the methods when being applied on the complex brain structure: (i) a large population in each data group; (ii) more section planes around each subject; (iii) other possible mathematical algorithms to assemble the estimates on multiple section planes from the same subject; (iv) a higher dense test grid projected upon each section plane. Specifically, in the third suggestion aforementioned, when the number of sections measured in each subject is three, which is the same as we did (i.e. three orthogonal sections) in this study, arithmetic means (i.e. average of sum) of the three estimates in each subject (Figure 7.4) can have bigger p values of t-tests (thus less significant power) than geometric means (i.e. cube root) (Figure 7.9), which suggests there may be other better algorithms to pursue the means.

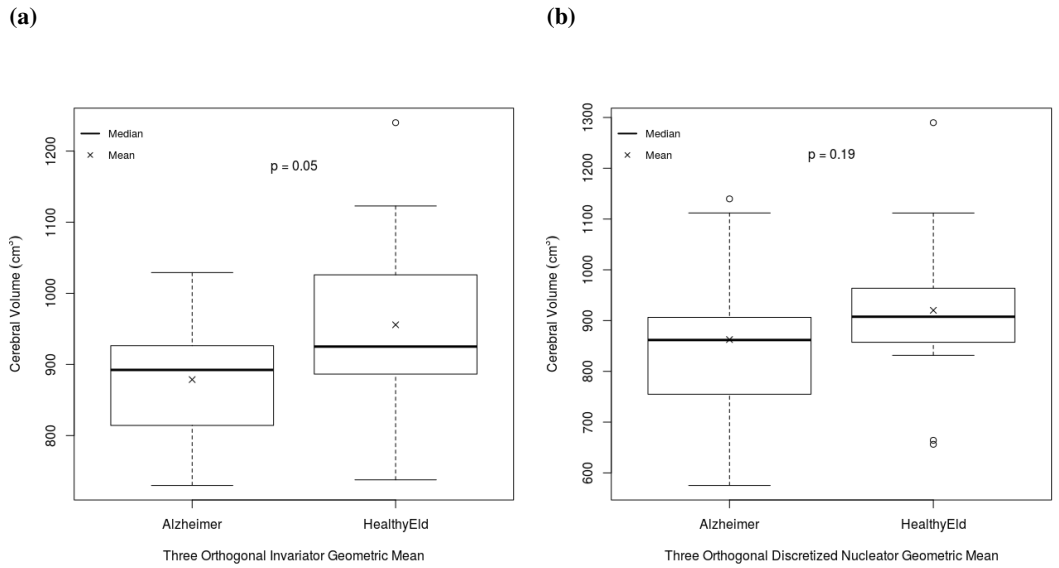

Figure 7.9: The comparison of cerebral parenchymal volumes between 13 AD patients and 13 healthy elderly subjects measured by: (a) the INV ortrip method, geometric means (cube root) instead of arithmetic means (average of sum) of three section planes in each subject and (b) the DN ortrip method, geometric means.

7.5 Conclusions

Methodologically, two stereological methods (i.e. the CAVALIERI and ICAV methods) show high agreement to the automated FREESURFER software in the adult cerebral parenchymal volume comparison. However, perhaps due to the small sample size in this study, the other two stereological methods (i.e. the INV and DN methods) show low correlations with FREESURFER when the INV and DN methods are applied in single pivotal sectioning planes. Nevertheless, when the INV ortrip and DN ortrip methods are applied, the correlations with FREESURFER software are improved to high degree, and the group mean values show difference between AD and health subjects. Clinically, there is a significant reduction in the cerebral volume in AD patients.

7.6 Acknowledgement

Thanks to Dr. Mirjam SCHUBERT for kindly providing MRI data. Thanks to Lucy HISCOX for the inter-reliability study.

Chapter 8

Ageing Volumetric Atrophy in Brain Regions can be Influenced by Alzheimer's Disease

8.1 Introduction

Structural MRI provides a platform for neuroimaging tools to investigate brain tissues of human adults in vivo. Both automated image processing techniques such as FREESURFER [38] and manual techniques such as stereology (e.g. the INV method [28]) enable volumetric measurement of brain structures.

Brain tissues atrophy is observed along with both physiological ageing and neurodegenerative diseases such as AD. Different MRI modalities (e.g. T1-weighted, T2* relaxometry and Diffusion Tensor Imaging (DTI)) have been compared on each brain region to investigate morphological changes with ageing in healthy adults, suggesting that using multiple imaging biomarkers together can detect ageing-related brain tissue changes better [14]. T1-weighted MRI has also been used to investigate the shrinkage rate of each brain region with ageing in healthy adults. Additionally, hypertension is found accelerating the ageing-related shrinkage of hippocampus while sex, brain size or education seems to have no influences on brain ageing course in healthy subjects [99]. Ageing-related atrophy can also be relieved by cardiorespiratory fitness in several brain regions. But some other regions which are most influenced by ageing can be impervious to the benefits of cardiorespiratory fitness [46].

To assess the brain atrophy progression, using indices of changes of relative atrophy ratios of regional brain volume to global brain volume has been suggested instead of using indices of absolute regional atrophy volumes, which can reduce the effect of inter-individual variation and the effect of sex [87]. In AD patients, the brain to cerebrospinal fluid (CSF) volume ratio index has been applied to analyse global brain atrophy. Using this index, the influence by factors such as age, intracranial volume, education and presence of apolipoprotein E (ApoE) $\varepsilon 4$ allele on brain atrophy can be detected too [93].

Is the progression pattern of brain atrophy different between normal ageing in health and

pathological ageing in AD? A possible way AD can affect the ageing progression is to alter the endogenous mechanical pressure within brain tissues. Pressure equivalents of 5.92 and 3.43 $mmHg$ are reported in AD patients and in healthy elderly subjects, respectively [81]. Another indirect evidence for the hypothesis of mechanical reaction is the reduction of mechanical stiffness of brain tissues, which has been observed in normal ageing [104], but more significant in AD [90], using Magnetic Resonance Elastography (MRE) which maps brain viscoelastic properties.

The aims of this chapter are to: (1) test different volume ratios as potential imaging biomarkers for AD patients, e.g. volume ratios of brain to intracranial space, each brain region to whole brain, hippocampal subfields to hippocampal hemispheres and brainstem subfields to brainstem; (2) investigate difference of the changing patterns of the above volume ratios with ageing progression between AD patients and healthy elderly subjects; (3) examine the sensitivity of the INV method to detect group difference between AD patients and healthy elderly subjects, using one of the above volume ratio indices (i.e. the volume ratio of cerebrum to intra-cranium), and then compare the results with those from an automated software.

8.2 Materials and Methods

8.2.1 Participants

40 AD patients and 22 healthy elderly volunteers were recruited for brain MRI (T1-weighted) scans in Munich Germany. In this study, participants between the maximal common age scope of 47 and 71 in both groups were selected, which comprised 27 AD patients (14 females, mean age 61.5 ± 6.6 SD, range $47-70$) and 16 healthy elderly controls (10 females, mean age 60.9 ± 7.6 SD, range $49-71$). There was no statistical difference in age between patients and controls ($t = 0.25, p = 0.80$). All study procedures received ethical approval from the participating institution, and all participants were given written informed consent prior to testing.

8.2.2 MRI Acquisition

Brain MRI data were acquired at the university hospital KLINIKUM RECHTS DER ISAR of the Munich Technical University, Germany. 15 AD patients and six elderly volunteers were scanned in one SIEMENS BIOGRAPH MMR 3 tesla MR-PET scanner, and 12 AD patients and 10 elderly volunteers were scanned in one PHILIPS ACHIEVA 3 Tesla scanner. The scanning protocol comprised two 3D T1-weighted sequences (see Chapter 7 Table 7.1).

8.2.3 Image Analysis

FREESURFER Volumetry

Automated volumetric analysis was performed by FREESURFER (6.0 Beta) software on a LINUX cluster. Manual edits were performed on the auto-segmentation output of each individual on a LINUX (UBUNTU) laptop, and then the modified data were re-run by FREESURFER

on the cluster. The final segmentation were checked again by the same rater. Additional hippocampal subfields and brainstem subfields analyses were also performed.[1][2] All the entries in the lists of volumetric results (Table 8.1) for the total 43 subjects were collected for comparison.[3]

Table 8.1: Information of files containing volumetric results from FREESURFER software is listed.

File	File Path	FREESURFER Version	Structures
aseg.stats	(SubjectA)/stats	5.* and 6.0 Beta	All structures volumes
lh.hippoSfVolumes-T1.v10.txt	(SubjectA)/mri	6.0 Beta	Hippocampus Left
rh.hippoSfVolumes-T1.v10.txt	(SubjectA)/mri	6.0 Beta	Hippocampus Right
brainstemSsVolumes.v10.txt	(SubjectA)/mri	6.0 Beta	Brainstem

INVARIATOR Volumetry

Manual volumetric analysis were applied using the INV method. All of the 43 MRI data were semi-automated rotated by an in-house R script (Appendix B) comprising FSL functions to get one IR rotated pivotal section for each data (see Chapter 2). For each subject, the pivotal section plane was made into two copies, and each was superimposed with an identical UR test grid using an in-house IMAGEJ script (Appendix C). The size of the square lattices was set to $35\ mm \times 35\ mm$, and the measuring reference lines for the INV method were generated based on the test grids (see Chapter 3).

The cerebral and intra-cranial volumes were measured for each data using another in-house IMAGEJ script (see Chapter 4, Appendix D). The cerebral volume did not include ventricles or CSF. For the intra-cranial volume, the spinal cord was cut parallel to the bottom of the cerebellum (Figure 8.1).

8.2.4 Statistical Analysis

In the FREESURFER analysis, firstly the comparison of the cerebrum (excluding ventricles), the brain (including ventricles) and the intracranial volumes were made between the AD and the health groups. Secondly the volume ratios of the brain and the cerebrum (both with and without ventricles) to the intra-cranium were compared between the two groups. Thirdly the volume ratios of each sub-structure to the brain (including ventricles) were compared to inspect group differences. In each comparison, the maximum and minimum values of volume or ratio were excluded to enhance the reliability.

Correlational relationship between volumes and ageing in both the AD and the health groups were plotted. The analysis of covariance (ANCOVA) were performed to explore the effects of ageing on volume changes (if slopes of regression lines were different from zero),

[1] https://surfer.nmr.mgh.harvard.edu/fswiki/HippocampalSubfields
[2] https://surfer.nmr.mgh.harvard.edu/fswiki/BrainstemSubstructures
[3] https://surfer.nmr.mgh.harvard.edu/fswiki/asegstats2table

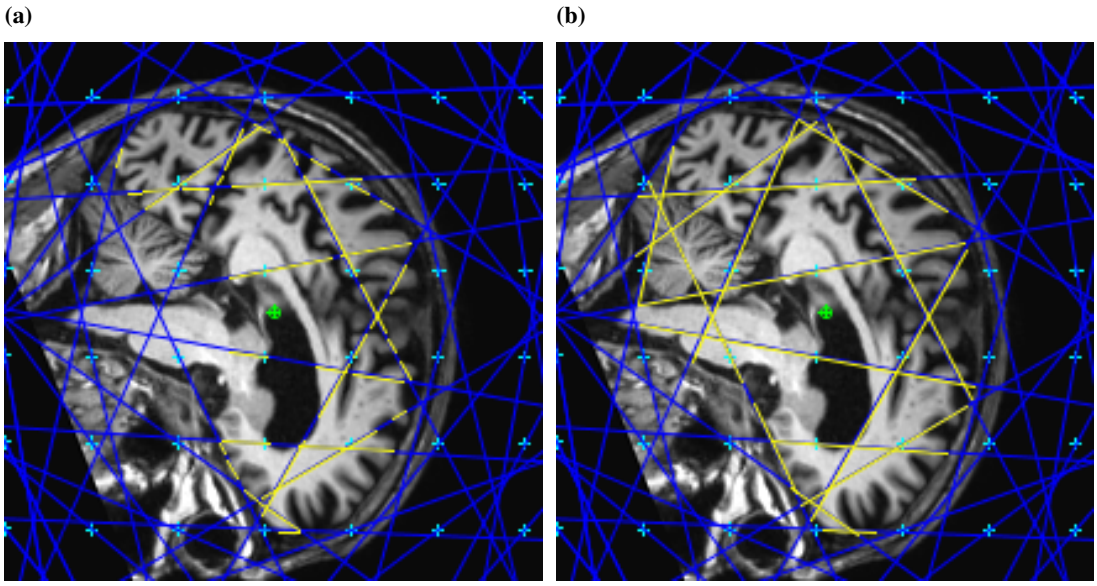

Figure 8.1: Estimation of (a) cerebral and (b) intra-cranial volumes by the INV method on one IR rotated section plane of one AD brain MR image.

groups on volume changes (intercepts) and interaction between ageing and groups (differences of slopes between the AD and the health groups).[4]

In manual estimation by the INV method, the cerebral volumes (excluding ventricles, this measure was the same as that in Chapter 7 but had different subjects recruited), the intra-cranial volumes and the volume ratios of cerebrum to intra-cranium were all compared between the AD and the health groups. Besides, the mean values were compared with those obtained from FREESURFER software.

For both FREESURFER and the INV method analyses, one-tailed two samples t-tests were performed and the null hypothesis to be examined was that the volumes of each tested brain structures or the volume ratios of brain structures to the brain or the intra-cranium obtained by either of the approaches in AD patients was no less (or greater) than those from the healthy elderly controls. All the statistical calculation and graphs drawing were performed by R software.

8.3 Results

8.3.1 FREESURFER Volumetry

For all the subjects, the FREESURFER volume analysis showed that the intracranial volumes of the AD patients were not significantly bigger than those of the healthy elderly subjects ($p = 0.054$) while the brain volumes (including ventricles) were not significantly smaller in AD ($p = 0.054$). Both the brain and the intracranial volumes increased in older people in both

[4] http://r-eco-evo.blogspot.co.uk/2011/08/comparing-two-regression-slopes-by.html

the healthy and AD groups while there was no significant difference between the slopes in the health and AD groups (Table 8.2, Figure 8.2, 8.3).

Table 8.2: Columns: names of measured structures, the mean volumes (cm^3) in both the AD and the health groups, p values by t-test (one-tailed less) between the two groups, and p values by ANCOVA for the effects by age, group and the interaction between age and group. Rows: 'SupraTentorialNotVent' includes cerebrum and excludes cerebellum, brainstem and ventricles; 'BrainSegVol' includes the whole brain above brain stem, ventricles and CSF; 'EstimatedTotalIntraCranialVol' estimates total intracranial volume.

Structures	Mean Volumes		T-Test (P Value)	ANCOVA (P Value)		
	Alzheimer	HealthyEld	1-Tailed Less	Age	Group	Age:Group
	cm^3		AD/HV	(slope)	(intercept)	(slope diff)
SupraTentorialVolNotVent	831.21	905.71	0.002	0.260	0.010	0.346
BrainSegVol	1006.70	1053.37	0.054	0.435	0.138	0.869
EstimatedTotalIntraCranialVol	1485.79	1386.60	0.946	0.058	0.089	0.440

The volume ratios of brain (with and without ventricles), supratentorial space (with and without ventricles) and brainstem to the intracranial space were significantly smaller in AD than those in health ($p < 0.01$). The descending trend of volume ratios of both the brain and supratentorial space to the intracranial space in older people in AD group were not significantly slower than those in health group. Meanwhile, the brainstem proportion decreased by ageing in AD but increased in health, however, the difference was not statistically significant (Table 8.3, Figure 8.2).

Table 8.3: Columns: the mean ratios (in percentage) in both the AD and the health groups, p values by t-test (one-tailed less) between the two groups, and p values by ANCOVA for the effects by age, group and the interaction between age and group. Rows (volume ratios to the intracranial volumes): brain (with and without ventricles), supratentorial (with and without ventricles) and brainstem.

Structures	Mean Ratio		T-Test (P Value)	ANCOVA (P Value)		
To	Alzheimer	HealthyEld	1-Tailed Less	Age	Group	Age:Group
IntraCranialVol	%		AD/HV	(slope)	(intercept)	(slope diff)
BrainSegVol	67.69	76.59	0.000	0.236	0.000	0.536
BrainSegVolNotVent	64.28	74.54	0.000	0.134	0.000	0.620
SupraTentorialVol	59.01	67.55	0.000	0.406	0.000	0.804
SupraTentorialVolNotVent	55.99	65.82	0.000	0.226	0.000	0.874
Brain.Stem	1.35	1.46	0.009	0.880	0.016	0.344

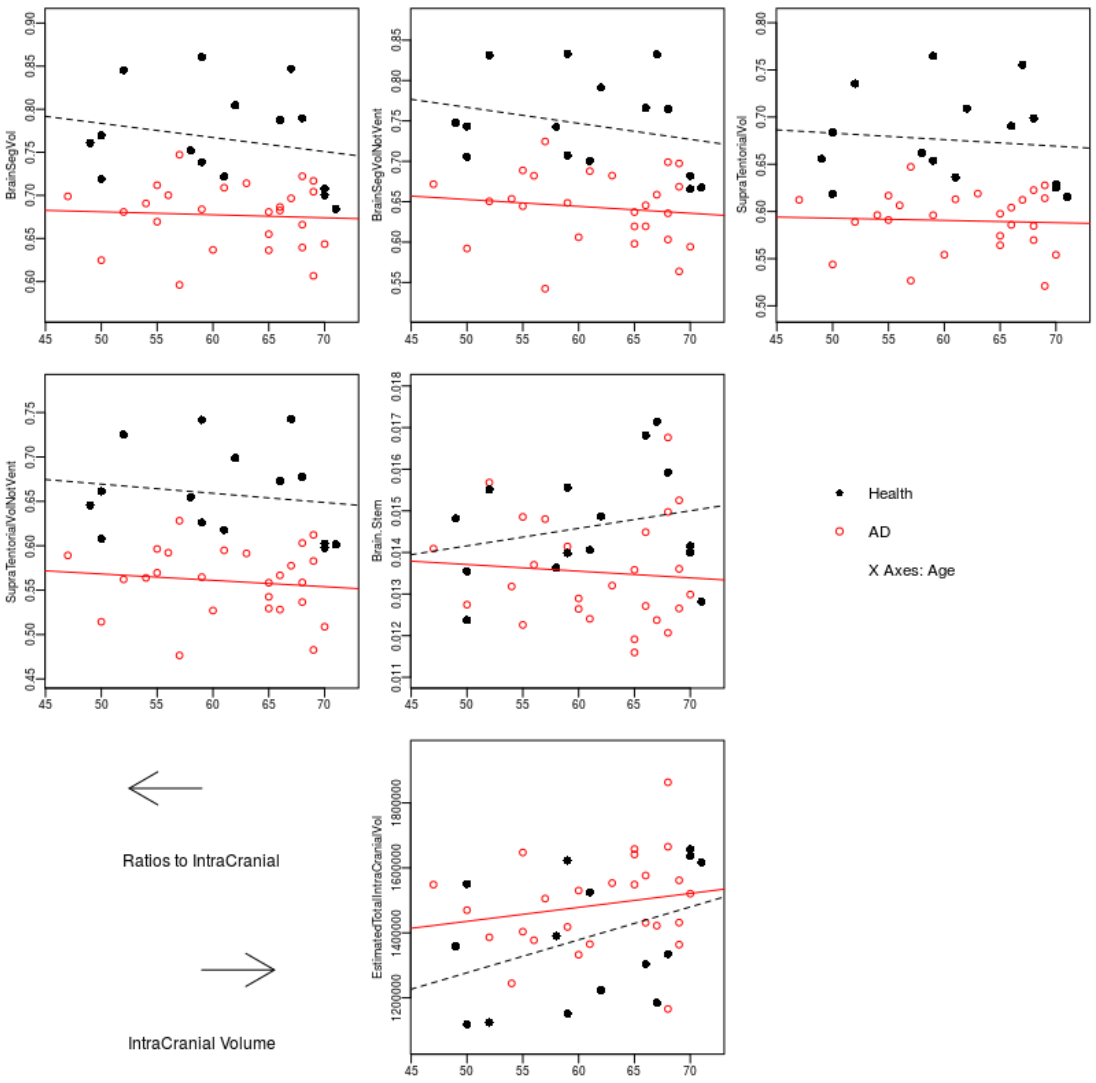

Figure 8.2: Volume ratios changes by ageing in both the AD patients and the healthy elderly subjects. The first five images (before leftwards arrow): the ratios of brain (with and without ventricles) volumes, supratentorial (with and without ventricles) volumes and brainstem volumes to the intracranial volumes. The last image (after rightwards arrow): the intracranial volumes.

The volume ratios of cortical grey matter (left, right and total) to brain (with ventricles) in AD were significantly smaller than those in health ($p < 0.01$) while the volume ratios of subcortical and total grey matter to brain were not significantly smaller. There were also significant differences in the volume ratio changes by ageing of the right cortex, total cortex and total grey matter between AD and health ($p < 0.05$), but the changes of volume ratios were not significantly different in either left cortex or subcortical grey matter (Table 8.4, Figure 8.3).

The volume ratios of cerebral white matter (left, right and total) to the brain were also significantly smaller in AD ($p < 0.05$). The volume ratios decreased by ageing in AD but increased in health, and the differences were significant in all the ratios of left, right and total cerebral white matter to the brain ($p < 0.05$) (Table 8.4, Figure 8.3).

For the subcortical structures in both left and right hemispheres, the volume ratios of hippocampus, amygdala and accumbens to brain (including ventricles) were all significantly smaller in AD than those in health ($p < 0.01$). The ratios of pallidum and ventral diencephalon to the brain were significantly bigger in AD ($p < 0.01$). The left putamen ratio was significantly smaller in AD ($p = 0.037$) but the right putamen ratio was not ($p = 0.064$). There were no significant differences in thalamus and caudate volume ratios between the two groups. As age grew, the changes of the volume ratios of all the above subcortical structures in both the hemispheres were similar in both the AD and the health groups (Table 8.4, Figure 8.4).

For the corpus callosum, both the middle-anterior and middle-posterior parts had significant smaller volume ratios to the brain (including ventricles) in AD than those in health ($p < 0.05$). The atrophy trends of corpus callosum ratios by ageing were close to each other between both the groups (Table 8.4, Figure 8.5).

The volume ratios of cerebellar cortex in both the left and right hemispheres were significantly bigger in AD than those in health ($p < 0.05$). However, the ratios differences were not significant in the cerebellar white matter. The negative correlations of cerebellar cortex volume ratios with ageing in both the hemispheres were significantly apparent in the health group ($p < 0.05$) while the correlations were similar in cerebellar white matter volume ratios changes with ageing (Table 8.4, Figure 8.6).

The volume ratios of all the ventricles except for the 4th and 5th ventricles (i.e. lateral ventricles (left and right), inferior lateral ventricles (or inf-lat-vent, left and right, in the medial temporal lobe or known as the temporal horn) and the 3rd ventricle) and CSF to the brain (with ventricles) were significantly bigger in AD than those in health ($p < 0.01$). The 5th ventricle volume ratio to brain became bigger by ageing in health controls but smaller in AD patients, and the difference was statistically significant ($p < 0.05$). The volume ratios of all the other ventricles and CSF kept on growing bigger in similar rates by ageing in both the groups (Table 8.4, Figure 8.7).

The volume ratios of both the left and right choroid plexus to the brain (with ventricles) were significantly bigger in AD than those in health ($p < 0.01$). No volume ratios differences of left and right vessels were found between the two groups. The correlations of volume ratios of choroid plexus and vessels in both the hemispheres to the brain with ageing were similar between the two groups (Table 8.4, Figure 8.8).

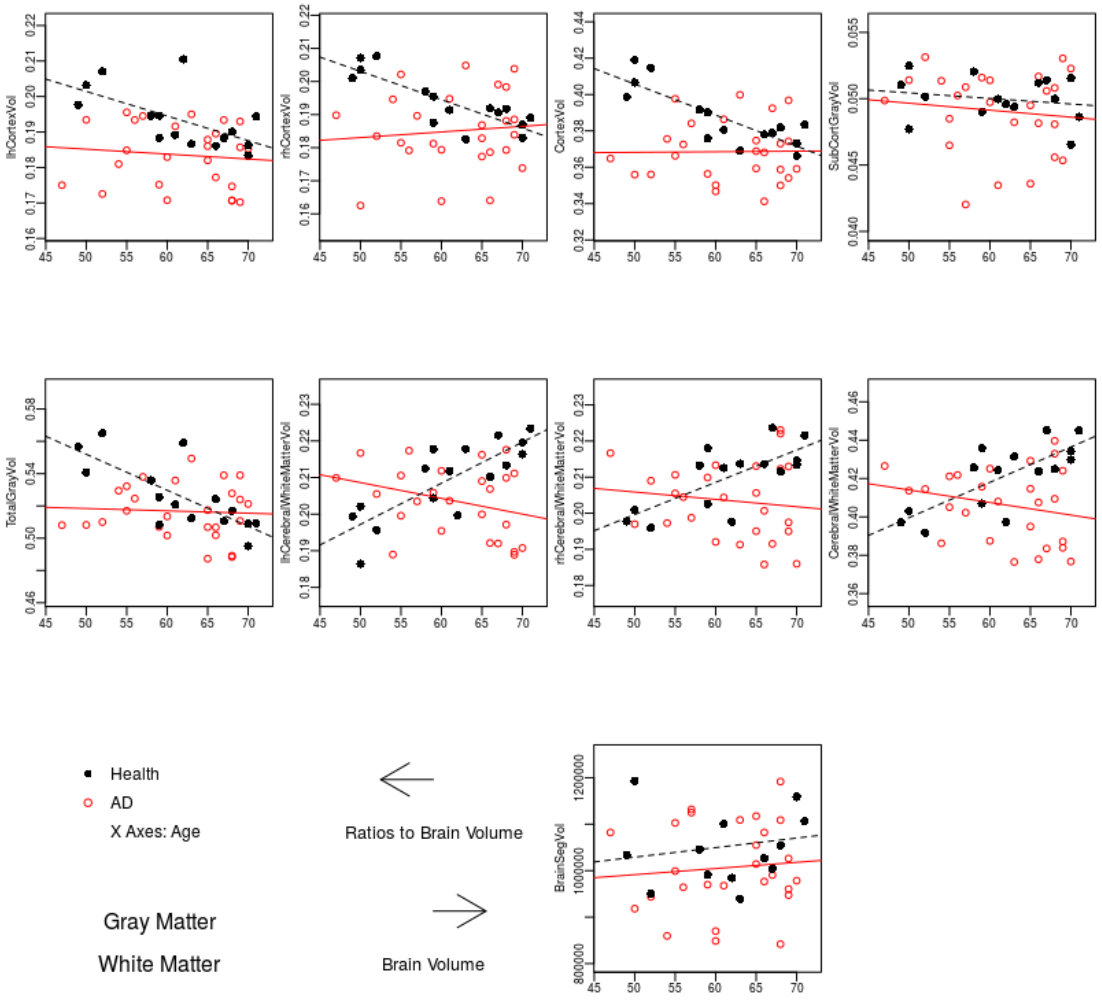

Figure 8.3: Changes of volume ratios of grey and white matter to the brain by ageing in both the AD patients and the healthy elderly subjects. The first five images: the ratios of grey matter (left cortex, right cortex, cortex, subcortical grey and total grey) volumes to the brain (with ventricles) volumes. The following three images: the ratios of white matter (left, right and total cerebral white) volumes to the brain (with ventricles) volumes. The last image: the brain (with ventricles) volumes.

Table 8.4: Columns: the mean ratios (in percentage) in the AD and the health groups, p values by t-test (one-tailed less and one-tailed greater) between the two groups, and p values by ANCOVA for the effects by age, group and the interaction between age and group. Rows (Volume ratios to the brain (with ventricles) volumes): structures from the 'aseg.stats' files in the FREESURFER volume analyses. Sig.: significance, $* < 0.05, ** < 0.01, *** < 0.001$.

Structures (left or right)	Mean Volume Ratio		T-Test (P Value)				ANCOVA (P Value)					
To	Alzheimer	HealthyEld	1-Tailed Less		1-Tailed Greater		Age		Group		Age:Group	
BrainSegVol	%		AD/HV	Sig.	AD/HV	Sig.	(slope)	Sig.	(intercept)	Sig.	(slope diff)	Sig.
Left.Lateral.Ventricle	1.99	1.14			0.000	***	0.060		0.000	***	0.801	
Left.Inf.Lat.Vent	0.13	0.05			0.000	***	0.034	*	0.000	***	0.388	
Left.Cerebellum.White.Matter	1.35	1.31	0.866		0.134		0.022	*	0.218		0.960	
Left.Cerebellum.Cortex	4.84	4.50			0.011	*	0.054		0.003	**	0.019	*
Left.Thalamus.Proper	0.60	0.59	0.819		0.181		0.371		0.373		0.170	
Left.Caudate	0.33	0.33	0.320		0.680		0.263		0.577		0.429	
Left.Putamen	0.43	0.45	0.037	*			0.662		0.067		0.865	
Left.Pallidum	0.17	0.16			0.002	**	0.292		0.008	**	0.625	
X3rd.Ventricle	0.23	0.15			0.000	***	0.035	*	0.000	***	0.854	
X4th.Ventricle	0.20	0.18	0.916		0.084		0.184		0.248		0.332	
Brain.Stem	1.98	1.93	0.910		0.090		0.551		0.220		0.130	
Left.Hippocampus	0.31	0.34	0.002	**			0.109		0.008	**	0.649	
Left.Amygdala	0.12	0.14	0.000	***			0.236		0.001	**	0.677	
CSF	0.15	0.10			0.000	***	0.920		0.000	***	0.563	
Left.Accumbens.area	0.03	0.04	0.002	**			0.436		0.002	**	0.100	
Left.VentralDC	0.38	0.36			0.001	**	0.452		0.006	**	0.499	
Left.vessel	0.01	0.01	0.478		0.522		0.472		0.936		0.145	
Left.choroid.plexus	0.15	0.12			0.001	**	0.120		0.003	**	0.598	
Right.Lateral.Ventricle	1.89	0.93			0.000	***	0.031	*	0.000	***	0.562	
Right.Inf.Lat.Vent	0.12	0.05			0.000	***	0.276		0.000	***	0.795	
Right.Cerebellum.White.Matter	1.34	1.28	0.917		0.083		0.137		0.140		0.367	
Right.Cerebellum.Cortex	4.85	4.57			0.026	*	0.090	*	0.013	*	0.032	*
Right.Thalamus.Proper	0.58	0.58	0.433		0.567		0.435		0.922		0.286	
Right.Caudate	0.34	0.34	0.425		0.575		0.189		0.771		0.907	
Right.Putamen	0.42	0.44	0.064		0.936		0.664		0.130		0.287	
Right.Pallidum	0.18	0.16			0.000	***	0.689		0.003	**	0.693	
Right.Hippocampus	0.32	0.36	0.000	***			0.319		0.000	***	0.257	
Right.Amygdala	0.14	0.16	0.000	***			0.385		0.001	**	1.000	
Right.Accumbens.area	0.04	0.05	0.001	**			0.207		0.002	**	0.855	
Right.VentralDC	0.37	0.35			0.000	***	0.869		0.002	**	0.716	
Right.vessel	0.01	0.01	0.522		0.478		0.650		0.977		0.639	
Right.choroid.plexus	0.14	0.12			0.004	**	0.027	*	0.010	*	0.480	
X5th.Ventricle	0.00	0.00	0.829		0.171		0.890		0.319		0.048	*
Optic.Chiasm	0.02	0.02	0.907		0.093		0.225		0.177		0.330	
CC_Posterior	0.09	0.09	0.600		0.400		0.353		0.855		0.827	
CC_Mid_Posterior	0.03	0.04	0.032	*			0.027	*	0.042	*	0.141	
CC_Central	0.03	0.04	0.107		0.893		0.076		0.245		0.447	
CC_Mid_Anterior	0.04	0.04	0.030	*			0.047	*	0.053		0.150	
CC_Anterior	0.08	0.08	0.169		0.831		0.476		0.358		0.943	
BrainSegVolNotVent	94.98	97.20	0.000	***			0.086		0.000	***	0.891	
lhCortexVol	18.35	19.33	0.001	**			0.069		0.001	**	0.166	
rhCortexVol	18.50	19.37	0.004	**			0.172		0.013	*	0.029	*
CortexVol	36.86	38.72	0.001	**			0.020	*	0.001	**	0.013	*
lhCerebralWhiteMatterVol	20.36	20.95	0.040	*			0.234		0.029	*	0.000	***
rhCerebralWhiteMatterVol	20.35	21.01	0.020	*			0.291		0.035	*	0.018	*
CerebralWhiteMatterVol	40.64	42.11	0.009	**			0.393		0.010	*	0.003	**
SubCortGreyVol	4.91	5.00	0.114		0.886		0.431		0.300		0.931	
TotalGreyVol	51.67	52.60	0.078		0.922		0.013	*	0.083		0.010	**
SupraTentorialVol	87.19	88.06	0.006	**			0.092		0.003	**	0.055	
SupraTentorialVolNotVent	82.71	85.75	0.000	***			0.414		0.000	***	0.372	

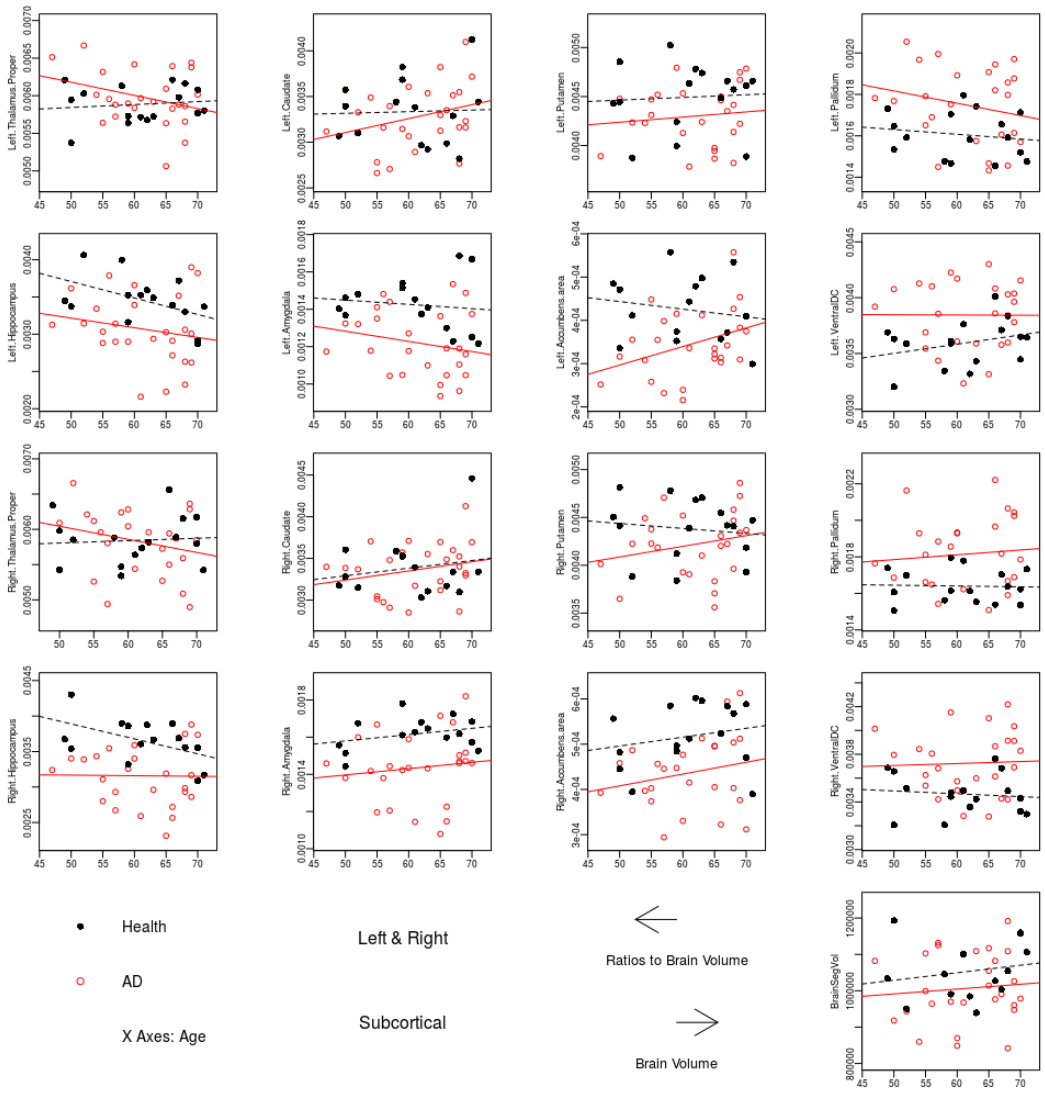

Figure 8.4: Changes of volume ratios of subcortical structures to the brain by ageing in both the AD patients and the healthy elderly subjects. The sturctures included thalamus, caudate, putamen, pallidum, hippocampus, amygdala, accumbens and ventral diencephalon, which were divided into the left hemisphere (the first eight images in order) and the right hemisphere (the following eight images in order). The last image: the brain (including ventricles) volumes.

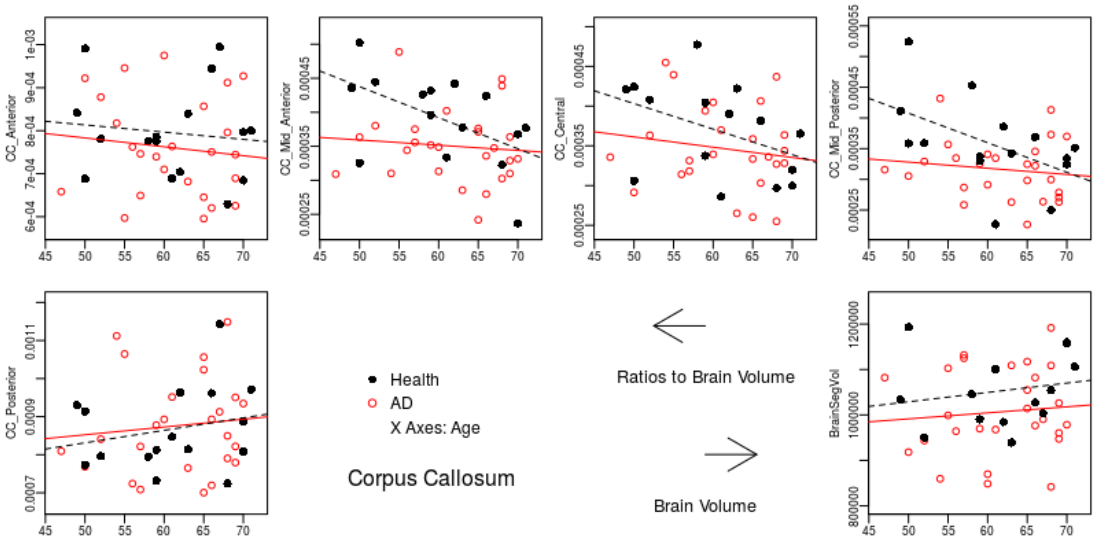

Figure 8.5: Changes of volume ratios of corpus callosum to the brain by ageing in both the AD patients and the healthy elderly subjects. The first five images: volume ratios of anterior, middle-anterior, central, middle-posterior and posterior parts of corpus callosum. The last image: the brain (with ventricles) volumes.

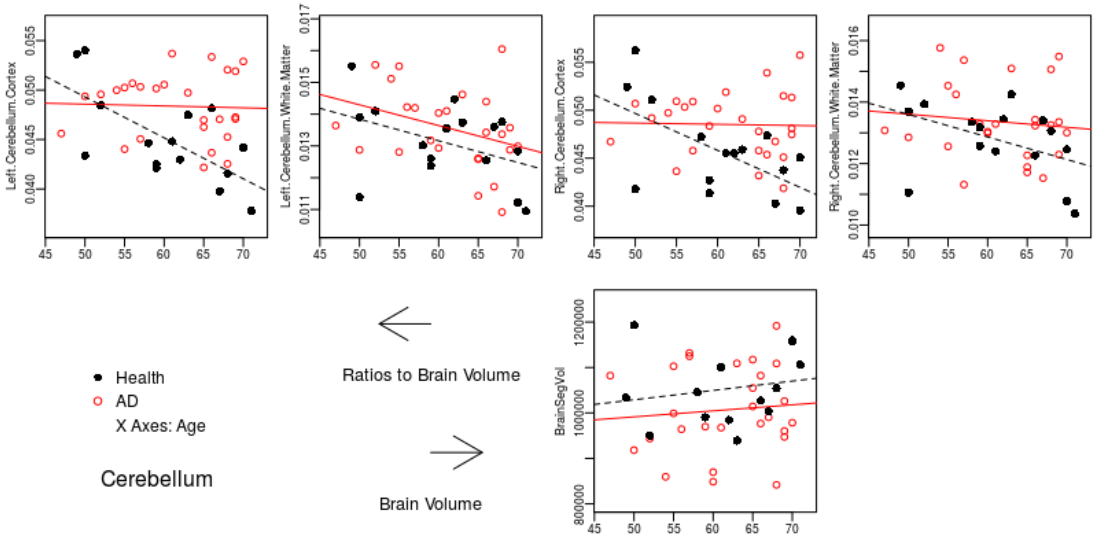

Figure 8.6: Changes of volume ratios of cerebellum to the brain by ageing in both the AD patients and the healthy elderly subjects. The first four images: volume ratios of left cerebellar cortex, left cerebellar white matter, right cerebellar cortex and right cerebellar white matter. The last image: the brain (with ventricles) volumes.

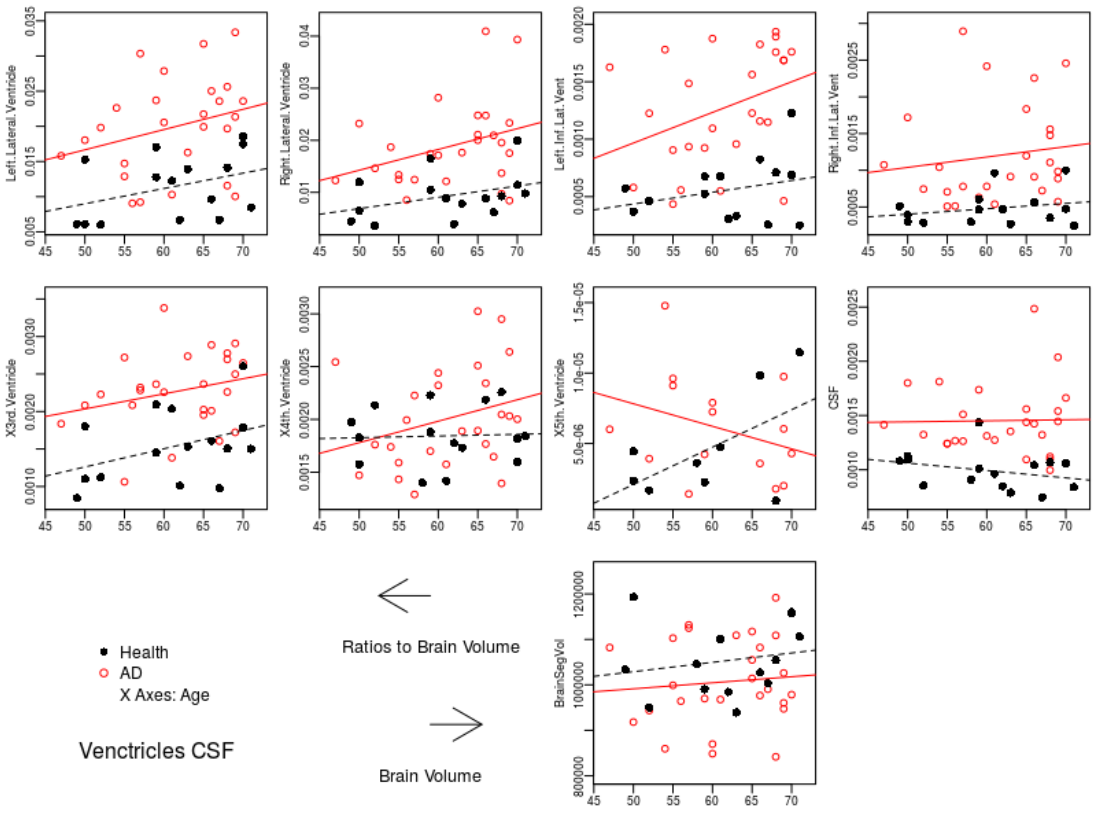

Figure 8.7: Changes of volume ratios of ventricles and CSF to the brain by ageing in both the AD patients and the healthy elderly subjects. The first eight images: volume ratios of left lateral ventricle, right lateral ventricle, left-inf-lat-vent, right-inf-lat-vent, 3rd ventricle, 4th ventricle, 5th ventricle and CSF. The last image: the brain (including ventricles) volumes.

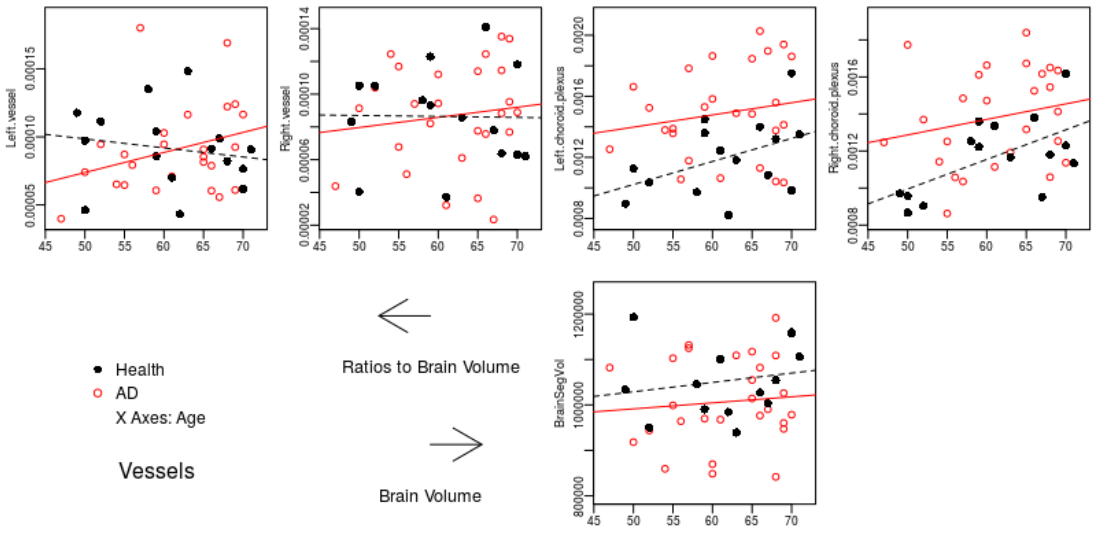

Figure 8.8: Changes of volume ratios of vessels to the brain by ageing in both the AD patients and the healthy elderly subjects. The first four images: volume ratios of left vessel, right vessel, left choroid plexus and right choroid plexus. The last image: the brain (with ventricles) volumes.

Specifically, in the hippocampal subfields, the volume ratios of left fimbria to the whole left hippocampus, right fimbria and right molecular layer HP to the whole right hippocampus were significantly smaller in AD than those in health ($p < 0.05$). On the other hand, the ratios of left hippocampal fissure, left CA3 and left CA4 to the left hippocampus and right hippocampal fissure to the right hippocampus were significantly bigger in AD ($p < 0.01$). The changes of the volume ratios by ageing were mostly similar in both the AD and the health groups, except that the ratios of left fimbria and left HATA to the left hippocampus got smaller in AD but bigger in health, and the ratio of right presubiculum to the right hippocampus got bigger in AD but smaller in health. The differences of the last three ratios changes were all statistically significant ($p < 0.05$) (Table 8.5, Figure 8.9).

Table 8.5: Columns: the mean ratios (in percentage) in the AD and the health groups, p values by t-test (one-tailed less and one-tailed greater) between the two groups, and p values by ANCOVA for the effects by age, group and the interaction between age and group. Rows (Volume ratios to the whole hippocampus in left and right respectively): subfields from the '?h.hippoSfVolumes-T1.v10.txt' files in the FREESURFER 6.0Beta volume analyses. Sig.: significance, $* < 0.05$.

Structures in the side of	Mean Volume Ratio		T-Test (P Value)				ANCOVA (P Value)					
left to left_Whole_hippocampus	Alzheimer	HealthyEld	1-Tailed Less		1-Tailed Greater		Age		Group		Age:Group	
right to right_Whole_hippocampus	%		AD/HV	Sig.	AD/HV	Sig.	(slope)	Sig.	(intercept)	Sig.	(slope diff)	Sig.
left_Hippocampal_tail	15.53	16.14	0.124		0.876		0.370		0.282		0.671	
left_subiculum	12.43	12.83	0.052		0.948		0.912		0.117		0.718	
left_CA1	18.80	18.36	0.938		0.062		0.167		0.141		0.400	
left_hippocampal_fissure	6.41	5.28			0.000	***	0.025	*	0.000	***	0.857	
left_presubiculum	9.06	9.16	0.305		0.695		0.647		0.620		0.827	
left_parasubiculum	1.92	1.81	0.838		0.162		0.724		0.376		0.690	
left_molecular_layer_HP	16.10	16.20	0.202		0.798		0.180		0.435		0.354	
left_GC.ML.DG	8.42	8.32	0.825		0.175		0.062		0.379		0.387	
left_CA3	6.33	5.73			0.001	**	0.502		0.008	**	0.650	
left_CA4	7.45	7.16			0.008	**	0.007	**	0.016	*	0.573	
left_fimbria	2.06	2.58	0.002	**			0.017	*	0.005	**	0.015	*
left_HATA	1.72	1.82	0.077		0.923		0.913		0.120		0.016	*
left/right_Whole_hippocampus	95.89	94.29	0.801		0.199		0.058		0.362		0.609	
right_Hippocampal_tail	15.76	16.08	0.271		0.729		0.392		0.578		0.815	
right_subiculum	11.90	12.06	0.212		0.788		0.811		0.459		0.532	
right_CA1	19.03	19.06	0.446		0.554		0.575		0.862		0.658	
right_hippocampal_fissure	6.39	5.17			0.000	***	0.128		0.000	***	0.351	
right_presubiculum	8.35	8.17	0.829		0.171		0.572		0.335		0.011	*
right_parasubiculum	1.86	1.75	0.928		0.072		0.854		0.202		0.626	
right_molecular_layer_HP	16.12	16.37	0.034	*			0.664		0.087		0.523	
right_GC.ML.DG	8.67	8.67	0.502		0.498		0.080		0.897		0.318	
right_CA3	6.76	6.50	0.885		0.115		0.401		0.250		0.390	
right_CA4	7.62	7.47	0.914		0.086		0.019	*	0.197		0.980	
right_fimbria	1.93	2.24	0.042	*			0.021	*	0.083		0.987	
right_HATA	1.77	1.85	0.077		0.923		0.489		0.239		0.889	
right/left_Whole_hippocampus	104.90	106.31	0.263		0.737		0.048	*	0.469		0.616	

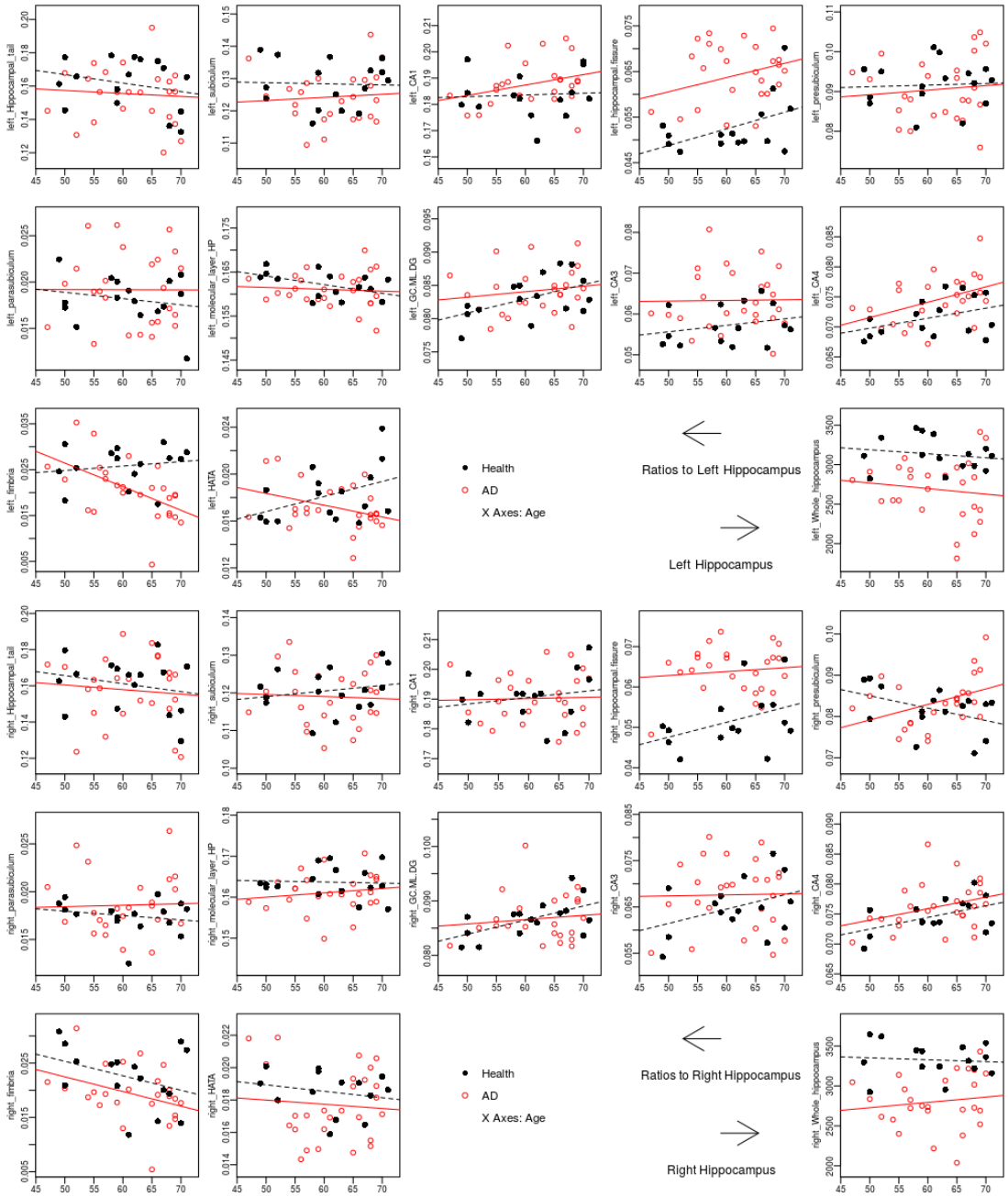

Figure 8.9: Changes of volume ratios of hippocampal subfields to the respective left or right whole hippocampus by ageing in both the AD patients and the healthy elderly subjects. The subfields included hippocampal tail, subiculum, CA1, hippocampal fissure, presubiculum, parasubiculum, molecular layer HP, GC-ML-DG, CA3, CA4, fimbria and HATA, which were divided into the left hemisphere (the first 12 images in order) plus one image for the volume of the left hippocampus, and the right hemisphere (the following 12 images in order) plus one image for the volume of the right hippocampus.

Lastly, in the brainstem subfields, only pons had significant smaller volume ratios to the whole brainstem in AD than that in health ($p < 0.05$). There were no significant difference of volumes ratios in the other brainstem subfields (i.e. medulla, superior cerebellar peduncle (SCP) and midbrain) between the two groups. The correlations of volume ratios changes with ageing were similar in all the four brainstem subfields between AD and health groups (Table 8.6, Figure 8.10).

Table 8.6: Columns: the mean ratios (in percentage) in the AD and the health groups, p values by t-test (one-tailed less and one-tailed greater) between the two groups, and p values by ANCOVA for the effects by age, group and the interaction between age and group. Rows (Volume ratios to the whole brainstem): medulla, pons, SCP and midbrain, which were all from the 'brainstemSsVolumes.v10.txt' files in the FREESURFER 6.0Beta volume analyses.

Structures	Mean Volume Ratio		T-Test (P Value)		ANCOVA (P Value)		
To	Alzheimer	HealthyEld	1-Tailed Less	1-Tailed Greater	Age	Group	Age:Group
Whole_brainstem	%		AD/HV		(slope)	(intercept)	(slope diff)
Medulla	18.30	18.04	0.814	0.186	0.198	0.323	0.546
Pons	56.32	57.01	0.013		0.080	0.017	0.248
SCP	1.00	0.98	0.695	0.305	0.240	0.527	0.712
Midbrain	24.35	24.08	0.893	0.107	0.457	0.250	0.214

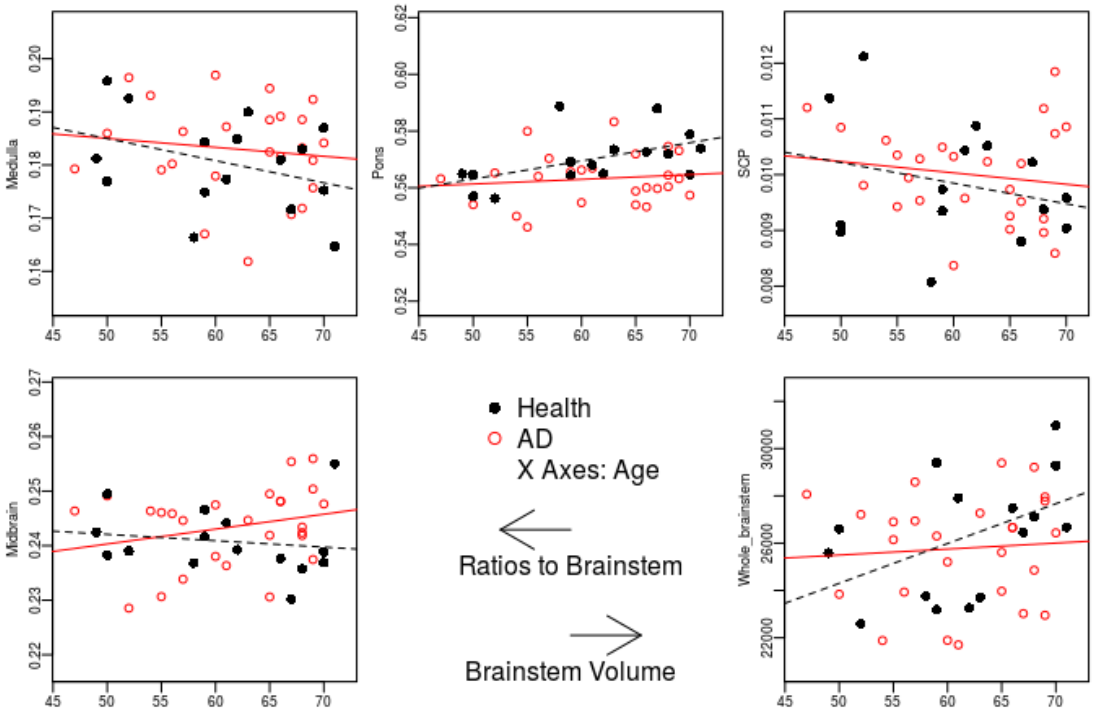

Figure 8.10: Changes of volume ratios of brainstem subfields to the whole brainstem by ageing in both the AD patients and the healthy elderly subjects. The first four images: volume ratios of medulla, pons, SCP and midbrain. The last image: the whole brainstem volumes.

8.3.2 The INVARIATOR Volumetry

The volumes and volume ratios obtained using the INV method are shown below (Table 8.7). The volume ratio of cerebrum to intra-cranium was significantly smaller in the AD group than that in the health group ($p < 0.01$). There were no significant difference of the cerebral and the intra-cranial volumes between the two groups. The means of volume ratios estimated by the INV method were around 10% bigger in both the groups than those obtained in FREESURFER (Figure 8.11, 8.12).

Table 8.7: The cerebral volume, the intra-cranial volume and the volume ratio of cerebrum to intra-cranium in both the AD and the health groups measured by the INV method.

Alzheimer's Disease				Healthy Elderly Subjects			
ID	Cerebral Volume cm^3	Intracranial Volume cm^3	Ratio	ID	Cerebral Volume cm^3	Intracranial Volume cm^3	Ratio
MRM_003	1347	1548	0.870	HV_AB	1358	1624	0.836
MRM_005	670	1195	0.561	HV_AE	750	1328	0.565
MRM_007	816	1591	0.513	HV_AK	1088	1347	0.807
MRM_018	707	1753	0.403	HV_DK	885	1041	0.850
MRM_030	1477	1781	0.829	HV_GH	1002	1364	0.735
MRM_032	733	998	0.735	HV_GJ	970	1235	0.786
MRM_039	736	1158	0.635	HV_GK	1140	1878	0.607
MRM_046	1160	1605	0.722	HV_HJ	1618	1902	0.850
MRM_049	741	1500	0.494	HV_KCM	1104	1293	0.854
MRM_054	753	930	0.810	HV_PJ	807	1345	0.600
MRM_055	779	1573	0.495	HV_003	1006	1376	0.731
MRM_063	934	1696	0.551	HV_008	657	1035	0.634
MRM_065	1076	1488	0.723	HV_010	885	1320	0.670
MRM_069	652	948	0.687	HV_013	1401	1794	0.781
MRM_082	657	904	0.727	HV_014	747	825	0.905
MRM_084	1129	1630	0.693	HV_015	732	1325	0.553
MRM_089	800	1430	0.559				
MRM_099	896	1668	0.537				
MRM_100	903	1579	0.572				
MRM_105	837	1067	0.784				
MRM_109	1498	1818	0.824				
MRM_112	771	1484	0.520				
MRM_115	965	1756	0.550				
MRM_116	896	1479	0.606				
MRM_118	636	1239	0.513				
MRM_121	727	1457	0.499				
MRM_124	623	1323	0.471				

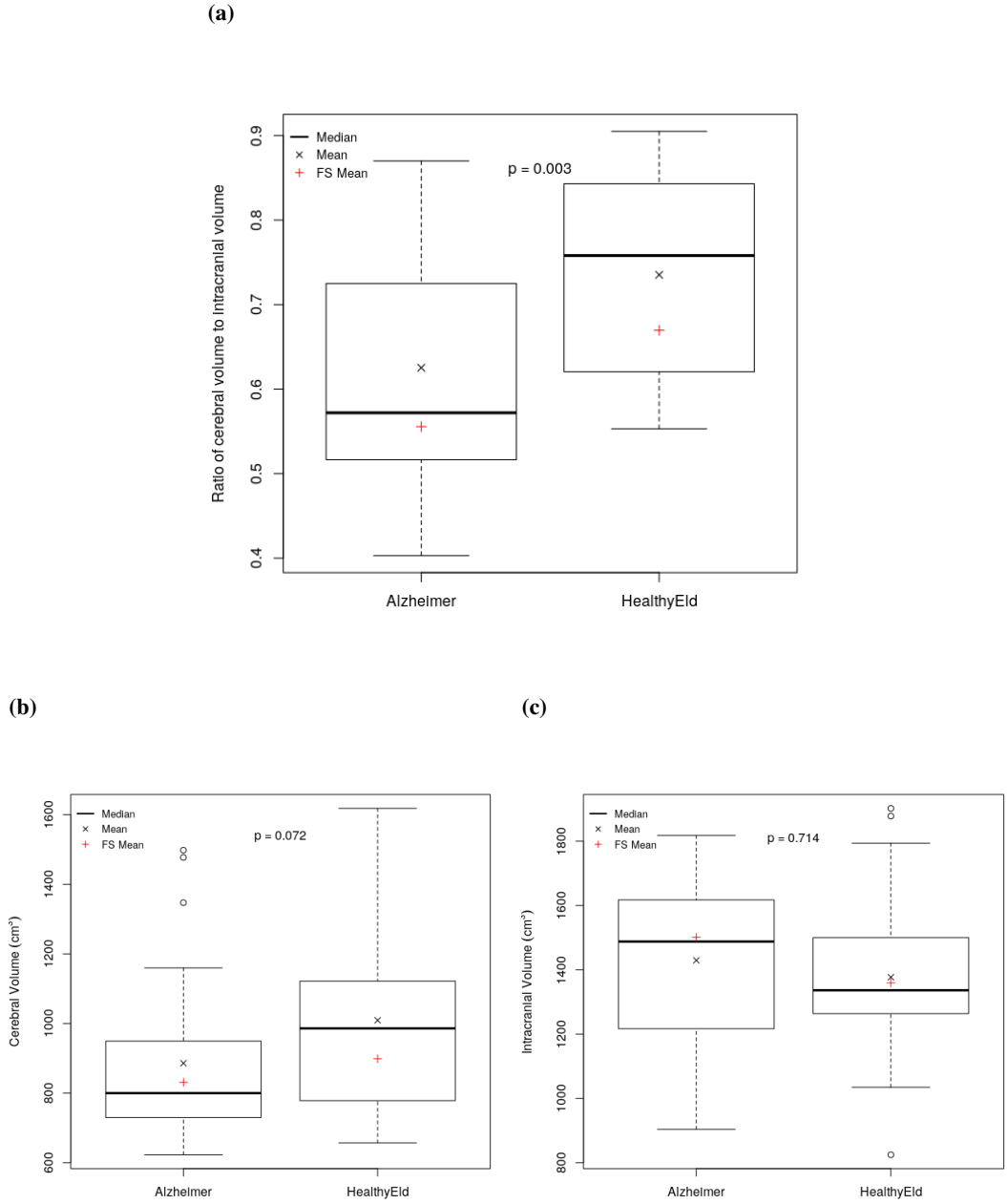

Figure 8.11: (a) the volume ratio of cerebrum to intra-cranium, (b) the cerebral volume and (c) the intra-cranial volume in both the AD and health groups measured by the INV method. The red crosses are the mean values in each group measured by FREESURFER, which are added as references.

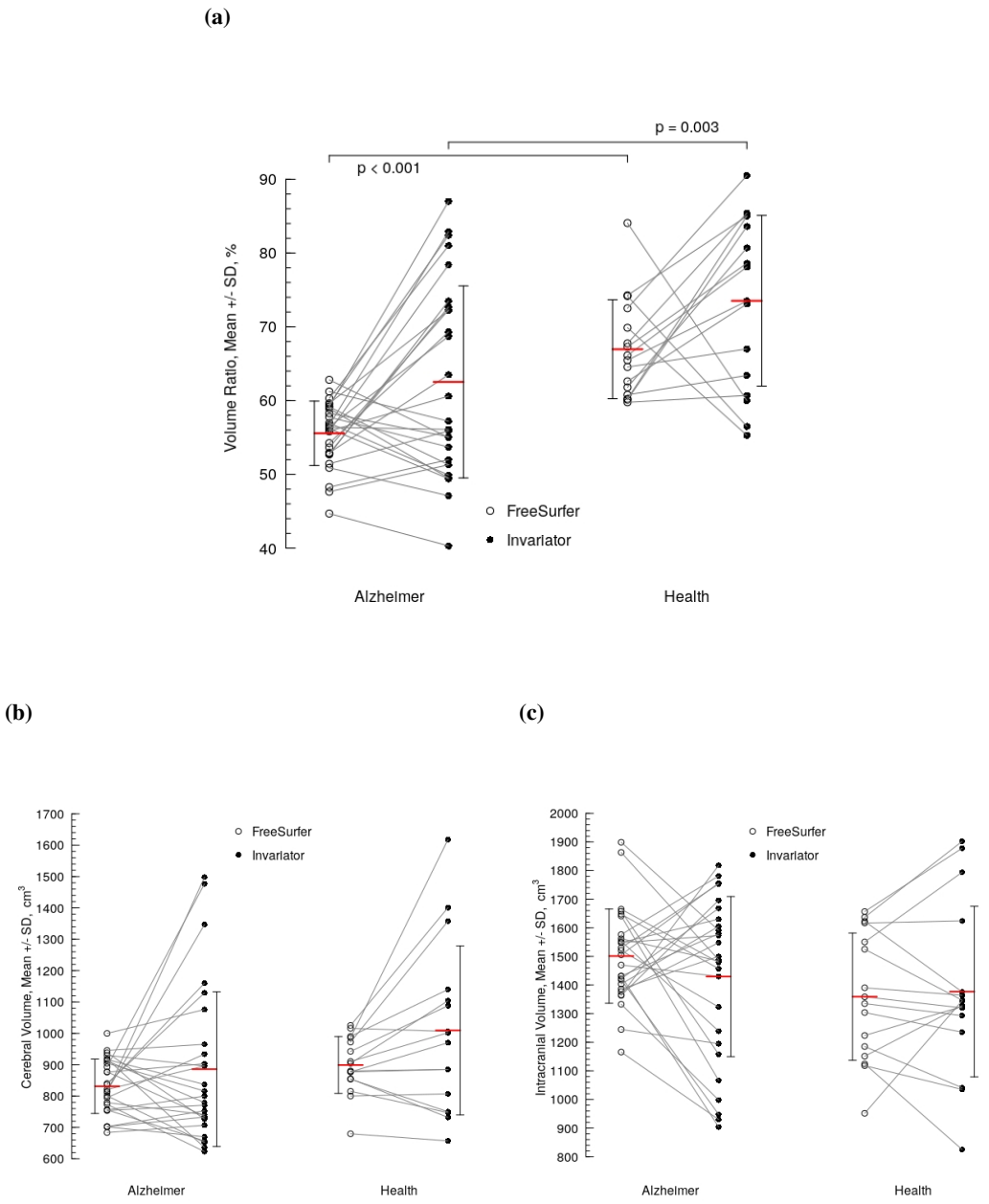

Figure 8.12: Paired comparison between results obtained from FREESURFER and the INV method. (a) Ratios of cerebral volumes to intra-cranial volumes in both the AD and health groups; (b) cerebral volumes in both the AD and health groups; (c) intra-cranial volumes in both the AD and health groups. Mean (red horizontal bars) and SD values are displayed in each group.

8.4 Discussion

The comparison of absolute volume of each brain region is influenced by inter-individual difference, which can hide the significance of difference between groups. Using volume ratios of each brain region to whole brain can be an option to investigate ageing-related brain shrinkage in AD patients.

In summary, we observed the following volume ratio indices from FREESURFER which showed difference between AD patients and healthy controls in Table 8.8.

Table 8.8: Volume ratios difference between AD patients and healthy controls ($* < 0.05$).

Numerator of Ratio	Denominator of Ratio	AD < Health	AD > Health
brain (with or without ventricles)	intracranial space	*	
supratentorial space (with or without ventricles)	intracranial space	*	
brainstem	intracranial space	*	
cortical grey matter (left, right, total)	brain (with ventricles)	*	
cerebral white matter (left, right, total)	brain (with ventricles)	*	
hippocampus (left, right)	brain (with ventricles)	*	
amygdala (left, right)	brain (with ventricles)	*	
accumbens (left, right)	brain (with ventricles)	*	
pallidum (left, right)	brain (with ventricles)		*
ventral diencephalon (left, right)	brain (with ventricles)		*
putamen (left)	brain (with ventricles)	*	
corpus callosum (middle-anterior, middle-posterior)	brain (with ventricles)	*	
cerebellar cortex (left, right)	brain (with ventricles)		*
lateral ventricle (left, right)	brain (with ventricles)		*
inf-lat-vent (left, right)	brain (with ventricles)		*
3rd ventricle	brain (with ventricles)		*
CSF	brain (with ventricles)		*
choroid plexus (left, right)	brain (with ventricles)		*
fimbria (left)	hippocampus (left)	*	
fimbria (right)	hippocampus (right)	*	
molecular layer HP (right)	hippocampus (right)	*	
hippocampal fissure (left)	hippocampus (left)		*
CA3 (left)	hippocampus (left)		*
CA4 (left)	hippocampus (left)		*
hippocampal fissure (right)	hippocampus (right)		*
pons	brainstem	*	

We also observed the following ratio indices in Table 8.9, showing difference of volume ratios changes associated with ageing between AD patients and healthy elderly subjects.

Our results indicate that the volume ratios of most brain parenchyma tissues (e.g. cerebral cortical grey matter, cerebral white matter and hippocampus) to the brain are smaller in AD patients than healthy elderly subjects. Meanwhile, the ratios of some brain regions (especially the ventricles) to the brain are bigger in AD patients.

Besides, our results also indicate that the volume shrinkage pattern with ageing in several brain regions can be altered in AD patients in comparison with healthy elderly subjects. How-

Table 8.9: Difference of volume ratios changes associated with ageing between AD patients and healthy elderly subjects.

Numerator of Vol Ratio	Denominator of Vol Ratio
cortex (right, total)	brain (including ventricles)
grey matter (total)	brain (including ventricles)
cerebral white matter (left, right, total)	brain (including ventricles)
cerebellar cortex (left, right)	brain (including ventricles)
5th ventricle	brain (including ventricles)
fimbria (left)	hippocampus (left)
HATA (left)	hippocampus (left)
presubiculum (right)	hippocampus (right)

ever, the changes of the ageing-related atrophy progression pattern do not happen to all of the regions which already showed difference of volume ratios in groups between AD and health. This suggests that AD may affect only several specific sub-regions on ageing, and this affection can present a different brain shrinkage progression pattern.

In the hippocampal subfields, CA1 has been highlighted on the focal atrophy during the early stages of AD, before atrophy spreading to other subfields [32]. In this study, although we did not observe significant difference of the volume ratios in both left and right CA1, difference was found in absolute volume comparisons in hippocampal subfields between the two groups (Table 8.10).

As a cross-sectional study, also due to the small sample size and the narrow age scope, the sensitivity of this study is limited. Further comparisons with ageing-related atrophy progression in mild cognitive impairment (MCI), or grouping our AD patients into early-onset AD and late-onset AD by the clinical presentation and age of onset, may give more comprehensive understanding to the current results.

Besides, the FREESURFER software applied in this study was still under development and was not a stable release. In this trial version FREESURFER newly enabled analyses on hippocampal subfields and brainstem subfields (Table 8.1). Therefore our results can be also different from future stable versions of FREESURFER or using other image analysis software packages.

Meanwhile, we also tested the manual analysis using the INV method on the same dataset to verify the difference of volume ratio of cerebrum to intra-cranium between AD and health. The results not only displayed a lower mean volume ratio value in the AD group, but also showed a significant lower group difference from 27 AD patients in comparison with 16 healthy elderly subjects. The cerebral and the intra-cranial volumes did not show significant difference between the two groups. FREESURFER did not find significant difference in intra-cranial volume between the two groups as well, but detected significantly smaller volume in AD patients' cerebrum. The mean intra-cranial volume values are close to each other by the two methods in both the AD and the health groups. However, the mean cerebral volume values are both smaller using FREESURFER in the two groups in comparison with those estimated by the INV method, which we have not been able to find a reason.

Table 8.10: Volume comparisons of hippocampal subfields between AD and healthy controls ($* < 0.05, ** < 0.01, *** < 0.001$).

Hippo Sub-Structures	Mean Volume cm^3		1-Tailed Less T-Test	Signif
	Alzheimer	HealthyEld	AD/HV P Value	
left_Hippocampal_tail	413.84	501.27	0.000	***
left_subiculum	335.31	400.80	0.000	***
left_CA1	508.74	567.81	0.003	**
left_hippocampal.fissure	171.62	163.92	0.828	
left_presubiculum	243.85	285.28	0.000	***
left_parasubiculum	51.08	57.31	0.038	*
left_molecular_layer_HP	434.27	506.13	0.000	***
left_GC.ML.DG	223.06	262.18	0.000	***
left_CA3	169.26	178.75	0.119	
left_CA4	196.97	225.74	0.000	***
left_fimbria	55.45	82.06	0.000	***
left_HATA	46.91	56.22	0.001	**
left_Whole_hippocampus	2685.84	3128.98	0.000	***
right_Hippocampal_tail	437.92	531.17	0.000	***
right_subiculum	335.10	399.86	0.000	***
right_CA1	538.59	628.99	0.000	***
right_hippocampal.fissure	178.84	169.62	0.870	
right_presubiculum	234.33	270.61	0.000	***
right_parasubiculum	51.91	58.39	0.006	**
right_molecular_layer_HP	453.28	543.27	0.000	***
right_GC.ML.DG	243.77	287.94	0.000	***
right_CA3	190.77	212.31	0.005	**
right_CA4	214.39	247.18	0.000	***
right_fimbria	55.73	72.91	0.003	**
right_HATA	49.78	60.90	0.000	***
right_Whole_hippocampus	2803.60	3326.37	0.000	***

8.5 Conclusion

In conclusion, we tested the volume ratios of brain regions to the brain to investigate the difference between AD patients and healthy controls in macroscopic images. Besides, we investigated the influence of AD on ageing-related brain atrophy progression. Furthermore, the INV method was shown to be capable of detecting the decline of volume ratio of cerebrum to intracranium in AD patients. Our study can be helpful in searching for imaging biomarkers in AD research while the biomarkers can be used in both the automated and the manual approaches.

8.6 Acknowledgements

Thanks to Dr. Mirjam SCHUBERT for kindly providing MRI data.

Chapter 9

Conclusion

In this PhD study, three novel stereological methods (i.e. the ICAV, INV and DN methods) were applied on a commercial software (i.e. ANALYZE) with the procedures described in Chapter 5 and Appendix A. Together with the CAVALIERI method, the four stereological methods can also be performed using freely available software packages (i.e. FSL, R, IMAGEJ and EASYMEASURE). The R script described in Chapter 2 and Appendix B performs three orthogonal IR rotations on MR images automatically, which can also be used to generate transverse, coronal and sagittal views of MR images. The script can be applied on any anatomical structures, especially, brain MR images can be aligned to the MNI152 template, which gives a more consistent 3D position of brain. The IMAGEJ script described in Chapter 3 and Appendix C generates rotated UR grids for INV and DN methods on MR image slices automatically, and the IMAGEJ script described in Chapter 4 and Appendix D records segment lengths measurement for INV and DN methods on MR image slices automatically. The two IMAGEJ scripts work together to estimate volume efficiently using INV and DN methods.

We applied the CAVALIERI, ICAV, INV and DN methods on fetal brain volume estimation on MR images using ANALYZE software (Chapter 5). High reliability is shown for inter- and intra-rater studies (Pearson's $r > 0.997$). The ICAV method estimates volume accurately in individual measurement while the INV and DN methods work efficiently in population mean volume estimation. CE for the ICAV method is low ($< 3\%$) in both the second and third trimesters of GA, while CEs for the INV and DN methods are decreased to around 10% in both trimesters when results from three orthogonal sampling directions are combined. The fetal brain in maternal substance misuse group is smaller than that in the normal development group although difference is not significant.

We made a slice-by-slice comparison between the CAVALIERI method and FREESURFER software on one adult cerebral parenchymal volume estimation (Chapter 6). The point counting strategy adopted in the CAVALIERI method is consistent with the pial surface segmentation in FREESURFER, and there is no significant difference between the volume obtained from FREESURFER and that estimated using the CAVALIERI method.

We applied the CAVALIERI, ICAV, INV and DN methods by using three in-house scripts conveniently on measuring cerebral parenchymal volume in a cohort of AD patients and healthy

elderly participants in MR images, and we compared the results with those obtained from FREESURFER (Chapter 7). Both the inter- and intra-rater studies show good consistency. The average time cost in each brain measurement is less than 15 mins for each of the four stereological methods (Table 9.1). The CAVALIERI and ICAV methods are as reliable as the FREESURFER software in cerebral volume estimation, which all found significantly smaller cerebral volume in AD patients. The INV and DN methods require a larger sample size to detect the difference between AD patients and healthy elderly subjects (Figure 9.1, 9.2).

We performed volumetric analysis on each brain region of a cohort of AD patients and healthy elderly participants in MR images using FREESURFER software to investigate potential imaging biomarkers for AD (Chapter 8). The volume ratios of many regions of brain parenchyma to whole brain are smaller in AD patients while the volume ratios of ventricles to whole brain are bigger in AD patients. Among these changes the volume ratio of cerebral parenchyma to intra-cranium is used as one potential imaging biomarker. We applied the INV method manually to repeat the test of this imaging biomarker and again significant difference was found between AD patients and healthy elderly subjects. Besides, we also investigated the difference of ageing-related brain volume ratios atrophy of each brain regions to whole brain between AD patients and healthy controls. In several brain regions, AD brains are smaller which we interpret as more atrophied.

Future work will be done in estimating surface area by the ICAV and INV methods. Especially a new version of the INV method has been updated for the area recently [27].

In summary, this PhD study makes the ICAV, INV and DN methods be conveniently available, efficient and reliable manual methods to estimate human brain volume on MR images. The stereological methods are consistent with the automated software in volume estimation while manual methods have wider application.

Table 9.1: Total time cost for estimating one adult brain volume using the CAVALIERI, ICAV, INV, DN methods and FREESURFER software, respectively.

	One Adult Brain Volume Estimation				
	Stereological Methods				Auto Software
Time (mins)	CAVALIERI	ICAV	INV	DN	FREESURFER
Semi-auto Ortrip R/FSL Rotaion of MR Images	< 4	< 4	< 4	< 4	/
Semi-auto IMAGEJ Test Grid Generation	/	/	0	0	/
Semi-auto IMAGEJ Measure Generation	/	/	0	0	/
Manual Point Counting or Length Estimation	≈ 10	≈ 10	≈ 8	≈ 2	/
Total Time (mins)	≈ 15	≈ 15	≈ 12	≈ 6	$\geqslant$ 20 hours[a]

[a] https://surfer.nmr.mgh.harvard.edu/fswiki/ReconAllRunTimes

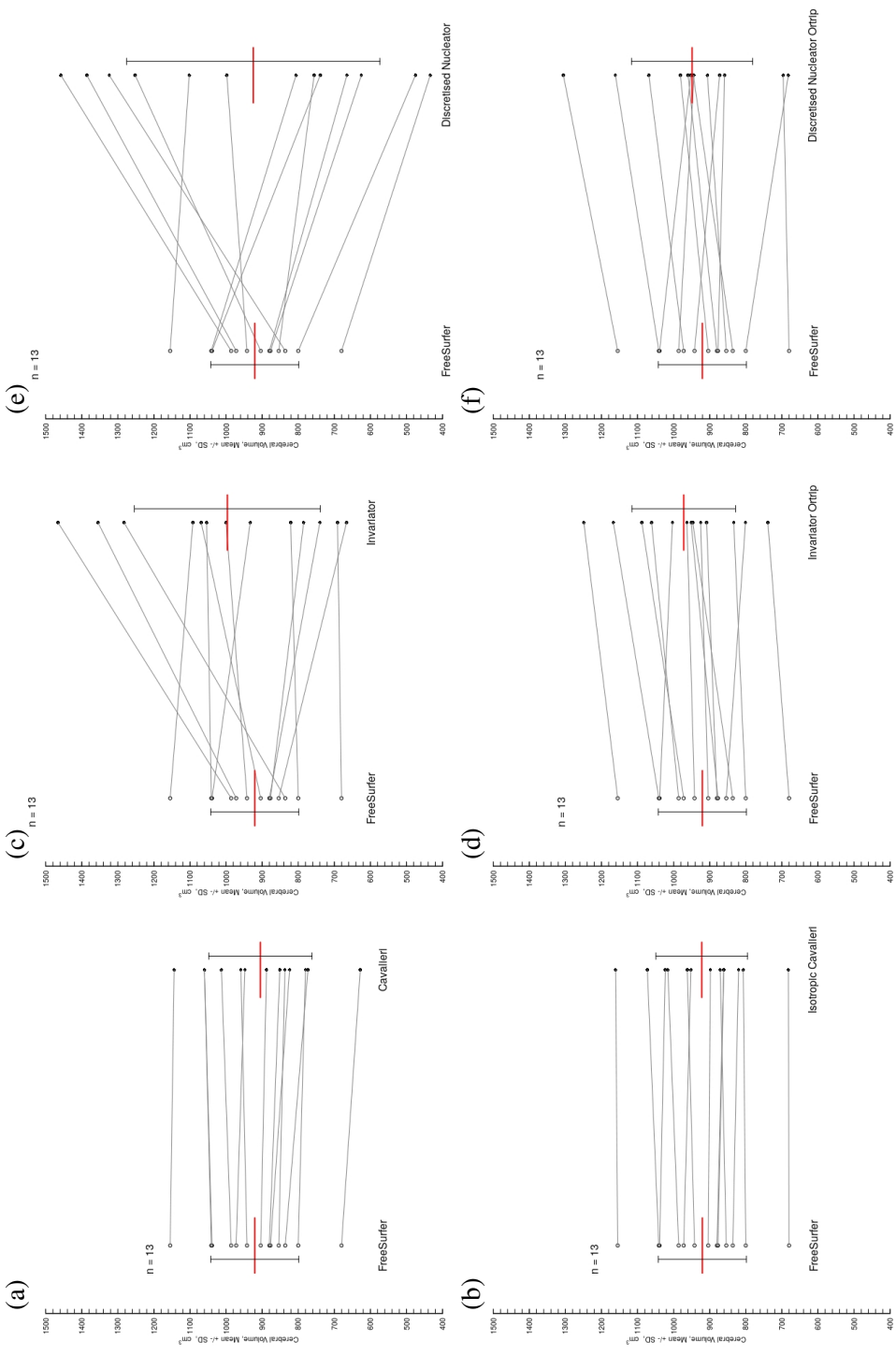

Figure 9.1: Paired comparison among cerebral volumes obtained from 13 healthy adults by FREESURFER and stereological methods. (a) FREESURFER vs the CAVALIERI method; (b) FREESURFER vs the ICAV method; (c) FREESURFER vs the INV method; (d) FREESURFER vs the INV ortrip method; (e) FREESURFER vs the DN method; (f) FREESURFER vs the DN ortrip method. Mean (red horizontal bars) and SD values are displayed in each group.

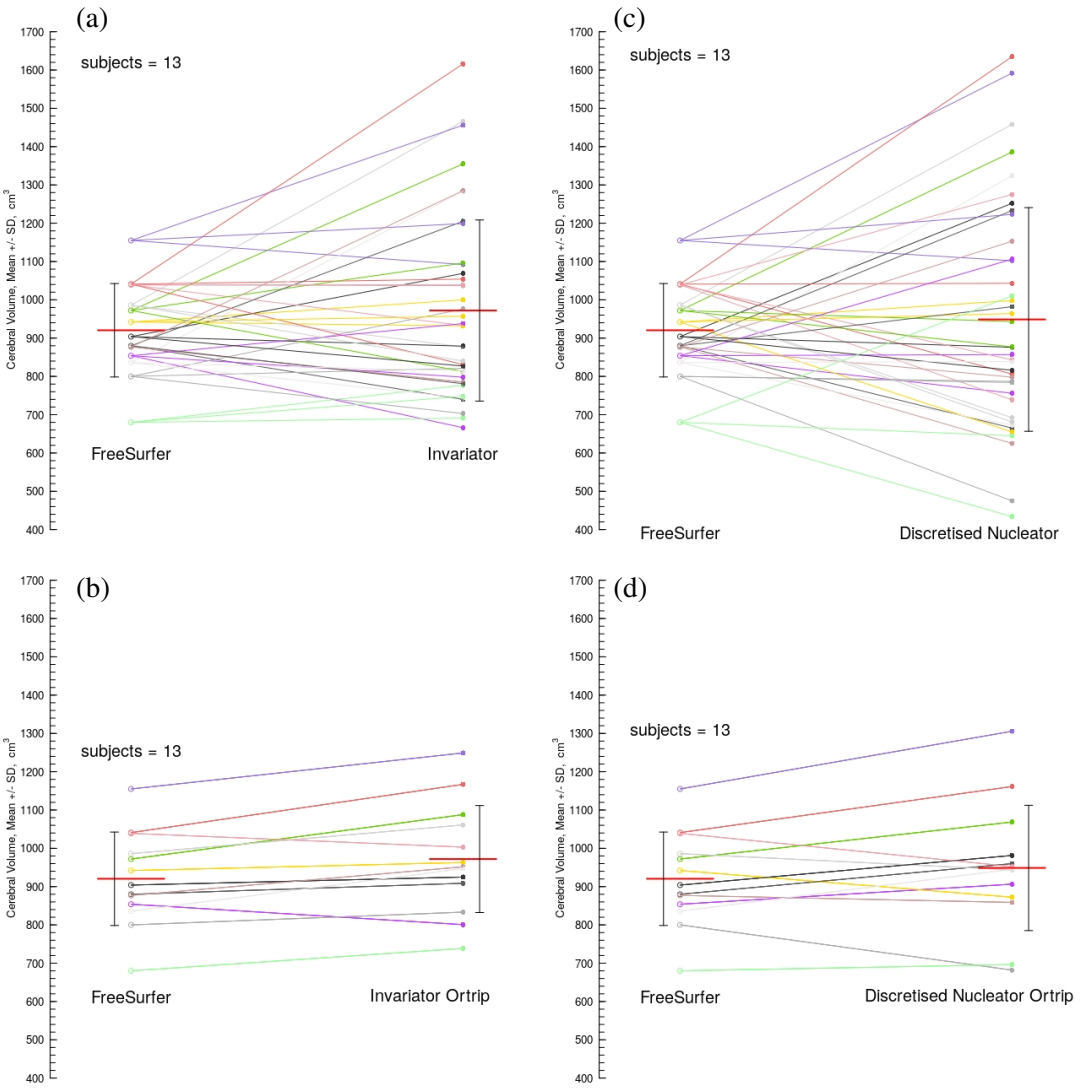

Figure 9.2: Paired comparison among cerebral volumes obtained from 13 healthy adults by FREESURFER, the INV, INV ortrip, DN and DN ortrip methods. Volume estimates for same adult are connected in same colour. (a) FREESURFER vs the INV ortrip method in three orthogonal views of each subject; (b) FREESURFER vs the INV ortrip method with mean value of each subject; (c) FREESURFER vs the DN ortrip method in three orthogonal views of each subject; (d) FREESURFER vs the DN ortrip method with mean value of each subject. Mean (red horizontal bars) and SD values are displayed in each group.

Appendix A

Two Protocols of three orthogonal IUR rotations using ANALYZE software

The protocols using the ANALYZE software for rotations were applied in fetal brain study in Chapter 5.

A.1 Work flow 1: using ANALYZE MATRIX tool

Step	Angle	ANALYZE Menu	Operation	Step Illustration
Adjustment to Common Position & Padded into Cubic (Preparation)				
0-1	0 90 180	Oblique Sections Main Panel	With monitoring of Reference Cube, using Matrix Tool to rotate about $Y(up)/X(right)/Z(inner)$-Axes, and Output in Reformat Entire Volume, Generate Slices. In Save As option, Flip by $Z(up)/X(right)/Y(inner)$-Axes.	Adjusting all the brains in the same position (Reference Cube): i.e. head top vertex points the negative axis Oz $(-Oz)$, and the nose points the negative axis Ox $(-Ox)$ (Visually, a head lies facing left with the head top faceing user).
0-2	cubic	Main Panel	In Save As option, Force Cubic in Resize, Pad in cubic, and Output a 3D volume file in ANALYZE7.5 format.	Isotropic cubic image for every design before rotation.
Random Rotation Section After Preparation (Oblique Sections Menu)				
1-1	90	Matrix Tool	Rotation X-Axis	Vertical up the normal vector of initial section planes
1-2	θ	Matrix Tool	Rotation X-Axis	The INV & The DN
1-3	ϕ	Matrix Tool	Rotation Y-Axis	
1-4	/	Output	Single Slice	
1-5	t_1	FLY	Elevate Up Offset	The ICAV
1-6	T, N_T	Output	Maneuver FLY Elevate Up. T=Fly Values, N_T=Number of Maneuvers, and Current Slice in Middle.	N_T should be even slices to keep the above offset slice central
First Orthogonal Section After Preparation (Oblique Sections Menu)				
2-1	τ	Matrix Tool	Rotation Y-Axis	Additional random rotation of the first orthogonal section plane
2-2	θ	Matrix Tool	Rotation X-Axis	The INV Ortrip & The DN Ortrip
2-3	ϕ	Matrix Tool	Rotation Y-Axis	
2-4	/	Output	Single Slice	
2-5	t_2	FLY	Elevate Up Offset	The ICAV Ortrip
2-6	T, N_T	Output	Maneuver FLY Elevate Up	
Second Orthogonal Section After Preparation (Oblique Sections Menu)				
3-1	$90 + \tau$	Matrix Tool	Rotation Y-Axis	Orthogonal to the above two sections
3-2	θ	Matrix Tool	Rotation X-Axis	The INV Ortrip & The DN Ortrip
3-3	ϕ	Matrix Tool	Rotation Y-Axis	
3-4	/	Output	Single Slice	
3-5	t_3	FLY	Elevate Up Offset	The ICAV Ortrip
3-6	T, N_T	Output	Maneuver FLY Elevate Up	

A.2 Work flow 2: using ANALYZE MATRIX and FLY tools

Step	Angle	ANALYZE Menu	Operation	Step Illustration
Adjustment to Common Position & Padded into Cubic (Preparation)				
0-1	0 90 180	Oblique Sections Main Panel	With monitoring of Reference Cube, using Matrix Tool to rotate about $Y(up)/X(right)/Z(inner)$-Axes, and Output in Reformat Entire Volume, Generate Slices. In Save As Option, Flip by $Z(up)/X(right)/Y(inner)$-Axes.	Adjusting all the brains in the same position (Reference Cube): i.e. head top vertex points the negative axis Oz $(-Oz)$, and the nose points the negative axis Ox $(-Ox)$ (Visually, a head lies facing left with the head top faceing user).
0-2	cubic	Main Panel	In Save As option, Force Cubic in Resize, Pad in cubic, and Output a 3D volume file in ANALYZE7.5 format.	Isotropic cubic image for every design before rotation.
Random Rotation Section After Preparation (Oblique Sections Menu)				
1-1	90	Matrix Tool	Rotation X-Axis	Vertical up the normal vector of initial section planes
1-2	θ	Matrix Tool	Rotation X-Axis	The INV & The DN
1-3	ϕ	Matrix Tool	Rotation Y-Axis	
1-4	/	Output	Single Slice	
1-5	t_1	FLY	Elevate Up Offset	The ICAV
1-6	T, N_T	Output	Maneuver FLY Elevate Up. T=Fly Values, N_T=Number of Maneuvers, and Current Slice in Middle.	N_T should be even slices to keep the above offset slice central
First Orthogonal Section After Preparation (Oblique Sections Menu)				
2-1	90	Matrix Tool	Rotation X-Axis	Vertical up the normal vector of initial section planes
2-2	θ	Matrix Tool	Rotation X-Axis	The INV Ortrip & The DN Ortrip
2-3	ϕ	Matrix Tool	Rotation Y-Axis	
2-4	90	FLY	Pitch Down	
2-5	τ	FLY	Roll Right	
2-6	/	Output	Single Slice	
2-7	t_2	FLY	Elevate Up Offset	The ICAV Ortrip
2-8	T, N_T	Output	Maneuver FLY Elevate Up	
Second Orthogonal Section After Preparation (Oblique Sections Menu)				
3-1	90	Matrix Tool	Rotation X-Axis	Vertical up the normal vector of initial section planes
3-2	θ	Matrix Tool	Rotation X-Axis	The INV Ortrip & The DN Ortrip
3-3	ϕ	Matrix Tool	Rotation Y-Axis	
3-4	90	FLY	Pitch Down	
3-5	τ	FLY	Roll Right	
3-6	90	FLY	Roll Right	
3-7	/	Output	Single Slice	
3-8	t_3	FLY	Elevate Up Offset	The ICAV Ortrip
3-9	T, N_T	Output	Maneuver FLY Elevate Up	

Appendix B

Three orthogonal IR rotations of MRI images by R script

This R rotation script is illustrated in Chapter 2.

```
#### Isotropically random (IR) rotation on MR images of any
    anatomical structures, Version 1.

## Table of contents

# 1) load MRI NIfTI data;
# 2) or load MRI DICOM files and transfer to NIfTI format;
# 3) input rotation angles manually or auto-generate rotation
    angles randomly;
# 4) convert to radiological convention;
# 5) resample to isotropic voxel size;
# 6) align brain images to the MNI152 template position;
# 7) pad to cubic space;
# 8) orient the starting position to a transverse view with nose
    downwards (2D central section plane), or alternatively to a
    sagittal view with nose leftwards;
# 9) generate three orthogonal rotation matrices (2 methods) and
    quaternions;
# 10) rotate the MRI images using the angles input or generated in
    step (3);
# 11) output the 3D MRI images in Analyze7.5 format (for
    EasyMeasure), pivotal section planes, and the lists of rotation
    matrices, rotation angles in degrees and radians;
# 12) generate the Invariator/DisNucleator grid, and overlay the
    grid to the image (ImageJ grid macro);
# 13) length measurement and intersect counting on the grid (ImageJ
    measure macro).
```

```
## install and library packages

# sudo R # in terminal
# install.packages("svDialogs") # in R console #
   packageVersion("svDialogs") # '0.9.57'
# install.packages("oro.dicom")     # packageVersion("oro.dicom") #
   '0.5.0'
# install.packages("oro.nifti")     # packageVersion("oro.nifti") #
   '0.7.2'
# install.packages("rotations")     # packageVersion("rotations") #
   '1.5'
# install.packages("rgl")           # packageVersion("rgl") #
   '0.97.0'
# install.packages("RNiftyReg")     # packageVersion("RNiftyReg") #
   '2.5.0'

# FSL 5.0.8 software installed
# install.packages("fslr")          # packageVersion("fslr") # '2.0'

library(svDialogs)  # dlgList, dlgDir, dlgMessage, dlgOpen, dlgInput
library(oro.dicom)  # readDICOM, dicom2nifti
library(oro.nifti)  # readNIfTI, writeNIfTI, datatype,
   convert.datatype, quatern_b, quaternion2rotation
library(fslr)       # readnii/readNIfTI2, flirt, fslroi, fslswapdim,
   fslchfiletype, flirt_apply
library(rotations)  # as.SO3, as.Q4
library(rgl)        # rotationMatrix
library(RNiftyReg)  # decomposeAffine, buildAffine, applyTransform,
   readNifti, writeNifti, writeAffine

# sessionInfo()
# Sys.info()["sysname"]

system.choice <- dlgList(choices = c("Linux-Ubuntu", "MAC"),
   multiple = FALSE, preselect = NULL,
title = "Which operation system (OS) is running?")$res

if (system.choice == "Linux-Ubuntu") { # fslr path for FSL
   installed in Ubuntu
  options(fsl.path = '/usr')
  options(fsl_pre = 'fsl5.0-')
  options(fsl.outputtype = 'NIFTI')
} else {                          # fslr path for FSL installed in
   Mac, other Linux
  options(fsl.path = '/usr/share/fsl/5.0')
  have.fsl()
```

```
  options(fsl.outputtype = 'NIFTI')
}

## set a working directory

setwd(dlgDir(default = getwd(),
         title = "Choose an output folder, it doesn't need to be
            the input MRI data folder.")$res)

## choose input anatomy as brain or other structures

anatomy.choice <- dlgList(choices = c("Brain (will be aligned to
    MNI152 template)", "Other Structures"),
                multiple = FALSE, preselect = NULL,
                title = "Which anatomy structure is analysed?")$res

## choose input format as NIfTI or DICOM

data.choice <- dlgList(choices = c("NIfTI", "DICOM"), multiple =
    FALSE, preselect = NULL,
             title = "Choose one MRI data format")$res

if (!length(data.choice)) {
  cat("You cancelled the choice\n")
  } else {
  cat("You selected:\n")
  print(data.choice)
}

### load MRI NIfTI data
# e.g. to enable the image centre to be within parenchyma, auto
    cropping a FOV using dcm2nii (mricron) software,
# which aslo transfer a DICOM file to the NIfTI format, using the
    bash command as shown below:
# bash$ dcm2nii -g n -x y ~/24_R/R_Scripts/R_MRI/HV_AB_Dicom/
# besides, FSL robustfov also extracts a fixed size of FOV, but
    only in the superior-inferior direction (z-aixs),
# which means robustfov does not remove the empty/noise only space
    in x,y- axes.

# 'readnii' (fslr package) calls 'readNIfTI' (oro.nifti package),
    but sets the reorientation to FALSE by default

# to check the left/right direction and radiological/neurological
    convention of the MRI images,
# http://nifti.nimh.nih.gov/nifti-1/data: avg152T1_LR_nifti.nii.gz
```

```
    (radio), avg152T1_RL_nifti.nii.gz (neuro).

# dlgOpen() code:
    https://r-forge.r-project.org/scm/viewvc.php/*checkout*/pkg/svDialogs/R/dlgOpen.R?roo

dlgFilters.mri <- matrix(c(
  "NIfTI (*.nii,*.nii.gz)", "*.nii;*.nii.gz",
  "ANALYZE (*.hdr,*.img)","*.hdr;*.img"), ncol = 2, byrow = TRUE)

rownames(dlgFilters.mri) <- c("NIfTI", "ANALYZE")

if (data.choice == "NIfTI") {
  dlgMessage("Please choose one or multiple input NIfTI files (.nii
     / .nii.gz) in one directory.")$res

  data.nii <- dlgOpen(title = "Select one NIfTI file", filters =
     rbind(dlgFilters.mri["NIfTI", ], dlgFilters["All", ]),
     multiple = TRUE)$res
  num.sample <- length(data.nii)
  output.nii <- sub("\\.gz", "", basename(data.nii))
  output.name <- sub("\\.nii", "", basename(output.nii))
}

### load MRI DICOM files

if (data.choice == "DICOM") {
  dlgMessage("Please choose one input DICOM directory or one
     directory containing all the DICOM directories.")$res

  data.dcm.folder <- dlgDir(default = getwd(), title = "Select one
     DICOM directory")$res
  single.multiple <- length(list.dirs(data.dcm.folder))
  if (single.multiple == 1) {
    data.dcm <- data.dcm.folder
  } else {
    data.dcm <- list.dirs(data.dcm.folder)[-1]
  }
  num.sample <- length(list.dirs(data.dcm))
  output.name <- basename(data.dcm)
}

### set rotation angles

angle.choice <- dlgList(choices = c("Auto isotropically random (IR)
    rotation",
                    "Manual assignment four angles", "No rotatons
```

```
                        three orthogonal sections"),
                multiple = FALSE, preselect = NULL,
                title = "Assign the rotation angles (radians)
                    automatically or manually")$res

if (!length(angle.choice)) {
  angle.choice = "No rotatons three orthogonal sections"
}

num.random <- replicate(num.sample, runif(7,0,1), simplify=TRUE)

if (angle.choice == "Auto isotropically random (IR) rotation") {
  Phi.all <- 2 * pi * num.random[1, ]
  Theta.all <- acos (1 - 2 * num.random[2, ])
  Tau.all <- 2 * pi * num.random[3, ]
  Psi.all <- 2 * pi * num.random[4, ]
} else if (angle.choice == "Manual assignment four angles") {
  Phi <- as.numeric(dlgInput(message = "Phi\n\nhorizontal rotation
     angle \n[0, 2*pi] in radian values\n\ne.g. pi/2 =
     1.57079632679490\n",
                 default = "0")$res)
  Theta <- as.numeric(dlgInput(message = "Theta\n\nvertical
     rotation angle \n[0, pi] in radian values\n\ne.g. pi/2 =
     1.57079632679490\n",
                 default = "0")$res)
  Tau <- as.numeric(dlgInput(message = "Tau\n\noblique axis spin
     angle \n[0, 2*pi] in radian values\n\ne.g. pi/2 =
     1.57079632679490\n",
                 default = "0")$res)
  Psi <- as.numeric(dlgInput(message = "Psi\n\nthree orthogonal
     sections rotation angle \n[0, 2*pi] in radian values\n\ne.g.
     pi/2 = 1.57079632679490\n",
                 default = "0")$res)
} else {
  Phi <- 0
  Theta <- 0
  Tau <- 0
  Psi <- 0
}

## set other parameters

# voxel.size <- as.numeric(dlgInput("Isotropic Voxel Size",
   '1')$res)
voxel.size <- 1
```

```
# cav.int.mm <- as.numeric(dlgInput("Cavalieri / IsotropicCavalieri
    Slicing Interval in mm", '15')$res)
cav.int.mm <- 15

## image processing

for ( i in 1:num.sample) {
  if (data.choice == "NIfTI") {
    data.nifti <- readnii(data.nii[i])
  }

  if (data.choice == "DICOM") {
    data.dicom <- readDICOM(path = data.dcm[i])

  # names(data.dicom)
  # head(data.dicom$hdr)
  # image(t(data.dicom$img[[1]]), col = grey(0:64 / 64), axes =
     FALSE, xlab = '', ylab = '')

  # transfer to NIfTI format

  data.nifti <- dicom2nifti(dcm = data.dicom,
                  datatype = 4, units = c('mm', 'sec'), rescale =
                     FALSE, reslice = TRUE,
                  qform = TRUE, sform = TRUE, DIM = 3, descrip =
                     'SeriesDescription', aux.file = NULL)

  # slotNames(data.nifti)
  # range(data.nifti)
  # convert.datatype()
  # datatype(data.nifti)
  # quatern_b(data.nifti)
  # qform(data.nifti)
  # sform(data.nifti)
  # image(data.nifti)
  # orthographic(data.nifti, col.crosshairs = 'green')

  # writeNIfTI(nim = data.nifti, 'HV_AB', onefile = TRUE, gzipped =
     FALSE)
  }

  if (angle.choice == "Auto isotropically random (IR) rotation") {
    Phi <- Phi.all[i]
    Theta <- Theta.all[i]
    Tau <- Tau.all[i]
    Psi <- Psi.all[i]
```

```
}

### convert to radiological convention

data.ori.info <- fslgetorient(data.nifti) # RADIOLOGICAL

# if need to switch, make sure switch both the data and the
    header information, using fslswapdim and fslorient

# the "x y z" flags in fslswapdim refer to the LR SI AP
    directions respectively, rather than the XYZ- axes

if (data.ori.info == "NEUROLOGICAL") {
  data.rad.data <- fslswapdim(file = data.nifti, a = '-x', b =
      'y', c = 'z')
  data.rad <- fslorient(file = data.rad.data, opts =
      '-forceradiological')
} else {
  data.rad <- data.nifti
}

### resample to isotropic voxel size 1 x 1 x 1

data.vox <- flirt(infile = data.rad, reffile = data.rad, opts =
    paste('-applyisoxfm', voxel.size))

### brain image aligns to the MNI152 template position

# if the data is a head/brain image, to make the brains align in
    the same way to the XYZ- axes from the beginning,
# use FSL FLIRT v6.0 tool: Input -> Ref Image, Ref =
    MNI152_T1_1mm.nii.gz, DOF = Rigid Body (6),
# Advanced Options: Images = Not aligned, but same orientation.

if (anatomy.choice == "Brain (will be aligned to MNI152
    template)") {
  if (system.choice == "Linux-Ubuntu") {
    data.align <- flirt(infile = data.vox, reffile =
        '/usr/share/fsl/data/standard/MNI152_T1_1mm.nii.gz', dof
        = 6,
                opts = '-bins 256 -cost corratio -searchrx -90 90
                    -searchry -90 90 -searchrz -90 90 -interp
                    trilinear')
} else {
    data.align <- flirt(infile = data.vox, reffile =
        file.path(fsldir(), "data", "standard",
```

```
        "MNI152_T1_1mm_brain"), dof = 6,
                opts = '-bins 256 -cost corratio -searchrx -90 90
                    -searchry -90 90 -searchrz -90 90 -interp
                    trilinear')
}
} else {
    data.align <- data.vox
}

### pad to cubic space

dim.max <- max(dim(data.align))

dim.centre <- (dim.max - 1) / 2

dim.x0 <- (dim(data.align)[1] - dim.max) / 2
dim.y0 <- (dim(data.align)[2] - dim.max) / 2
dim.z0 <- (dim(data.align)[3] - dim.max) / 2

data.cube <- fslroi(file = data.align, xmin = dim.x0, xsize =
    dim.max, ymin = dim.y0, ysize = dim.max,
            zmin = dim.z0, zsize = dim.max)

### orient the starting position to a same transverse view or a
    same sagittal view

data.orient <- fslswapdim(file = data.cube, a = 'RL', b = 'PA', c
    = 'IS') # transverse view
# data.orient <- fslswapdim(file = data.cube, a = 'AP', b = 'SI',
    c = 'RL') # sagittal view

# data.orient.std <- fslreorient2std(file = data.orient)

# the command fslreorient2std does not change the
    radiological/neurological ordering,
# but does perform 90/180/270 degree rotations as needed,
# fslreorient2std auto determines in FSL whether to do fslswapdim
    with LR PA IS or RL PA IS, and then run the right one.

### generate three orthogonal rotation matrices (2 methods) and
    quaternions

degrees.rotation <- round(cbind(Phi, Theta, Tau, Psi) / pi * 180)

# slice.thick <- unique(extractHeader(data.dicom$hdr,
    'SliceThickness'))
```

```
# slice.space <- unique(extractHeader(data.dicom$hdr,
    'SpacingBetweenSlices'))

cav.int.vox <- cav.int.mm / voxel.size

offsets.interval <- t(floor(cav.int.vox * num.random[5:7, i]))

degrees.offsets <- cbind(degrees.rotation, cav.int.mm,
    offsets.interval)
colnames(degrees.offsets) <- c('Phi', 'Theta', 'Tau', 'Psi',
    'Slicing_mm', 'Offset1_vox', 'Offset2_vox', 'Offset3_vox')
rownames(degrees.offsets) <- 'Data'

# coordinates axes change along with the rotation by 'fslswapdim'
    command into different initial views

x <- c(1, 0, 0) # coordinates for transverse view
y <- c(0, 1, 0) # coordinates for transverse view
z <- c(0, 0, 1) # coordinates for transverse view

# x <- c(0, 1, 0) # coordinates for sagittal view
# y <- c(0, 0, 1) # coordinates for sagittal view
# z <- c(1, 0, 0) # coordinates for sagittal view

## rotation method 1 (3 orthogonal sections, 0XY-plane transverse
    section, initially transverse view)
#               (starting position: initial 3D brain head top up,
    nose inside right)
#               (orthogonal sections: rotating the IR rotated
    brain around X or Y -axis for 90 degree)
#               (spin the orthogonal sections around the other Y
    or X -axis for Psi)

# in FIJI volume viewer plugin, the 0XYZ coordinates (from 0, X
    -> left, Z -> up, Y -> inside) horizontally clockwise rotated
    45 degree
# if a horizontal or vertical plane in 0XYZ coordinates can be
    denoted by two endpoints in its diagonal as (0,0,0) -> (1,1,1)
# starting transverse view: 3D brain stands vertically up, with
    nose towards right vertical inside plane (0,1,0) -> (1,1,1),
# and head top to horizontal top plane (0,0,1) -> (1,1,1), neck
    bottom towards 0XY horizontal bottom plane (0,0,0) -> (1,1,0)

v.ini <- c(0, 0, 1) # creat a vector representing the head top
    along the +Z-axis
```

```
r1 <- as.SO3(z, Phi) # rotate the brain around Z-axis for Phi
r2 <- as.SO3(x, Theta) # rotate the brain around X-axis for Theta
r12 <- r1 + r2     # rotation sequence: r2 -> r1
v12 <- drop(v.ini %*% matrix(r12, 3, 3)) # the new axis after
    rotation
r3 <- as.SO3(v12, Tau) # spin around the new axis for tau

v123 <- drop(v12 %*% matrix(r3, 3, 3)) # the new axis after spin
r.orth1 <- r3 + r1 + r2 # IR rotation, r2 -> r1 -> r3
identical(round(v123, 2), round(drop(v.ini %*% matrix(r.orth1, 3,
    3)), 2)) # two ways should be the same, "TRUE"

r4 <- as.SO3(y, pi/2) # rotate the rotated 3D brain around Y-axis
    for 90 degree
r5 <- as.SO3(x, Psi) # rotate the orthogonal plane around X-axis
    for Psi
r.orth2 <- r5 + r4 + r3 + r1 + r2 # 1st orthogonal section plane
    rotation

r6 <- as.SO3(x, -pi/2) # rotate the rotated 3D brain around
    X-axis for 90 degree
r7 <- as.SO3(y, Psi) # rotate the orthogonal plane around Y-axis
    for Psi
r.orth3 <- r7 + r6 + r3 + r1 + r2 # 2nd orthogonal section plane
    rotation

r.orth3.2 <- r6 + r5 + r4 + r3 + r1 + r2
r8 <- as.SO3(z, -pi/2)
r.orth3.3 <- r8 + r6 + r5 + r4 + r3 + r1 + r2 # another way to
    generate the 2nd orthogonal section plane rotation
identical(round(r.orth3, 2), round(r.orth3.3, 2)) # two ways
    should be the same, "TRUE"

all_rs <- as.SO3(rbind(r1, r2, r3, r4, r5, r6, r7, r8, r.orth1,
    r.orth2, r.orth3))

r.orth1.mat <- matrix(r.orth1, nrow = 3, ncol = 3, byrow = FALSE)
r.orth1.mat44 <- rotationMatrix(matrix = r.orth1.mat)

r.orth2.mat <- matrix(r.orth2, nrow = 3, ncol = 3, byrow = FALSE)
r.orth2.mat44 <- rotationMatrix(matrix = r.orth2.mat)

r.orth3.mat <- matrix(r.orth3, nrow = 3, ncol = 3, byrow = FALSE)
r.orth3.mat44 <- rotationMatrix(matrix = r.orth3.mat)

# q.orth1 <- as.Q4(r.orth1)
```

```
# qv.orth1 <- as.vector(q.orth1)
# quaternion2rotation(qv.orth1[2], qv.orth1[3], qv.orth1[4])

# plot(all_rs, center = id.SO3, col = 1: nrow(all_rs),
#     label_points=c('r1', 'r2', 'r3', 'r4', 'r5', 'r6', 'r7',
    'r8', 'r.orth1', 'r.orth2', 'r.orth3'), interactive = FALSE)

### rotate the image

r.orth1.transform <- buildAffine(angles =
    decomposeAffine(r.orth1.mat44)$angles, source = data.orient,
    anchor = 'centre')
data.orth1 <- applyTransform(r.orth1.transform, data.orient)

r.orth2.transform <- buildAffine(angles =
    decomposeAffine(r.orth2.mat44)$angles, source = data.orient,
    anchor = 'centre')
data.orth2 <- applyTransform(r.orth2.transform, data.orient)

r.orth3.transform <- buildAffine(angles =
    decomposeAffine(r.orth3.mat44)$angles, source = data.orient,
    anchor = 'centre')
data.orth3 <- applyTransform(r.orth3.transform, data.orient)


### output ANALYZE images, pivotal section planes & rotation
    matrices

writeNifti(image = data.orth1, file = 'data_orth1', datatype =
    'auto')
writeNifti(image = data.orth2, file = 'data_orth2', datatype =
    'auto')
writeNifti(image = data.orth3, file = 'data_orth3', datatype =
    'auto')

outcav.1 <- paste(output.name[i], '_orth1', sep = '')
outcav.2 <- paste(output.name[i], '_orth2', sep = '')
outcav.3 <- paste(output.name[i], '_orth3', sep = '')
outinv.1 <- paste(output.name[i], '_orth1_inv', sep = '')
outinv.2 <- paste(output.name[i], '_orth2_inv', sep = '')
outinv.3 <- paste(output.name[i], '_orth3_inv', sep = '')

flirt(infile = 'data_orth1', reffile = 'data_orth1', outfile =
    outcav.1, opts = '-datatype short')
flirt(infile = 'data_orth2', reffile = 'data_orth2', outfile =
    outcav.2, opts = '-datatype short')
```

```
flirt(infile = 'data_orth3', reffile = 'data_orth3', outfile =
    outcav.3, opts = '-datatype short')

file.remove('data_orth1.nii', 'data_orth2.nii', 'data_orth3.nii')

fslroi(file = outcav.1, outfile = outinv.1, xmin = 0, xsize =
    dim.max, ymin = 0, ysize = dim.max, zmin = dim.centre, zsize =
    1)
fslroi(file = outcav.2, outfile = outinv.2, xmin = 0, xsize =
    dim.max, ymin = 0, ysize = dim.max, zmin = dim.centre, zsize =
    1)
fslroi(file = outcav.3, outfile = outinv.3, xmin = 0, xsize =
    dim.max, ymin = 0, ysize = dim.max, zmin = dim.centre, zsize =
    1)

fslchfiletype(file = outcav.1, outfile = outcav.1, filetype =
    'ANALYZE')
fslchfiletype(file = outcav.2, outfile = outcav.2, filetype =
    'ANALYZE')
fslchfiletype(file = outcav.3, outfile = outcav.3, filetype =
    'ANALYZE')

file.remove(paste(outcav.1, '.nii.gz', sep = ''), paste(outcav.2,
    '.nii.gz', sep = ''), paste(outcav.3, '.nii.gz', sep = ''))

fslchfiletype(file = outinv.1, outfile = outinv.1, filetype =
    'ANALYZE')
fslchfiletype(file = outinv.2, outfile = outinv.2, filetype =
    'ANALYZE')
fslchfiletype(file = outinv.3, outfile = outinv.3, filetype =
    'ANALYZE')

file.remove(paste(outinv.1, '.nii.gz', sep = ''), paste(outinv.2,
    '.nii.gz', sep = ''), paste(outinv.3, '.nii.gz', sep = ''))

# FSL fslmaths data_orth1_dt4.img data_orth1.img -odt short

write.table(x = degrees.offsets, file = paste(output.name[i],
    '_degrees_offsets.txt', sep = ''),
row.names = TRUE, col.names = NA, sep = ' ')
write.table(x = c(Phi, Theta, Tau, Psi), file =
    paste(output.name[i], '_radians.txt', sep = ''),
row.names = TRUE, col.names = NA, sep = ' ')

write.table(x = r.orth1.mat44, file = paste(outcav.1,
    '_mat44.mat', sep = ''), row.names = FALSE, col.names = FALSE,
```

```
      sep = ' ')
  write.table(x = r.orth2.mat44, file = paste(outcav.2,
      '_mat44.mat', sep = ''), row.names = FALSE, col.names = FALSE,
      sep = ' ')
  write.table(x = r.orth3.mat44, file = paste(outcav.3,
      '_mat44.mat', sep = ''), row.names = FALSE, col.names = FALSE,
      sep = ' ')
}
```

Appendix C

INV/DN Rotated UR Grid ImageJ Macro

This IMAGEJ gridding script is illustrated in Chapter 3.

```
/**
Invariator/Discretized Nucleator Grid Tool, updated with ImageJ
    v1.52e

Installation:
Save this text file in the ImageJ/macros/toolsets folder. Then you
    can use the '>>' drop down menu in IJ window to activate it.

Usage:
This ImageJ macro tool works as the 2nd step, in collaboration with
    the R script "rotation_3ortho_nii_dcm_mni152_method1.r" (or the
    other twin version
    "rotation_3ortho_nii_dcm_mni152_method2_app.r") for generating
    an isotropic triplet of orthogonal rotated pivotal sections as
    the 1st step, and the other ImageJ macro tool
    "measure_inv_dn.txt" for length measuring as the 3rd step, to
    estimate the volume or surface area of a 3D object in Magnetic
    Resonance Imaging (MRI) images, using two new stereological
    methods based on papers from Professor Luis Cruz-Orive.

This Invariator/Discretized Nucleator Grid tool generates an
    anticlockwise rotated and uniformly random (UR) grid, a centre
    point of the square image file (as the pivitol point), and test
    lines specific for either Invariator or Discretized Nucleator
    method.

All the grids, points and lines are optional in the pop-up menu to
    choose for different methods or purposes. Two images will be
```

```
    generated, when the line option is chosen as "Invariator &
    Discretized Nucleator", two kinds of lines are plotted on
    different images, otherwise, the two images are exactly the
    same. The last line option "Cavalieri on single slice"
    illutrates the Cavalieri method for volume and surface area
    estimations.

Three types of parameters for the grid are reflected in the "IUR
    Stereological Grid" window: a) grid lattice side length; b) grid
    lattice area; c) test points number per shortest side of the
    image.

After generating the grid with/without lines, the parameters of the
    grid (lattice side length, area, grid starting position offsets,
    grid rotation angle, image size, image voxel size) and the
    analysis starting date & time will be recorded in a text window.
    The finishing time will be shown in the same text window if the
    macro tool "measure_inv.txt" is used.

Kaiming Yin
The University of Edinburgh, UK
6 July, 2018
*/

macro "Invariator Discretized Nucleator Grid Tool
    -C000L0880L4477o8844o1b33ob133" {

//help
html = "<html>"
+"<h1><font color=navy>IUR Stereological Grid</h1>"
+"<font color=navy>For the Invariator and the Discretized Nucleator
    methods<font color=black><br><br>"
+"The grid can be set isotropic in direction and uniform random
    offset in the starting position<br><br>"
+"<b><font color=purple>Grid density</b> can be set by the size
    (side length / area) of the grid lattice or by the number of the
    points (crosses)<br><br>"
+"<font color=purple><b><u>Options:</u></b><br>"
+"<b>New Overlay</b> - removes previous overlays<br>"
+"<b><font color=red>Isotropic & Random Offset</b> - randomises the
    IUR grid direction and location<br>"
+"<b><font color=purple>Line thickness</b> - determines the width
    of test lines for both stereolgical methods<br><br>"
+"<b>Regular Points (Crosses)</b> - each cross per grid<br>"
+"<b>Central Point (Encircled Cross)</b> - one additional point per
    grid in the centre of the image<br><br>"
```

```
+"<b>Set Scale<font color=black></b> image scale in width and
    height, which are reflected in the 'invariator/discretized
    nucleator grid parameters' window<br><br>"
+"<b><font color=green>Volume & Surface Area Formulae:</b><br><br>"
+"<font color=green> <i><u>Invariator volume formula:</u></i> Vol =
    lattice area * sum(lengths of hitting test lines)<br>"
+"<i><u>Invariator surface area formula:</u></i> Area = 2 * lattice
    area * sum(intersects of hitting test lines)<br>"
+"<i><u>Discretised Nucleator volume formula:</u></i> Vol = 2 *
    lattice area * sum(lengths of hitting test lines)<br>"

//Initial dialog
Dialog.create("IUR Stereological Grid, ImageJ v1.52e");
Dialog.setInsets(0, 20, 0);
items = newArray(" By grid lattice side length", "By grid lattice
    area ", "By points number ");
Dialog.addRadioButtonGroup("Set grid dimensions:", items, 3, 1, "
    By grid lattice side length");
Dialog.addMessage("Recommend to use an isotropic image in 1*1*1
    voxel size.");
Dialog.addHelp(html);
Dialog.show();
dimensions = Dialog.getRadioButton();
getPixelSize(unit, pw, ph, pd); //or getVoxelSize(vw, vh, vd, unit)
    both do not work correctly on dicom format so use commandlines
    below in voxel size paragraph

//Main dialog box
Dialog.create("Grid parameters");
Dialog.addMessage("GENERAL: ANTICLOCKWISE ROTATION AROUND IMAGE
    CENTRE");
items = newArray("Isotropic & Random Offsets ", " Assigned
    Orientation & Offsets", "No Rotation & Half Offsets ");
Dialog.addRadioButtonGroup("Set grid dimensions:", items, 3, 1,
    "Isotropic & Random Offsets ");
Dialog.addMessage("   If Assigned Orientation & Offsets:");
Dialog.addSlider("Isotropic rotation angle =", -90, 90, 30.1234);
Dialog.addNumber("X-axis offset =", 35, 0, 2, " "+unit);
Dialog.addNumber("Y-axis offset =", 35, 0, 2, " "+unit);
Dialog.addCheckbox(" New Overlay", true);
Dialog.addNumber("Line thickness =", 1,0,2,"voxels");

if (dimensions==" By grid lattice side length")
Dialog.addNumber("Lattice side length =", 35, 0, 2, " "+unit);
else if (dimensions=="By grid lattice area ")
Dialog.addNumber("Lattice area =", 12.25, 2, 8, " cm^2");
```

```
else
Dialog.addNumber("Cross number =", 6, 0, 2, "per short side");

Dialog.addSlider("Grid lattice size percentage randomiser: +/-",
    0.0, 1.0, 0.15);

Dialog.addMessage("   TEST POINTS:");
items = newArray(" Regular Points (Crosses)", " Central Point
    (Encircled Cross)");
Dialog.addCheckboxGroup(1,2,items,newArray(true, true));
Dialog.addChoice("Regular Points Color:", newArray("cyan", "red",
    "yellow", "green", "blue", "magenta", "orange", "black",
    "white"));
Dialog.addChoice("Central Point color:", newArray("green",
    "yellow", "red", "blue", "cyan", "magenta", "orange", "black",
    "white"));
items = newArray(" Invariator & Discretized Nucleator", "Invariator
           ", "Discretized Nucleator     ", "Cavalieri On Single
    Image Slice ");
Dialog.addRadioButtonGroup("   TEST LINES:", items, 4, 1, "
    Invariator & Discretized Nucleator");
Dialog.addChoice("Line color:", newArray("blue", "magenta",
    "orange", "yellow", "red", "cyan", "green", "black", "white"));
Dialog.addHelp(html);
Dialog.show();

name = getTitle();
dir = getDirectory("image");
getDateAndTime(year,month,week,day,hour,min,sec,msec);
MonthNames =
    newArray("Jan","Feb","Mar","Apr","May","Jun","Jul","Aug","Sep","Oct","Nov","Dec");

//grid parameters
offset = Dialog.getRadioButton();
gridangle = -Dialog.getNumber();
xoff = Dialog.getNumber();
yoff = Dialog.getNumber();
new = Dialog.getCheckbox();
t = Dialog.getNumber();
dimens = Dialog.getNumber();
dirandom = Dialog.getNumber();
twopoints = newArray(2);
for (i=0; i< 2; i++)
twopoints[i] = Dialog.getCheckbox();
rglar = twopoints[0];
cntrl = twopoints[1];
```

```
rpcolor = Dialog.getChoice();
cpcolor = Dialog.getChoice();
testline = Dialog.getRadioButton();
lcolor = Dialog.getChoice();

//image scale
getDimensions(width, height, channels, slices, frames);
if (width>=height) ss = height;
else ss = width;

//voxel size
info = getImageInfo();
info1 = split(info, "\n");
i = 0; //to get the first voxel size info only because in dicom
    format imagej adds "Voxel size: 1x1x1 pixel^3" wrongly at the end
while (i<info1.length) {
if(matches(info1[i], ".*Pixel Spacing.*") || startsWith(info1[i],
    "Pixel size") || startsWith(info1[i], "Voxel size")) {
info2 = info1[i]; //print(i, info1[i]);
i = info1.length;
}
i++;
}
info3 = split(info2, " ");
if (info3[0] == "Pixel" || info3[0] == "Voxel")
info4 = split(info3[2], "x"); //analyze format
else
info4 = split(info3[3], "\\"); //dicom format
scaleheight = height*info4[0]; //pixel spacing = row spacing
    (vertical) \ column spacing (horizontal)
scalewidth = width*info4[1];

//lattice size
if (dimensions==" By grid lattice side length")
latticeside = dimens;
else if (dimensions=="By grid lattice area ")
latticeside = sqrt(dimens)*10;
else
latticeside = ss/dimens;

if (offset==" Assigned Orientation & Offsets")
dirandom = 0;
latticerandom = latticeside+latticeside*dirandom*(2*random-1);
pointr = round(latticerandom);

//check overlay
```

```
if (new == true) Overlay.remove;

//creating random offset
iso = gridangle/180*PI;

if (offset=="Isotropic & Random Offsets ") {
off1 = random;
off2 = random;
iso = (random-0.5)*PI;
} else if (offset=="No Rotation & Half Offsets ") {
off1 = off2 = 0.5;
iso = 0;
}

if (iso != 0)
outputangle = -iso/PI*180;
else
outputangle = 0;

if (offset=="Isotropic & Random Offsets " || offset=="No Rotation &
    Half Offsets ") {
xoff = round(pointr*off1);
yoff = round(pointr*off2);
}

setLineWidth(t);

setOption("ExpandableArrays", true);
imageIDs = newArray;
if (nImages == 0)
exit("There is no image open");
else
imageIDs[0] = getImageID();

//image central point
x0 = (width - width%2)/2;
y0 = (height - height%2)/2;

//regular points
for (j=1; j<=slices; j++) {
selectImage(imageIDs[0]);
if (slices > 1)
Stack.setSlice(j);
run("Duplicate...", " ");
for (i=nImages-1; i<=nImages; i++) {
if (i== (nImages-1))
```

```
selectImage(imageIDs[0]);
else {
selectImage(i);
imageIDs = Array.concat(imageIDs, getImageID());
}
run("Remove Overlay");

//initial coordinates lines start XY
x1 = x0 + (xoff - width%latticeside/2)*cos(iso) - (yoff -
    width%latticeside/2)*sin(iso);
x2 = x1 - pointr/16;
x3 = x1 + pointr/16;
y1 = y0 + (xoff - width%latticeside/2)*sin(iso) + (yoff -
    width%latticeside/2)*cos(iso);
y2 = y1 - pointr/16;
y3 = y1 + pointr/16;

//between lines + (down) loop
while ( (abs(x1)+abs(y1)) <= (width+height) ) {
//initial coordinates first point within line XY
x11 = x1;
x21 = x2;
x31 = x3;
y11 = y1;
y21 = y2;
y31 = y3;
//within line + (right) add points loop
while ( (abs(x11)+abs(y11)) <= (width+height) ) {
if (x11>=0 && x11<=width && y11>=0 && y11<=height) {
if (rglar == true){
if (testline != "Cavalieri On Single Image Slice " || (testline ==
    "Cavalieri On Single Image Slice " && i== (nImages-1))) {
setColor(rpcolor);
//cross horizontal bar
Overlay.drawLine(x21,y11,x31,y11);
//cross vertical bar
Overlay.drawLine(x11,y21,x11,y31);
Overlay.add;
}
} else if (testline == "Cavalieri On Single Image Slice " && i==
    (nImages-1)) {
setColor(rpcolor);
//cross horizontal bar
Overlay.drawLine(x21,y11,x31,y11);
//cross vertical bar
Overlay.drawLine(x11,y21,x11,y31);
```

```
Overlay.add;
}
//testlines for INV, DN, INV & DN
if (testline == "Invariator                    " || (testline == "
    Invariator & Discretized Nucleator" && i== (nImages-1))) {
a = atan((x0-x11)/(y0-y11));
ssca = ss * cos(a);
sssa = ss * sin(a);
setColor(lcolor);
Overlay.drawLine(x11-ssca,y11+sssa,x11+ssca,y11-sssa);
Overlay.add;
} else if (testline == "Discretized Nucleator " || (testline == "
    Invariator & Discretized Nucleator" && i== nImages)) {
setColor(lcolor);
Overlay.drawLine(x0,y0,x11,y11);
Overlay.add;
} else if (testline == "Cavalieri On Single Image Slice " && i==
    nImages) {
setColor(lcolor);
Overlay.drawLine(x11,y11,x11+pointr*cos(iso),y11+pointr*sin(iso));
Overlay.drawLine(x11,y11,x11-pointr*sin(iso),y11+pointr*cos(iso));
Overlay.add;
}
}
x11 += pointr * cos(iso);
x21 += pointr * cos(iso);
x31 += pointr * cos(iso);
y11 += pointr * sin(iso);
y21 += pointr * sin(iso);
y31 += pointr * sin(iso);
}

//initial coordinates first point within line XY
x11 = x1;
x21 = x2;
x31 = x3;
y11 = y1;
y21 = y2;
y31 = y3;
//within line - (left) add points loop
while ( (abs(x11)+abs(y11)) <= (width+height) ) {
if (x11>=0 && x11<=width && y11>=0 && y11<=height) {
if (rglar == true){
if (testline != "Cavalieri On Single Image Slice " || (testline ==
    "Cavalieri On Single Image Slice " && i== (nImages-1))) {
setColor(rpcolor);
```

```
//cross horizontal bar
Overlay.drawLine(x21,y11,x31,y11);
//cross vertical bar
Overlay.drawLine(x11,y21,x11,y31);
Overlay.add;
}
} else if (testline == "Cavalieri On Single Image Slice " && i==
    (nImages-1)) {
setColor(rpcolor);
//cross horizontal bar
Overlay.drawLine(x21,y11,x31,y11);
//cross vertical bar
Overlay.drawLine(x11,y21,x11,y31);
Overlay.add;
}
//testlines for INV, DN, INV & DN
if (testline == "Invariator                    " || (testline == "
    Invariator & Discretized Nucleator" && i== (nImages-1))) {
a = atan((x0-x11)/(y0-y11));
ssca = ss * cos(a);
sssa = ss * sin(a);
setColor(lcolor);
Overlay.drawLine(x11-ssca,y11+sssa,x11+ssca,y11-sssa);
Overlay.add;
} else if (testline == "Discretized Nucleator " || (testline == "
    Invariator & Discretized Nucleator" && i== nImages)) {
setColor(lcolor);
Overlay.drawLine(x0,y0,x11,y11);
Overlay.add;
} else if (testline == "Cavalieri On Single Image Slice " && i==
    nImages) {
setColor(lcolor);
Overlay.drawLine(x11,y11,x11-pointr*cos(iso),y11-pointr*sin(iso));
Overlay.drawLine(x11,y11,x11-pointr*sin(iso),y11+pointr*cos(iso));
Overlay.add;
}
}
x11 -= pointr * cos(iso);
x21 -= pointr * cos(iso);
x31 -= pointr * cos(iso);
y11 -= pointr * sin(iso);
y21 -= pointr * sin(iso);
y31 -= pointr * sin(iso);
}
x1 -= pointr * sin(iso);
x2 -= pointr * sin(iso);
```

```
x3 -= pointr * sin(iso);
y1 += pointr * cos(iso);
y2 += pointr * cos(iso);
y3 += pointr * cos(iso);
}

//initial coordinates lines start XY
x1 = x0 + (xoff - width%latticeside/2)*cos(iso) - (yoff -
    width%latticeside/2)*sin(iso);
x2 = x1 - pointr/16;
x3 = x1 + pointr/16;
y1 = y0 + (xoff - width%latticeside/2)*sin(iso) + (yoff -
    width%latticeside/2)*cos(iso);
y2 = y1 - pointr/16;
y3 = y1 + pointr/16;

//between lines - (up) loop
while ( (abs(x1)+abs(y1)) <= (width+height) ) {
//initial coordinates first point within line XY
x11 = x1;
x21 = x2;
x31 = x3;
y11 = y1;
y21 = y2;
y31 = y3;
//within line + (right) add points loop
while ( (abs(x11)+abs(y11)) <= (width+height) ) {
if (x11>=0 && x11<=width && y11>=0 && y11<=height) {
if (rglar == true){
if (testline != "Cavalieri On Single Image Slice " || (testline ==
    "Cavalieri On Single Image Slice " && i== (nImages-1))) {
setColor(rpcolor);
//cross horizontal bar
Overlay.drawLine(x21,y11,x31,y11);
//cross vertical bar
Overlay.drawLine(x11,y21,x11,y31);
Overlay.add;
}
} else if (testline == "Cavalieri On Single Image Slice " && i==
    (nImages-1)) {
setColor(rpcolor);
//cross horizontal bar
Overlay.drawLine(x21,y11,x31,y11);
//cross vertical bar
Overlay.drawLine(x11,y21,x11,y31);
Overlay.add;
```

```
}
//testlines for INV, DN, INV & DN
if (testline == "Invariator                    " || (testline == "
    Invariator & Discretized Nucleator" && i== (nImages-1))) {
a = atan((x0-x11)/(y0-y11));
ssca = ss * cos(a);
sssa = ss * sin(a);
setColor(lcolor);
Overlay.drawLine(x11-ssca,y11+sssa,x11+ssca,y11-sssa);
Overlay.add;
} else if (testline == "Discretized Nucleator " || (testline == "
    Invariator & Discretized Nucleator" && i== nImages)) {
setColor(lcolor);
Overlay.drawLine(x0,y0,x11,y11);
Overlay.add;
} else if (testline == "Cavalieri On Single Image Slice " && i==
    nImages) {
setColor(lcolor);
Overlay.drawLine(x11,y11,x11+pointr*cos(iso),y11+pointr*sin(iso));
Overlay.drawLine(x11,y11,x11+pointr*sin(iso),y11-pointr*cos(iso));
Overlay.add;
}
}
x11 += pointr * cos(iso);
x21 += pointr * cos(iso);
x31 += pointr * cos(iso);
y11 += pointr * sin(iso);
y21 += pointr * sin(iso);
y31 += pointr * sin(iso);
}

//initial coordinates first point within line XY
x11 = x1;
x21 = x2;
x31 = x3;
y11 = y1;
y21 = y2;
y31 = y3;
//within line - (left) add points loop
while ( (abs(x11)+abs(y11)) <= (width+height) ) {
if (x11>=0 && x11<=width && y11>=0 && y11<=height) {
if (rglar == true){
if (testline != "Cavalieri On Single Image Slice " || (testline ==
    "Cavalieri On Single Image Slice " && i== (nImages-1))) {
setColor(rpcolor);
//cross horizontal bar
```

```
Overlay.drawLine(x21,y11,x31,y11);
//cross vertical bar
Overlay.drawLine(x11,y21,x11,y31);
Overlay.add;
}
} else if (testline == "Cavalieri On Single Image Slice " && i==
    (nImages-1)) {
setColor(rpcolor);
//cross horizontal bar
Overlay.drawLine(x21,y11,x31,y11);
//cross vertical bar
Overlay.drawLine(x11,y21,x11,y31);
Overlay.add;
}
//testlines for INV, DN, INV & DN
if (testline == "Invariator                    " || (testline == "
    Invariator & Discretized Nucleator" && i== (nImages-1))) {
a = atan((x0-x11)/(y0-y11));
ssca = ss * cos(a);
sssa = ss * sin(a);
setColor(lcolor);
Overlay.drawLine(x11-ssca,y11+sssa,x11+ssca,y11-sssa);
Overlay.add;
} else if (testline == "Discretized Nucleator " || (testline == "
    Invariator & Discretized Nucleator" && i== nImages)) {
setColor(lcolor);
Overlay.drawLine(x0,y0,x11,y11);
Overlay.add;
} else if (testline == "Cavalieri On Single Image Slice " && i==
    nImages) {
setColor(lcolor);
Overlay.drawLine(x11,y11,x11-pointr*cos(iso),y11-pointr*sin(iso));
Overlay.drawLine(x11,y11,x11+pointr*sin(iso),y11-pointr*cos(iso));
Overlay.add;
}
}
x11 -= pointr * cos(iso);
x21 -= pointr * cos(iso);
x31 -= pointr * cos(iso);
y11 -= pointr * sin(iso);
y21 -= pointr * sin(iso);
y31 -= pointr * sin(iso);
}
x1 += pointr * sin(iso);
x2 += pointr * sin(iso);
x3 += pointr * sin(iso);
```

```
y1 -= pointr * cos(iso);
y2 -= pointr * cos(iso);
y3 -= pointr * cos(iso);
}
Overlay.show;
}
}

//central encircled point
if (cntrl == true && testline != "Cavalieri On Single Image Slice
    "){
setColor(cpcolor);
for (i=0; i<imageIDs.length; i++) {
selectImage(imageIDs[i]);
x1 = x0 - pointr/16;
x2 = x0 + pointr/16;
y1 = y0 - pointr/16;
y2 = y0 + pointr/16;
Overlay.drawLine(x1,y0,x2,y0);
Overlay.drawLine(x0,y1,x0,y2);
Overlay.drawEllipse(x1, y1, pointr/8, pointr/8);
Overlay.add;
Overlay.show;
}
}

//printing the parameters of the grid
window = isOpen("invariator/discretized nucleator grid parameters");
title = "[invariator/discretized nucleator grid parameters]";
if (window == false){
run("Text Window...", "name="+ title +"width=60 height=16 menu");
setLocation(0, 0);
}
print(title, replace(testline," ","")+" grid for image:
    ["+name+"]");
print(title, "\nStart time: "+hour+":"+min+":"+sec+",
    "+toString(day)+" "+MonthNames[month]+" "+toString(year));
print(title, "\n\nImage size = "+width+"x"+height+" voxels");
print(title, "\n"+info2);
print(title, "\nPhysically width = "+scalewidth/10+" cm, height =
    "+scaleheight/10+" cm");
print(title, "\n\nGrid lattice side length = "+pointr+" voxels");
print(title, "\nPhysically grid lattice length =
    "+pointr*info4[1]+" cm x "+pointr*info4[0]+" cm and grid lattice
    area = "+pointr*info4[1]*pointr*info4[0]/100+" cm^2");
print(title, "\nGrid points number approx =
```

```
    "+round(width*height/pointr/pointr));
print(title, "\nX-axis offset = "+xoff+" voxels, Y-axis offset =
    "+yoff+" voxels");
print(title, "\nRotation angle = "+outputangle+" degree
    anticlockwise around centre");
print(title, "\n _ _ _ _ _ _ _ _ _ _ _ _\n\n");
```

Appendix D

INV/DN Length Measure ImageJ Macro

This IMAGEJ measuring script is illustrated in Chapter 4.

```
/**
Invariator/Nucleator Measure Tool, updated with ImageJ v1.52e

Installation:
Save this text file in the ImageJ/macros/toolsets folder. Then you
    can use the '>>' drop down menu in IJ window to activate it.

Usage:
This macro tool works as the 3rd step, in collaboration with the R
    script "rotation_3ortho_nii_dcm_mni152_method1.r" (or the other
    twin version "rotation_3ortho_nii_dcm_mni152_method2_app.r") for
    generating an isotropic triplet of orthogonal rotated pivotal
    sections as the 1st step, and the other macro tool
    "grid_inv_dn.txt" for generating a rotated and uniformly random
    (UR) grid, a centre point and lines as the 2nd step, to estimate
    the volume or surface area of a 3D object in Magnetic Resonance
    Imaging (MRI) images, using two new stereological methods based
    on the papers from Professor Luis Cruz-Orive.

The Invariator/Nucleator Measure tool measures the lengths of
    segments, records the results in ROI manager, and saves the data
    and image when finished.

Left-click on the image and drag the mouse to draw the segment,
    drag the either end of the segment to correct the length, repeat
    until satisfied.

Right-click anywhere on the image to finish the drawing of the
```

```
    selected segment. Once it is finished, this segment can not be
    edited any more, but it still can be deleted and redrawn. Next
    left-click will start on a new segment measurement.

After finishing all measures, double click on the tool icon, choose
    the method of Invariator or Discretized Nucleator respectively
    in the pop-up menu, the results (measures, segments record and
    the segments drawing image) will be saved in the same directory
    where the original image is. The finishing time will be shown in
    the same text window as the macro tool "grid_inv.txt" uses,
    which records the starting time for the analysis of this data.
*/

macro "Invariator Measure Tool -C000L0df0P51d155d559d95ddd0" {

leftButton=16;
rightButton=4;
shift=1;
ctrl=2;
alt=8;

setOption("DisablePopupMenu", true);

setLineWidth(1);
roiManager("Show All without labels");
getCursorLoc(x, y, z, flags);
x1=x2=x;
y1=y2=y;

  while (flags!=0) {
  getCursorLoc(x, y, z, flags);
  if (x!=x1 || y!=y1) {
  makeLine(x1, y1, x, y);
  x2=x; y2=y;
  wait(10);
  }
  }

  if (x!=x1 || y!=y1) {
  roiManager("Add");
  ind=roiManager("count");
  roiManager("Select", ind-1);
  lastname=call("ij.plugin.frame.RoiManager.getName", ind-1);
  invariatormeasure(x1, y1, x2, y2);
  }
}
```

```
function invariatormeasure(x1, y1, x2, y2) {

  while (flags&rightButton==0){
  while (flags&leftButton==0 && flags&rightButton==0) {
  getCursorLoc(x, y, z, flags);
  x3=x; y3=y;
  d13=sqrt((x1-x3)*(x1-x3)+(y1-y3)*(y1-y3));
  d23=sqrt((x2-x3)*(x2-x3)+(y2-y3)*(y2-y3));
  wait(10);
  }

  ind=roiManager("count");
  if (ind == 0) {
  roiManager("Add");
  ind=1;
  }
  roiManager("Select", ind-1);
  selectname=call("ij.plugin.frame.RoiManager.getName", ind-1);
  if (lastname != selectname) exit("The last line was
     deleted/renamed, draw a new line now.");

  while (flags&leftButton!=0) {
  getCursorLoc(x, y, z, flags);
  if (d13 <= d23) {
  makeLine(x, y, x2, y2);
  x1=x; y1=y;
  } else {
  makeLine(x1, y1, x, y);
  x2=x; y2=y;
  }
  roiManager("Update");
  wait(10);
  }
  }
  roiManager("Deselect");
}

macro 'Invariator Measure Tool Options...' {
  Dialog.create("Invariator Measure, V1");
  Dialog.setInsets(0, 20, 0);
  items = newArray("Invariator ", "  Discretized Nucleator");
  Dialog.addRadioButtonGroup("Finish the method", items, 2, 1, "");
  Dialog.show;
  finish = Dialog.getRadioButton();
```

```
name = getTitle();
dotIndex = lastIndexOf(name, ".");
name1 = substring(name, 0, dotIndex);
barsuffix = matches(name1,".*-.");
if (barsuffix == 1) {
     barIndex = lastIndexOf(name1, "-");
     name2 = substring(name1, 0, barIndex);
   } else {
     name2 = name1;
   }
dir = getDirectory("image");
id1 = getImageID();
if (dir == "") {
  if (nImages == 2) {
     ids = newArray(nImages);
     for (i=0; i < ids.length; i++){
       selectImage(i+1);
       ids[i] = getImageID();
     }
     if (id1 == ids[0]) id2 = ids[1];
       else id2 = ids[0];
     selectImage(id2);
     dir = getDirectory("image");
     selectImage(id1);
  }
}
path = dir+name1;
path2 = dir+name2;

counts=roiManager("count");
roilist=newArray(counts);
for(i=0; i<counts; i++) roilist[i] = i;

if (finish == "Invariator  ") {
  roiManager("Deselect");
  roiManager("Save", path+"_inv.zip");
  run("Set Measurements...", " redirect=None decimal=3");
  roiManager("Measure");
  saveAs("Results", path+"_inv.xls");
  roiManager("Show All with labels");
  run("From ROI Manager");
  run("Flatten");
  saveAs("PNG", path+"_inv.png");
  close();
} else if (finish == " Discretized Nucleator") {
  roiManager("Deselect");
```

```
    roiManager("Save", path+"_dn.zip");
    run("Set Measurements...", " redirect=None decimal=3");
    roiManager("Measure");
    saveAs("Results", path+"_dn.xls");
    roiManager("Show All with labels");
    run("From ROI Manager");
    run("Flatten");
    saveAs("PNG", path+"_dn.png");
    close();
  }

  window = isOpen("Invariator/Nucleator grid parameters");
  window1 = isOpen(name2+" parameters.txt");
  if (window1 == true) title = "["+name2+" parameters.txt]";
  else title = "[Invariator/Nucleator grid parameters]";
  if (window == false && window1 == false){
    run("Text Window...", "name="+ title +"width=60 height=16
        menu");
    setLocation(0, 0);
  }
  getDateAndTime(year,month,week,day,hour,min,sec,msec);
  if (finish == "Invariator  ") print(title, "\n"+path+"_inv");
    else if (finish == " Discretized Nucleator") print(title,
        "\n"+path+"_dn");
  print(title, "\n\nfinish time: "+hour+":"+min+":"+sec);
  print(title, "\n _____\n");
  if (window1 == true) selectWindow(name2+" parameters.txt");
  else selectWindow("Invariator/Nucleator grid parameters");
  saveAs("Text", path2+" parameters.txt");

  roiManager("Select", roilist);
  roiManager("Delete");

  if (isOpen("Results")) {
    selectWindow("Results");
    run("Close");
  }
}
```

References

[1] D. Adler and D. Murdoch. *rgl: 3D visualization using OpenGL*, 2016. R package version 0.95.1441.

[2] J. Ahdidan, C. A. Raji, E. A. DeYoe, J. Mathis, K. Noe, J. Rimestad, T. K. Kjeldsen, J. Mosegaard, J. T. Becker, and O. Lopez. Quantitative neuroimaging software for clinical assessment of hippocampal volumes on MR imaging. *Journal of Alzheimer's Disease*, 49(3):723–732, 2015.

[3] I. Akdogan, Y. Kiroglu, S. Onur, and N. Karabuluti. The volume fraction of brain ventricles to total brain volume: a computed tomography stereological study. *Folia Morphologica*, 69(4):193–200, 2010.

[4] American College of Obstetricians and Gynecologists. *Your pregnancy and childbirth: month to month*. The American College of Obstetricians and Gynecologists, Washington, DC, 6th edition, 2015.

[5] K. Andersen, B. B. Andersen, and B. Pakkenberg. Stereological quantification of the cerebellum in patients with Alzheimer's disease. *Neurobiology of Aging*, 33(1):197.e11–20, 2012.

[6] A. Baddeley, E. Jensen, N. Reid, N. Keiding, R. Tibshirani, T. Louis, H. Tong, and V. Isham. *Stereology for statisticians*. Chapman & Hall/CRC, New York, 2004.

[7] A. J. Baddeley, H. J. Gundersen, and L. M. Cruz-Orive. Estimation of surface area from vertical sections. *Journal of Microscopy*, 142(Pt 3):259–276, 1986.

[8] O. Bas, N. Acer, N. Mas, H. S. Karabekir, O. Y. Kusbeci, and B. Sahin. Stereological evaluation of the volume and volume fraction of intracranial structures in magnetic resonance images of patients with Alzheimer's disease. *Annals of Anatomy*, 191(2):186–195, 2009.

[9] D. A. Bateman and C. A. Chiriboga. Dose-response effect of cocaine on newborn head circumference. *Pediatrics*, 106(3):E33, 2000.

[10] J. M. Bland and D. G. Altman. Measuring agreement in method comparison studies. *Statistical Methods in Medical Research*, 8(2):135–160, 1999.

[11] A. C. Breeze, F. A. Gallagher, D. J. Lomas, G. C. Smith, C. C. Lees, and Cambridge Post-Mortem MRI Study Group. Postmortem fetal organ volumetry using magnetic resonance imaging and comparison to organ weights at conventional autopsy. *Ultrasound in Obstetrics & Gynecology*, 31(2):187–193, 2008.

[12] C. Buss, S. Entringer, J. M. Swanson, and P. D. Wadhwa. The role of stress in brain development: the gestational environment's long-term effects on the brain. *Cerebrum*, 2012:4, 2012.

[13] J. L. Chepkoech, K. B. Walhovd, H. Grydeland, A. M. Fjell, and Alzheimer's Disease Neuroimaging Initiative. Effects of change in Freesurfer version on classification accuracy of patients with Alzheimer's disease and mild cognitive impairment. *Human Brain Mapping*, 37(5):1831–1841, 2016.

[14] A. Cherubini, M. E. Caligiuri, P. Péran, U. Sabatini, C. Cosentino, and F. Amato. Brain tissues atrophy is not always the best structural biomarker of physiological aging: a multimodal cross-sectional study. In *37th Annual International Conference of the IEEE Engineering in Medicine and Biology Society (EMBC)*, pages 5436–5440, Milan, August 2015. IEEE.

[15] J. Clayden, M. Modat, and P. Daga. *RNiftyReg: image registration using the NiftyReg library*, 2016. R package version 2.2.0.

[16] L. Clerx, E. H. Gronenschild, C. Echavarri, F. Verhey, P. Aalten, and H. I. Jacobs. Can Freesurfer compete with manual volumetric measurements in Alzheimer's disease? *Current Alzheimer Research*, 12(4):358–367, 2015.

[17] S. Y. Coleman and C. J. Pritchett. Random rotations in simulation with computer 3-D reconstruction. *Acta Stereologica*, 9(2):207–218, 1990.

[18] K. S. Cover, R. A. van Schijndel, A. Versteeg, K. K. Leung, E. R. Mulder, R. A. Jong, P. J. Visser, A. Redolfi, J. Revillard, B. Grenier, D. Manset, S. Damangir, P. Bosco, H. Vrenken, B. W. van Dijk, G. B. Frisoni, F. Barkhof, and Alzheimer's Disease Neuroimaging Initiative, neuGRID. Reproducibility of hippocampal atrophy rates measured with manual, Freesurfer, AdaBoost, FSL/FIRST and the MAPS-HBSI methods in Alzheimer's disease. *Psychiatry Research*, 252:26–35, 2016.

[19] S. R. Cox, T. I. McKenzie, B. S. Aribisala, N. A. Royle, S. E. MacPherson, A. M. MacLullich, M. E. Bastin, J. M. Wardlaw, I. J. Deary, and K. J. Ferguson. Volumetric and correlational implications of brain parcellation method selection: a 3-way comparison in the frontal lobes. *Journal of Computer Assisted Tomography*, 40(1):53–60, 2016.

[20] L. M. Cruz-Orive. Stereology of single objects. *Journal of Microscopy*, 186(2):93–107, 1997.

[21] L. M. Cruz-Orive. A new stereological principle for test lines in three-dimensional space. *Journal of Microscopy*, 219(Pt 1):18–28, 2005.

[22] L. M. Cruz-Orive. Stereology: old and new. In V. Capasso, G. Aletti, and A. Micheletti, editors, *Proceedings of the 10th European Congress of ISS*, The MIRIAM Project Series, pages 3–14, Bologna, June 2009. ESCULAPIO Pub. Co.

[23] L. M. Cruz-Orive. Flowers and wedges for the stereology of particles. *Journal of Microscopy*, 243(1):86–102, 2011.

[24] L. M. Cruz-Orive. Uniqueness properties of the invariator, leading to simple computations. *Image Analysis & Stereology*, 31(2):89–98, 2012.

[25] L. M. Cruz-Orive. Variance predictors for isotropic geometric sampling, with applications in forestry. *Statistical Methods & Applications*, 22(1):3–31, 2013.

[26] L. M. Cruz-Orive, J. Gelšvartas, and N. Roberts. Sampling theory and automated simulations for vertical sections, applied to human brain. *Journal of Microscopy*, 253(2):119–150, 2014.

[27] L. M. Cruz-Orive and X. Gual-Arnau. The invariator design: an update. *Image Analysis & Stereology*, 34(3):147–159, 2015.

[28] L. M. Cruz-Orive, M. L. Ramos-Herrera, and E. Artacho-Pérula. Stereology of isolated objects with the invariator. *Journal of Microscopy*, 240(2):94–110, 2010.

[29] A. M. Dale, B. Fischl, and M. I. Sereno. Cortical surface-based analysis. I. segmentation and surface reconstruction. *Neuroimage*, 9(2):179–194, 1999.

[30] A. M. Dale and M. I. Sereno. Improved localizadon of cortical activity by combining EEG and MEG with MRI cortical surface reconstruction: a linear approach. *Journal of Cognitive Neuroscience*, 5(2):162–176, 1993.

[31] K. N. Dancause, D. P. Laplante, C. Oremus, S. Fraser, A. Brunet, and S. King. Disaster-related prenatal maternal stress influences birth outcomes: project Ice Storm. *Early Human Development*, 87(12):813–820, 2011.

[32] R. de Flores, R. La Joie, and G. Chételat. Structural imaging of hippocampal subfields in healthy aging and Alzheimer's disease. *Neuroscience*, 309:29–50, 2015.

[33] R. de Flores, R. La Joie, B. Landeau, A. Perrotin, F. Mézenge, V. de La Sayette, F. Eustache, B. Desgranges, and G. Chételat. Effects of age and Alzheimer's disease on hippocampal subfields: comparison between manual and Freesurfer volumetry. *Human Brain Mapping*, 36(2):463–474, 2015.

[34] R. S. Desikan, F. Ségonne, B. Fischl, B. T. Quinn, B. C. Dickerson, D. Blacker, R. L. Buckner, A. M. Dale, R. P. Maguire, B. T. Hyman, M. S. Albert, and R. J. Killiany. An

automated labeling system for subdividing the human cerebral cortex on MRI scans into gyral based regions of interest. *Neuroimage*, 31(3):968–980, 2006.

[35] J. A. DiPietro, M. F. Novak, K. A. Costigan, L. D. Atella, and S. P. Reusing. Maternal psychological distress during pregnancy in relation to child development at age two. *Child Development*, 77(3):573–587, 2006.

[36] L. D. Eggert, J. Sommer, A. Jansen, T. Kircher, and C. Konrad. Accuracy and reliability of automated gray matter segmentation pathways on real and simulated structural magnetic resonance images of the human brain. *PLoS One*, 7(9):E45081, 2012.

[37] A. Fedorov, R. Beichel, J. Kalpathy-Cramer, J. Finet, J. C. Fillion-Robin, S. Pujol, C. Bauer, D. Jennings, F. Fennessy, M. Sonka, J. Buatti, S. Aylward, J. V. Miller, S. Pieper, and R. Kikinis. 3D Slicer as an image computing platform for the quantitative imaging network. *Magnetic Resonance Imaging*, 30(9):1323–1341, 2012.

[38] B. Fischl. FreeSurfer. *Neuroimage*, 62(2):774–781, 2012.

[39] B. Fischl and A. M. Dale. Measuring the thickness of the human cerebral cortex from magnetic resonance images. *Proc Natl Acad Sci U S A*, 97(20):11050–11055, 2000.

[40] B. Fischl, A. Liu, and A. M. Dale. Automated manifold surgery: constructing geometrically accurate and topologically correct models of the human cerebral cortex. *IEEE Transactions on Medical Imaging*, 20(1):70–80, 2001.

[41] B. Fischl, D. H. Salat, E. Busa, M. Albert, M. Dieterich, C. Haselgrove, A. van der Kouwe, R. Killiany, D. Kennedy, S. Klaveness, A. Montillo, N. Makris, B. Rosen, and A. M. Dale. Whole brain segmentation: automated labeling of neuroanatomical structures in the human brain. *Neuron*, 33(3):341–355, 2002.

[42] B. Fischl, D. H. Salat, A. J. van der Kouwe, N. Makris, F. Ségonne, B. T. Quinn, and A. M. Dale. Sequence-independent segmentation of magnetic resonance images. *Neuroimage*, 23(Suppl. 1):S69–S84, 2004.

[43] B. Fischl, M. I. Sereno, and A. M. Dale. Cortical surface-based analysis. II: inflation, flattening, and a surface-based coordinate system. *Neuroimage*, 9(2):195–207, 1999.

[44] B. Fischl, M. I. Sereno, R. B. Tootell, and A. M. Dale. High-resolution intersubject averaging and a coordinate system for the cortical surface. *Human Brain Mapping*, 8(4):272–284, 1999.

[45] B. Fischl, A. van der Kouwe, C. Destrieux, E. Halgren, F. Ségonne, D. H. Salat, E. Busa, L. J. Seidman, J. Goldstein, D. Kennedy, V. Caviness, N. Makris, B. Rosen, and A. M. Dale. Automatically parcellating the human cerebral cortex. *Cerebral Cortex*, 14(1):11–22, 2004.

[46] M. A. Fletcher, K. A. Low, R. Boyd, B. Zimmerman, B. A. Gordon, C. H. Tan, N. Schneider-Garces, B. P. Sutton, G. Gratton, and M. Fabiani. Comparing aging and fitness effects on brain anatomy. *Frontiers in Human Neuroscience*, 10:286, 2016.

[47] K. Friston, J. Ashburner, S. Kiebel, T. Nichols, and W. Penny. *Statistical parametric mapping: the analysis of functional brain images*. Academic Press, London, 2007.

[48] C. Furlong, M. García-Fiñana, M. Puddephat, A. Anderson, K. Fabricius, N. Eriksen, B. Pakkenberg, and N. Roberts. Application of stereological methods to estimate post-mortem brain surface area using 3T MRI. *Magnetic Resonance Imaging*, 31(3):456–465, 2013.

[49] M. García-Fiñana, S. S. Keller, and N. Roberts. Confidence intervals for the volume of brain structures in cavalieri sampling with local errors. *Journal of Neuroscience Methods*, 179(1):71–77, 2009.

[50] A. S. Garden and N. Roberts. Fetal and fetal organ volume estimations with magnetic resonance imaging. *American Journal of Obstetrics & Gynecology*, 175(2):442–448, 1996.

[51] S. S. Ghosh, S. Kakunoori, J. Augustinack, A. Nieto-Castanon, I. Kovelman, N. Gaab, J. A. Christodoulou, C. Triantafyllou, J. D. Gabrieli, and B. Fischl. Evaluating the validity of volume-based and surface-based brain image registration for developmental cognitive neuroscience studies in children 4 to 11 years of age. *Neuroimage*, 53(1):85–93, 2010.

[52] P. Grosjean. *SciViews-R: a GUI API for R*. UMONS, MONS, Belgium, 2014.

[53] X. Gual-Arnau and L. Cruz-Orive. New rotational integrals in space forms, with an application to surface area estimation. *Applications of Mathematics*, 61(4):489–501, 2016.

[54] H. J. Gundersen, P. Bagger, T. F. Bendtsen, S. M. Evans, L. Korbo, N. Marcussen, A. Møller, K. Nielsen, J. R. Nyengaard, and B. Pakkenberg. The new stereological tools: disector, fractionator, nucleator and point sampled intercepts and their use in pathological research and diagnosis. *APMIS*, 96(10):857–881, 1988.

[55] H. J. Gundersen, T. F. Bendtsen, L. Korbo, N. Marcussen, A. Møller, K. Nielsen, J. R. Nyengaard, B. Pakkenberg, F. B. Sørensen, and A. Vesterby. Some new, simple and efficient stereological methods and their use in pathological research and diagnosis. *APMIS*, 96(5):379–394, 1988.

[56] H. J. Gundersen, E. B. Jensen, K. Kiêu, and J. Nielsen. The efficiency of systematic sampling in stereology–reconsidered. *Journal of Microscopy*, 193(Pt 3):199–211, 1999.

[57] R. E. Gur, P. E. Cowell, A. Latshaw, B. I. Turetsky, R. I. Grossman, S. E. Arnold, W. B. Bilker, and R. C. Gur. Reduced dorsal and orbital prefrontal gray matter volumes in schizophrenia. *Archives of General Psychiatry*, 57(8):761–768, 2000.

[58] X. Han, J. Jovicich, D. Salat, A. van der Kouwe, B. Quinn, S. Czanner, E. Busa, J. Pacheco, M. Albert, R. Killiany, P. Maguire, D. Rosas, N. Makris, A. Dale, B. Dickerson, and B. Fischl. Reliability of MRI-derived measurements of human cerebral cortical thickness: the effects of field strength, scanner upgrade and manufacturer. *Neuroimage*, 32(1):180–194, 2006.

[59] L. V. Hansen, J. R. Nyengaard, J. B. Andersen, and E. B. Jensen. The semi-automatic nucleator. *Journal of Microscopy*, 242(2):206–215, 2011.

[60] J. H. He. Zu-Geng's axiom vs Cavalieri's theory. *Applied Mathematics and Computation*, 152(1):9–15, 2004.

[61] R. Heinen, W. H. Bouvy, A. M. Mendrik, M. A. Viergever, G. J. Biessels, and J. de Bresser. Robustness of automated methods for brain volume measurements across different MRI field strengths. *PLoS One*, 11(10):E0165719, 2016.

[62] M. A. Howard, N. Roberts, M. García-Fiñana, and P. E. Cowell. Volume estimation of prefrontal cortical subfields using MRI and stereology. *Brain research. Brain research protocols*, 10(3):125–138, 2003.

[63] V. Howard and M. G. Reed. *Unbiased stereology: three-dimensional measurement in microscopy*. Advanced Methods. Garland Science, London, 2nd edition, 2004.

[64] J. E. Iglesias, J. C. Augustinack, K. Nguyen, C. M. Player, A. Player, M. Wright, N. Roy, M. P. Frosch, A. C. McKee, L. L. Wald, B. Fischl, K. Van Leemput, and Alzheimer's Disease Neuroimaging Initiative. A computational atlas of the hippocampal formation using ex vivo, ultra-high resolution MRI: application to adaptive segmentation of in vivo MRI. *Neuroimage*, 115:117–137, 2015.

[65] J. E. Iglesias, K. Van Leemput, P. Bhatt, C. Casillas, S. Dutt, N. Schuff, D. Truran-Sacrey, A. Boxer, B. Fischl, and Alzheimer's Disease Neuroimaging Initiative. Bayesian segmentation of brainstem structures in MRI. *Neuroimage*, 113:184–195, 2015.

[66] M. Jenkinson, P. Bannister, M. Brady, and S. Smith. Improved optimization for the robust and accurate linear registration and motion correction of brain images. *Neuroimage*, 17(2):825–841, 2002.

[67] M. Jenkinson and S. Smith. A global optimisation method for robust affine registration of brain images. *Medical Image Analysis*, 5(2):143–156, 2001.

[68] A. M. Jørgensen, L. Marner, and B. Pakkenberg. No change in total length of white matter fibers in Alzheimer's disease. *Neuroscience*, 157(4):878–883, 2008.

[69] J. Jovicich, S. Czanner, D. Greve, E. Haley, A. van der Kouwe, R. Gollub, D. Kennedy, F. Schmitt, G. Brown, J. Macfall, B. Fischl, and A. Dale. Reliability in multi-site structural MRI studies: effects of gradient non-linearity correction on phantom and human data. *Neuroimage*, 30(2):436–443, 2006.

[70] S. S. Keller, G. Baker, J. J. Downes, and N. Roberts. Quantitative MRI of the prefrontal cortex and executive function in patients with temporal lobe epilepsy. *Epilepsy & Behavior*, 15(2):186–195, 2009.

[71] S. S. Keller, J. S. Gerdes, S. Mohammadi, C. Kellinghaus, H. Kugel, K. Deppe, E. B. Ringelstein, S. Evers, W. Schwindt, and M. Deppe. Volume estimation of the thalamus using freesurfer and stereology: consistency between methods. *Neuroinformatics*, 10(4):341–350, 2012.

[72] S. S. Keller and N. Roberts. Measurement of brain volume using MRI: software, techniques, choices and prerequisites. *Journal of Anthropological Sciences*, 87:127–151, 2009.

[73] S. S. Keller, N. Roberts, M. García-Fiñana, S. Mohammadi, E. B. Ringelstein, S. Knecht, and M. Deppe. Can the language-dominant hemisphere be predicted by brain anatomy? *Journal of Cognitive Neuroscience*, 23(8):2013–2029, 2011.

[74] S. S. Keller, N. Roberts, and W. Hopkins. A comparative magnetic resonance imaging study of the anatomy, variability, and asymmetry of Broca's area in the human and chimpanzee brain. *Journal of Neuroscience*, 29(46):14607–14616, 2009.

[75] M. J. Kempton, T. S. Underwood, S. Brunton, F. Stylios, A. Schmechtig, U. Ettinger, M. S. Smith, S. Lovestone, W. R. Crum, S. Frangou, S. C. Williams, and A. Simmons. A comprehensive testing protocol for MRI neuroanatomical segmentation techniques: evaluation of a novel lateral ventricle segmentation method. *Neuroimage*, 58(4):1051–1059, 2011.

[76] K. Kim, P. A. Habas, F. Rousseau, O. A. Glenn, A. J. Barkovich, and C. Studholme. Intersection based motion correction of multislice MRI for 3-D in utero fetal brain image formation. *IEEE Transactions on Medical Imaging*, 29(1):146–158, 2010.

[77] F. Klauschen, A. Goldman, V. Barra, A. Meyer-Lindenberg, and A. Lundervold. Evaluation of automated brain MR image segmentation and volumetry methods. *Human Brain Mapping*, 30(4):1310–1327, 2009.

[78] J. S. Krouwer. Why Bland-Altman plots should use X, not (Y+X)/2 when X is a reference method. *Statistics in Medicine*, 27(5):778–780, 2008.

[79] L. Kubínová and J. Janácek. Estimating surface area by the isotropic fakir method from thick slices cut in an arbitrary direction. *Journal of Microscopy*, 191(2):201–211, 1998.

[80] L. Y. Lam and K. Shen. The Chinese concept of Cavalieri's principle and its applications. *Historia Mathematica*, 12(3):219–228, 1985.

[81] M. Levy Nogueira, O. Lafitte, J. M. Steyaert, H. Bakardjian, B. Dubois, H. Hampel, and L. Schwartz. Mechanical stress related to brain atrophy in Alzheimer's disease. *Alzheimer's & Dementia*, 12(1):11–20, 2016.

[82] B. B. Little and L. M. Snell. Brain growth among fetuses exposed to cocaine in utero: asymmetrical growth retardation. *Obstetrics & Gynecology*, 77(3):361–364, 1991.

[83] J. M. Lucocq. Efficient quantitative morphological phenotyping of genetically altered organisms using stereology. *Transgenic Research*, 16(2):133–145, 2007.

[84] D. M. Lyons and K. J. Parker. Stress inoculation-induced indications of resilience in monkeys. *Journal of Traumatic Stress*, 20(4):423–433, 2007.

[85] K. N. Mayer, B. Latal, W. Knirsch, I. Scheer, M. von Rhein, B. Reich, J. Bauer, K. Gummel, N. Roberts, and R. O. Tuura. Comparison of automated brain volumetry methods with stereology in children aged 2 to 3 years. *Neuroradiology*, 58(9):901–910, 2016.

[86] T. M. Mayhew. A review of recent advances in stereology for quantifying neural structure. *Journal of Neurocytology*, 21(5):313–328, 1992.

[87] M. Menendez and O. Arias-Carrión. Indices of regional brain atrophy: formulae and nomenclature. *Cureus*, 7(8):E295, 2015.

[88] R. P. Michel and L. M. Cruz-Orive. Application of the Cavalieri principle and vertical sections method to lung: estimation of volume and pleural surface area. *Journal of Microscopy*, 150(Pt 2):117–136, 1988.

[89] P. R. Mouton, L. J. Martin, M. E. Calhoun, G. Dal Forno, and D. L. Price. Cognitive decline strongly correlates with cortical atrophy in Alzheimer's dementia. *Neurobiology of Aging*, 19(5):371–377, 1998.

[90] M. C. Murphy, J. Huston, C. R. Jack, K. J. Glaser, A. Manduca, J. P. Felmlee, and R. L. Ehman. Decreased brain stiffness in Alzheimer's disease determined by magnetic resonance elastography. *Journal of Magnetic Resonance Imaging*, 34(3):494–498, 2011.

[91] J. Muschelli, E. Sweeney, M. Lindquist, and C. Crainiceanu. fslr: connecting the FSL software with R. *The R Journal*, 7(1):163–175, 2015.

[92] J. R. Nyengaard and H. J. G. Gundersen. Sampling for stereology in lungs. *European Respiratory Review*, 15(101):107–114, 2006.

[93] C. Orellana, D. Ferreira, J. S. Muehlboeck, P. Mecocci, B. Vellas, M. Tsolaki, I. Kłoszewska, H. Soininen, S. Lovestone, A. Simmons, L. O. Wahlund, E. Westman,

and AddNeuronMed consortium and for the Alzheimer's Disease Neuroimaging Initiative. Measuring global brain atrophy with the brain volume/cerebrospinal fluid index: normative values, cut-offs and clinical associations. *Neurodegenerative Diseases*, 16(1-2):77–86, 2016.

[94] H. R. Pardoe, G. S. Pell, D. F. Abbott, and G. D. Jackson. Hippocampal volume assessment in temporal lobe epilepsy: how good is automated segmentation? *Epilepsia*, 50(12):2586–2592, 2009.

[95] J. L. Powell, P. A. Lewis, R. I. Dunbar, M. García-Fiñana, and N. Roberts. Orbital prefrontal cortex volume correlates with social cognitive competence. *Neuropsychologia*, 48(12):3554–3562, 2010.

[96] M. J. Puddephat. *Computer interface for convenient application for stereological methods for unbiased estimation of volume and surface area: studies using MRI with particular reference to the human brain*. Phd thesis, University of Liverpool, Liverpool, 1998.

[97] A. Qiu, A. Rifkin-Graboi, H. Chen, Y. S. Chong, K. Kwek, P. D. Gluckman, M. V. Fortier, and M. J. Meaney. Maternal anxiety and infants' hippocampal development: timing matters. *Translational Psychiatry*, 3:E306, 2013.

[98] R Core Team. *R: a language and environment for statistical computing*. R Foundation for Statistical Computing, Vienna, Austria, 2016.

[99] N. Raz, U. Lindenberger, K. M. Rodrigue, K. M. Kennedy, D. Head, A. Williamson, C. Dahle, D. Gerstorf, and J. D. Acker. Regional brain changes in aging healthy adults: general trends, individual differences and modifiers. *Cerebral Cortex*, 15(11):1676–1689, 2005.

[100] M. J. Rivkin, P. E. Davis, J. L. Lemaster, H. J. Cabral, S. K. Warfield, R. V. Mulkern, C. D. Robson, R. Rose-Jacobs, and D. A. Frank. Volumetric MRI study of brain in children with intrauterine exposure to cocaine, alcohol, tobacco, and marijuana. *Pediatrics*, 121(4):741–750, 2008.

[101] R. A. Robb and D. P. Hanson. A software system for interactive and quantitative visualization of multidimensional biomedical images. *Australasian Physical and Engineering Science in Medicine*, 14(1):9–30, 1991.

[102] N. Roberts. Manual morphometry. In A. W. Toga, editor, *Brain mapping: an encyclopedic reference*, pages 333–343. Academic Press, Waltham, 2015.

[103] N. Roberts, M. J. Puddephat, and V. McNulty. The benefit of stereology for quantitative radiology. *British Journal of Radiology*, 73(871):679–697, 2000.

[104] I. Sack, K. J. Streitberger, D. Krefting, F. Paul, and J. Braun. The influence of physiological aging and atrophy on brain viscoelastic properties in humans. *PLoS One*, 6(9):E23451, 2011.

[105] C. A. Sandman, E. P. Davis, C. Buss, and L. M. Glynn. Exposure to prenatal psychobiological stress exerts programming influences on the mother and her fetus. *Neuroendocrinology*, 95(1):7–21, 2012.

[106] J. Schindelin, I. Arganda-Carreras, E. Frise, V. Kaynig, M. Longair, T. Pietzsch, S. Preibisch, C. Rueden, S. Saalfeld, B. Schmid, J. Y. Tinevez, D. J. White, V. Hartenstein, K. Eliceiri, P. Tomancak, and A. Cardona. Fiji: an open-source platform for biological-image analysis. *Nature Methods*, 9(7):676–682, 2012.

[107] D. Schmitter, A. Roche, B. Maréchal, D. Ribes, A. Abdulkadir, M. Bach-Cuadra, A. Daducci, C. Granziera, S. Klöppel, P. Maeder, R. Meuli, G. Krueger, and Alzheimer's Disease Neuroimaging Initiative. An evaluation of volume-based morphometry for prediction of mild cognitive impairment and Alzheimer's disease. *NeuroImage: Clinical*, 7:7–17, 2015.

[108] C. A. Schneider, W. S. Rasband, and K. W. Eliceiri. NIH Image to ImageJ: 25 years of image analysis. *Nature Methods*, 9(7):671–675, 2012.

[109] R. Schneider and W. Weil. *Stochastic and integral geometry*. Probability and Its Applications. Springer-Verlag Berlin Heidelberg, 2008.

[110] F. Ségonne, A. M. Dale, E. Busa, M. Glessner, D. Salat, H. K. Hahn, and B. Fischl. A hybrid approach to the skull stripping problem in MRI. *Neuroimage*, 22(3):1060–1075, 2004.

[111] L. T. Singer, A. Salvator, R. Arendt, S. Minnes, K. Farkas, and R. Kliegman. Effects of cocaine/polydrug exposure and maternal psychological distress on infant birth outcomes. *Neurotoxicology and Teratology*, 24(2):127–135, 2002.

[112] S. M. Smith, M. Jenkinson, M. W. Woolrich, C. F. Beckmann, T. E. Behrens, H. Johansen-Berg, P. R. Bannister, M. De Luca, I. Drobnjak, D. E. Flitney, R. K. Niazy, J. Saunders, J. Vickers, Y. Zhang, N. De Stefano, J. M. Brady, and P. M. Matthews. Advances in functional and structural MR image analysis and implementation as FSL. *Neuroimage*, 23(Suppl. 1):S208–S219, 2004.

[113] B. Stanfill, H. Hofmann, and U. Genschel. rotations: an R package for SO(3) data. *The R Journal*, 6(1):68–78, 2014.

[114] C. Studholme. Mapping fetal brain development in utero using magnetic resonance imaging: the Big Bang of brain mapping. *Annual Review of Biomedical Engineering*, 13:345–368, 2011.

[115] E. R. Weibel. *Stereological methods vol 1: practical methods for biological morphometry*. Academic Press Inc., London, 1979.

[116] M. W. Weiner, D. P. Veitch, P. S. Aisen, L. A. Beckett, N. J. Cairns, J. Cedarbaum, R. C. Green, D. Harvey, C. R. Jack, W. Jagust, J. Luthman, J. C. Morris, R. C. Petersen, A. J. Saykin, L. Shaw, L. Shen, A. Schwarz, A. W. Toga, J. Q. Trojanowski, and Alzheimer's Disease Neuroimaging Initiative. 2014 update of the Alzheimer's disease neuroimaging initiative: a review of papers published since its inception. *Alzheimer's & Dementia*, 11(6):E1–120, 2015.

[117] M. J. West. *Basic stereology for biologists and neuroscientists*. Cold Spring Harbor Laboratory Press, Cold Spring Harbor, New York, 2012.

[118] B. Whitcher, V. J. Schmid, and A. Thornton. Working with the DICOM and NIfTI data standards in R. *Journal of Statistical Software*, 44(6):1–29, 2011.

[119] B. Zuckerman, D. A. Frank, R. Hingson, H. Amaro, S. M. Levenson, H. Kayne, S. Parker, R. Vinci, K. Aboagye, and L. E. Fried. Effects of maternal marijuana and cocaine use on fetal growth. *New England Journal of Medicine*, 320(12):762–768, 1989.